Structural Investigation of Hydrophobically Modified Thermoresponsive Polymers and Their Influence on the Rheology of Microemulsions

vorgelegt von
M. Sc.
Albert Prause
ORCID: 0000-0001-9267-1220

von der Fakultät II – Mathematik und Naturwissenschaften
der Technischen Universität Berlin
zur Erlangung des akademischen Grades

Doktor der Naturwissenschaften
Dr. rer. nat.

genehmigte Dissertation

Promotionsausschuss:

Vorsitzender: Prof. Dr. Peter Strasser
Gutachter: Prof. Dr. Michael Gradzielski
Gutachterin: Prof. Dr. Christine M. Papadakis

Tag der wissenschaftlichen Aussprache: 09. Januar 2023

Berlin 2023

Abstract

A library of nonsymmetrical thermosensitive BAB* block copolymers was investigated in terms of their aggregation behavior and rheological properties as a function of temperature in aqueous solutions. Additionally, these block copolymers were used to study the modification of temperature-dependent rheological properties of microemulsions. The block copolymers comprise a permanently hydrophilic poly(N,N-dimethylacrylamide) (pDMAm) block "A", a permanently hydrophobic n-dodecyl (C_{12}) chain as end-group "B", and a thermoresponsive (TR) block "B*" featuring a lower critical solution temperature (LCST). To vary the chemical nature and LCST behavior, different polyacrylamides, *i.e.*, poly(N-n-propylacrylamide) (pNPAm), poly(N,N-diethylacrylamide) (pDEAm), poly(N-isopropyl-acrylamide) (pNiPAm), and poly(N-acryloylpyrrolidine) (pNAP), were introduced as TR blocks. Additionally, the length of the TR block was varied systematically as well as the architecture of the block copolymer, for which three types were employed, *i.e.*, BAB*, B_2AB^*, and $B(AB^*)_2$.

The influence of the length of the TR block on the aggregation behavior and temperature response was studied via light and neutron scattering (SLS, DLS, and SANS). For TR blocks with more than 40 monomer units, a marked hydrophobic interaction occurs above the LCST, leading to ordered, well-structured clusters of micellar aggregates. Thus, the temperature-dependent mesoscopic organization of aggregates can be tuned by the length and type of the TR block.

The temperature response of rheological properties was investigated and compared for the various copolymer architectures. Depending on the TR block and the copolymer architecture, their solution's viscosity can increase significantly with rising temperature. These results are well in line with the observed mesoscopic organization obtained by SLS, DLS, and SANS experiments. Additionally, fluorescence experiments using the solvatochromic probe Prodan revealed a direct relationship between the increased viscosity and the formation of additional hydrophobic domains of TR blocks. Consequently, the viscoelastic properties of aqueous solutions can be tuned temperature dependently by carefully designing these copolymers.

Following this, the viscoelastic properties of low-viscous oil-in-water (O/W) microemulsions (MEs) can also be adjusted. For a properly chosen ME concentration, these block copolymers lead to a viscosity increase with rising temperature. At a polymer concentration of about $22\,\mathrm{g\,L^{-1}}$, the most pronounced enhancement was observed for the pNPAm-based systems, with factors up to about 3, 5, and 8 for BAB*, B_2AB^*, and $B(AB^*)_2$, respectively. The enhancement is caused by the formation of a transient network mediated by TR blocks, as evidenced by the direct correlation between the viscosity enhancement and the attraction strength. This kind of tailored temperature-dependent viscosity control of surfactant-based systems could therefore be advantageous for applications requiring a high hydrophobic payload, which is accomplished by the droplet microemulsion.

Zusammenfassung

Verschiedene asymmetrische, wärmeempfindliche BAB*-Blockcopolymere wurden hinsichtlich ihres Aggregationsverhaltens und ihrer rheologischen Eigenschaften in wässrigen Lösungen temperaturabhängig studiert. Zusätzlich wurde unter Verwendung dieser Blockcopolymere die Veränderung der temperaturabhängigen rheologischen Eigenschaften von Mikroemulsionen untersucht. Die Blockcopolymere bestehen aus einem permanent hydrophilen Poly(N,N-dimethylacrylamid)-Block (pDMAm) „A", einer permanent hydrophoben n-dodecyl-Endgruppe (C_{12}) „B" und einem thermoresponsiven (TR) Block „B*", der eine *lower critical solution temperature* (LCST) aufweist. Um die chemische Natur und das LCST-Verhalten zu variieren, wurden die Polyacrylamide Poly(N-n-propylacrylamid) (pNPAm), Poly(N,N-diethylacrylamid) (pDEAm), Poly(N-isopropylacrylamid) (pNiPAm) und Poly(N-acryloylpyrrolidin) (pNAP) als TR-Blöcke eingeführt. Die Länge der TR-Blöcke sowie die Architektur der Blockcopolymere wurden systematisch variiert. Drei verschiedene Architekturen, BAB*, B_2AB* und $B(AB*)_2$, wurden untersucht.

Der Einfluss der Länge des TR-Blocks auf das Aggregationsverhalten und die Temperaturabhängigkeit wurde mittels Licht- und Neutronenstreuung (SLS, DLS und SANS) untersucht. Bei TR-Blöcken aus über 40 Monomereinheiten tritt eine ausgeprägte hydrophobe Wechselwirkung oberhalb der LCST auf, die zu geordneten, gut strukturierten Aggregaten führt. Somit kann die temperaturabhängige mesoskopische Organisation der Aggregate durch die Länge und Art des TR-Blocks beeinflusst werden.

Die Temperaturabhängigkeit der viskoelastischen Eigenschaften wurde für die verschiedenen Copolymer-Architekturen untersucht und verglichen. Je nach TR-Block und Architektur kann die Viskosität der Lösung mit steigender Temperatur deutlich zunehmen. Diese Ergebnisse stimmen gut mit den strukturellen Erkenntnissen überein, die durch SLS-, DLS- und SANS-Experimente gewonnen wurden. Darüber hinaus zeigten Fluoreszenzexperimente mit der solvatochromen Sonde Prodan einen direkten Zusammenhang zwischen der erhöhten Viskosität und der Bildung zusätzlicher hydrophober Domänen bestehend aus TR-Blöcken. Durch sorgfältiges Design dieser Copolymere können die viskoelastischen Eigenschaften wässriger Lösungen temperaturabhängig angepasst werden.

Die Viskosität von Öl-in-Wasser (O/W) Mikroemulsionen (ME) konnte durch Zugabe der Blockcopolymere temperaturabhängig beeinflusst werden. Der ausgeprägteste Viskositätsanstieg wurde für die pNPAm-basierten Systeme gefunden. Bei einer Polymerkonzentration von $22\,\mathrm{g\,L^{-1}}$ wurden für die Architekturen BAB*, B_2AB* bzw. $B(AB*)_2$ Viskositätsanstiege um das 3-, 5- und 8-fache beobachtet. Die direkte Korrelation zwischen der attraktiven Wechselwirkung und der Viskositätserhöhung deutet auf die Ausbildung eines TR-Block-vermittelten Netzwerks hin. Diese Art der maßgeschneiderten temperaturabhängigen Viskositätskontrolle von Tensidsystemen sollte daher für Anwendungen von Vorteil sein, die eine hohe hydrophobe Nutzlast erfordern, welches durch die Mikroemulsionströpfchen gewährleistet wird.

Danksagung

Die Arbeit an meiner Promotion wurde von vielen hilfsbereiten Menschen aktiv unterstützt. Im Folgenden möchte ich mich bei allen Personen bedanken, die sich Zeit dafür genommen haben.

An erster Stelle möchte ich Prof. Michael Gradzielski danken, dass er mir die Möglichkeit gab, in seiner Arbeitsgruppe mit diesem Thema zu promovieren. Vielen Dank für den stets vorhandenen Freiraum, die hilfreichen Gespräche und die zahlreichen Vorschläge, das Thema zu bearbeiten. Zusätzlich wurde ich von ihm durch zahlreiche wertvolle Diskussionen, viele nützliche Kommentare und einem breiten Erfahrungsschatz sehr unterstützt.

Prof. André Laschewsky und Michelle Hechenbichler möchte ich für die erfolgreiche und umfangreiche Zusammenarbeit im Projekt danken. Die Diskussionen mit und Anmerkungen von Prof. André Laschewsky waren stets hilfreich. Michelle Hechenbichler danke ich für die Synthese der Polymere, ohne die diese Arbeit nicht möglich gewesen wäre. Bei Prof. Christine Papadakis bedanke ich mich herzlich für die Übernahme des Zweitgutachtens. Prof. Peter Strasser danke ich für die Übernahme des Prüfungsvorsitzes.

Der Deutschen Forschungsgemeinschaft (DFG) danke ich für die Finanzierung des Projektes. Weiterer Dank geht an das Institut Laue–Langevin (ILL), dem Heinz–Maier–Leibnitz Zentrum (MLZ) in Kooperation mit dem Forschungszentrum Jülich und der *ISIS Pulsed Neutron Source* für die bewilligten Messzeiten und die dazugehörige finanzielle Unterstützung sowie an die Kontaktpersonen vor Ort, die die Messzeiten überhaupt möglich machten.

Besonderer Dank geht an Robert Schmidt, der mich bei der Arbeit im Labor tatkräftig unterstützte. Jana Lutzki danke ich für die Messung der Brechungsindexinkremente. Miriam Simon danke ich für die Cryo-TEM aufnahmen, das Korrekturlesen meiner Arbeit sowie der gemeinsam verbrachten Zeit während meiner Promotion. Vivian Spiering und Rahel Marschall danke ich für die gemeinsam verbrachte Zeit und das Korrekturlesen meiner Arbeit. Zusätzlich bedanke ich mich bei Sebastian Bayer, Anja Hörmann, Olga Kuzminskaya sowie beim gesamten Stranski-Laboratorium für die tolle Zeit, die Kaffeepausen und die Unterstützung bei Fragen und Problemen.

Vielen Dank geht auch an die GKSHP-Gruppe, die durch zahlreiche sportlichen Aktivitäten, Kaffee und Kuchen Abwechselung in den Alltag gebracht hat. Insbesondere geht ein großer Dank an Anni und Basti im Café Strönisch.

Bei Jessica, Birte, Ina und Tjebbe bedanke ich mich ganz besonders für die zahlreichen Tätigkeiten, Tage und Abende, die wir gemeinsam verbracht haben. Spezieller Dank geht nochmal an Ina und Birte für das Coworking und Korrekturlesen meiner Arbeit.

Zu guter Letzt möchte ich mich ganz lieb bei meiner Familie bedanken. Meinen Eltern, Angela und Dietmar, danke ich für die bedingungslose Unterstützung während meiner Promotion, auch wenn es manchmal schwierig zu erklären ist, was ich da eigentlich die ganze Zeit mache. Der größte Dank geht an meine Partnerin Julia für die ganze Unterstützung und die zusätzliche Betreuung von unserem Sohn Gustav.

Contents

Chapter 1

General Introduction

1.1 Hydrophobically Modified Thermoresponsive Block Copolymers

In aqueous solutions, amphiphiles, consisting of a hydrophilic and a hydrophobic part, commonly self-assemble and form larger structures. An amphiphile is also known as a surfactant which comprises a hydrophilic head and a hydrophobic tail. The self-assemble process is governed by an increase in entropy via reducing the contact area between water and the hydrophobic part of an amphiphile. This effect is called hydrophobic effect and leads to the formation of micellar aggregates in aqueous solutions. The shape of the formed micelles can be correlated via the packing parameter $p = v/a_0 l$ with the surfactant's molecular dimensions, $i.\,e.$, the volume of the hydrophobic part (v), the head group area (a_0), and length of the hydrophobic tail (l).[1] Accordingly, spherical micelles are formed for $p \leq 1/3$. For $1/3 < p \leq 1/2$, rod-like or worm-like micelles are formed. Vesicles are formed for $1/2 < p \leq 1$, while for $p = 1$, lamellar structures can also be expected. Values for p larger than 1 would lead to inverse structures. This concept was developed for low molecular weight surfactants. However, it can also be applied to amphiphilic polymers.[2]

In case of amphiphilic polymers, such as simple AB type block copolymers, where A is a hydrophilic block and B is a hydrophobic block, similar self-assembled micellar structures are formed in aqueous solutions.[2–5] When the hydrophobic B block comprises an alkyl chain, $e.\,g.$, a n-dodecyl chain, the copolymer can be called a hydrophobically modified (HM) block copolymer. For block copolymers, various block sequences can be conceived, such as AB, BAB, ABC, and more, where C generally is a third block of different chemical composition compared to A and B. These block copolymers can form different micellar structures, $e.\,g.$, core-corona (symmetric, star-like, crew-cut), hairy, flower-like, and more.[2] With a focus on BAB type block copolymers, flower-like micelles or networks are formed in aqueous solutions.[6,7] The network formation occurs when hydrophobic B blocks form domains in solution which are interconnected by hydrophilic A blocks. This type of association of BAB copolymers offers a simple way of controlling the solution's rheology by forming transient networks.[8–11] Typically, the strength of the copolymer solution's rheological properties depends on the number of interconnections per B domain, the chemical structure of the block copolymer, and especially the type and length of the B block.

In commercial applications, BAB copolymers are often used as rheological modifiers for water-based systems, such as paints[12] or coatings[13]. However, as temperature rises, these systems experience an inherent reduction of rheological properties, such as viscosity, which is linked to the required activation energy to break network nodes. With increasing temperature, the probability rises that the B blocks are not contained inside the self-assembled network nodes which leads to severe reduction or loss of solution's viscoelastic properties. To counterbalance this, additional network nodes need to be formed with increasing temperature, either progressively or above a certain threshold. Consequently, a temperature-responsive B* block would solve this problem for a symmetrical B*AB* copolymer in solution and could be beneficial for certain applications. For this thermally induced response, a B* block with a lower critical solution temperature (LCST) can be suitable. Above the LCST, the initially hydrophilic B* block undergoes a coil-to-globular transition after which the B* block renders more hydrophobic. This transition would then lead to the formation of additional domains that could physically cross-link (Scheme 1.1).
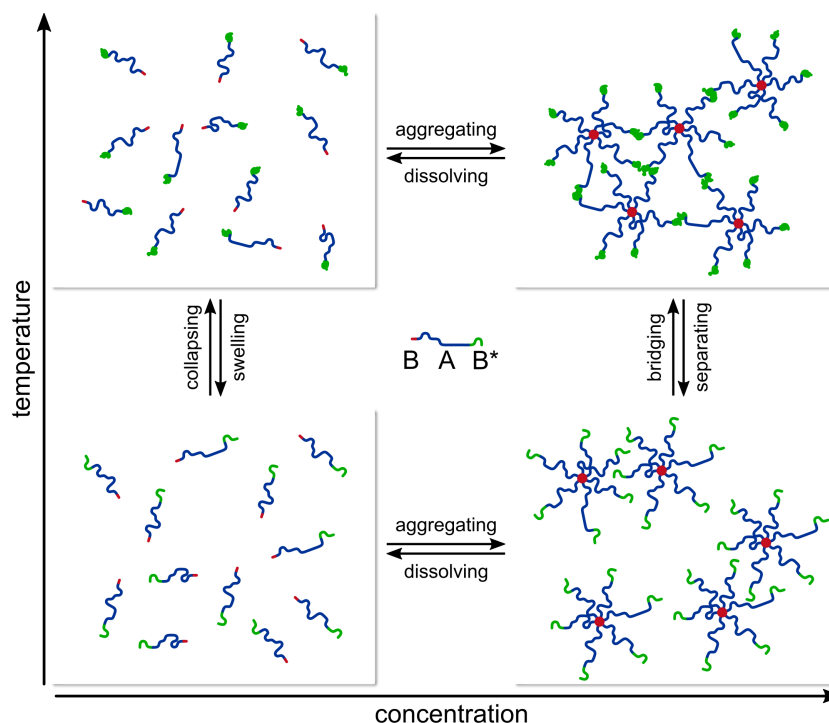
Scheme 1.1: Schematic drawing of temperature and concentration dependent behavior of hydrophobically modified thermoresponsive (HMTR) block copolymers in solution. The permanently hydrophobic block B is red (-), the permanently hydrophilic block A is blue (〜), and the thermoresponsive (TR) block B* is green (〜•).

According to phenomenological observations, three different LCST phase transition types can be classified.[14] Type I is considered to be the *classical* case of the Flory–Huggins solution theory without an "off-zero" limiting critical point, where the cloud point of the polymer solution largely depends on the molecular weight of the polymer. For instance, polymers following this type are poly(*N*,*N*-diethylacrylamide) (pDEAm),[15] and poly(*N*-

vinyl caprolactam)[16]. Type II exhibits one "off-zero" limiting critical point, which results in a cloud point that is rather independent of the molecular weight of the polymer. For example, poly(N-isopropylacrylamide) (pNiPAm) is behaving according to this type.[17] Type III is the combination of Type I and II with two "off-zero" limiting critical points, where at low polymer volume fractions the cloud point follows the Type I behavior while at higher volume fractions the Type II behavior is observed. Here, poly(methyl vinyl ether) can be stated as an example.[17]

In the case of symmetrical temperature-responsive block copolymers, several studies have been published with various block copolymers.[18–25] Recently, different copolymers with thermoresponsive (TR) properties were reviewed for different healthcare purposes, such as drug delivery via mucosal and topical application or as injectable hydrogels.[25] In case of drug delivery, various hydrophobic substances, *i. e.*, ketoprofen,[18] spironolactone,[18] levonorgestrel,[20] and insulin,[19] were investigated in terms of their delivery and release. For this purpose, assemblies of pEG–pLGA–pEG and pLGA–pEG–pLGA (pEG: poly(ethylene glycol), pLGA: poly(lactic-*co*-glycolic acid)) block copolymers were used. According to this, Basu *et al.* (2016)[22] studied thermosensitive hydrogels formed by block copolymers of the ABA and BAB type comprising pEG, pLA (poly(lactic acid)), and pLGA. Comparing the ABA and BAB types, Cui *et al.* (2019)[24] found in a comparative study that ABA copolymers form hydrophobic channels which lead to gel formation while BAB copolymers exhibit a bridge dominant gel state followed by a channel dominant gel state.

Other block copolymers, such as the well-known pEO–pPO–pEO block copolymers (Pluronics) or pNiPAm–pDMAm–pNiPAm (pNiPAm: poly(N-isopropylacrylamide), pDMAm: poly(N,N-dimethylacrylamide)) were also investigated. For the pEO–pPO–pEO block copolymers, the thermoreversible hydrogel formation was studied under physiological conditions.[26,27] The block copolymer more similar to the ones used in this work, pNiPAm–pDMAm–pNiPAm, showed a formation of thermoreversible hydrogels above a concentration of 7.5 % by weight, where the pDMAm block bridges formed pNiPAm domains.[21] Additionally, other pNiPAm-based block copolymers, pNiPAm–pEG–pNiPAm, were investigated in terms of their self-assembly in solution via nuclear magnetic resonance (NMR) spectroscopy, light scattering, and small-angle neutron scattering (SANS). Above the LCST, the pNiPAm blocks were forming nanoparticles while the middle pEG block either bridges these nanoparticles, which leads to larger clusters, or simply folds back to form a loop.[23]

1.2 Microemulsions

Microemulsions are ternary systems that can be thought of as surfactant stabilized binary systems of two immiscible liquids.[28] They can form spontaneously and are thermodynamically stable, for which a very low interfacial tension is essential.[29] In many cases, one liquid is water, and the other is a hydrophobic oil. Thus, oil-in-water (O/W), water-in-oil

(W/O), or bicontinuous microemulsions (MEs) can be formed depending on the proportion between the two components. However, microemulsions can also be observed for polar liquids other than water as well as without a surfactant.[30]

Microemulsions can assume the shape of bicontinuous structures or droplets.[31] The droplet size of microemulsions typically ranges between 5 and 30 nm.[32] Adding an alcohol as cosurfactant is a commonly used method for lowering the interfacial tension, which allows for bigger ME droplets to be thermodynamically stable. The solubilization capacity of the ME is proportional to their size and increases as the droplet size increases. This relation can be used to tune and increase the amount of solubilized oil for a given surfactant concentration.[33]

Due to their thermodynamic stability, well-defined structure, and high solubilization capacities of hydrophobic substances, microemulsions are frequently employed in research and industrial applications.[34] In fundamental research, they were employed as well-defined model systems or considered as loaded micellar systems, *e. g.*, to study the structural control of polyelectrolyte–microemulsion complexes,[35] or the immobilization of microemulsions in mesoporous silica materials.[36] For industrial purposes, microemulsions are used in cosmetics,[37] detergency,[38,39] soil remediation,[40] nanosized reactors for the formation of nanoparticles or catalysts,[41–43] solubilizing pharmaceuticals and agrochemicals for the purpose of drug delivery,[44] and more.
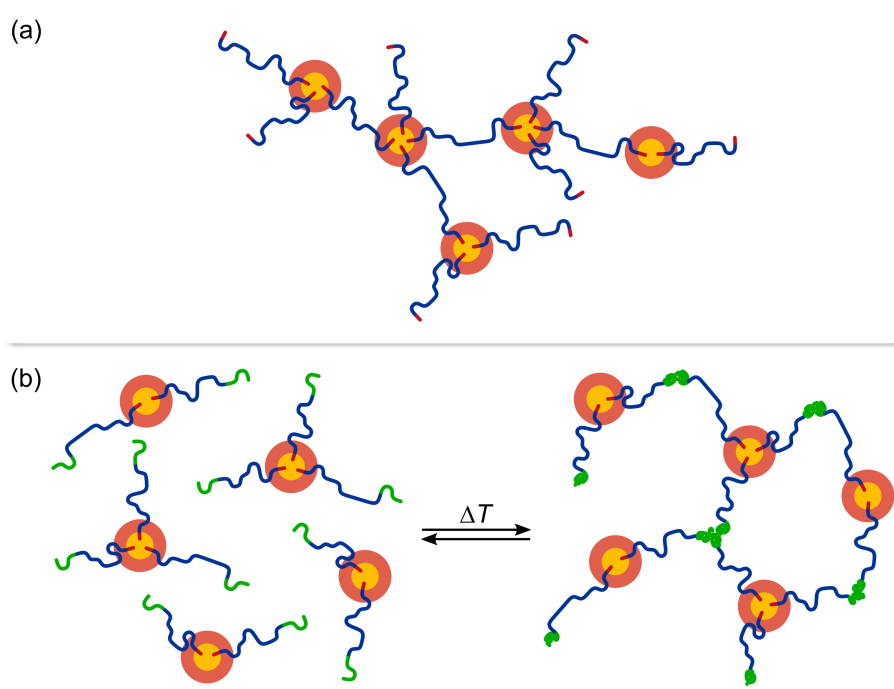
1.3 Mixtures of Microemulsions and Hydrophobically Modified Thermoresponsive Block Copolymers

The thermodynamic stability, structural sizes in the nanometer range, and a tunable solubilization capacity are major benefits of microemulsions. However, its low viscosity can be a significant drawback for many applications.[45] Thus, increasing and controlling the viscosity of microemulsions is an important research area in colloid science. There are basically two methods that can be used to control the viscosity of microemulsions, either gelling the aqueous solution[46] or bridging the microemulsion droplets via admixing of polymers.[47–50]

Following the approach of bridging the microemulsion droplets, the added polymer must have at least two distinct hydrophobic stickers, *e. g.*, a BAB block copolymer, which act as anchors inside the microemulsion droplets (Scheme 1.2a). The hydrophobic sticker should have an anchoring affinity that is high enough to obtain a sufficient bridging of the droplets.[51] Additionally, to achieve an effective bridging of microemulsion droplets, the size of the polymer should be in the range of the average droplet distance. This relation was investigated by Testard *et al.* (2008)[52] and Sarraguça *et al.* (2008)[53] via Monte–Carlo simulations. They found that the potential minimum is located at a droplet distance in the range of the end-to-end distance of the polymer.[52] A major parameter that influences the droplet–polymer interactions was found to be the polymer-to-droplet ratio. This ratio can be changed either by increasing the polymer concentration or decreasing the

microemulsion concentration. However, a decreasing microemulsion concentration would automatically lead to an increasing average droplet distance. Other parameters, such as the contour length and the stiffness of the polymer, play a minor role as long as the polymer does not get too long or too stiff.[53]

Quantitative information about the bridging interaction of such networks can be deduced via small-angle neutron scattering (SANS) experiments. Maccarrone *et al.* (2007)[54] showed that effective bridging starts to take place at an average droplet distance of 2.6 times the end-to-end distance of the polymer and reaches an equilibrium at about 1.3 times. Experimentally, the influence of the polymer-to-droplet ratio was investigated by Malo de Molina *et al.* (2015)[55]. For sufficiently high polymer-to-droplet ratios (approximately 4) and the droplet distances that matches the range of the polymer end-to-end distance, a space-filling network of bridged microemulsion droplets can be observed. With decreasing polymer-to-droplet ratio, clusters become smaller until only single decorated droplets can be observed.[55]

Scheme 1.2: Schematic drawing of ME–polymer mixtures with (a) conventional BAB block copolymers and (b) thermoresponsive BAB* block copolymers. The microemulsion droplet is orange (●), the permanently hydrophobic block B is red (-), the permanently hydrophilic block A is blue (∿), and the thermoresponsive (TR) block B* is green (⌒►●).

As mentioned above, the reduction of viscoelastic properties of BAB block copolymer solutions with increasing temperature can have an adverse effect, which might be avoided or can be tuned preferably. For that purpose, it is necessary that the block copolymer comprises a thermoresponsive (TR) B* block that can form additional domains with increasing temperature in order to physically cross-link the microemulsion droplets (Scheme 1.2b). This temperature-dependent hydrophobicity of one B block is achieved by using

a polymer block which exhibits a lower critical solution temperature (LCST). Especially, for the purpose of bridging via the formation of additional domains, it is important that the TR block is not preferably incorporated into the microemulsion droplet. For instance, it is expectably the case for pNiPAm as thermoresponsive polymer, for which a water content well around 40 % was observed above the LCST.[56,57] In a previous study of a ME–polymer mixture, it was shown via Förster resonance energy transfer (FRET) experiments that C$_{12}$-*block*-pDMAm-*block*-pNiPAm block copolymers bridge the microemulsion droplets by forming additional pNiPAm domains above the LCST.[58]

In this context, it seems reasonable to have one hydrophobic part B of the copolymer permanently anchored within the microemulsion droplets and an additional TR block B* that forms interconnecting domains at higher temperatures. This type of copolymer design gives the possibility of joining the droplets into a network with improved temperature-dependent viscoelastic properties. In this case, the viscosity would be determined by the binding strength between the TR blocks. The binding strength of these domains would mainly depend on the number of blocks in each domain and their residence time, which defines the system's structural relaxation time.

1.4 Motivation

As described above, adjusting and controlling the rheological properties, especially the viscosity, of aqueous solutions is very important for all kinds of applications. For this purpose, various types of polymers can be used, such as BAB block copolymers, where the hydrophobic B blocks self-assemble and form hydrophobic domains in solution. These domains can then be considered as nodes of a polymer network. However, for applications which involve or rely on different temperatures, the viscosity would be reduced with increasing temperature. This reduction is basically governed by an increased probability of crossing activation barriers with rising thermal energy. The retention time of B blocks inside the hydrophobic domains reduces accordingly which would lead to fewer and weaker network nodes. To counteract this, the formation of additional network nodes can be beneficial with increasing temperature. A temperature-responsive block B* can be introduced into the block copolymer. For that purpose, the LCST phase transition behavior can be exploited which would cause the B* block of the polymer to undergo a coil-to-globular transition. This transition is referred to as a transition from hydrophilic to hydrophobic and would lead to a formation of interconnecting B* domains.

The aim of this work is to modify rheological properties of low-viscous microemulsions as a function of temperature (Scheme 1.3). Temperature-controllable and adjustable viscosity may be desirable for applications where there is especially contact with human skin, such as cosmetics and drug delivery through the skin.[44,59] In other words, it could be useful to have a rather low-viscous microemulsion at room temperature that can be applied to human skin via spraying. Upon contact with the human skin (up to a temperature of about 37 °C), the solution should then become more viscous to
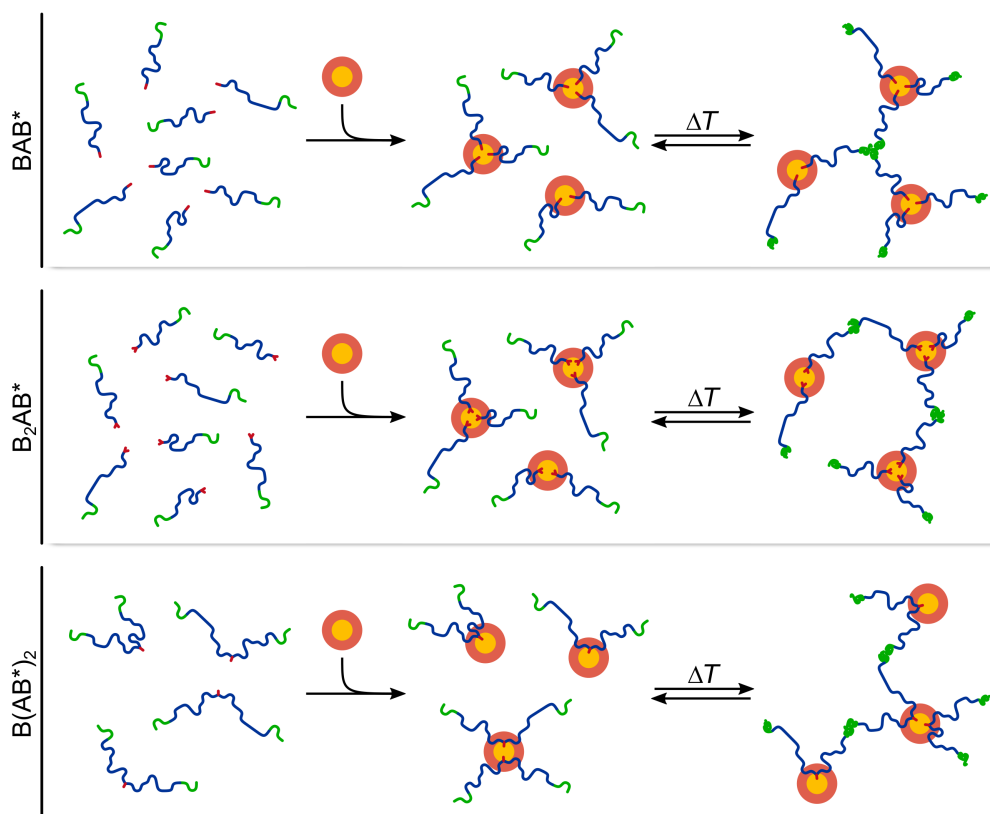
Scheme 1.3: Conceptual design of interconnecting microemulsion (ME) droplets for the three different block copolymer architectures, *i. e.*, BAB*, B$_2$AB* (increased hydrophobic interaction), and B(AB*)$_2$ (increased thermoresponsive interaction). The microemulsion droplet is orange (⬤), the permanently hydrophobic block B is red (-), the permanently hydrophilic block A is blue (〰), and the thermoresponsive (TR) block B* is green (➜●).

reduce its ability to flow. For this purpose, hydrophobically modified thermoresponsive (HMTR) BAB* block copolymers were conceptualized, where the permanently hydrophobic B block can anchor inside the microemulsion droplets while the B* block can form additional domains once the LCST is exceeded. As a result, a library of HMTR polymers was synthesized comprising block copolymers with TR blocks with varying lengths and chemical structures of the comprising monomers, *i. e.*, *N*-*n*-propylacrylamide (NPAm, LCST(pNPAm) $\approx 22\,^\circ$C[60]), *N*,*N*-diethylacrylamide (DEAm, LCST(pDEAm) $\approx 30\,^\circ$C[61]), *N*-isopropylacrylamide (NiPAm, LCST(pNiPAm) $\approx 32\,^\circ$C[62]), and *N*-acryloylpyrrolidine (NAP, LCST(pNAP) $\approx 55\,^\circ$C[60,63]). In addition, three different block copolymer architectures, *i. e.*, BAB*, B$_2$AB*, and B(AB*)$_2$, were synthesized for which either the hydrophobic (B$_2$AB*) or the thermoresponsive (B(AB*)$_2$) interaction is enhanced. An overview of all investigated block copolymers can be found in Table 2.3.

In the following chapters, this library of block copolymers will be investigated for various concentrations in the temperature window between $20\,^\circ$C and $60\,^\circ$C. The influence of the TR block length as well as LCST type and value will be explored with respect to the phase behavior, the aggregation behavior, and the mesoscopic organization in solution.

Furthermore, the temperature-dependent rheological properties of the three architectures will be studied for the block copolymer in solution as well as in combination with microemulsions. The structural mesoscopic picture will be correlated with the macroscopically observed rheological properties to allow for adjusting and fine-tuning of the structural and rheological response as a function of temperature. The investigations are mainly divided into three parts:

- Chapter 3: Influence of the thermoresponsive block length on the aggregation behavior in aqueous solution.

- Chapter 4: Influence of the copolymer architecture, *i. e.*, BAB*, B_2AB^*, and $B(AB^*)_2$, on the temperature-dependent rheological behavior in aqueous solution.

- Chapter 5: Modification of rheological properties of microemulsions as a function of temperature.

Chapter 2

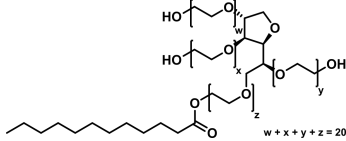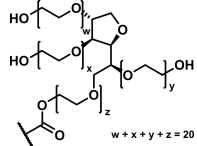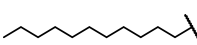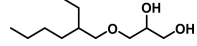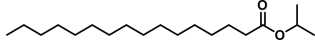# Theoretical Background

2.1 Materials

2.1.1 Chemicals
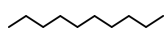
The chemicals used to synthesize the various block copolymers are specified in Prause *et al.* (2022)[64] for the BAB* block copolymers and in Prause *et al.* (2023)[65] for the B$_2$AB* and B(AB*)$_2$ block copolymers. Further details of the block copolymers and their components are summarized in Tables 2.2, 2.3, and 2.4.

The homopolymers poly(*N*-*n*-propylacrylamide) (pNPAm, $M_n \approx 15\,\text{kg mol}^{-1}$), and poly(*N*,*N*-diethylacrylamide) (pDEAm, $M_n \approx 13\,\text{kg mol}^{-1}$) were synthesized by Jan Weiss and René Steinbrecher, respectively, from the Group of André Laschewsky and were used as received. The homopolymer poly(*N*-isopropylacrylamide) (pNiPAm, $M_n \approx 15\,\text{kg mol}^{-1}$, Polymer Source, USA), the fluorescent dye 1-[6-(dimethylamino)naphthalen-2-yl]propan-1-one (Prodan, $> 98\,\%$, TCI Deutschland GmbH, Eschborn, Germany), and the surfactant *n*-dodecyl-β-D-maltopyranoside (C$_{12}$-β-D-maltoside, Anatrace Products, USA) were used as received.

For the microemulsions, the surfactant polyethylene glycol (20) sorbitan monolaurate (Tween20, Sigma Aldrich), the cosurfactant 2-ethylhexylglycerin (EHG, Clariant Produkte), and the oils isopropyl palmitate (IPP, $\geq 90\,\%$, Sigma Aldrich) and *n*-decane (C$_{10}$, $\geq 98\,\%$, Fluka) were used as received. Further details of the microemulsion components are summarized in Table 2.1.

Water (H$_2$O) was purified by a Millipore Milli-Q Plus system (Merck Millipore, Darmstadt, Germany, resistivity $18.2\,\text{M}\Omega\,\text{cm}$). Heavy water (D$_2$O, $99.9\,\%$ D content, Deutero GmbH, Kastellaun, Germany), was filtered with a cellulose acetate (CA) or poly(vinylidene fluoride) (PVDF) membrane filter ($0.45\,\mu\text{m}$) prior to use.

Table 2.1: Overview of microemulsion components with the corresponding values for the number averaged molecular weight (M_n), partial specific volume (V_sp), molecular volume (V_n), and scattering length density (*SLD*).

| Building block	Chemical structure	M_n / $\text{kg}\,\text{mol}^{-1}$	V_sp / $\text{cm}^3\,\text{g}^{-1}$	V_n / nm^3	*SLD* / $10^{-4}\,\text{nm}^{-2}$
D$_2$O	—	20.03	0.903	0.0300	6.38
Tween20 (surf)		1227.7	0.913	1.8618	0.768
Tween20 (head)		1071.4	0.846	1.4847	1.067
Tween20 (tail)		156.31	1.351	0.3772	−0.475
EHG (co)		204.31	1.040	0.3527	0.606
IPP (oil)		298.51	1.173	0.5815	−0.073
n-decane (oil)		142.29	1.369	0.3237	−0.489

2.1.2 Block Copolymers

The studied hydrophobically modified thermoresponsive (HMTR) block copolymers were synthesized via reversible-addition-fragmentation chain-transfer (RAFT) polymerization by Michelle Hechenbichler (Group of André Laschewsky). The detailed descriptions of the syntheses and analytical tools used for the molecular characterization can be found in Prause *et al.* (2022)[64] and Prause *et al.* (2023)[65].

Synthesis Exemplarily, the synthesis is described for the hydrophobically modified (HM) homopolymer $C_{12}DMAm_{168}$ (**BA**). The monomer *N,N*-dimethylacrylamide (DMAm, 17.5 mL, 16.9 g, 0.170 mol, 202 eq.), the initiator 1,1′-azobis(cyclohexanecarbonitrile) (V-40, 20.6 mg, 0.0843 mmol, 0.1 eq.), and the chain transfer agent **CTA-L** (0.4426 g, 0.8415 mmol, 1.0 eq., Scheme 2.1a) were dissolved in benzene (76 mL). After purging the solution for 45 min with argon in a flask, the flask was immersed into an oil bath preheated to a temperature of 90 °C. The solution was stirred for 3 h. Afterwards, the reaction was stopped by letting air into the flask. Concurrently, the flask was cooled with liquid nitrogen. The purification of the polymer was performed in two subsequent precipitation steps. For precipitation, dietyhl ether was used. The polymer was dried under reduced pressure, redissolved in distilled water and lyophilized. The polymer yield was 10.98 g (63 %). Accordingly, the degree of polymerisation determined by yield (DP_n^{theo}) was 168 and was calculated based on the used molar ratio of DMAm to **CTA-L** multiplied by the conversion of the monomer. The monomer conversion was approximated by the polymer yield.

The thermoresponsive (TR) block copolymers were synthesized via a subsequent RAFT polymerization. The already synthesized hydrophobically modified (HM) homopolymer $C_{12}DMAm_{168}$ (**BA**, Scheme 2.1a) was used as a macro chain transfer agent. Exemplarily, this synthesis step is described for the HMTR polymer $C_{12}DMAm_{168}NiPAm_{15}$. $C_{12}DMAm_{168}$ (1.03 g, 0.050 mol) and *N*-isopropylacrylamide (NiPAm, 0.2269 g, 2.01 mmol, 40 eq.) were dissolved in benzene (5.1 mL). The initiator V-40 was dissolved in benzene and added as a stock solution (0.61 mL, $2 \, \text{g L}^{-1}$, equivalent to 5.0 µmol, 0.1 eq.). In the flask, the mixture was purged for 40 min with argon. Afterwards, the flask was immersed into an oil bath preheated to a temperature of 90 °C. The solution was stirred for 4 h. The reaction was stopped by letting air into the flask and cooling with liquid nitrogen. The block copolymer was purified and isolated analogous to the above-mentioned procedure. The polymer yield was 1.03 g (82 %).

The exemplary above-stated syntheses correspond to the BAB* copolymer architecture (Scheme 2.1a). In general, for the three architectures, *i. e.*, BAB*, B₂AB*, and B(AB*)₂, different chain transfer agents were used (Scheme 2.1), namely **CTA-L**, **CTA-T**, and **CTA-Y**, respectively. In the first polymerization step, the **CTA-L**, **CTA-T**, and **CTA-Y** yield the hydrophobically modified polymers $C_{12}DMAm_{168}$ (**BA**), $(C_{12})_2DMAm_{158}$ (**B₂A**), and $C_{12}(DMAm_{172})_2$ (**BA₂**), respectively. For the second
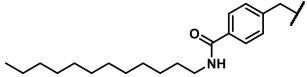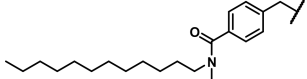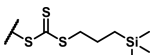
polymerization step, these hydrophobically modified copolymers were used as macro chain transfer agents to obtain the corresponding hydrophobically modified thermoresponsive block copolymers of the copolymer architectures BAB*, B$_2$AB*, and B(AB*)$_2$, respectively. The employed acrylamide monomers were *N-n*-propylacrylamide (NPAm), *N,N*-diethylacrylamide (DEAm), *N*-isopropylacrylamide (NiPAm), and *N*-acryloylpyrrolidine (NAP).
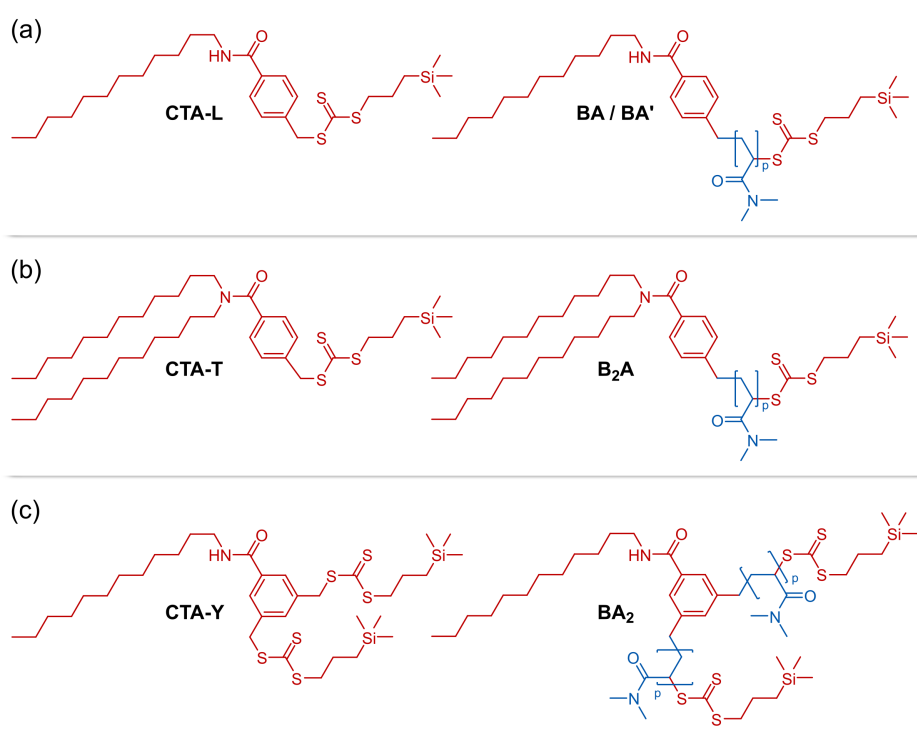
Scheme 2.1: Chain transfers agents (first polymerization step) and macro chain transfer agents (second polymerization step) for the different block copolymer architectures: (a) BAB* (1st: **CTA-L**, 2nd: **BA**), (b) B$_2$AB* (1st: **CTA-T**, 2nd: **B$_2$A**), and (c) B(AB*)$_2$ (1st: **CTA-Y**, 2nd: **BA$_2$**).

Physical Properties The building blocks of the synthesized block copolymers are summarized in Table 2.2. The chemical structure is displayed as they appear incorporated into the polymer. The Z-group and the R^x-group is part of the used RAFT agent which are supposed to remain from the synthesis. Due to the three different architectures, *i. e.*, BAB*, B_2AB^*, and $B(AB^*)_2$, the three R-groups, *i. e.*, R^1, R^2, and R^3, were used to obtain the desired hydrophobic modification, respectively.

Table 2.2: Overview of building blocks of the block copolymers with the corresponding values for the number averaged molecular weight (M_n), partial specific volume (V_{sp}) (taken from Wohlfarth (2010)[66] if not otherwise specified), molecular volume (V_n), and scattering length density (*SLD*).

Building block	Chemical structure	M_n / kg mol^{-1}	V_{sp} / cm^3 g^{-1}	V_n / nm^3	*SLD* / 10^{-4} nm^{-2}
D$_2$O	—	20.03	0.903	0.0300	6.38
R^1-group		302.48	1^a	0.5023	0.771
R^2-group		470.81	1^a	0.7818	0.236
R^3-group		317.52	1^a	0.5273	0.648
Z-group		223.46	1^a	0.3711	0.084
DMAm		99.13	0.846	0.1393	1.058
NPAm		113.16	0.896^c	0.1684	1.432
DEAm		127.19	0.846^b	0.1787	0.732
NiPAm		113.16	0.896	0.1684	1.432
NAP		125.17	0.846^b	0.1758	1.169

^{a} Assumption because no value was found in literature for the structure. ^{b} No value was found in literature, DMAm value was taken instead. ^{c} No value was found in literature, NiPAm value was taken instead.

The library of synthesized HMTR block copolymers and the corresponding values for the degree of polymerisation (DP_n), number averaged molecular weight (M_n), and dispersity ($Đ$) are shown in Table 2.3.

Table 2.3: Overview of the HMTR block copolymers with corresponding values for the degree of polymerisation (DP_n), number averaged molecular weight (M_n), and dispersity ($Đ$). The copolymers are grouped by their architecture BAB*, B₂AB*, and B(AB*)₂.

Polymer	DP_n		M_n / kg mol^{-1}				$Đ^e$
	theo^a	NMR^b	theo^a	NMR^b	SEC^c	UV/Vis^d	
BAB*							
DMAm$_{187}^f$	187	208	18.9	20.9	19	20	1.18
C$_{12}$DMAm$_{168}$	168	213	17.1	21.6	18	19	1.25
C$_{12}$DMAm$_{127}$	127	157	13.1	16.0	14	14	1.18
C$_{12}$DMAm$_{127}$NPAm$_{31}$	31^g	45^g	16.6	21.1	20	28	1.25
C$_{12}$DMAm$_{168}$DEAm$_{14}$	14^g	14^g	18.9	23.4	19	23	1.19
C$_{12}$DMAm$_{168}$DEAm$_{27}$	27^g	45^g	20.1	27.3	22	25	1.25
C$_{12}$DMAm$_{127}$DEAm$_{48}$	48^g	90^g	19.2	27.4	21	23	1.18
C$_{12}$DMAm$_{168}$NiPAm$_{15}$	15^g	11^g	18.8	22.8	21	25	1.25
C$_{12}$DMAm$_{168}$NiPAm$_{33}$	33^g	34^g	20.8	25.4	22	25	1.26
C$_{12}$DMAm$_{127}$NiPAm$_{50}$	50^g	66^g	18.8	23.5	23	26	1.21
C$_{12}$DMAm$_{168}$NAP$_{16}$	16^g	18^g	19.1	23.9	21	32	1.16
C$_{12}$DMAm$_{168}$NAP$_{27}$	27^g	36^g	20.4	26.1	24	30	1.16
B₂AB*							
(C$_{12}$)$_2$DMAm$_{158}$	158	193	16.4	19.8	18	18	1.14
(C$_{12}$)$_2$DMAm$_{158}$NPAm$_{32}$	32^g	32^g	20.4	23.4	24	32	1.11
(C$_{12}$)$_2$DMAm$_{158}$DEAm$_{22}$	22^g	25^g	19.2	22.7	20	22	1.13
(C$_{12}$)$_2$DMAm$_{158}$NiPAm$_{21}$	21^g	18^g	18.7	21.9	21	29	1.14
B(AB*)₂							
C$_{12}$(DMAm$_{172}$)$_2$	172	181	35.0	36.8	30	34	1.14
C$_{12}$(DMAm$_{172}$NPAm$_{49}$)$_2$	49^g	51^g	47.2	48.3	43	57	1.26
C$_{12}$(DMAm$_{172}$DEAm$_{29}$)$_2$	29^g	29^g	42.3	43.3	36	48	1.14
C$_{12}$(DMAm$_{172}$NiPAm$_{32}$)$_2$	32^g	32^g	42.2	44.0	40	44	1.15

^{a} Value was approximated by determined yield and used for further calculations. ^{b} Number was approximated by ^{1}H NMR spectroscopy via the trimethylsilyl signal of the Z-group. ^{c} Polystyrene was used as standard for calibration and 0.1 %$_{wt}$ LiBr in NMP was used as eluent. ^{d} Number was approximated by UV/Vis spectroscopy in methanol using the π–π^* transition band of the C=S double bond of the Z-group at 309 nm. ^{e} Dispersity (M_w/M_n) was determined by SEC data. ^{f} R-group is only a simple benzyl group without hydrophobic modification. ^{g} Value refers to DP_n of each thermoresponsive block.

In Table 2.4 additional physical properties, *i.e.*, contour length of polymer (L_p), end-to-end distance (R_ee), refractive index increment ($\mathrm{d}n/\mathrm{d}c_\mathrm{g}$), mass density of polymer (ρ_p), and scattering length density of polymer (SLD_p), of the polymers are summarized which were used for further analysis.

Table 2.4: Overview of additional physical properties, namely the contour length of polymer (L_p), end-to-end distance (R_ee), refractive index increment ($\mathrm{d}n/\mathrm{d}c_\mathrm{g}$), mass density of polymer (ρ_p), and scattering length density of polymer (SLD_p), for the HMTR block copolymers. The copolymers are grouped by their architecture BAB*, $\mathrm{B_2AB^*}$, and $\mathrm{B(AB^*)_2}$.

Polymer	L_p / nm	$R_\mathrm{ee}{}^a$ / nm	$\mathrm{d}n/\mathrm{d}c_\mathrm{g}$ / $\mathrm{cm^3\,g^{-1}}$	ρ_p / $\mathrm{g\,cm^{-3}}$	SLD_p / $10^{-4}\,\mathrm{nm^{-2}}$
BAB*					
$\mathbf{DMAm_{187}}$	47	13.3	0.146(4)	1.163	1.039
$\mathbf{C_{12}DMAm_{168}}$	42	12.3	0.154(4)	1.175	1.037
$\mathbf{C_{12}DMAm_{127}}$	32	9.2	0.154(4)	1.173	1.031
$\mathbf{C_{12}DMAm_{127}NPAm_{31}}$	40	10.0	0.150(3)	1.150	1.119
$\mathbf{C_{12}DMAm_{168}DEAm_{14}}$	46	12.1	0.153(5)	1.176	1.009
$\mathbf{C_{12}DMAm_{168}DEAm_{27}}$	49	11.1	0.149(4)	1.177	0.987
$\mathbf{C_{12}DMAm_{127}DEAm_{48}}$	54	9.1	0.152(5)	1.176	0.957
$\mathbf{C_{12}DMAm_{168}NiPAm_{15}}$	46	13.2	0.154(5)	1.170	1.074
$\mathbf{C_{12}DMAm_{168}NiPAm_{33}}$	51	14.0	0.153(4)	1.164	1.111
$\mathbf{C_{12}DMAm_{127}NiPAm_{50}}$	55	12.0	0.150(3)	1.160	1.139
$\mathbf{C_{12}DMAm_{168}NAP_{16}}$	46	13.1	0.159(4)	1.176	1.051
$\mathbf{C_{12}DMAm_{168}NAP_{27}}$	49	14.4	0.147(4)	1.177	1.059
$\mathbf{B_2AB^*}$					
$\mathbf{(C_{12})_2DMAm_{158}}$	40	13.3	0.160(3)	1.173	1.015
$\mathbf{(C_{12})_2DMAm_{158}NPAm_{32}}$	48	10.3	0.150(3)	1.175	1.045
$\mathbf{(C_{12})_2DMAm_{158}DEAm_{22}}$	45	10.0	0.165(3)	1.174	0.974
$\mathbf{(C_{12})_2DMAm_{158}NiPAm_{21}}$	45	11.5	0.150(3)	1.165	1.070
$\mathbf{B(AB^*)_2}$					
$\mathbf{C_{12}(DMAm_{172})_2}$	87	20.9^b	0.147(3)	1.186	1.050
$\mathbf{C_{12}(DMAm_{172}NPAm_{49})_2}$	111	21.6^b	0.149(3)	1.168	1.168
$\mathbf{C_{12}(DMAm_{172}DEAm_{29})_2}$	101	18.1^b	0.149(3)	1.185	0.994
$\mathbf{C_{12}(DMAm_{172}NiPAm_{32})_2}$	103	23.3^b	0.148(3)	1.173	1.119

^{a} End-to-end distance (R_ee) is based on radius of gyration (R_g) at $25\,^\circ\mathrm{C}$ and computed via $R_\mathrm{ee} = (6\langle R_\mathrm{g}{}^2\rangle)^{1/2}$ which is, strictly speaking, only valid for a Gaussian coil. ^{b} For the $\mathrm{B(AB^*)_2}$ architecture, R_ee corresponds to the distance between the ends of the two B* blocks.

In the Chapters 4 and 5, the influence of different block copolymer architectures are studied. The copolymers are labeled based on their architecture. The various TR blocks are ordered according to their LCST and encoded via an appended number: pNPAm as "B*-1", pDEAm as "B*-2", and pNiPAm as "B*-3". For the investigated copolymers, the assignment of architecture-based labels is summarized in Table 2.5.

Table 2.5: Architecture-based labels of HMTR block copolymers used for studying the influence of different block copolymer architectures.

Architecture	Label	Polymer
BAB*		
	BA	$\mathbf{C_{12}DMAm_{168}}$
	BA$'$	$\mathbf{C_{12}DMAm_{127}}$
	BAB*-1	$\mathbf{C_{12}DMAm_{127}NPAm_{31}}$
	BAB*-2	$\mathbf{C_{12}DMAm_{168}DEAm_{27}}$
	BAB*-3	$\mathbf{C_{12}DMAm_{168}NiPAm_{33}}$
B_2AB*		
	B$_2$A	$\mathbf{(C_{12})_2DMAm_{158}}$
	B$_2$AB*-1	$\mathbf{(C_{12})_2DMAm_{158}NPAm_{32}}$
	B$_2$AB*-2	$\mathbf{(C_{12})_2DMAm_{158}DEAm_{22}}$
	B$_2$AB*-3	$\mathbf{(C_{12})_2DMAm_{158}NiPAm_{21}}$
$B(AB*)_2$		
	BA$_2$	$\mathbf{C_{12}(DMAm_{172})_2}$
	B(AB*-1)$_2$	$\mathbf{C_{12}(DMAm_{172}NPAm_{49})_2}$
	B(AB*-2)$_2$	$\mathbf{C_{12}(DMAm_{172}DEAm_{29})_2}$
	B(AB*-3)$_2$	$\mathbf{C_{12}(DMAm_{172}NiPAm_{32})_2}$

2.2 Methods

2.2.1 Sample Preparation

Block Copolymer Solutions

For each polymer, a stock solution was prepared with a mass concentration of about $55\,\mathrm{g\,L^{-1}}$. The lower concentrated samples were obtained by diluting these stock solutions by admixing of solvent. The prepared polymer concentrations were approximately 55, 22, 11, and $5.5\,\mathrm{g\,L^{-1}}$. The preparations were carried out on a balance where each component was weighed. All samples were prepared with filtered D_2O as the solvent.

Microemulsions

The used microemulsions (MEs) were based on polyethylene glycol (20) sorbitan mono-laurate (Tween20) as surfactant, 2-ethylhexylglycerin (EHG) as co-surfactant, isopropyl palmitate (IPP) or n-decane as oil, and D_2O as solvent. This microemulsion was reported by Schmidt (2020)[67] in his bachelor thesis. The surfactant and cosurfactant concentrations were set to be $50\,\mathrm{mmol\,L^{-1}}$ in the final ME–polymer mixtures. Table 2.6 summarizes the reference MEs with the same concentrations as used in the mixtures. The amount of dissolved oil was chosen to be approximately $10\,\%$ below the solubilization limit at $20\,°\mathrm{C}$. For the preparation of the n-decane-containing ME, the concentration was adjusted to match the dissolved volume of IPP. The initial ME stock solutions were prepared with a surfactant concentration of $100\,\mathrm{mmol\,L^{-1}}$, a cosurfactant-to-surfactant ratio ($c_{\mathrm{co}}/c_{\mathrm{surf}}$) of 1, and a oil-to-surfactant ratio ($c_{\mathrm{oil}}/c_{\mathrm{surf}}$) of 0.5 for IPP or 0.75 for n-decane. All preparation were carried out on a balance and used only filtered D_2O as the solvent.

Table 2.6: Overview of the microemulsion (ME) composition. The MEs are defined based on the surfactant (Tween20, surf) concentration which is given as the molar concentration (c). The concentration of cosurfactant (EHG, co) and oil is given as a ratio normalized to the molar concentration of surfactant (c_{surf}).

ME	Oil	c_{surf} $\mathrm{mmol\,L^{-1}}$	$c_{\mathrm{co}}/c_{\mathrm{surf}}$ —	$c_{\mathrm{oil}}/c_{\mathrm{surf}}$ —	$M_{\mathrm{w}}{}^{a}$ $\mathrm{kg\,mol^{-1}}$	$R_{\mathrm{s}}{}^{b}$ nm
ME-1	IPP	41	1.01	0.46	91	3.2
ME-2	n-decane	49	1.00	0.74	95	3.3
ME-3	IPP	51	1.02	0.50	114	3.5
ME-4	IPP	52	1.00	0.50	100^{c}	3.4

[a] Mass averaged molecular weight (M_{w}) of microemulsion droplets estimated by SANS at $25\,°\mathrm{C}$, see Equation 2.13. [b] Spherical radius (R_{s}) based on M_{w} and the composition of the microemulsion. [c] M_{w} based on SLS data. As $S(0)$, the value for **ME-3** was considered.

Mixtures of Microemulsion and Block Copolymers

The ME–polymer mixtures were prepared by using the polymer and ME stock solutions. For that purpose, the ME stock solution was diluted by D_2O and polymer stock solution. The final composition of ME–polymer mixtures was set to a surfactant concentration of about $50\,\mathrm{mmol\,L^{-1}}$ and polymer concentration of about $22\,\mathrm{g\,L^{-1}}$ (Table 2.7). The samples were prepared by weight on a balance.

Table 2.7: Overview of ME–polymer mixtures at fixed polymer and microemulsion's surfactant concentration of about $22\,\mathrm{g\,L^{-1}}$ and $50\,\mathrm{mmol\,L^{-1}}$, respectively. The polymer concentration is given as mass concentration (c_g) and molar concentration (c). The molar concentration of microemulsion droplets (c_ME) and the ratio of polymer chains per microemulsion droplet ($N_\mathrm{p}/N_\mathrm{ME}$) are given at $25\,^\circ\mathrm{C}$ and $55\,^\circ\mathrm{C}$.

Polymer	ME	Polymer		c_ME / $\mathrm{mmol\,L^{-1}}$		$N_\mathrm{p}/N_\mathrm{ME}$	
		c_g / $\mathrm{g\,L^{-1}}$	c / $\mathrm{mmol\,L^{-1}}$	$25\,^\circ\mathrm{C}$	$55\,^\circ\mathrm{C}$	$25\,^\circ\mathrm{C}$	$55\,^\circ\mathrm{C}$
BA	**ME-1**[a]	17.5	1.021	0.579	0.369	1.8	2.8
	ME-4	22.2	1.294	0.610	0.322	2.1	4.0
B$_2$A	**ME-2**	22.4	1.370	0.654	0.430	2.1	3.2
	ME-4	22.2	1.359	0.611	0.323	2.2	4.2
BA$_2$	**ME-3**	21.8	0.624	0.603	0.319	1.0	2.0
BAB*-1	**ME-2**	21.9	1.316	0.649	0.426	2.0	3.1
	ME-4	22.3	1.342	0.554	0.302	2.4	4.5
B$_2$AB*-1	**ME-2**	22.3	1.094	0.649	0.426	1.7	2.6
	ME-4	22.1	1.086	0.614	0.324	1.8	3.4
B(AB*-1)$_2$	**ME-3**	21.8	0.473	0.617	0.326	0.8	1.5
BAB*-2	**ME-1**[a]	18.0	0.871	0.565	0.360	1.5	2.4
	ME-4	21.4	1.039	0.616	0.325	1.7	3.2
B$_2$AB*-2	**ME-2**	22.1	1.153	0.648	0.426	1.8	2.7
	ME-4	22.3	1.165	0.614	0.324	1.9	3.6
B(AB*-2)$_2$	**ME-3**	22.0	0.519	0.606	0.320	0.9	1.6
BAB*-3	**ME-1**[a]	18.1	0.864	0.565	0.360	1.5	2.4
	ME-4	21.4	1.021	0.613	0.324	1.7	3.2
B$_2$AB*-3	**ME-2**	22.3	1.192	0.653	0.429	1.8	2.8
	ME-4	22.4	1.193	0.612	0.323	1.9	3.7
B(AB*-3)$_2$	**ME-3**	21.8	0.516	0.602	0.318	0.9	1.6

[a] Polymer and microemulsion's surfactant concentration of about $18\,\mathrm{g\,L^{-1}}$ and $41\,\mathrm{mmol\,L^{-1}}$, respectively.

The ME–polymer mixtures with varying polymer and microemulsion's surfactant concentrations of about 4, 9, 18, and $22\,\mathrm{g\,L^{-1}}$ and 25, 50, and $100\,\mathrm{mmol\,L^{-1}}$, respectively, were prepared similarly by varying the amount of D_2O and the polymer stock solution (Table 2.8).

Table 2.8: Overview of ME–polymer mixtures at varying polymer and microemulsion's surfactant concentrations of about 4, 9, 18, and $22\,\mathrm{g\,L^{-1}}$ and 25, 50, and $100\,\mathrm{mmol\,L^{-1}}$, respectively. The polymer concentration is given as mass concentration (c_g) and molar concentration (c). The molar concentration of microemulsion droplets (c_{ME}) and the ratio of polymer chains per microemulsion droplet (N_p/N_{ME}) are given at $25\,°\mathrm{C}$ and $55\,°\mathrm{C}$.

Polymer	ME	Polymer		c_{ME} / $\mathrm{mmol\,L^{-1}}$		N_p/N_{ME}	
		c_g / $\mathrm{g\,L^{-1}}$	c / $\mathrm{mmol\,L^{-1}}$	$25\,°\mathrm{C}$	$55\,°\mathrm{C}$	$25\,°\mathrm{C}$	$55\,°\mathrm{C}$
Variation of polymer concentration							
BA	**ME-1**	4.6	0.266	0.581	0.370	0.5	0.7
	ME-1	8.7	0.507	0.578	0.368	0.9	1.4
	ME-1[a]	17.5	1.021	0.579	0.369	1.8	2.8
	ME-4[a]	22.2	1.294	0.610	0.322	2.1	4.0
BAB*-2	**ME-1**	4.3	0.210	0.588	0.375	0.4	0.6
	ME-1	8.7	0.421	0.572	0.364	0.7	1.2
	ME-1[a]	18.0	0.871	0.565	0.360	1.5	2.4
	ME-4[a]	21.4	1.039	0.616	0.325	1.7	3.2
BAB*-3	**ME-1**	4.1	0.195	0.588	0.375	0.3	0.5
	ME-1	8.8	0.420	0.572	0.364	0.7	1.2
	ME-1[a]	18.1	0.864	0.565	0.360	1.5	2.4
	ME-4[a]	21.4	1.021	0.613	0.324	1.7	3.2
Variation of microemulsion concentration							
B$_2$A	**ME-2**	22.3	1.365	0.334	0.227	4.1	6.0
	ME-2[a]	22.4	1.370	0.654	0.430	2.1	3.2
	ME-2	22.9	1.397	1.263	0.876	1.1	1.6
B$_2$AB*-1	**ME-2**	22.3	1.093	0.336	0.229	3.3	4.8
	ME-2[a]	22.3	1.094	0.649	0.426	1.7	2.6
	ME-2	22.2	1.090	1.277	0.885	0.9	1.2
B$_2$AB*-2	**ME-2**	22.2	1.157	0.335	0.228	3.5	5.1
	ME-2[a]	22.1	1.153	0.648	0.426	1.8	2.7
	ME-2	22.0	1.147	1.281	0.888	0.9	1.3
B$_2$AB*-3	**ME-2**	22.5	1.200	0.334	0.227	3.6	5.3
	ME-2[a]	22.3	1.192	0.653	0.429	1.8	2.8
	ME-2	22.4	1.195	1.271	0.881	0.9	1.4

[a] Identical with ME–polymer samples listed in Table 2.7.

2.2.2 Turbidimetry

The temperature dependent transmission was measured with a Cary 5000 spectrometer (Varian), applying heating and cooling rates of $0.5\,\mathrm{K\,min^{-1}}$. Temperatures are precise within $0.5\,\mathrm{K}$. The cloud point is determined as the temperature onset of the decay of the transmission curve.

All turbidimetry measurement were conducted by Michelle Hechenbichler (Group of André Laschewsky) at *Fraunhofer Institute of Applied Polymer Research IAP* in Golm, Potsdam.

2.2.3 Visual Inspection

The analysis of the photos was conducted to extract turbidity information. The samples were heated in a thermo-mixer to the given temperature and equilibrated for $15\,\mathrm{min}$. Subsequently, the samples were positioned in an acrylic sample holder located in a photo box with lighting from above. To minimize cooling, the photos were taken with an iPhone XS mounted to a tripod immediately afterwards. Each photo was cropped to the region of interest (ROI) and converted to gray scale. The region of interest included the bottom-filled part of the cuvette and the background alongside the cuvette. The gray values of the ROI were averaged vertically to obtain one gray value for each point in the horizontal direction. Afterwards, gray values were normalized with the gray value of the acrylic sample holder, the obtained values were multiplied by 255, and the background level was subtracted. Due to the curvature of the cuvette, the gray value of the center of the cuvette was taken.

2.2.4 Phase Separation

The macroscopic phase separation of the samples was investigated by visual inspection and static light scattering. Due to the longer measurement times, *i.e.*, about $1\,\mathrm{h}$ per temperature, the light scattering data were used to determine the macroscopic phase separation temperature, referred to as CP_{LCST}. The CP_{LCST} was set to the value at which the scattering intensity stopped increasing and started to decrease. If no transition was observed below $60\,^{\circ}\mathrm{C}$, a $3\,\mathrm{h}$ waiting period was used to see if the sample began to phase separate at $60\,^{\circ}\mathrm{C}$.

2.2.5 Rheology

The rheology measurements were conducted on a MCR 502 WESP rheometer (Anton Paar) with a temperature-controlled cone-plate geometry and a CP50-1/TG cone (diameter of $50.0\,\mathrm{mm}$, angle of 1.00°, gap size of $0.101\,\mathrm{mm}$). The studied temperature range was set to 20–$60\,^{\circ}\mathrm{C}$. A solvent trap was used to prevent the evaporation of the solvent during the temperature ramp. For oscillation experiments a frequency sweep was performed from 0.05 to $100\,\mathrm{Hz}$ (angular frequency of 0.314–$628\,\mathrm{s^{-1}}$) with a deformation of $2\,\%$. The deformation

was checked via an amplitude sweep at 1 Hz to fit well into the linear viscoelastic regime (LVE). The temperature-dependent shear moduli, $i.\,e.$, storage modulus (G') and loss modulus (G''), were analyzed at a frequency of 1 Hz. Moreover, shear experiments were performed with a shear-rate ($\dot{\gamma}$) from 0.5 to $50\,\text{s}^{-1}$. With the obtained dynamic viscosity (η) as a function of $\dot{\gamma}$, the zero-shear viscosity (η_0) was determined by a linear extrapolation in a double-logarithmic representation to $\dot{\gamma} = 0$. The zero-shear viscosity can be extracted from the intercept of the corresponding linear equation $\log \eta = A \cdot \log \dot{\gamma} + \log \eta_0$, where A is the slope in the double-logarithmic representation.

2.2.6 Fluorescence

Fluorescence measurements were performed with a fluorescence spectrometer F-4500 (Hitachi) in the emission scan mode. The excitation wavelength was set to 340 nm and the spectra were recorded from 350 to 650 nm with a scan-rate of $240\,\text{nm}\,\text{min}^{-1}$. The excitation and emission slits were set to 5 nm each. The temperature of the sample holder was controlled by a thermostat. The samples were preheated with a heating block to minimize the time to reach thermal equilibrium. For each temperature, three spectra were recorded and averaged accordingly.

The investigated samples were prepared separately based on an aqueous Prodan solution ($1\,\text{µmol}\,\text{L}^{-1}$ in D_2O). This solution was prepared by adding a droplet of an ethanol–Prodan solution ($1\,\text{mmol}\,\text{L}^{-1}$) to a vial, the ethanol was evaporated, and the appropriate amount of filtered D_2O was added. The solvatochromism of Prodan is used to probe the polarity of its environment.[68,69]

2.2.7 Cryogenic Transmission Electron Microscopy

Cryo-TEM specimens were prepared on perforated carbon film grids. The grids were plasma-etched in a PELCO EasiGlow glow-discharger (Ted Pella Inc., Redding, CA) to increase their hydrophilicity. Specimens were then prepared in a controlled environment vitrification system (CEVS) at 25 °C and 100 % relative humidity.[70,71] Specimens were imaged by an FEI Tecnai T12 G2 TEM, operated at 120 kV, or an FEI Talos F200C, FEG-equipped high-resolution TEM, operated at 200 kV. Specimens were equilibrated inside the microscope below −178 °C in Oxford CT-3500 (Oxford Instruments, Abingdon, England), or Gatan 626 (Gatan, Pleasanton, CA) cryo-holders, and imaged using a low-dose imaging procedure to minimize electron-beam radiation-damage and a Volta phase plate (only on Talos F200C) to enhance contrast. Images were recorded digitally by a Gatan US1000 high-resolution CCD camera (on the Tecnai T12 G2) or FEI Falcon III, direct-imaging camera (on Talos F200C).

All cryo-TEM experiments were conducted by Miriam Simon (Group of Yeshayahu Talmon) at *Technion* in Haifa.

2.2.8 Light Scattering

General Setup

The light scattering measurements were performed with a 3Dspectrometer (LSinstruments). The setup was equipped with a He-Ne laser which operates at a wavelength (λ) of 632.8 nm with a maximum power of 21 mW. The vat was temperature-controlled by a thermostat and filled with decahydronaphthalene (decalin) to match the refractive index of the cuvettes. The studied temperature range was set to 20–60 °C. The experiments were conducted in a scattering angle (2θ) range of 30 to 135° with steps of 5°. At each angle the sample was measured three times with a duration of 60 s each.

The analysis of the light scattering data was done with the software SimplightQt.[72]

Static Light Scattering

The static light scattering (SLS) intensity $I(q)$, known as Rayleigh ratio, was computed based on the measured count-rates (CRs) of the sample (sam), solvent (sol) and toluene (tol) and the corresponding laser intensity (P).

$$I(q) = \frac{CR_{\text{sam}}/P_{\text{sam}} - CR_{\text{sol}}/P_{\text{sol}}}{CR_{\text{tol}}/P_{\text{tol}}} \cdot \left(\frac{n_0}{n_{\text{tol}}}\right)^2 \cdot I_{\text{tol}} \tag{2.1}$$

with $I_{\text{tol}} = 1.37 \cdot 10^{-5} \text{ cm}^{-1}$ as Rayleigh ratio of toluene[73] at 25 °C for absolute scaling, n_0 as the refractive index of the solvent, n_{tol} as the refractive index of toluene, and q as modulus of the scattering vector.

The forward scattering intensity $I(0)$ is proportional to the mass of the scattering entities and can be estimated by the Guinier law (Equation 2.2) in the q range of 0.0132–0.0244 nm^{-1} (60–135°).

$$I(q) = I(0) \cdot e^{-(R_{\text{g}} \cdot q)^2/3} \tag{2.2}$$

where R_{g} is the radius of gyration.

The effective aggregation number of the aggregates was calculated by Equation 2.3 based on the forward scattering intensity $I(0)$:

$$N_{\text{eff}} = \frac{I(0)}{K \cdot c_{\text{g}} \cdot M_{\text{n}} \cdot Đ} \tag{2.3}$$

where $K = \frac{4\pi^2 n_0^2}{N_{\text{Av}}\lambda}(\mathrm{d}n/\mathrm{d}c_{\text{g}})^2$ is the contrast factor for light scattering with n_0 as refractive index of the solvent, N_{Av} as Avogadro's number, λ as wavelength of the laser, c_{g} is the mass concentration, M_{n} is the number averaged molecular weight, $Đ$ is the dispersity, and $\mathrm{d}n/\mathrm{d}c_{\text{g}}$ is the refractive index increment. The refractive index increment was determined by Jana Lutzki with an Orange Analytics 19″ dn/dc instrument.

The refractive index increment of the microemulsions (MEs) can be approximated via the composition and the refractive index of the pure substances n_i and their density ρ_i.

$$\mathrm{d}n/\mathrm{d}c_\mathrm{g} \approx \sum_i \phi_i \frac{\Delta n}{\Delta c_\mathrm{g}} \text{with} \quad \frac{\Delta n}{\Delta c_\mathrm{g}} = \frac{n_i - n_0}{\rho_i} \tag{2.4}$$

where ϕ_i is the volume fraction of the component i in the ME, n_i the refractive index of the pure substances, *i. e.*, 1.4685 for Tween20, 1.4496 for EHG, and 1.4376 for IPP, and ρ_i the density of the pure substances, *i. e.*, 1.095 for Tween20, 0.962 for EHG, and 0.8525 for IPP. The computed $\frac{\Delta n}{\Delta c_\mathrm{g}}$ values for Tween20, EHG, and IPP are 0.1283, 0.1264, and 0.1286 mL g^{-1}, respectively. Thus, for the microemulsions **ME-1**, **ME-3**, and **ME-4**, the $\mathrm{d}n/\mathrm{d}c_\mathrm{g}$ value evaluates approximately to 0.1281 mL g^{-1}.

Dynamic Light Scattering

The analysis of DLS data was performed with two different methods: (a) the analysis of the initial slope and (b) the optimized regularization technique (ORT). The analysis of the initial slope uses a simple exponential decay function (see Equation 2.5).

$$g^{(2)}(\tau) - 1 = \beta \cdot e^{-2\Gamma\tau} \tag{2.5}$$

where $g^{(2)}(\tau)$ is the intensity autocorrelation function, β the coherence factor of the instrument (approximately 0.9 for the used instrument), Γ the decay-rate, and τ the correlation time. The measured correlation data $(g^{(2)}(\tau)-1)$ were fitted in the τ range from $1 \cdot 10^{-9}$ to $1 \cdot 10^{-5}$ s. With the obtained decay rates, the diffusion coefficient (D) was fitted according to

$$\Gamma = D \cdot q^2 \tag{2.6}$$

in the q range of 0.0132–0.0244 nm^{-1} (60–135°). The diffusion coefficient was converted to a hydrodynamic radius (R_h) via the Stokes–Einstein equation (2.7).

$$R_\mathrm{h} = \frac{k_\mathrm{B} \cdot T}{6 \cdot \pi \cdot \eta \cdot D} \tag{2.7}$$

The ORT analysis focuses on the reconstruction of a decay-rate distribution, which is inversely proportional to a correlation time distribution ($\tau = 1/\Gamma$). The decay-rate distribution can be converted to the diffusion coefficient domain and then to the hydrodynamic radius domain via the Equations 2.6 and 2.7. For reconstructing the correlation time distribution, which is usually framed as an inverse Laplace-transform, the ORT algorithm was adapted, which was published by Glatter *et al.* (1991)[74] and is similar to the CONTIN algorithm developed by Provencher (1982)[75].

The experimental field autocorrelation function ($g^{(1)}$), computed via the Siegert-relation $g^{(2)}(\tau) - 1 = \beta(g^{(1)}(\tau))^2$, can be represented as a weighted sum of field autocorrelation function, where $g_i^{(1)}(\tau)$ is the field autocorrelation function of a known decay-rate distribution of the ith component.

$$g^{(1)}(\tau) = \sum_i w_i g_i^{(1)}(\tau) \tag{2.8}$$

For a given normalized log-norm distribution

$$L(x, x_c, \sigma) = \frac{1}{\sqrt{2\pi}\sigma x} \cdot e^{-(\ln x - \ln x_c)^2 / 2\sigma^2} \tag{2.9}$$

where x_c and σ are the median and standard deviation of the log-norm distribution, respectively, the Laplace-transform is defined as

$$g_i^{(1)}(\tau) = \int_0^\infty L(s, \Gamma_i, \sigma_i) \cdot e^{-s \cdot \tau} \mathrm{d}s \tag{2.10}$$

where Γ_i is predefined to cover a specific range of decay-rates and σ_i is the logarithmic spacing of the Γ_i values. A corresponding weight (w_i) is obtained for each Γ_i value. Due to the use of a normalized log-norm distributions, the obtained weights can be used for displaying purposes.

2.2.9 Small-Angle Neutron Scattering

Instrumental Setups

KWS-1 At *Heinz Maier–Leibnitz Zentrum* (MLZ, Garching, Germany), the SANS instrument KWS-1[76,77] was used with three configurations. The wavelength (λ), collimation (l_{C}), and sample–detector distance (l_{SD}) for the configuration "high q", "mid q", and "low q" were set to 0.5, 0.5, and 1.2 nm, 8, 8, and 20 m, and 2, 8, and 20 m, respectively. The covered q range was 0.018–4.0 nm^{-1}. The samples were measured in Hellma QS cells with a path length of 2 mm. The sample temperature was controlled via the sample holder. The data reduction and absolute scaling was performed with the software QtiKWS (now QtiSAS).[78]

D11 The SANS instrument D11[79] at *Institut Laue–Langevin* (ILL, Grenoble, France) was used with three configurations. For the configuration "high q", "mid q", and "low q", the wavelength (λ) was set to 0.6 nm and the collimation (l_{C}), and sample–detector distance (l_{SD}) were set to 4, 8, and 40.5 m, and 1.4, 8, and 39 m, respectively. The samples were measured in Hellma QS cells with a path length of 1 mm. The sample temperature was controlled via the sample holder. The covered q range was 0.021–4.4 nm^{-1}. The data reduction and absolute scaling was done with the software GRASP.[80]

D33 The SANS instrument D33[81] at *Institut Laue–Langevin* (ILL, Grenoble, France) was used with two setups: a setup with three configurations and a setup with a single configuration. The samples were measured in Hellma QS cells with a path length of 2 mm for polymer solutions and 1 mm for microemulsion-based solutions. The sample temperature was controlled via the sample holder.

For the setup with three configuration, the wavelength (λ), collimation (l_C), and sample–detector distance (l_{SD}) were set to 0.46, 0.46, and 1.3 nm, 2, 8, and 12 m, and 2, 8, and 12 m, respectively. The covered q range was 0.025–5.8 nm^{-1}. The data reduction and absolute scaling was performed with the software LAMP.[82]

The setup with one configuration uses two separate detectors. One detector was fixed in the front at a sample–detector distance (l_{SD}) of 1.2 m and the other detector was moved to a l_{SD} of 13.3 m. The wavelength and collimation (l_C) were set to 0.6 nm and 12.8 m, respectively. The covered q range was 0.031–4.7 nm^{-1}. The data reduction and absolute scaling was performed with the software GRASP.[80]

ZOOM At ISIS Pulsed Neutron Source (STFC Rutherford Appleton Laboratory, Didcot, U.K.) the SANS instrument ZOOM[83] was used in time-of-flight (TOF) mode with a wavelength band ranging from 0.175 to 1.65 nm. The collimation (l_C) and sample–detector distance (l_{SD}) were set to 4 m and 8 m, respectively. The covered q range was 0.038–7.2 nm^{-1}. The data reduction and absolute scaling was performed with the software Mantid.[84]

SANS2D Additional SANS measurements at ISIS Pulsed Neutron Source were conducted at the instrument SANS2D.[83,85] This instrument was used in TOF mode with a wavelength band ranging from 0.175 to 1.44 nm. The collimation (l_C) and sample–detector distance (l_{SD}) were set to 8 m. The covered q range was 0.026–7.9 nm^{-1}. The data reduction and absolute scaling was performed with the software Mantid.[84]

Instrumental smearing

The instrumental smearing of the calculated intensities was performed with the instrument-supplied uncertainties σ_q. The implementation follows the SASview documentation for a pinhole setup.[86] The smeared intensity is computed via Equation 2.11.

$$I_{\mathrm{smeared}}(q_i) = \sum_j \left[\frac{1}{2} \operatorname{erf}\left(\frac{(q_i + q_{i+1})/2 - q_j}{\sqrt{2}\sigma_{q,j}} \right) - \frac{1}{2} \operatorname{erf}\left(\frac{(q_i + q_{i-1})/2 - q_j}{\sqrt{2}\sigma_{q,j}} \right) \right] I(q_j) \tag{2.11}$$

where $\operatorname{erf}(x) = \frac{2}{\sqrt{\pi}} \int_0^x e^{-t^2} \mathrm{d}t$ is the Gaussian errorfunction. For setups with multiple configurations, each configuration is smeared independently.

Analysis of Small-Angle Neutron Scattering Data

Incoherent Background   The incoherent background (I_{bkg}) arises mainly from the incoherently scattered neutrons of hydrogen (H) atoms and dominates mainly in the high q region. This contribution was determined by fitting the high q region ($q \geq 1.5\,\mathrm{nm}^{-1}$) with a simple power-law (Equation 2.12). The intensity following a power-law can be written as

$$I(q) = A \cdot q^{-f} + I_{\mathrm{bkg}} \tag{2.12}$$

where A is a scaling prefactor and f is the power-law exponent. For mass fractals, the power-law exponent corresponds to the mass fractal dimension of the scattering object. The incoherent background is subtracted for all displayed scattering curves and is used for further analyses as a fixed parameter.

Effective Aggregation Number   The determination of the effective aggregation number from SANS data is very similar to that of light scattering data. The main difference is the observed q range and therefore the observable aggregate size. A plateau-like regime in the log–log scaled scattering data was used to estimate the forward scattering intensity $I(0)$ via the Guinier law (Equation 2.2). From the obtained $I(0)$ value, the effective aggregation number can be calculated via Equation 2.3 with the corresponding contrast factor $K = \frac{(SLD_{\mathrm{sol}} - SLD_{\mathrm{p}})^2}{\rho_{\mathrm{p}}{}^2 N_{\mathrm{Av}}}$ where SLD_{sol} is the scattering length density of the solvent, SLD_{p} is the scattering length density of the polymer, and ρ_{p} is the mass density of the polymer.

Molecular Weight of Microemulsion Droplets   The mass averaged molecular weight (M_{w}) of microemulsion (ME) droplets was also calculated from the forward scattering intensity $I(0)$ estimated via the Guinier law (Equation 2.2).

$$M_{\mathrm{w}} = \frac{I(0)}{S(0) \cdot K \cdot \phi_{\mathrm{ME}} \cdot \rho_{\mathrm{ME}}} \tag{2.13}$$

where $K = \frac{(SLD_{\mathrm{sol}} - SLD_{\mathrm{ME}})^2}{\rho_{\mathrm{ME}}{}^2 N_{\mathrm{Av}}}$ is the contrast factor for the microemulsion, ϕ_{ME} is the volume fraction of the microemulsion, SLD_{sol} is the scattering length density of the solvent, SLD_{ME} is the scattering length density of the microemulsion, ρ_{ME} is the averaged mass density of a microemulsion droplet, and $S(0)$ is the structure factor at $q = 0$. The $S(0)$ value was obtained from the fit of the sticky hard-sphere structure factor (Equation 2.53, $S(0) \approx S_{\mathrm{shs}}(0)$).

Polymer Coil with Excluded Volume   The scattering of polymer coils in solution can be described by

$$I_{\text{coil}}(q) = \phi_{\text{p}} \cdot V_{\text{n,p}} \cdot (SLD_{\text{sol}} - SLD_{\text{p}})^2 \cdot P_{\text{coil}}(q) + I_{\text{bkg}} \tag{2.14}$$

where ϕ_{p} and $V_{\text{n,p}}$ are the volume fraction and the molecular volume of the polymer, respectively, and $P_{\text{coil}}(q)$ is the form factor of a polymer chain with excluded volume.

$$P_{\text{coil}}(q) = \frac{1}{\nu U^{1/2\nu}} \cdot \gamma\left(\frac{1}{2\nu}, U\right) - \frac{1}{\nu U^{1/\nu}} \cdot \gamma\left(\frac{1}{\nu}, U\right) \tag{2.15}$$

with $\gamma(s, x) = \int_0^x t^{s-1} e^{-t} \mathrm{d}t$ as the incomplete gamma function. The variable U is defined based on the statistical segment length (a), the degree of polymerization (n), and the excluded volume parameter (ν), which is inversely proportional to the mass fractal dimension of the polymer ($f_{\text{p}} = 1/\nu$). This relationship can be transformed to be dependent on the radius of gyration (R_{g}) and ν.

$$U = \frac{q^2 a^2 n^{2\nu}}{6} = \frac{q^2 {R_{\text{g}}}^2 (2\nu + 1)(2\nu + 2)}{6} \tag{2.16}$$

The value of f_{p} was constrained between 1 and 3 (1: stiff rod, $\approx 5/3$: fully swollen chain, 2: Gaussian chain, > 2: collapsed chain, 3: homogenous sphere)

Clustered Polymer-Micelles   The clustered polymer-micelle model was inspired by Zinn *et al.* (2017)[87] and comprises the formation of polymer-micelles and their clustering. This model consists of a micellar form factor (P_{mic}), a pearl-necklace chain form factor[88] (S_{clu}), to account for the clustering of the micelles, and an effective hard-sphere structure factor ($S_{\text{hs}}^{\text{eff}}$), to consider the excluded volume of the micelles. Accordingly, the scattering intensity can be written as

$$I(q) = \frac{\phi_{\text{p}}}{V_{\text{mic}}} \cdot S_{\text{clu}}(q) \cdot P_{\text{mic}}(q) \cdot S_{\text{hs}}^{\text{eff}}(q) + I_{\text{bkg}} \tag{2.17}$$

where ϕ_{p} is the polymer volume fraction and $V_{\text{mic}} = N_{\text{agg}} \cdot V_{\text{n,p}}$ is the micelle volume, which is computed via the aggregation number (N_{agg}) and the molecular volume of the polymer ($V_{\text{n,p}}$).

The micellar form factor (P_{mic}) was first described by Pedersen and Gerstenberg (1996)[89]. A modified version was published by Hammouda and M. H. Kim (2017)[90], which uses polymer chains with excluded volume, and was later summarized by Wei and Hore (2021)[91]. The micellar form factor (*cf.* Scheme 2.2a) is written as

$$P_{\text{mic}}(q) = P_{\text{csh}}(q) + N_{\text{agg}} P_{\text{p}}(q) + 2N_{\text{agg}}^2 X_{\text{csh–p}}(q) + N_{\text{agg}}(N_{\text{agg}} - 1) X_{\text{p–p}}(q) \tag{2.18}$$

where P_{csh} is the form factor of a core-shell sphere, P_{p} is the form factor of a polymer chain in the corona, and $X_{\text{csh–p}}$ and $X_{\text{p–p}}$ are the core-shell–polymer and polymer–polymer interference terms, respectively.
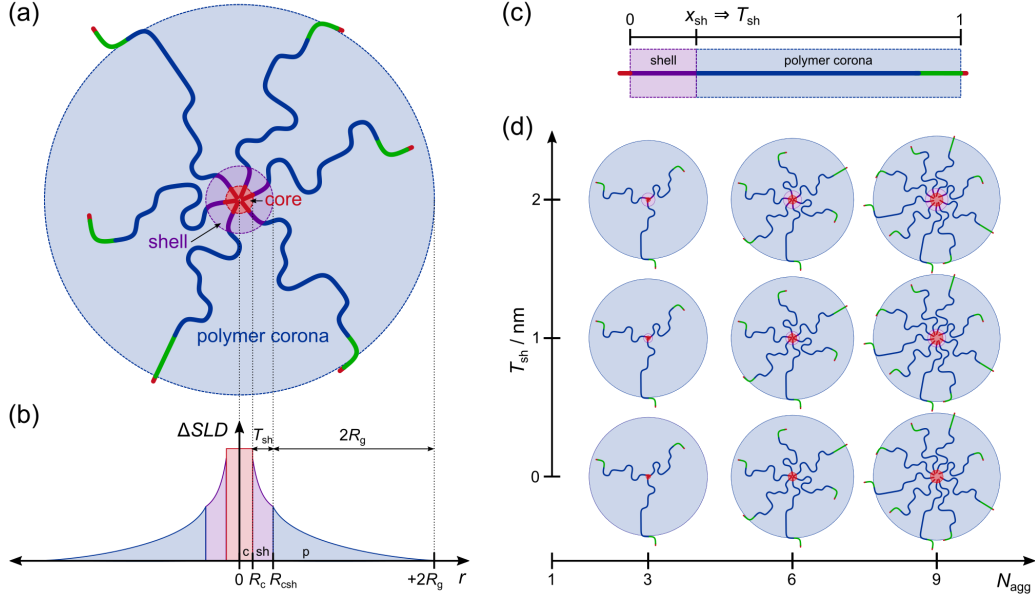
Scheme 2.2: (a) Schematic drawing of a polymer micelle described by the micellar form factor $P_{\mathrm{mic}}(q)$ (Equation 2.18). (b) Scattering length density (SLD) profile of the polymer micelle with the three segments, core (red, c), shell (purple, sh), and polymer corona (blue, p) consisting of the hydrophobic R-groups, the fraction x_{sh} of polymer chains in the shell, and the remaining fraction of each polymer chain represented as polymer coils, respectively. The total micellar radius is defined as $R_{\mathrm{mic}} = R_{\mathrm{csh}} + 2R_{\mathrm{g}}$ with $R_{\mathrm{csh}} = R_{\mathrm{c}} + T_{\mathrm{sh}}$. (c) Representation of the fraction x_{sh} which translates into a shell thickness T_{sh}. (d) Sketched polymer micelles show different aggregation numbers (N_{agg}) and shell thicknesses (T_{sh}) resulting from x_{sh}.

The core-shell form factor (P_{csh}) is the square of the scattering amplitude (A_{csh}). This form factor describes the scattering of a hydrophobic core and a hydrophilic shell, which is made up of a fraction of the polymer (*cf.* Scheme 2.2b/c). The core-shell scattering amplitude is defined as

$$A_{\mathrm{csh}}(q) = V_{\mathrm{c}} \cdot (SLD_{\mathrm{sol}} - SLD_{\mathrm{c}}) \cdot A_{\mathrm{c}}(q) + V_{\mathrm{sh}} \cdot (SLD_{\mathrm{sol}} - SLD_{\mathrm{sh}}) \cdot A_{\mathrm{sh}}(q) \qquad (2.19)$$

where V_i, SLD_i, and A_i are the volume, the scattering length density, and the scattering amplitude, respectively. The index i refers to the core (c), shell (sh), and solvent (sol).

The amplitude of the core (A_{c}) can be written as

$$A_{\mathrm{c}}(q) = 3 \cdot \frac{\sin(qR_{\mathrm{c}}) - qR_{\mathrm{c}} \cdot \cos(qR_{\mathrm{c}})}{(qR_{\mathrm{c}})^3} \qquad (2.20)$$

where $R_{\mathrm{c}} = \sqrt[3]{\frac{3V_{\mathrm{c}}}{4\pi}}$ is the radius of the core.

The volume and scattering length density of the core are computed by

$$V_c = N_{agg} \cdot V_{n,\text{R-group}} \tag{2.21}$$

$$SLD_c = SLD_{\text{R-group}} \tag{2.22}$$

with $V_{n,\text{R-group}}$ and $SLD_{\text{R-group}}$ as the volume and scattering length density of the R-group, respectively.

For the shell, an exponentially decaying density profile (n_{sh}) is directly transformed to obtain the corresponding scattering amplitude of the shell (A_{sh}).

$$n_{sh}(r) = \frac{r^{-x}}{1 + e^{(r-R_{csh})/(\sigma R_{csh})}} \tag{2.23}$$

where $x = 4/3$ is a scaling factor for star-like micelles,[87] σ is the relative width of the shell surface (set to $1\,\%$), and $R_{csh} = R_c + T_{sh}$ is the core-shell radius with T_{sh} as the thickness of the shell. Correspondingly, the scattering amplitude of the shell (A_{sh}) is computed using the Debye equation.

$$A_{sh}(q) = \frac{\int_{R_c}^{\infty} n_{sh}(r) \cdot j_0(qr) \cdot 4\pi r^2 \mathrm{d}r}{\int_{R_c}^{\infty} n_{sh}(r) \cdot 4\pi r^2 \mathrm{d}r} \tag{2.24}$$

where $j_0(x) = \sin(x)/x$ is the spherical Bessel function of 0th order. The shell thickness is calculated based on the volume of the shell (V_{sh}) and the given density profile (n_{sh}).

The volume and scattering length density of the shell are calculated via

$$V_{sh} = N_{agg} \cdot x_{sh} \cdot (V_{\text{pDMAm}} + V_{\text{pTR}}) \tag{2.25}$$

$$SLD_{sh} = \frac{V_{\text{pDMAm}} \cdot SLD_{\text{DMAm}} + V_{\text{pTR}} \cdot SLD_{\text{TR}}}{V_{\text{pDMAm}} + V_{\text{pTR}}} \tag{2.26}$$

with $V_{\text{pDMAm}} = DP_{n,\text{DMAm}}^{\text{theo}} \cdot V_{n,\text{DMAm}}$ and $V_{\text{pTR}} = DP_{n,\text{TR}}^{\text{theo}} \cdot V_{n,\text{TR}}$. Here, DP_n^{theo} is the corresponding theoretically calculated degree of polymerisation of the pDMAm or pTR block, V_n is the corresponding molecular volume of the DMAm or TR unit, and x_{sh} is the polymer chain fraction in the shell.

The form factor of a polymer chain in the corona (P_p) is written as

$$P_p(q) = V_p^2 \cdot (SLD_{sol} - SLD_p)^2 \cdot P_{coil}(q) \tag{2.27}$$

where P_{coil} is the form factor of a polymer coil with excluded volume according to Equation 2.15. The volume of a polymer chain in the corona (V_p) is computed via

$$V_p = (1 - x_{sh}) \cdot (V_{\text{pDMAm}} + V_{\text{pTR}}) + V_{n,\text{Z-group}} \tag{2.28}$$

with $V_{n,\text{Z-group}}$ as the volume of the Z-group.

The corresponding scattering length density (SLD_p) is defined as

$$SLD_\mathrm{p} = \frac{(1 - x_\mathrm{sh}) \cdot (V_\mathrm{pDMAm} \cdot SLD_\mathrm{DMAm} + V_\mathrm{pTR} \cdot SLD_\mathrm{TR}) + V_\mathrm{n,Z\text{-}group} \cdot SLD_\mathrm{Z\text{-}group}}{(1 - x_\mathrm{sh}) \cdot (V_\mathrm{pDMAm} + V_\mathrm{pTR}) + V_\mathrm{n,Z\text{-}group}}$$

(2.29)

where $SLD_\mathrm{Z\text{-}group}$ is the scattering length density of the Z-group.

The two interference terms, *i. e.*, the core-shell–polymer ($X_\mathrm{csh-p}$) and polymer–polymer ($X_\mathrm{p-p}$) interference terms, are defined as

$$X_\mathrm{csh-p}(q) = A_\mathrm{csh}(q) \cdot j_0(qR_\mathrm{csh}) \cdot A_\mathrm{p}(q)$$

(2.30)

$$\text{and} \quad X_\mathrm{p-p}(q) = [j_0(qR_\mathrm{csh}) \cdot A_\mathrm{p}(q)]^2$$

(2.31)

where $A_\mathrm{p}(q)$ is the amplitude of a polymer coil with excluded volume. The polymer coil amplitude can be written as

$$A_\mathrm{p}(q) = V_\mathrm{p} \cdot (SLD_\mathrm{sol} - SLD_\mathrm{p}) \cdot \left[\frac{1}{2\nu U^{1/2\nu}} \cdot \gamma\left(\frac{1}{2\nu}, U\right) \right] \quad .$$

(2.32)

The pearl-necklace chain form factor (S_clu) was used to account for the clustering of polymer-micelles.[87,88] This form factor considers the correlation between pearls along the necklace-like chain (Scheme 2.3b).

$$S_\mathrm{clu}(q) = (1 - p_\mathrm{clu}) \cdot S_{\lfloor N_\mathrm{clu} \rfloor}(q) + p_\mathrm{clu} \cdot S_{\lfloor N_\mathrm{clu} \rfloor + 1}(q)$$

(2.33)

$$\text{with} \quad S_N(q) = \frac{2}{N} \left[\frac{N}{1 - j_0(qd_\mathrm{clu})} - \frac{N}{2} - \frac{1 - j_0(qd_\mathrm{clu})^N}{[1 - j_0(qd_\mathrm{clu})]^2} \cdot j_0(qd_\mathrm{clu}) \right]$$

(2.34)

where $d_\mathrm{clu} = 2R_\mathrm{hs}$ is the spacing of the pearls, which is fixed by the hard-sphere radius, N_clu is the number of polymer-micelles per pearl-necklace chain. Due to the necessity of an integer for N, a linear combination weighted by p_clu of the floored integer values $\lfloor N_\mathrm{clu} \rfloor$ and $\lfloor N_\mathrm{clu} \rfloor + 1$ is introduced to fulfill $N_\mathrm{clu} \geq 1$.

To account for the excluded volume occupied by the polymer-micelles, a simple hard-sphere potential according to the Percus–Yevick approximation was used as a structure factor.[92] The hard-sphere structure factor (S_hs) is given by

$$S_\mathrm{hs}(q) = \frac{1}{1 + 24\phi_\mathrm{hs} \cdot G(2qR_\mathrm{hs})}$$

(2.35)

$$\text{with} \quad G(x) = \frac{A}{x^3}[\sin(x) - x \cdot \cos(x)]$$

$$+ \frac{B}{x^4}\left[2x \cdot \sin(x) + (1 - x^2) \cdot \cos(x) - 2\right]$$

$$+ \frac{C}{x^6}\left[-x^4 \cdot \cos(x) + 4\left([3x^2 - 6] \cdot \cos(x) + [x^3 - 6x] \cdot \sin(x) + 6\right)\right]$$

$$\text{and} \quad A = \frac{(1 + 2\phi_\mathrm{hs})^2}{(1 - \phi_\mathrm{hs})^4}, B = \frac{-6\phi_\mathrm{hs} \cdot (1 + \phi_\mathrm{hs}/2)^2}{(1 - \phi_\mathrm{hs})^4}, C = \frac{^{1/2}\phi_\mathrm{hs} \cdot (1 + 2\phi_\mathrm{hs})^2}{(1 - \phi_\mathrm{hs})^4}$$

where R_hs is the hard-sphere radius and ϕ_hs is the hard-sphere volume fraction.
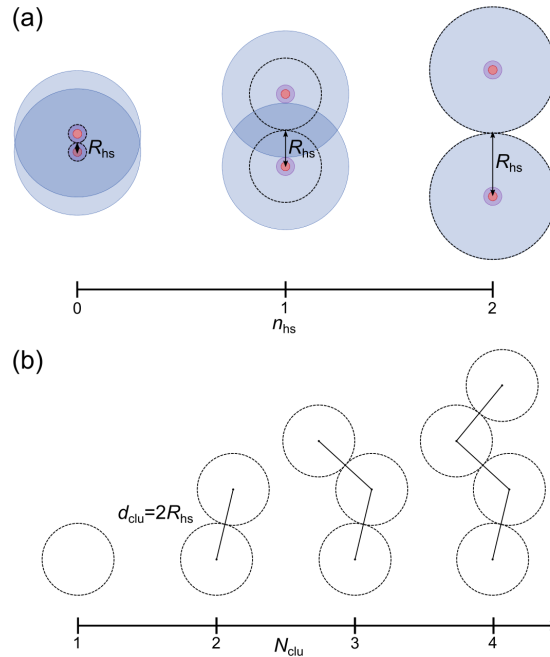
Scheme 2.3: (a) Hard-sphere interaction of polymer micelles within the defined boundaries of $0 \leq n_{\mathrm{hs}} \leq 2$ ($R_{\mathrm{hs}} = R_{\mathrm{csh}} + n_{\mathrm{hs}} \cdot R_{\mathrm{g}}$) which allows for a penetration of the polymer corona. (b) Representation of the pearl-necklace-like clustering of polymer micelles with a micellar distance of $d_{\mathrm{clu}} = 2R_{\mathrm{hs}}$.

R_{hs} is defined in terms of the micellar dimensions R_{csh} and R_{g} with n_{hs} as

$$R_{\mathrm{hs}} = R_{\mathrm{csh}} + n_{\mathrm{hs}} \cdot R_{\mathrm{g}} \tag{2.36}$$

where $0 \leq n_{\mathrm{hs}} \leq 2$ is introduced to account for interpenetration of the polymer corona (Scheme 2.3a). The hard-sphere volume fraction (ϕ_{hs}) is defined as $\phi_{\mathrm{hs}} = {}^{1}N \cdot \frac{4}{3}\pi R_{\mathrm{hs}}{}^{3}$ with ${}^{1}N = \frac{\phi_{\mathrm{p}}}{V_{\mathrm{mic}}}$ where ${}^{1}N$ is the number density of polymer-micelles. It is important to mention that this relation cannot be imposed for high number densities and for samples phase-separating at higher temperatures because of the large extent of interpenetration and the additional attractive interactions. Thus, ϕ_{hs} was treated as an additional variable parameter.

According to the decoupling approach, an effective hard-sphere structure factor can be defined as

$$S_{\mathrm{hs}}^{\mathrm{eff}}(q) = 1 + \beta(q) \cdot (S_{\mathrm{hs}}(q) - 1) \tag{2.37}$$

where $\beta(q) = A_{\mathrm{mic}}(q)^{2}/P_{\mathrm{mic}}(q)$ is the quotient of the squared micellar scattering amplitude (A_{mic}) and the micellar form factor (P_{mic}).

The micellar scattering amplitude (A_{mic}) is defined as

$$A_{\mathrm{mic}}(q) = A_{\mathrm{csh}}(q) + N_{\mathrm{agg}} A_{\mathrm{p}}(q) \tag{2.38}$$

with A_{csh} as core-shell scattering amplitude (Equation 2.19) and A_{p} as scattering amplitude of a polymer coil with exlcuded volume (Equation 2.32).

This clustered polymer-micelle model was used with basically 4 free parameters, *i. e.*, the aggregation number (N_{agg}), the polymer chain fraction in the shell (x_{sh}), the number of micelles per cluster (N_{clu}), and the hard-sphere radius (R_{hs}), which is varied via the scaling parameter for R_{hs} (n_{hs}). Only for the above-mentioned cases (high concentrations, and samples phase-separating at higher temperature), the hard-sphere volume fraction (ϕ_{hs}) becomes a variable parameter in the boundaries of ϕ_{p} and a volume fraction of 0.494 at which a phase transition of hard-sphere occurs.[93]

Core-Shell Spheres   A spherical core-shell model can be used to model the aggregation of polymer chains with a simple core and shell consisting of the hydrophobic and hydrophilic parts, respectively, with constant *SLD* values. The model intensity can be written as

$$I_{\mathrm{csh}}(q) = \frac{\phi_{\mathrm{p}}}{N_{\mathrm{agg}} V_{\mathrm{p}}} \cdot |A_{\mathrm{csh}}(q)|^2 \cdot S_{\mathrm{hs}}(q) + I_{\mathrm{bkg}} \tag{2.39}$$

where ϕ_{p} is the volume fraction of polymer in solution, N_{agg} is the aggregation number, V_{p} is the molecular volume of a polymer chain, $S_{\mathrm{hs}}(q)$ is the hard-sphere structure factor (Equation 2.35), and I_{bkg} is the incoherent background.

The core-shell scattering amplitude (A_{csh}) is defined as

$$\begin{aligned} A_{\mathrm{csh}}(q) = &(SLD_{\mathrm{sol}} - SLD_{\mathrm{c}}) \cdot V_{\mathrm{c}} \cdot A(q, R_{\mathrm{c}}) \\ &+ (SLD_{\mathrm{sol}} - SLD_{\mathrm{sh}}) \cdot V_{\mathrm{sh}} \cdot [A(q, R_{\mathrm{csh}}) - A(q, R_{\mathrm{c}})] \end{aligned} \tag{2.40}$$

where SLD_i, V_i, and R_i are the scattering length density, volume, and radius, respectively, and $A(q, R_i)$ is the scattering amplitude of a homogenous sphere with radius R_i (Equation 2.41). The index i refers to the core (c), shell (sh), core-shell (csh), and solvent (sol).

The scattering amplitude of a sphere can be written as

$$A(q, R) = 3 \cdot \frac{\sin qR - qR \cdot \cos qR}{(qR)^3} \tag{2.41}$$

where R is the radius of the sphere.

The volume and scattering length density of the core were calculated as

$$V_{\mathrm{c}} = N_{\mathrm{agg}} \cdot V_{\mathrm{n,R\text{-}group}} + V_{\mathrm{n,R\text{-}group}} \tag{2.42}$$

$$SLD_{\mathrm{c}} = SLD_{\mathrm{R\text{-}group}} \tag{2.43}$$

where $V_{\mathrm{n,R\text{-}group}}$ and $SLD_{\mathrm{R\text{-}group}}$ are the molecular volume and scattering length density of the R-group, respectively.

For the shell, V_sh and SLD_sh are defined as

$$V_\text{sh} = N_\text{agg} \cdot (V_\text{pDMAm} + V_\text{pTR} + V_\text{n,Z-group} + V_\text{sol}) \tag{2.44}$$

$$\text{with} \quad V_\text{pDMAm} = DP_\text{n,DMAm}^\text{theo} \cdot V_\text{n,DMAm},$$

$$V_\text{pTR} = DP_\text{n,TR}^\text{theo} \cdot V_\text{n,TR},$$

$$V_\text{sol} = \alpha \cdot (V_\text{pDMAm} + V_\text{pTR} + V_\text{n,Z-group}),$$

and

$$SLD_\text{sh} = \frac{V_\text{pDMAm} \cdot SLD_\text{DMAm} + V_\text{pTR} \cdot SLD_\text{TR} + V_\text{n,Z-group} \cdot SLD_\text{Z-group} + V_\text{sol} \cdot SLD_\text{sol}}{V_\text{pDMAm} + V_\text{pTR} + V_\text{n,Z-group} + V_\text{sol}}$$

$$\tag{2.45}$$

where α is the swelling ratio of the shell, DP_n^theo is the corresponding theoretically calculated degree of polymerisation of the pDMAm and pTR block, and V_n is the corresponding molecular volume of the DMAm unit, TR unit, and Z-group. The molecular volume (V_n) and scattering length density (SLD) values are summarized in the Tables 2.1 and 2.2. The core and core-shell radius were calculated based on the corresponding volume via $R_i = \sqrt[3]{\frac{3V_i}{4\pi}}$.

The hard-sphere structure factor (Equation 2.35) is used to describe the repulsive interaction of the spherical aggregates. The hard-sphere radius (R_hs) was defined as a variable parameter in the boundaries of R_c and R_csh. Accordingly, the hard-sphere volume fraction (ϕ_hs) was computed based on the number density (^1N) of aggregates $\phi_\text{hs} = {}^1N \frac{4\pi}{3} R_\text{hs}{}^3$ with $^1N = \frac{\phi_\text{p}}{N_\text{agg} V_\text{p}}$.

The variable parameters of the core-shell spheres model are the aggregation number (N_agg), the swelling ratio (α), which quantifies the amount of solvent in the shell, and the hard-sphere radius (R_hs). The core-shell radius (R_csh) derived from the aggregation number and the swelling ratio of the shell.

Attractive Core-Shell Ellipsoids   To analyze the SANS data of the microemulsion-based systems, a SANS model consisting of core-shell ellipsoids interacting via a sticky hard-sphere potential was used. The scattering intensity (I_csh) is defined as

$$I_\text{csh}(q) = \frac{\phi_\text{ME}}{V_\text{ME}} \cdot P_\text{csh}(q) \cdot S_\text{shs}(q) + I_\text{p}(q) + I_\text{bkg} \tag{2.46}$$

where ϕ_ME is the volume fraction of the microemulsion components, *i.e.*, surfactant, cosurfactant, and oil, V_ME is the dry volume of a microemulsion droplet, P_csh is the ellipsoidal core-shell form factor, S_shs is the sticky hard-sphere structure factor by Baxter (1968)[94] (Equation 2.53), I_p is the scattering intensity of the added polymer (Equation 2.14), and I_bkg is the incoherent background.

The ellipsoidal core-shell form factor (P_{csh}) is computed via

$$P_{\text{csh}}(q) = \int_0^{\frac{\pi}{2}} |A_{\text{csh}}(q, \varphi\prime)|^2 \cdot \sin \varphi\prime \, \mathrm{d}\varphi\prime \tag{2.47}$$

which includes the orientational averaging of the ellipsoidal core-shell scattering amplitude (A_{csh}).

The ellipsoidal core-shell scattering amplitude can be written as

$$\begin{aligned} A_{\text{csh}}(q, \varphi) = {} & (SLD_{\text{sol}} - SLD_{\text{c}}) \cdot V_{\text{c}} \cdot A(q, R(\varphi, R_{\text{c}}, \varepsilon)) \\ & + (SLD_{\text{sol}} - SLD_{\text{sh}}) \cdot V_{\text{sh}} \cdot [A(q, R(\varphi, R_{\text{csh}}, \varepsilon)) - A(q, R(\varphi, R_{\text{c}}, \varepsilon))] \end{aligned} \tag{2.48}$$

where φ is the angle of orientation, SLD_i is the scattering length density, V_i is the volume, $A(q, R)$ is the scattering amplitude of a sphere (Equation 2.41), and $R(\varphi, R_i, \varepsilon) = \sqrt{R_i^2 \cdot \sin \varphi^2 + R_i^2 \varepsilon^2 \cdot \cos \varphi^2}$ is the radius as a function of the angle of orientation (φ), aspect ratio (ε, < 1: oblate, > 1: prolate, $= 1$: sphere), and the equatorial radius R_i of the ellipsoid ($R_i \varepsilon$ refers to the axial radius). The equatorial radius R_i is calculated from the corresponding volume via $R_i = \sqrt[3]{\frac{3V_i}{4\pi\varepsilon}}$. The index i refers to the core (c), shell (sh), core-shell (csh), and solvent (sol).

The volume (V_{c}) of the core is calculated as

$$\begin{aligned} V_{\text{c}} = {} & N_{\text{surf}} \cdot V_{\text{n,tail}} + N_{\text{co}} \cdot V_{\text{n,co}} \\ & + N_{\text{oil}} \cdot V_{\text{n,oil}} + N_{\text{p}}/N_{\text{ME}} \cdot V_{\text{n,R-group}} \end{aligned} \tag{2.49}$$

where N_i, $V_{\text{n},i}$, and SLD_i are the aggregation number, molecular volume, and scattering length density, respectively. The index i refers to surfactant (surf), surfactant's tail (tail), surfactant's head (head), cosurfactant (co), and oil of the corresponding microemulsion while the R-group belongs to the corresponding copolymer. Correspondingly, the scattering length density (SLD_{c}) is defined as

$$\begin{aligned} SLD_{\text{c}} = {} & SLD_{\text{tail}} \cdot \frac{N_{\text{surf}} \cdot V_{\text{n,tail}}}{V_{\text{c}}} + SLD_{\text{co}} \cdot \frac{N_{\text{co}} \cdot V_{\text{n,co}}}{V_{\text{c}}} \\ & + SLD_{\text{oil}} \cdot \frac{N_{\text{oil}} \cdot V_{\text{n,oil}}}{V_{\text{c}}} + SLD_{\text{R-group}} \cdot \frac{N_{\text{p}}/N_{\text{ME}} \cdot V_{\text{n,R-group}}}{V_{\text{c}}} \end{aligned} \tag{2.50}$$

with $N_{\text{p}}/N_{\text{ME}}$ as the ratio of polymer chains per microemulsion droplet.

Following this, the volume of the shell (V_{sh}) can be calculated via

$$V_{\text{sh}} = N_{\text{surf}} \cdot V_{\text{n,head}} + V_{\text{sol}} \quad \text{with} \quad V_{\text{sol}} = \alpha \cdot (N_{\text{surf}} \cdot V_{\text{n,head}}) \tag{2.51}$$

where V_{sol} is the volume of the solvent in the shell which is defined by the swelling ratio (α) of the shell. The corresponding scattering length density (SLD_{sh}) is defined as

$$SLD_{\text{sh}} = SLD_{\text{head}} \cdot \frac{N_{\text{surf}} \cdot V_{\text{n,head}}}{V_{\text{sh}}} + SLD_{\text{sol}} \cdot \frac{V_{\text{sol}}}{V_{\text{sh}}} \quad . \tag{2.52}$$

The values for the molecular volume (V_n) and the scattering length density (SLD) are summarized in Tables 2.1 and 2.2.

The sticky hard-sphere structure factor after Baxter (1968)[94] was applied and is defined as

$$S_\text{shs}(q) = \frac{1}{A(q)^2 + B(q)^2} \tag{2.53}$$

with $x = 2qR_\text{hs}$

$$A(q) = 1 + 12\phi_\text{hs}\left(a\left[\frac{\sin x - x\cos x}{x^3}\right] + b\left[\frac{1 - \cos x}{x^2}\right] - c\left[\frac{\sin x}{x}\right]\right),$$

$$B(q) = 12\phi_\text{hs}\left(a\left[\frac{1}{2x} - \frac{\sin x}{x^2} + \frac{1 - \cos x}{x^3}\right] + b\left[\frac{1}{x} - \frac{\sin x}{x^2}\right] - c\left[\frac{1 - \cos x}{x}\right]\right),$$

$$\text{and} \quad a = \frac{1 + 2\phi_\text{hs} - \mu}{(1 - \phi_\text{hs})^2}, b = \frac{-3\phi_\text{hs} + \mu}{2(1 - \phi_\text{hs})^2}, c = \frac{\lambda_\text{shs}}{12}, \mu = \lambda_\text{shs} \cdot \phi_\text{hs}(1 - \phi_\text{hs}) \tag{2.54}$$

where λ_shs is the parameter which controls the attraction strength, $i.\,e.$, attractive interaction, of the spheres. This parameter is 0 for purely repulsive interactions and increases with increasing attraction. The hard-sphere radius (R_hs) was defined as the volume equivalent radius (R_v) of the ellipsoid ($R_\text{v} = \sqrt[3]{\frac{3V_\text{csh}}{4\pi}}$). For samples with added copolymers, the hard-sphere radius was used as a variable parameter with the lower boundary of R_v. Accordingly, the hard-sphere volume fraction (ϕ_hs) was computed as $\phi_\text{hs} = {}^1N\frac{4\pi}{3}R_\text{v}^3\varepsilon$ with ${}^1N = \frac{\phi_\text{ME}}{V_\text{ME}}$ based on the number density (${}^1N$) of microemulsion droplets.

Chapter 3

Aggregation Behavior of Nonsymmetrically End-Capped Thermoresponsive Block Copolymers in Aqueous Solution

Copyright

This chapter is based on the published article

Author Contributions

A. Prause, M. Hechenbichler, A. Laschewsky, and M. Gradzielski conceptualized the block copolymers and the general experimental design. M. Hechenbichler synthesized the block copolymers and measured the turbidimetry data. A. Prause performed the experiments, if not otherwise specified, analyzed the data, and created the figures and schemes. B. von Lospichl measured the SANS data at KWS-1. A. Feoktystov, R. Schweins, and N. Mahmoudi were the local contacts at the SANS instruments KWS-1, D33, and ZOOM, respectively. The discussion of the results and writing of the manuscript was conducted jointly by A. Prause, M. Hechenbichler, A. Laschewsky, and M. Gradzielski. All authors approved on the final version of the manuscript.

Abstract
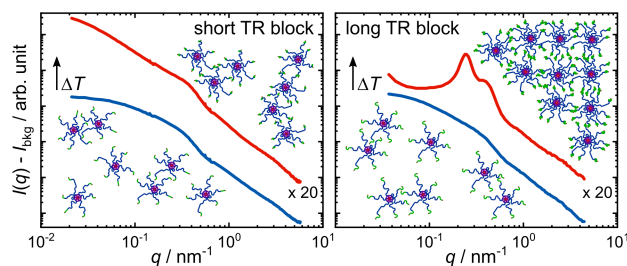
The thermosensitive aggregation behavior in aqueous solution of a library of amphiphilic BAB* copolymers is studied where "A" represents a long permanently hydrophilic poly(N,N-dimethylacrylamide) (pDMAm) block, "B" a permanently hydrophobic end with a n-dodecyl (C_{12}) chain, and "B*" a thermoresponsive (TR) block featuring a lower critical solution temperature (LCST). Four polyacrylamides are employed for B*, namely poly(N-n-propylacrylamide) (pNPAm), poly(N-isopropylacrylamide) (pNiPAm), poly(N,N-diethylacrylamide) (pDEAm), and poly(N-acryloylpyrrolidine) (pNAP), which differ with respect to the hydrophilicity of their amide side chains and LCST behavior. While blocks A and B were kept constant, the lengths of the TR blocks were varied systematically. These amphiphilic copolymers were studied as a function of concentration and temperature via light and neutron scattering (SLS, DLS, and SANS). For sufficiently long pNiPAm and pDEAm blocks ($DP_n > 40$), a pronounced hydrophobic effect at temperatures above the LCST transition results in well-structured, ordered aggregates. Thus, the aggregation can be controlled by choice and length of the TR block, thereby elucidating a so far hardly explored class of temperature-sensitive polymeric amphiphiles.

3.1 Introduction

Commonly, symmetrical triblock copolymers BAB with a long hydrophilic center block ("A") and two short hydrophobic end blocks ("B") are used to create polymers for rheological control (Scheme 3.1a).[95,96] The A block (Scheme 3.1b) or the B block (Scheme 3.1c) in a temperature-sensitive form can change from being hydrophilic to hydrophobic in response to a heat input, or vice versa. In this chapter, nonsymmetrical designs of the linear BAB* architecture were studied, where the long inner A block is permanently hydrophilic. The A block is enclosed by a small permanently hydrophobic end-group B ("hydrophobic sticker") on one end and a separate hydrophobic end block B* on the other end. The latter is intended to exhibit a LCST transition in water and is only conditionally hydrophobic (Scheme 3.1d). It should be noticed that in previous research, various telechelic polymers were investigated with end-caps made of long, permanently hydrophobic alkyl chains connected by varying number of arms of hydrophilic poly(N,N-dimethylacrylamide) (pDMAm). For these telechelic polymers, the concentration, and arm count influenced the formation of flower-like micelles and interconnected micellar networks.[7,97]
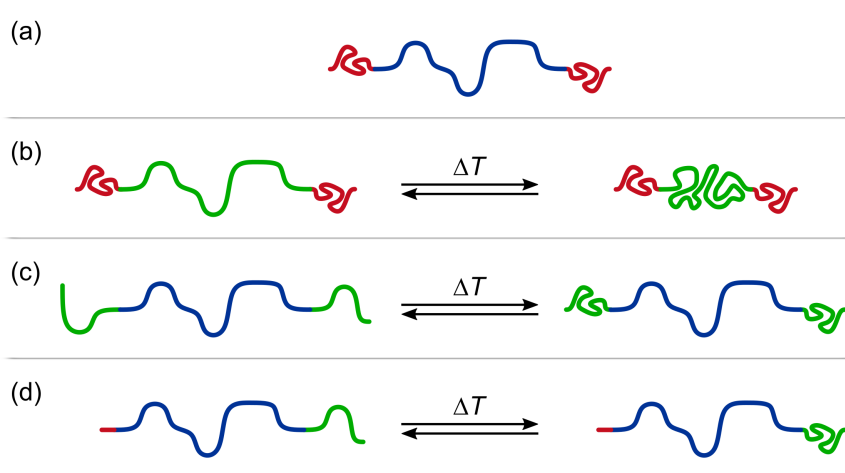
Scheme 3.1: Linear architectures of hydrophobically modified thermoresponsive (HMTR) block copolymers: (a) conventional design with permanently hydrophilic (blue) and hydrophobic (red) blocks, (b) conventional design with responsive (green, hydrophilic/hydrophobic) central block, (c) conventional design with two responsive (green, hydrophilic/hydrophobic) end blocks, (d) investigated design with one permanent hydrophobic (red) and one responsive (green, hydrophilic/hydrophobic) block.

In this study, similar to previous studies,[55,97,98] the permanently hydrophilic central block of the copolymers is build from the nonionic monomer N,N-dimethylacrylamide (DMAm, Scheme 3.2), whose polymers are permanently hydrophilic within the full temperature range of liquid water under atmospheric pressure.[99] The hydrophobic sticker group (R-group), which consists of an aromatic residue and an attached n-dodecyl (C_{12}) chain, is kept constant and corresponds structurally to a low molecular weight surfactant

(*cf.* Table 2.2). On the contrary, the responsive end block is altered by using four different acrylamide monomers, *i. e.*, *N-n*-propylacrylamide (NPAm), *N*-isopropylacrylamide (NiPAm), *N,N*-diethylacrylamide (DEAm), and *N*-acryloylpyrrolidine (NAP), whose homopolymers are known to exhibit their LCST transition in aqueous solution between 20 °C and 60 °C (see Scheme 3.2 for the monomers).[17,100] This chapter succeeds an earlier study of hydrophobically modified thermoresponsive (HMTR) polymers of this particular design that used poly(*N,N*-bis(2-methoxyethyl)acrylamide) (pbMOEAm) as a thermoresponsive block, but with impractically high transition temperatures.[101]
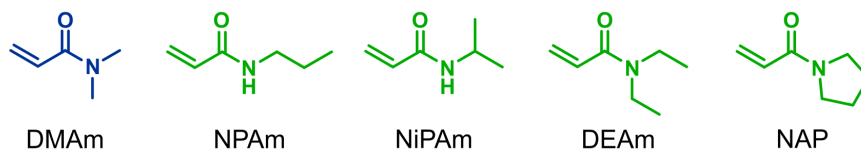
Scheme 3.2: Monomers used for synthesizing the HMTR block copolymers. The permanently hydrophilic first block is made of monomer *N,N*-dimethylacrylamide (DMAm, in blue). The thermoresponsive blocks with LCST behavior (in green) are made from monomers *N-n*-propylacrylamide (NPAm, LCST(pNPAm) $\approx$ 22 °C[60]), *N*-isopropylacrylamide (NiPAm, LCST(pNiPAm) $\approx$ 32 °C[62]), *N,N*-diethylacrylamide (DEAm, LCST(pDEAm) $\approx$ 30 °C[61]), and *N*-acryloylpyrrolidine (NAP, LCST(pNAP) $\approx$ 55 °C[60,63]).

Adapted with permission from Prause *et al.* (2022).[64] Copyright 2022 American Chemical Society.

In the following, the samples for turbidimetry were prepared in H_2O. In contrast, the samples for light and neutron scattering were prepared in D_2O. For example, the cloud point for pNiPAm in D_2O is increased by less than 1 K.[102,103] Accordingly, the difference between H_2O and D_2O as the solvent can be neglected.

3.2 Results and Discussion

3.2.1 Phase Transition Behavior

Temperature-dependent turbidimetry was used to examine the block copolymers' thermoresponsive behavior in aqueous solution at various concentrations (Figure 3.1). High molecular weight homopolymers of NPAm, NiPAm, DEAm and NAP (*cf.* Scheme 3.2) commonly exhibit LCST phase transitions at temperatures of $22\,°\text{C}$,[60] $32\,°\text{C}$,[62] $30\,°\text{C}$,[61] and $55\,°\text{C}$,[60,63] respectively. In contrast, pDMAm is soluble in water from 0 to $100\,°\text{C}$. Usually, the transition temperature rises as the block length decreases.[104,105]

Samples of $\mathbf{C_{12}DMAm_{168}NiPAm_{33}}$, $\mathbf{C_{12}DMAm_{168}DEAm_{27}}$, and their longer homologous showed a strong decrease in transmittance above their respective phase transition temperatures However, no macroscopic phase transition was detected for the block copolymers bearing very short thermoresponsive blocks with $DP_\text{n} < 20$. In comparison to the values normally reported for the homopolymers pNiPAm and pDEAm, the phase transition temperature of the respective block copolymers was significantly raised up to a temperature of $60\,°\text{C}$. The attached long hydrophilic pDMAm block and the associated hydrophilicity increase of the copolymers, as previously mentioned, are most likely responsible for this rise, which is only to a little extent a function of the short lengths of the thermoresponsive blocks.[63,98,101,106,107]
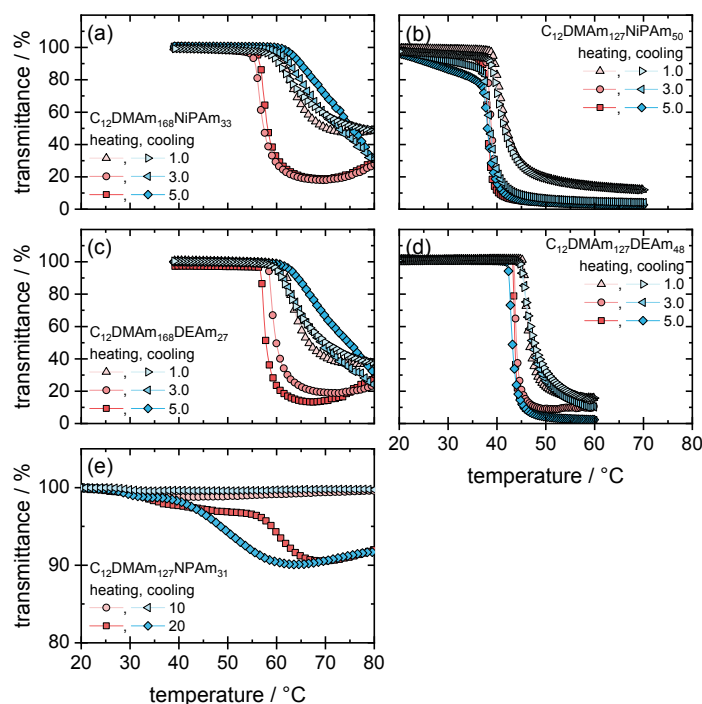
Figure 3.1: Temperature dependent turbidimetry (heating and cooling without stirring) as function of the polymer concentration of (a) $\mathbf{C_{12}DMAm_{168}NiPAm_{33}}$, (b) $\mathbf{C_{12}\text{-}DMAm_{127}NiPAm_{50}}$, (c) $\mathbf{C_{12}DMAm_{168}DEAm_{27}}$, (d) $\mathbf{C_{12}DMAm_{127}DEAm_{48}}$, and (e) $\mathbf{C_{12}DMAm_{127}NPAm_{31}}$. The concentrations are given in $\text{g\,L}^{-1}$.

The cloud points of the TR block copolymers approach those of their respective homopolymers as the TR blocks lengthen (see Figure 3.1). Despite the fact that the LCSTs of pNiPAm and pDEAm are nearly identical at about 32 °C and 30 °C, respectively, different behaviors were found for the block copolymers. While the cloud point of **C$_{12}$DMAm$_{127}$DEAm$_{48}$** is at a higher temperature of around 43–45 °C, that of **C$_{12}$-DMAm$_{127}$NiPAm$_{50}$** is at a temperature of around 38–39 °C (*cf.* Figure 3.1b/d). This disparity may be explained by the differing LCST types of the thermoresponsive polymers, Type I (Flory–Huggins-like) for pDEAm but Type II for pNiPAm.[17,108]

A more extreme divergence can be observed for **C$_{12}$DMAm$_{168}$NAP$_{27}$** which did not exhibit a distinct phase transition up to a temperature of 80 °C at a concentration of 5.0 g L^{-1}. The cloud point of the homopolymer pNAP, which also exhibits a LCST behavior of Type I, is already rather high at roughly 55 °C. Therefore, it appears likely that the addition of the hydrophilic pDMAm block will raise the cloud point even more above the interesting temperature range for water.

In contrast, the Z-group containing the trimethylsilyl (TMS) group is hydrophobic (though much less than the surfactant-like R-group). Due to its direct attachment to the thermoresponsive block, it will lower the polymers' phase transition temperature, partially offsetting the hydrophilic block's impact on the other side. Removing the Z-group intentionally, the cloud point for **C$_{12}$DMAm$_{168}$DEAm$_{27}$** rose from 50 °C to 59 °C for a concentration of 5.0 g L^{-1}, suggesting a substantial influence of the relatively tiny hydrophobic end-group directly attached to the thermoresponsive block on the cloud point (for further information, see the Supporting Information of Prause *et al.* (2022)[64]). However, it should be noted that the influence of bigger hydrophobic groups, such as the R-group, which can form distinct domains in water, tends to disappear.[109,110]

The block copolymer **C$_{12}$DMAm$_{127}$NPAm$_{31}$** has a very distinct behavior in aqueous solution when compared to the other copolymers (Figure 3.1e). The transmittance stays nearly steady at around 100 % up to a concentration of 10 g L^{-1}. But at a concentration of 20 g L^{-1}, the transmittance falls by 9 % and a two-step transition appears to be taking place. The transmittance begins to gradually decline in the first stage at a temperature of around 30 °C, which is a little higher than the phase transition temperature of 22 °C for pNPAm.[60] Once more, it is likely that the hydrophilic pDMAm block attached to the thermoresponsive block, which raises the phase transition temperature, is responsible for this behavior. The transmittance drops even more dramatically in the subsequent stage, but after reaching a minimum at about 65 °C, it starts to rise again. The cooling cycle also exhibits this two-step transition process (see Figure 3.1e), which means that stable aggregates are going through a reversible aggregation process without the system being stirred.

This observation can be compared with poly(*N*-ethylacrylamide) (pNEAm) reported by Weiss *et al.* (2011)[111], where the block copolymers only contain water-insoluble (yet partially swollen) blocks above the phase transition at about 70 °C. Even then, stable aggregates were still seen. However, when the ratio of the block length between the

hydrophilic pNEAm and the collapsed pNPAm block was larger than 1 : 1, clusters were seen in cryogenic transmission electron microscopy (cryo-TEM). The still relatively short hydrophilic pNEAm block, which would not be adequate to stabilize individual micelles, was used to explain the trend toward cluster formation.[111] Similar to **C₁₂DMAm₁₂₇-NPAm₃₁**, where the pNPAm block is shorter than the hydrophilic pNEAm blocks utilized in the reference,[111] less turbid solutions were obtained. In addition to the chemical structure of the thermoresponsive block and its length, these results imply that the ratio of the hydrophilic to the hydrophobic block has also a significant influence in the aggregation behavior of thermoresponsive block copolymers.
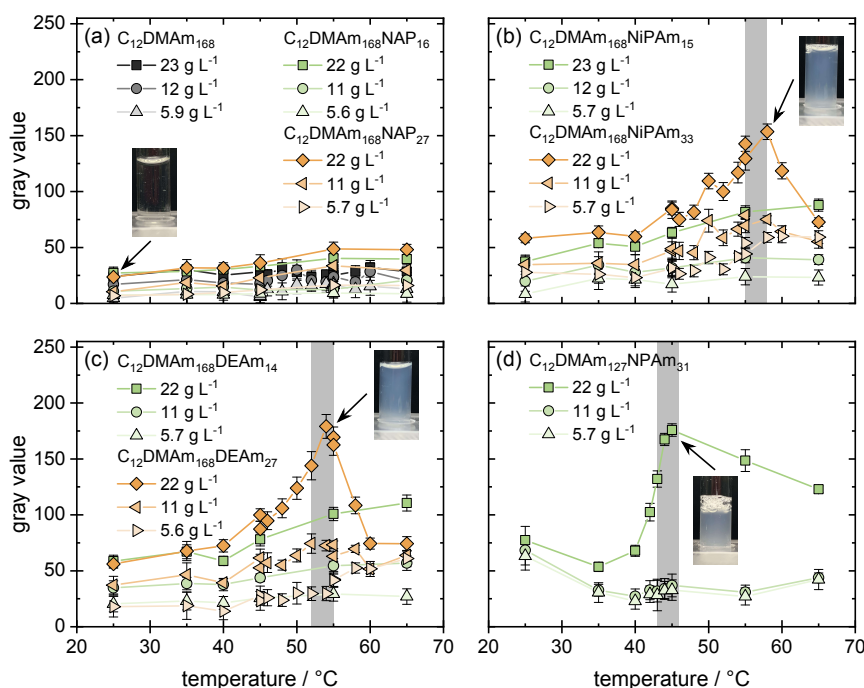
Figure 3.2: Phase behavior of polymers based on the visual analysis of photographs. The gray areas mark the temperature window of the macroscopically visible phase separation of **C₁₂DMAm₁₆₈NiPAm₃₃**, **C₁₂DMAm₁₆₈DEAm₂₇**, and **C₁₂DMAm₁₂₇NPAm₃₁**.

Reprinted with permission from Prause *et al.* (2022).[64] Copyright 2022 American Chemical Society.

Nonetheless, the substantial hysteresis between heating and cooling is distinctive for a thermoresponsive polyacrylamide containing NH groups, such as pNiPAm. The amide groups allow for intramolecular hydrogen bonding, which act as physical cross-linking sides in the collapsed state and must be broken during the re-dissolution process.[112] Figure 3.2, which quantifies the visual appearance as seen after a 15 min wait period by examining the samples' optical appearance in the pictures, also summarizes the thermoresponsive behavior. The results of turbidimetry (Figure 3.1) are generally confirmed by visual examinations, which also extend these results to highly concentrated samples. They specifically corroborate the unusual behavior of the **C₁₂DMAm₁₂₇NPAm₃₁** with an extra transition occurring at roughly 40 °C. This suggests that the pNPAm block has a lower affinity for association than the other TR blocks, which would make it more dynamic and prevent the development of a pronounced turbidity caused by macroscopic phase separation.

3.2.2 Aggregation Behavior

Light Scattering Studies

Static Light Scattering Light scattering investigations provided the first insights into the structure of the various polymers' aqueous solutions as a function of temperature and concentration. Figure A.1–A.3 (Appendix A) displays the static scattering intensity of the examined HMTR block polymers at various concentrations as a function of the magnitude of the scattering vector q. The Guinier law (Equation 2.2) was used to fit the low q data in order to obtain the extrapolated forward scattering intensity $I(0)$ for additional analysis. The extracted value for $I(0)$ was then transformed into the molecular weight of the scattering objects. The effective aggregation number $N_{\mathrm{eff}}^{\mathrm{SLS}}$ (Equation 2.3) was computed from this information and is shown in Figure 3.3 for various concentrations as a function of temperature.

Surprisingly, all HMTR polymers display an effective aggregation number greater than 10 for all temperatures. This finding does not imply that appropriate micellar aggregation always occurs, as this value is also seen for the homopolymer **DMAm$_{187}$**. It is, however, most likely the outcome of a network formation via entanglements, which is commonly noticed in small-angle scattering of polymers.[113] Even the homopolymer has a hydrophobic moiety as a result of RAFT polymerization, which might promote stronger entanglement associations.

The SANS results (described in more depth later in the Section 3.2.2) infer scattering patterns of single coils for **DMAm$_{187}$**, demonstrating unequivocally that no compacted aggregation occurs but that a looser sort of aggregation must exist. A significant upturn manifests at low q, or in the SLS q range, fully supporting the SLS findings. Due to the persistently hydrophilic nature of the pDMAm block, **DMAm$_{187}$** and the reference polymers without a TR block, namely **C$_{12}$DMAm$_{168}$** and **C$_{12}$DMAm$_{127}$**, exhibit no appreciable temperature dependency in the observed temperature range. Surprisingly, for **C$_{12}$DMAm$_{168}$**, $N_{\mathrm{eff}}^{\mathrm{SLS}}$ has the strongest effect with concentration. Between concentrations of 5.9 and $23\,\mathrm{g\,L^{-1}}$, $N_{\mathrm{eff}}^{\mathrm{SLS}}$ diminishes by roughly a factor of 4. Steric repulsion may be to account for this, as hydration of the hydrophilic block results in a substantially larger effective volume fraction. For the less hydrated TR blocks, this impact should be less pronounced. Additionally, when the temperature rises, they can provide more attractive interactions with one another.

The majority of HMTR polymers with a short TR block, *i. e.*, **C$_{12}$DMAm$_{168}$NiPAm$_{15}$**, **C$_{12}$DMAm$_{168}$NiPAm$_{33}$**, **C$_{12}$DMAm$_{168}$DEAm$_{14}$**, **C$_{12}$DMAm$_{168}$DEAm$_{27}$**, **C$_{12}$DMAm$_{168}$NAP$_{27}$**, and **C$_{12}$DMAm$_{127}$NPAm$_{31}$**, exhibit a little rise in $N_{\mathrm{eff}}^{\mathrm{SLS}}$ with increasing temperature, but this rise is not greatly influenced by concentration. The effective aggregation number $N_{\mathrm{eff}}^{\mathrm{SLS}}$ for **C$_{12}$DMAm$_{168}$NAP$_{16}$** is distinctive and starts out quite high at about 300 before progressively declining with increasing temperature, specifically above $45\,°\mathrm{C}$. The DLS data corroborate this observation (Figure A.4c).

45
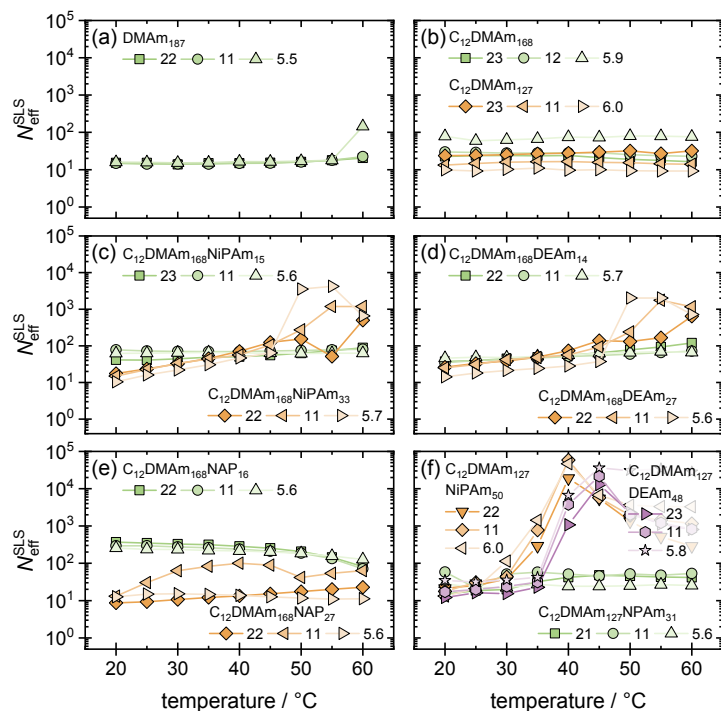
Figure 3.3: Effective aggregation number determined by SLS ($N_{\text{eff}}^{\text{SLS}}$) of HMTR polymers for the probed temperature range of 20–60 °C. According to Equation 2.3, $M_{\text{n}}^{\text{theo}}$ and $Đ$ were used as the molecular weight and dispersity of the corresponding HMTR polymers, respectively. Numbers in the labels refer to the mass concentration given in g L^{-1}. The estimated uncertainties are within the symbols.

As was previously shown in the turbidity investigations, only HMTR polymers with longer TR blocks exhibit a more pronounced temperature dependency (Figures 3.1 and 3.2). For the various studied systems, it is generally observed that $N_{\text{eff}}^{\text{SLS}}$ rises as temperature increases. Curiously, at lower concentrations, **C$_{12}$DMAm$_{168}$NiPAm$_{33}$** and **C$_{12}$-DMAm$_{168}$DEAm$_{27}$** demonstrate a more pronounced increase of $N_{\text{eff}}^{\text{SLS}}$ by more than one order of magnitude beginning at 45 °C (see Figure 3.3c/d). The beginning of the sample's phase separation is what causes the modest reduction that is visible at 60 °C. A similar impact is quite significant at $22 \, \text{g L}^{-1}$, when there is no obvious rise in $N_{\text{eff}}^{\text{SLS}}$, but there is a significant increase in intensity scatter because of the phase transition regime.

For **C$_{12}$DMAm$_{127}$NiPAm$_{50}$** and **C$_{12}$DMAm$_{127}$DEAm$_{48}$**, the increase of $N_{\text{eff}}^{\text{SLS}}$ is significantly more pronounced. The values for $N_{\text{eff}}^{\text{SLS}}$ are increasing by more than two orders of magnitude between 35 °C and 40 °C. It goes without saying that a TR block this length, consisting of around 50 repeat units, is necessary to provide strong sensitivity to the temperature increase. Aside with NAP, where the larger block results in noticeably lower values of $N_{\text{eff}}^{\text{SLS}}$ while the shorter block displays the highest aggregation numbers, the length of the TR block generally has no impact on $N_{\text{eff}}^{\text{SLS}}$. The substantially greater LCST of pNAP may be responsible for this. Thus, neither of the polymers **C$_{12}$DMAm$_{168}$NAP$_{16}$** nor **C$_{12}$DMAm$_{168}$NAP$_{27}$** exhibit a phase transition (see Figure 3.2a). As a result,

the pNAP block primarily functions as a hydrophilic block, and as its length increases, it reduces the packing parameter, causing the formation of smaller micellar aggregates. Finally, at $5.6\,\mathrm{g\,L^{-1}}$, a consistent $N_{\mathrm{eff}}^{\mathrm{SLS}}$ value of around 20 is seen for the HMTR polymer **$\mathrm{C_{12}DMAm_{127}NPAm_{31}}$**. As concentrations rise, $N_{\mathrm{eff}}^{\mathrm{SLS}}$ noticeably increases from $\sim$20 to $\sim$50 above $30\,^{\circ}\mathrm{C}$. The first step in the temperature-dependent transmission curves of the $20\,\mathrm{g\,L^{-1}}$ solution shown in Figure 3.1e coincides well with this minor transition.

Dynamic Light Scattering   In general, the dynamic light scattering (DLS) curves exhibit a reasonably fast and monomodal decay (for a complete set see Figures A.4–A.6). Only a few instances, such **$\mathrm{C_{12}DMAm_{168}NiPAm_{33}}$** or **$\mathrm{C_{12}DMAm_{168}DEAm_{27}}$**, show a significantly slower decay of the autocorrelation function. This rapid decrease is always found to correspond to hydrodynamic radii of 10–$25\,\mathrm{nm}$ as the main component when the data are analyzed using the optimized regularization technique (ORT) (for the complete set of data see Figures A.7–A.9). This size is very well in line with what is anticipated for micelles, which include a core made of n-dodecyl chains and extending hydrophilic chains with 170–200 monomer units.

For **$\mathrm{C_{12}DMAm_{127}NiPAm_{50}}$** and **$\mathrm{C_{12}DMAm_{127}DEAm_{48}}$**, the main peak shifts to a value of 80–$100\,\mathrm{nm}$ at $55\,^{\circ}\mathrm{C}$ (Figure 3.4), evidencing the temperature-induced secondary aggregation of the primary copolymer aggregates. However, the aggregate size of the hydrophobically modified pDMAm homopolymer system is barely impacted by an increase in temperature (Figures A.7b and A.9a). The copolymers with a short TR block show the same characteristic (Figures A.7–A.9).
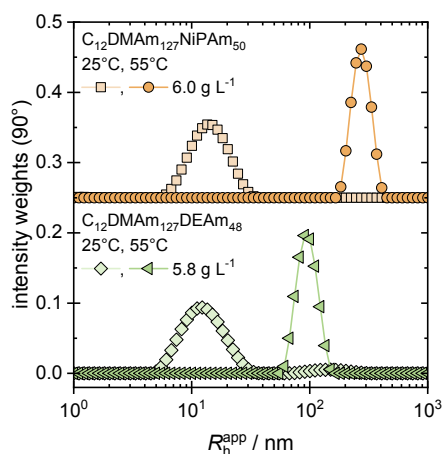
Figure 3.4: Exemplary intensity weighted size distributions of **$\mathrm{C_{12}DMAm_{127}NiPAm_{50}}$** and **$\mathrm{C_{12}DMAm_{127}DEAm_{48}}$** for the lowest concentration at $25\,^{\circ}\mathrm{C}$ and $55\,^{\circ}\mathrm{C}$ represented as weights of the underlying ORT analysis. The narrow distribution at $55\,^{\circ}\mathrm{C}$ arises from the scattering above the LCST.

Small-Angle Neutron Scattering Studies

Small-angle neutron scattering (SANS) experiments were carried out for the different polymers as a function of concentration and temperature in order to determine more precise structural information. Figures A.10–A.12 display the entire collection of SANS curves.

Polymer Coil Scattering and Aggregation Number Analysis With regard to the homopolymer **DMAm$_{187}$**, the scattering curve exhibits the predicted behavior for individual polymer coils at high q but diverges abruptly around $q < 0.08\,\mathrm{nm^{-1}}$, which is consistent with the presence of an entangled network of polymer chains (Figure 3.5a), as indicated by SLS. An effective structure factor can be deduced by dividing the scattering intensity ($I(q)$) by the polymer coils' calculated scattering intensity ($I_{\mathrm{coil}}(q)$, Equation 2.14), which is depicted in Figure 3.5b. A minimum S_{min} for the effective structure factor is clearly visible. The minimum can be explained by a correlation hole, or an attraction between the polymer chains, which becomes more marked with increasing concentration (Figure 3.5c). Accordingly, the scattering patterns imply single copolymer chains and no aggregates in solution. This observation is generally evident for the other copolymers as long as they do not exhibit sufficiently pronounced aggregation at higher temperatures.
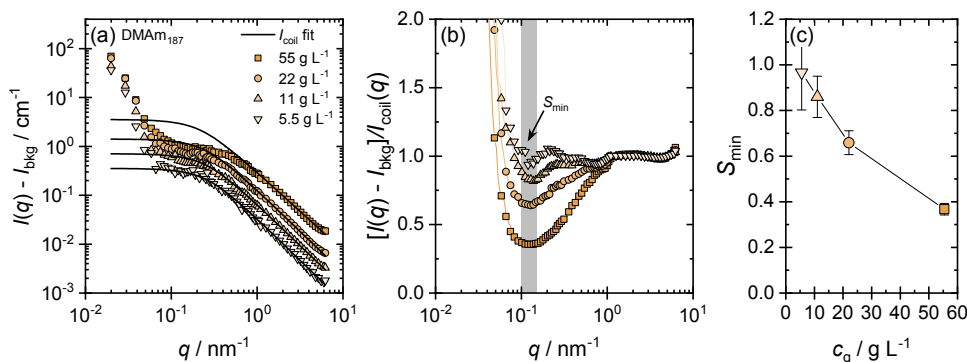
Figure 3.5: (a) Scattering curves of **DMAm$_{187}$** at $25\,^\circ\mathrm{C}$ with the corresponding polymer coil model (see Equation 2.14). The used molar weight $M_{\mathrm{n}}^{\mathrm{theo}}$ and *SLD*s were taken from Table 2.4. (b) Effective structure factor where the minimum (S_{min}) is highlighted with a gray area. (c) S_{min} as the minimum of the effective structure factor curves in the gray area plotted versus the mass concentration c_{g}.

Reprinted with permission from Prause *et al.* (2022).[64] Copyright 2022 American Chemical Society.

The scattering intensity at medium q ($\sim 0.1\,\mathrm{nm^{-1}}$) for the simple hydrophobically modified polymer **C$_{12}$DMAm$_{168}$** scales linearly with concentration (Figure A.10b). However, the scattering pattern varies consistently. It clearly features the scattering characteristics of a globular shape, which is especially visible at the highest concentration of $56\,\mathrm{g\,L^{-1}}$ (inset of Figure A.10b). At low concentrations, the scattering curves are comparable to those of individual coils in solution. Only a modest increase in scattering intensity, and consequently an increase in aggregation, occurs when the temperature is raised from $25\,^\circ\mathrm{C}$

to 50 °C (as seen in SLS, Figure 2.3b). A similar trend is seen for **C$_{12}$DMAm$_{127}$** (see Figure A.12a), with the exception that slightly larger aggregates are generated as demonstrated by the higher intensities in the mid and low q (see Figure 3.6). Here, a smaller head group area at the amphiphilic interface is expected for the shorter hydrophilic block of **C$_{12}$DMAm$_{127}$**. Using the concept of the packing parameter, larger micelles are then to be formed. Additionally, at a fixed mass concentration, a solution of this polymer includes more C$_{12}$ chains than its longer analog.
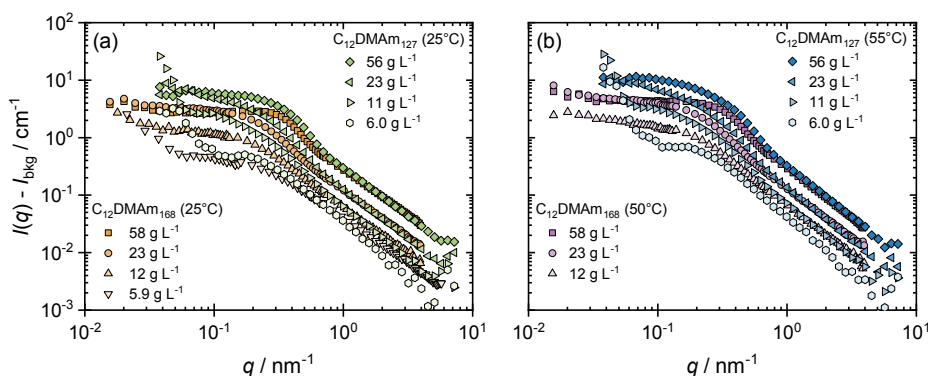
Figure 3.6: Comparison between SANS data of **C$_{12}$DMAm$_{168}$** and **C$_{12}$DMAm$_{127}$** at (a) 25 °C and at (b) 50/55 °C.

Figure 3.7a for the samples with $\sim$22 g L^{-1} gives a brief overview of the SANS patterns for the HMTR polymers at low and high temperatures. It demonstrates that there is a significant temperature response for pDEAm- and pNiPAm-containing polymers, while there is little difference for pNAP- and pNPAm-containing polymers.

The scattering curves for various concentrations of the HMTR polymers with a pNAP block (Figures 3.7a and A.10c/d) resemble their precursor homopolymer **C$_{12}$DMAm$_{168}$** extremely closely. This suggests that in terms of hydrophilicity, the pNAP block acts similarly to the pDMAm block. The intensity at low q is slightly higher at higher temperatures (55 °C) compared to **C$_{12}$DMAm$_{168}$**, indicating a slightly less repulsive interaction between the aggregates. The SANS intensity for **C$_{12}$DMAm$_{168}$NAP$_{27}$** only marginally increases between 0.2–0.6 nm^{-1}. It is consistent with light scattering measurements and points to a modest growth of aggregates without much more interconnection (Figure 3.3e). Evidently, for pNAP copolymers, the LCST transition is shifted to much higher temperatures. This pronounced shift effectively reduces the thermoresponsive characteristic in the useful temperature window and prevents any real association from occurring.

For the HMTR polymers including pNiPAm, the aggregation is a slightly increased (Figure A.11a/b) than for the basic pDMAm systems even at 25 °C. Accordingly, the aggregation is favored by the less hydrophilic pNiPAm block. There is always a noticeable rise in scattering intensity due to enhanced aggregation or clustering at higher temperatures (50/56 °C). A very substantial increase is only seen for **C$_{12}$DMAm$_{168}$NiPAm$_{33}$**, which is consistent with light scattering results (Figure 3.3b). With increasing concen-
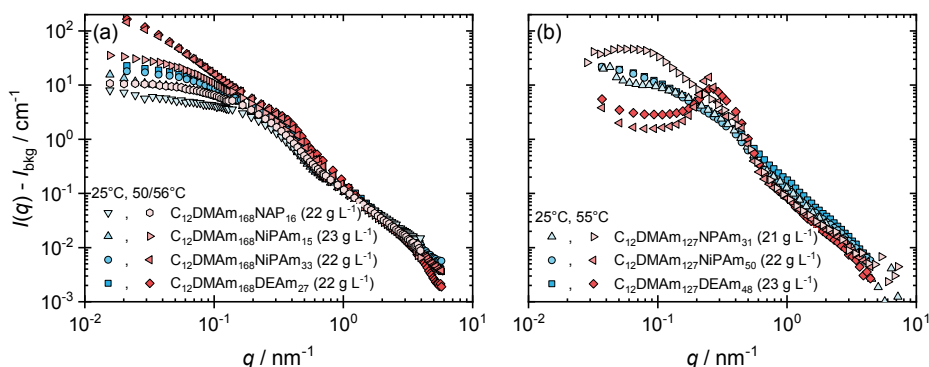
Figure 3.7: SANS intensity as a function of the modulus of the scattering vector q at 25 °C and 50/55/56 °C for: (a) $\mathbf{C_{12}DMAm_{168}NAP_{16}}$, $\mathbf{C_{12}DMAm_{168}NiPAm_{15}}$, $\mathbf{C_{12}DMAm_{168}NiPAm_{33}}$, and $\mathbf{C_{12}DMAm_{168}DEAm_{27}}$ (longer hydrophilic block) and (b) $\mathbf{C_{12}DMAm_{127}NPAm_{31}}$, $\mathbf{C_{12}DMAm_{127}NiPAm_{50}}$, and $\mathbf{C_{12}DMAm_{127}DEAm_{48}}$ (shorter hydrophilic block).

tration up to $22 \, \mathrm{g \, L^{-1}}$, substantially larger interconnected structures are formed. It is interesting to notice that for the highest concentration of $56 \, \mathrm{g \, L^{-1}}$, the intensity at low q decreases significantly (Figure A.11b). This decrease suggests a more constrained domain interconnection, a preserved and slightly more compact structure of the local domains, and a significantly increased steric repulsion in the system.

Compared to the pNiPAm systems, a very similar structural evolution and temperature response is seen for the pDEAm-based HMTR polymers. It implies that the hydrophobicity of the pDEAm and pNiPAm chains above the LCST is very similar. This similarity leads to comparable structural reorganization and network formation which can be seen in the low q upturn, especially noticeable for $c_{\mathrm{g}} = 22 \, \mathrm{g \, L^{-1}}$ (see Figure 3.7a). Nonetheless, the LCST block must apparently be at least 20 monomer units long in order to cause a substantial response with increasing temperature. Consequently, significant clustering is observed for $\mathbf{C_{12}DMAm_{168}NiPAm_{33}}$ and $\mathbf{C_{12}DMAm_{168}DEAm_{27}}$ due to increased hydrophobic interaction at higher temperatures, as shown by the rise in scattering intensity at low q.

SANS data for HMTR polymer samples with the shorter hydrophilic DMAm$_{127}$ block show aggregation behavior that is generally similar. But at higher temoeratures, the pNi-PAm- and pDEAm-containing samples exhibit a significantly more apparent and different tendency for self-assembly. $\mathbf{C_{12}DMAm_{127}DEAm_{48}}$ reveals a very noticeable ordering with increasing temperature. Although, for $\mathbf{C_{12}DMAm_{127}NiPAm_{50}}$, this effect can be observed to an even larger degree (see Figures 3.7 and A.12). For the $6.0 \, \mathrm{g \, L^{-1}}$ sample of $\mathbf{C_{12}DMAm_{127}NiPAm_{50}}$ at 56 °C, sharp correlation peaks have already been observed (see Figure A.12c), which point to a repeat distance of the hydrophobic domain of 35–40 nm, a high degree of ordering, and highly compacted hydrophobic domains. For $\mathbf{C_{12}DMAm_{127}DEAm_{48}}$, a little larger spacing is seen and a much broader correlation peak, both of which point to a lesser degree of ordering. Interestingly, a modest ordering can be seen even for $\mathbf{C_{12}DMAm_{127}NPAm_{31}}$ (Figure A.12b). Accordingly, a

temperature-induced self-assembly with a dense packing of compacted and ordered hydrophobic domains occurs for **C$_{12}$DMAm$_{127}$NiPAm$_{50}$** and **C$_{12}$DMAm$_{127}$DEAm$_{48}$**. In contrast, the temperature response for **C$_{12}$DMAm$_{168}$NAP$_{16}$** and **C$_{12}$DMAm$_{168}$-NiPAm$_{15}$** is only very minor. Additionally, it is also the case for other copolymers with a shorter TR block, as shown in Figure 3.7a.
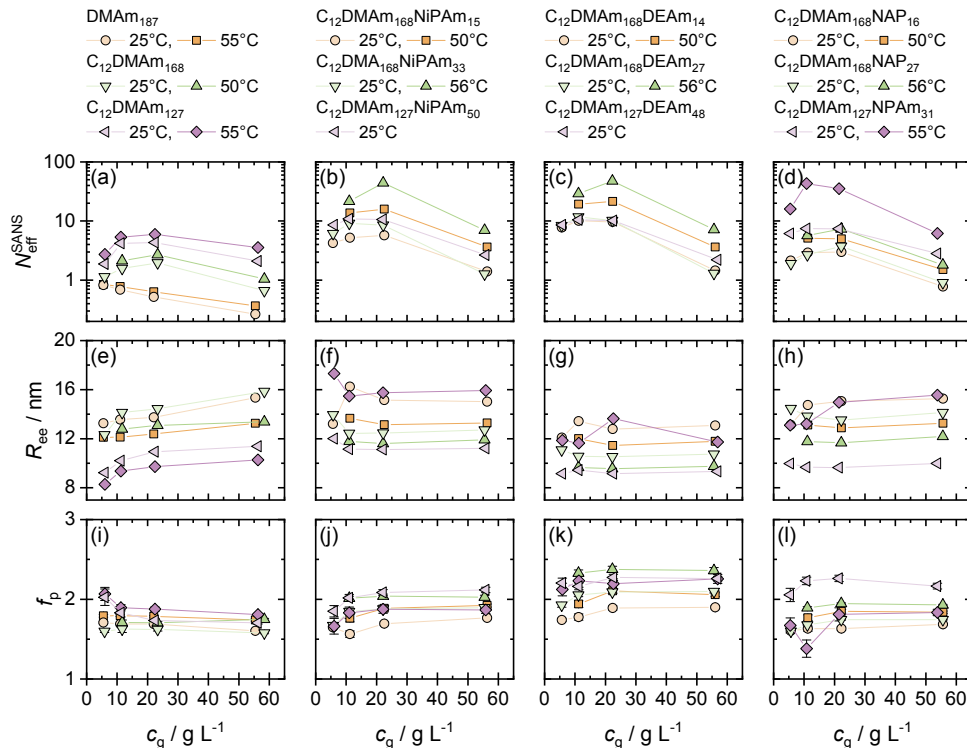
Figure 3.8: Parameters of the different analyses are shown for the studied HMTR polymers: (a–d) SANS-based effective aggregation numbers $N_{\mathrm{eff}}^{\mathrm{SANS}}$ derived from the Guinier analysis, (e–f) end-to-end distance (R_{ee}) of polymer coils ($R_{\mathrm{ee}} \approx 2.45 R_{\mathrm{g}}$, valid for a Gaussian coil with $f_{\mathrm{p}} = 2$), and (i–l) polymer mass fractal dimension (f_{p}) of the polymer chains in solution. The estimated uncertainties are within the symbols or given as error bars.

To determine the end-to-end distance (R_{ee}) and an effective aggregation number for the HMTR polymers, a first analysis of the scattering data was carried out. Equation 2.14 was used to fit the experimental data with a polymer coil model with excluded volume effect in order to estimate the end-to-end distance in the high q regime above $1.5\,\mathrm{nm}^{-1}$, using $R_{\mathrm{ee}} \approx (6\langle R_{\mathrm{g}}^2\rangle)^{1/2}$, where R_{g} is the radius of gyration. The values for R_{ee} are displayed in Figure 3.8e–h.

The difference in pDMAm block length of roughly 40 DMAm units between the polymers **C$_{12}$DMAm$_{127}$** and **C$_{12}$DMAm$_{168}$** is what causes the noticeable difference between them. The end-to-end distance is around 2 nm larger for **C$_{12}$DMAm$_{168}$** compared to **C$_{12}$DMAm$_{127}$**. For the end-to-end distance, which is primarily controlled by the permanently hydrophilic pDMAm block and by barely altering the length of the thermoresponsive block, the majority of investigated polymers show essentially no signifi-

cant temperature dependency. Only the polymers $\mathbf{C_{12}DMAm_{127}NiPAm_{50}}$ and $\mathbf{C_{12}}$-$\mathbf{DMAm_{127}DEAm_{48}}$ exhibit significantly larger R_{ee} values at 55 °C, which can be explained by temperature-induced bridging of the hydrophobic domains that have formed. Accordingly, the formation of new domains prevents the chains from folding back on itself and explains the more extended chains.

The effective aggregation number determined by SANS ($N_{\text{eff}}^{\text{SANS}}$) was calculated from the intensity at $q = 0$. The intermediate q range of 0.06–0.2 nm^{-1} was fitted with the Guinier law (Equation 2.2, see Figures A.10–A.12). Figure 3.8a–d displays the effective aggregation number ($N_{\text{eff}}^{\text{SANS}}$) for all studied polymers except for $\mathbf{C_{12}DMAm_{127}NiPAm_{50}}$ and $\mathbf{C_{12}DMAm_{127}DEAm_{48}}$. For both polymers, the scattering intensity at low q is significantly reduced due to the pronounced ordering. The $N_{\text{eff}}^{\text{SANS}}$ value essentially rises for all polymers with increasing concentration up to 22 g L^{-1}. Above this concentration, increased steric repulsion, *i. e.*, a structure factor, starts to play a substantial role. This structure factor influence is noticeable as a decrease in $N_{\text{eff}}^{\text{SANS}}$ with increasing concentration for all examined polymers. The reference homopolymer $\mathbf{DMAm_{187}}$, which is not hydrophobically modified, exhibits no formation of aggregates (*cf.* Figure 3.5). Thus, the low q upturn can be ascribed to chain entanglement as mentioned earlier. The $N_{\text{eff}}^{\text{SANS}}$ values of the HM homopolymers $\mathbf{C_{12}DMAm_{168}}$ and $\mathbf{C_{12}DMAm_{127}}$ are 3 and 8, respectively. These numbers reflect the formation of very loose micellar aggregates, caused by the extremely large pDMAm head group.

The behavior of pNAP-containing samples is quite comparable to $\mathbf{C_{12}DMAm_{168}}$ with an increased $N_{\text{eff}}^{\text{SANS}}$ value up to 8. Only the impact of a stronger structure factor is recognized while no temperature influence is apparent. For $\mathbf{C_{12}DMAm_{127}NPAm_{31}}$, the behavior at low temperatures is very similar to the precursor polymer $\mathbf{C_{12}DMAm_{127}}$. When heated to the higher temperature of 55 °C, the $N_{\text{eff}}^{\text{SANS}}$ value is increased to roughly 60. For the pNiPAm- and pDEAm-containing polymers, the $N_{\text{eff}}^{\text{SANS}}$ values range from 5 to 20 with increasing concentration up to 22 g L^{-1} at 25 °C, which resembles a similar trend observed by SLS (*cf.* Figure 3.3). At the higher temperature of 50/56 °C, the $N_{\text{eff}}^{\text{SANS}}$ values are increased to 20–50 due to the attractive interaction between the micellar aggregates. The difference in aggregation number between low and high temperatures increases as the pNiPAm or pDEAm block becomes longer. In general, the lower values at 54 g L^{-1} are attributed to the repulsive interactions.

Scattering Model Analysis The clustered polymer-micelle model was used to further quantify the SANS data of the investigated polymers (Equation 2.17, described in Section 2.2.9). This model assumes that micellar entities with an average aggregation number (N_{agg}) can be interconnected to create clusters resembling a pearl-necklace chain, which is described by the number of micelles per cluster (N_{clu}). The interaction between the individual micelles is taken into account through the excluded volume based on an effective hard-sphere radius (R_{hs}). Due to its proximity to the hydrophobic core, the polymer chain fraction in the shell (x_{sh}) is substantially more concentrated, which is considered

via the parameter x_{sh}. The remaining part of polymer chains, characterized by their radius of gyration (R_g), is incorporated into the polymer corona of the polymer-micelles. Figures A.13–A.15 (Appendix A) show the fits of the SANS data. The fit parameters of the polymer-micelle form factor are shown in the Figure 3.9. Additionally, for the pearl-necklace form factor and the hard-sphere structure factor, the fit parameters are displayed in Figure 3.10. The supplied core radius (R_c) and shell thickness (T_{sh}) for the polymer-micelle form factor are derived directly from the fit parameters N_{agg} and x_{sh}, respectively. They were computed to provide a more detailed structural understanding of the micelles. The hard-sphere radius (R_{hs}) and hard-sphere volume fraction (ϕ_{hs}), two additional structure factor parameters that were displayed for easier comparison, are closely related to the variable parameter n_{hs}. As mentioned in the paragraph of the scattering model in Section 2.2.9, the parameter ϕ_{hs} was used as a variable parameter for few samples, *i.e.*, samples with high concentrations, and samples phase-separating at higher temperatures, indicated by a prime or asterisk in Figure 3.10.
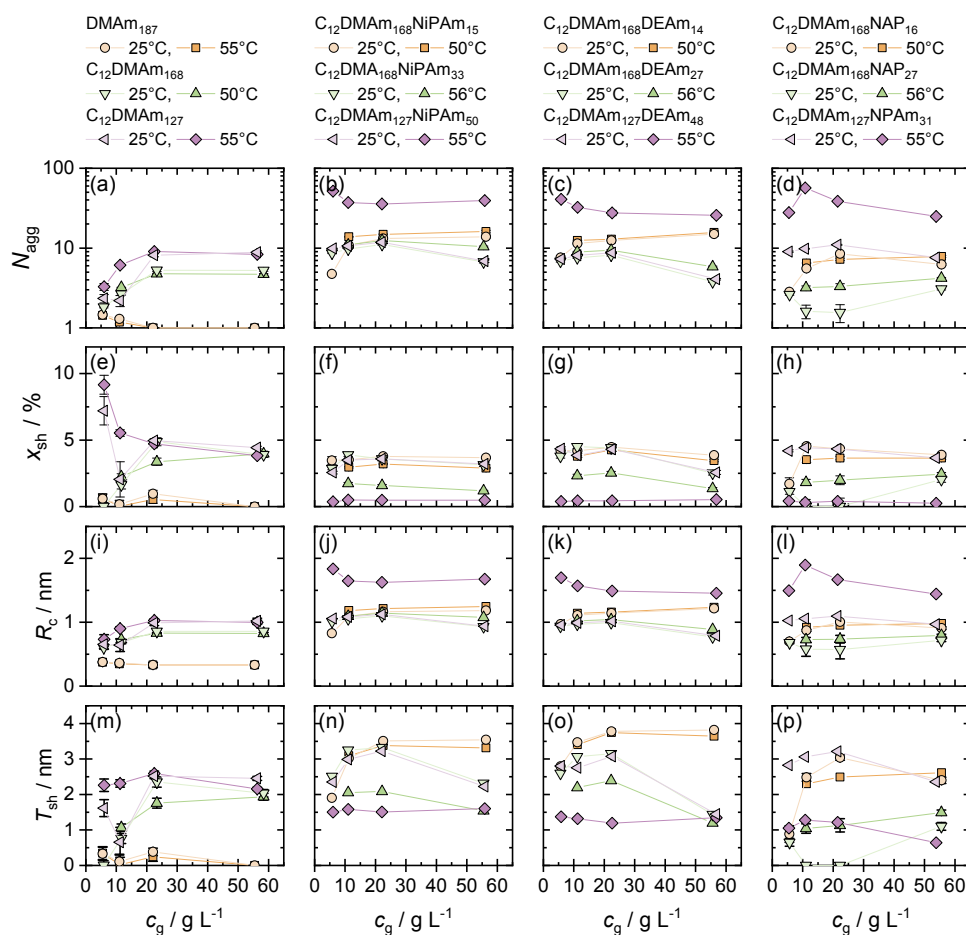
Figure 3.9: Polymer-micelle form factor parameters versus mass concentration are shown for the investigated HMTR polymers for two temperatures. R_c and T_{sh} depend on N_{agg} and x_{sh}, respectively, and were not used as variable parameters. The estimated uncertainties are within the symbols or given as error bars.
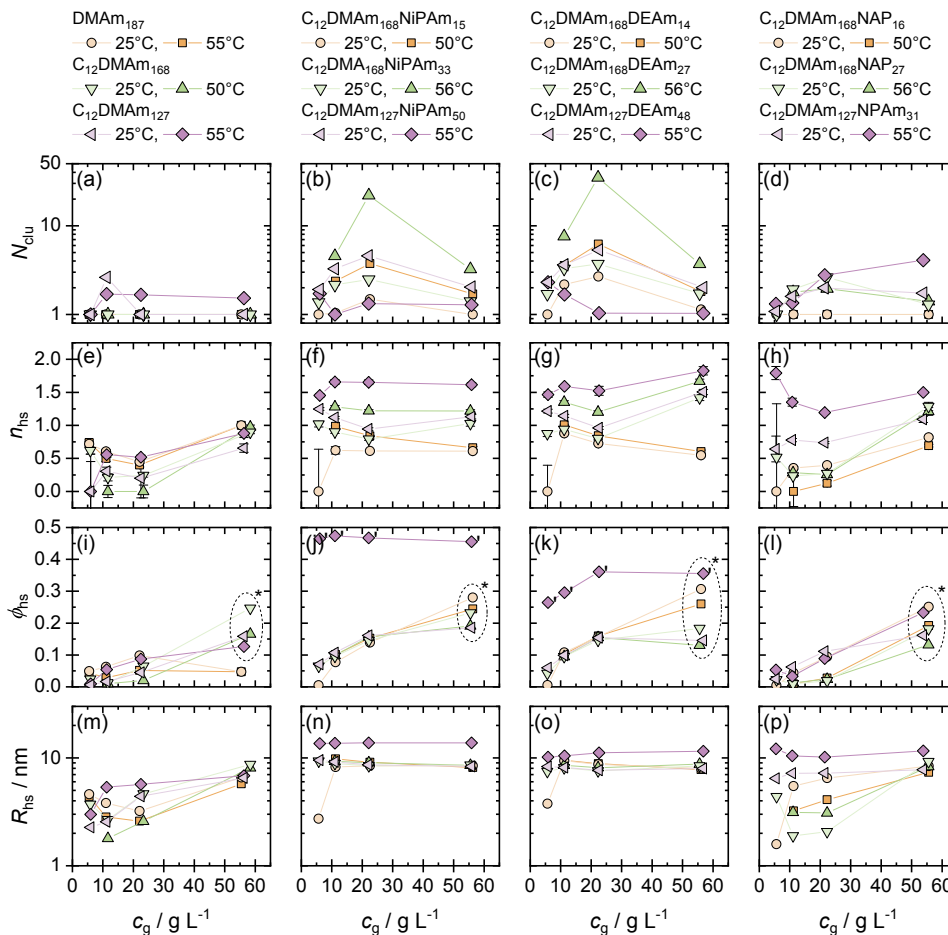
Figure 3.10: Structure factor parameters versus mass concentration are shown for the investigated HMTR polymers for the clustering and hard-sphere interactions of micelles. R_{hs} depends on n_{hs} and was not used as variable parameters. In general, ϕ_{hs} is not treated as a variable parameter. Only for the samples marked with a prime or asterisks, it was used as an additional variable parameter.

As previously mentioned, the homopolymer **DMAm₁₈₇** exists as single coils in solution. Its R_g value is essentially constant over the whole concentration range at about 5–6 nm. The mean aggregation number rises with concentration for the hydrophobically modified pDMAm homopolymers lacking a TR block, **C₁₂DMAm₁₆₈** and **C₁₂DMAm₁₂₇**. At 25 °C, N_{agg} is close to 2 and levels out just below 6 and 9 at 50/55 °C, respectively. The radius of gyration is slightly larger than that of the pDMAm homopolymer, as would be predicted for a micellar aggregate. Additionally, no clustering is anticipated due to the absence of a TR block. This is consistent with the observation that N_{clu} is 1 or almost 1. However, the extremely low aggregation number and the relatively low value of the parameter n_{hs} point to a possible penetration of the polymer corona of the polymer-micelles. In the event of coil entanglement, the penetration can result in slightly higher values for N_{clu}.

For the HMTR polymers with pNiPAm and pDEAm TR blocks, no marked difference is seen in the form and structure factor parameters. With increasing concentration for both temperatures, the aggregation numbers rose from 5 to 18. Only at 55 °C, significantly larger aggregation numbers are obtained for $\mathbf{C_{12}DMAm_{127}NiPAm_{50}}$ and $\mathbf{C_{12}DMAm_{127}DEAm_{48}}$ with values up to 50 and 40, respectively. The pronounced correlation peak is explained by this significant rise in aggregation. These two polymers behave in a manner reminiscent of pEO-pPO–pEO block copolymers (Pluronics), which agglomerate and may even form gels at higher temperatures.[114,115]

The R_g values ranging consistently between 4 and 7 nm, indicating that the local chain structure is essentially unchanged. For the pNiPAm and pDEAm systems, the number of clustered micelles is between 1 and 5 at 25 °C, essentially showing a weak attractive interaction that enhances with increasing TR block length. For the polymers with the shortest TR blocks, N_{clu} is roughly constant at the higher temperature. In contrast, a much greater attraction is observed for the longer TR blocks in the polymers $\mathbf{C_{12}}$-$\mathbf{DMAm_{168}NiPAm_{33}}$ and $\mathbf{C_{12}DMAm_{168}DEAm_{27}}$ at 56 °C. They exhibit cluster sizes of 4–40 micelles in the concentration range of 11–22 g L^{-1}. Above this concentration, the cluster sizes below 4 are caused by the tighter packing of polymer micelles.

The theoretically occupied volume fraction of micelles, which is derived from the number density of micelles and the total micellar radius, also reflects the tighter packing. This theoretical volume fraction increases from about 0.3 up to 2.5, although the high values just point to a significant micellar interpenetration and have no true physical meaning. According to this, N_{clu} values below 2 at 55 °C can be expected for the polymers with the longest TR blocks, $\mathbf{C_{12}DMAm_{127}NiPAm_{50}}$ and $\mathbf{C_{12}DMAm_{127}DEAm_{48}}$. As evidenced by the correlation peak, it indicates a significant increase in attractive interaction, which results in a formation of tightly packed polymer micelles with a high degree of ordering. The range of values for n_{hs}, a gauge of the polymer-micelle corona's steric repulsion, is between 0.5 and 1.8. Even though n_{hs} does not exhibit a strong concentration dependency, it increases with longer TR blocks. This finding can be explained by the expanding TR block, which encourages the development of distinct pNiPAm or pDEAm domains.

The hydrophobically modified pDMAm homopolymers $\mathbf{C_{12}DMAm_{168}}$ and the pNAP-containing HMTR polymers exhibit comparable behavior. With increasing concentration, the aggregation number increases from 2 to 10 (Figure 3.9d). As a result of the bigger hydrophilic group, $\mathbf{C_{12}DMAm_{168}NAP_{27}}$ exhibit slightly lower N_{agg} values than $\mathbf{C_{12}}$-$\mathbf{DMAm_{168}NAP_{16}}$. The radius of gyration and the fraction of polymer chains in the shell are essentially concentration independent with values of about 6 nm and 2–4 %, respectively. At 25 °C, the aggregation number of the polymer $\mathbf{C_{12}DMAm_{127}NPAm_{31}}$ with pNPAm as the TR block is about 10. At 55 °C, it rises to a comparable high value between 30 and 60. The polymer chain fraction in the shell is close to 5 % at 25 °C, and reduces to 0 % at 55 °C. The radius of gyration is slightly smaller than the values of the pNAP-based systems, $i.e.$, ~4 nm and 5–7 nm at 25 °C and 55 °C, respectively.

The decreased R_g suggests that the pNPAm block is less hydrated. At 25 °C, clustering for $\mathbf{C_{12}DMAm_{127}NPAm_{31}}$ is comparable to that of $\mathbf{C_{12}DMAm_{168}NAP_{27}}$ and is not particularly distinct. Here, it should be highlighted that the clustering serves as a gauge of the micellar aggregates' attraction to one another. Above $20\,\mathrm{g\,L^{-1}}$, N_{clu} rises from 3 to 5 at 55 °C. The polymer-micelles exhibit a similar interpenetration compared to the pNiPAm- and pDEAm-based systems. At 25 °C, n_{hs} is near 1, while at 55 °C, it ranges from 1.2 to 1.7. This shift basically reflects the formation of pNPAm domains at 55 °C.

3.3 Conclusion

In this chapter, nonsymmetrical hydrophobically modified thermoresponsive (HMTR) BAB* block copolymers were investigated in terms of their ability to self-assemble in aqueous solution. They comprise a long poly(*N,N*-dimethylacrylamide) (pDMAm) block of permanently hydrophilic part "A", a short persistently hydrophobic part "B" of constant size with a *n*-dodecyl (C_{12}) chain, and a terminal thermoresponsive (TR) block "B*" of various lengths, which features a lower critical solution temperature (LCST) transition characteristic. Because the permanently hydrophobic part B is a component of the R-terminus of the RAFT-made copolymers, it is substantially less sensitive to hydrolysis processes than the typically used hydrophobic groups attached via the Z-terminus. Various polyacrylamides, such as poly(*N-n*-propylacrylamide) (pNPAm), poly(*N*-isopropylacrylamide) (pNiPAm), poly(*N,N*-diethylacrylamide) (pDEAm), and poly(*N*-acryloylpyrrolidine) (pNAP), were employed as TR block B* which differ in terms of the value and type (Type I and Type II) of their LCST. In the temperature range of 20 to 60 °C, the aggregation behavior of these BAB* type copolymers was investigated as a function of concentration. Both the length of the thermoresponsive block and that of the pDMAm block were carefully altered.

The aggregation of these BAB* polymers results in typically small globular aggregates, as demonstrated by light and neutron scattering (SLS, DLS, and SANS), which is a direct consequence of the permanent hydrophobicity of the C_{12} end-group. The clustered polymer-micelle model was used to quantitatively assess the SANS data. This model describes both, the attracting and repulsive interactions that govern the self-assembling process as well as the aggregation itself. For the majority of the investigated systems, the temperature response is minor, only becoming truly significant for more than 20 monomer units in the TR block. Apparently, it appears that for the B* block based on pNAP, the transition temperature is merely shifted outside the selected temperature observation window. In contrast, for the polymers with pNiPAm and pDEAm B* blocks, an attractive interaction is observed above the effective transition temperature of the polymers. This effective transition temperature decreases with increasing TR block length. In particular, the polymers with a pNiPAm and pDEAm block of about 50 monomer units exhibit a significantly distinct aggregation behavior once the LCST is exceeded, as observed by SLS, DLS, and SANS. These polymers experience a very noticeable structural change at about
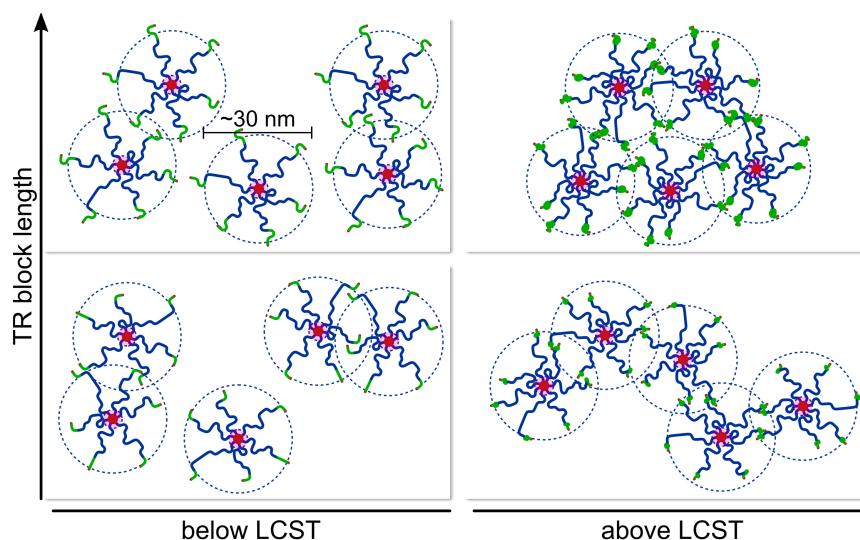
Scheme 3.3: Schematic description of the temperature-induced changes of self-assembly in the C_{12}-*block*-pDMAm-*block*-TR polymer systems.

35–40 °C, resulting in the formation of compacted, highly organized hydrophobic domains with an average spacing of about 35–40 nm. Thus, increasing the temperature causes a noticeable ordering. Surprisingly, this ordering is consistently seen across the entire experimental concentration range of 5–60 g L^{-1} which indicates that the thermoresponsive blocks predominately control the aggregation behavior.

All findings lead to the conclusion that the aggregation behavior can be altered as a function of temperature by altering the length as well as type of temperature-responsive B* block. Depending on the B* block selected, a rise in temperature may have little to no impact. But it may result in an increase in attractive interaction or the formation of compacted, highly structured aggregates. As a result, these systems enable customization of the self-assembling response, which may be useful in a range of applications, such as the field of cosmetics or delivery systems.

Chapter 4

Rheological Control of Aqueous Dispersions by Thermoresponsive Block Copolymers of Different Architectures

Copyright

This chapter is based on the published article

Author Contributions

A. Prause, M. Hechenbichler, A. Laschewsky, and M. Gradzielski conceptualized the block copolymers and the general experimental design. M. Hechenbichler synthesized and characterized the block copolymers. A. Prause performed the experiments, if not otherwise specified, analyzed the data, and created the figures and schemes. R. F. Schmidt performed the rheology experiments supervisded by A. Prause. M. Simon did the cryo-TEM work and analysis under supervision of Y. Talmon. S. Prévost and L. P. Cavalcanti were the local contacts at the SANS instruments D33, and SANS2D, respectively. The discussion of the results and writing of the manuscript was conducted jointly by A. Prause, M. Hechenbichler, A. Laschewsky, and M. Gradzielski. All authors approved on the final version of the manuscript.

Abstract
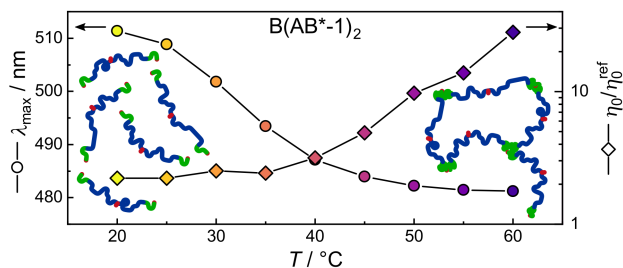
Temperature control of rheological properties of aqueous solutions can be achieved by the addition of amphiphilic polymers that show temperature dependent self-assembly. For this purpose, we explored non-symmetrical BAB* type copolymers with a permanently hydrophobic B unit, a permanently hydrophilic A block, and a thermo-switchable block B*. The latter undergoes a phase transition of the lower critical solution temperature (LCST) type. Both the architecture of these copolymers and the choice of the LCST-featuring blocks were systematically varied. The viscosity of their aqueous solutions can augment substantially with increasing temperature, depending on the specific polymer architecture and the choice of the thermoresponsive (TR) block. The macroscopic rheological changes were correlated with the results of static and dynamic light scattering (SLS, DLS) and small-angle neutron scattering (SANS) experiments, which showed a clear correlation with the mesoscopic organization of the respective systems. Furthermore, fluorescence studies with the solvatochromic probe Prodan showed a clear correlation of the enhanced viscosity to the formation of hydrophobic domains of the thermoresponsive block. Accordingly, such copolymers enable the tuning of the viscoelastic properties of aqueous solutions by their appropriate design.

4.1 Introduction

In the previous Chapter 3, a number of uncommon amphiphilic copolymers were examined which possess a nonsymmetrical architecture of the type BAB*.[64] As already mentioned, "B" is the permanently hydrophobic end-group containing a C_{12} chain, "A" is the permanently hydrophilic block comprised of poly(N,N-dimethylacrylamide) (pDMAm), and "B*" is the thermoresponsive (TR) block which is designed to exhibit a lower critical solution temperature (LCST) transition from hydrophilic to hydrophobic at temperatures between 20 and 60 °C. For the TR block B*, various polyacrylamides, $i.\,e.$, poly(N-n-propylacrylamide) (pNPAm, **B*-1**, LCST $\approx 22\,°C^{[60]}$), poly(N,N-diethylacrylamide) (pDEAm, **B*-2**, LCST $\approx 30\,°C^{[61]}$), and poly(N-isopropylacrylamide) (pNiPAm, **B*-3**, LCST $\approx 32\,°C^{[62]}$), were established. The reported LCSTs are the values for the corresponding high molecular weight homopolymers. Despite the fact that the obtained LCST is a function of TR block's molecular weight, it asymptotically approaches the homopolymer LCST with increasing block length. However, the accessible temperature window is somewhat predetermined by the chosen monomer.
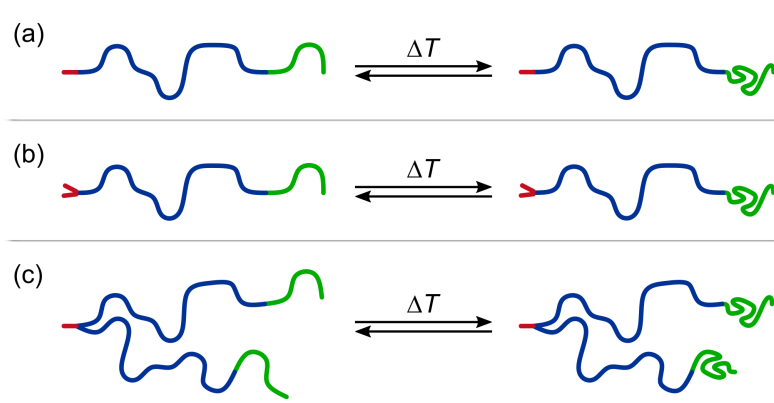
Scheme 4.1: Schematic architectures of the hydrophobically modified thermoresponsive block copolymers studied: (a) linear BAB* structure with one permanently hydrophobic (B, red), one permanently hydrophilic (A, blue), and one thermoresponsive block (B*, green), (b) B_2AB^* structure with two permanently hydrophobic, one permanently hydrophilic, and one thermoresponsive block, and (c) branched $B(AB^*)_2$ structure with one permanently hydrophobic block and two diblock branches bearing permanently hydrophilic and one thermoresponsive block each.

Reprinted with permission from Prause $et\,al.$ (2023).[65] Copyright 2023 American Chemical Society.

In addition to the already studied BAB* type, architectures of the B_2AB^* and $B(AB^*)_2$ types were investigated. The focus was set on the rheological behavior of the different block copolymer architectures and varying chemical structure of the TR block (see Scheme 4.1). For the B_2AB^* and $B(AB^*)_2$ types, either the hydrophobic effect is significantly enhanced, due to the two C_{12} chains, or the probability and strength for physical cross-links is favored, due to the branched structure with two B* blocks, respectively. Here, the rheological properties of aqueous copolymer solutions were studied as function of temperature at a

concentration of about $22\,\mathrm{g\,L^{-1}}$. To generate a mesoscopic picture, light and neutron scattering experiments were conducted for evaluating structural characteristics. Additionally, fluorescence probe studies were performed to probe the local environment's polarity by deploying the solvatochromic dye Prodan.[68,69]

The rheological and structural characteristics of various hydrophobically modified thermoresponsive (HMTR) copolymers in aqueous solution are discussed as a function of temperature in the following sections. The block copolymers are displayed in Scheme 4.2 and the corresponding architecture-based labels are summarized in Table 2.5. The goal is to correlate the rheological properties with the molecular structure of the copolymers and the type of TR block used. These characteristics were directly compared to the copolymer's self-assembly capabilities and mesoscopic organization as observed by light and neutron scattering. In addition, fluorescence probe studies were performed to find out how temperature affects the formation of hydrophobic domains in solution.
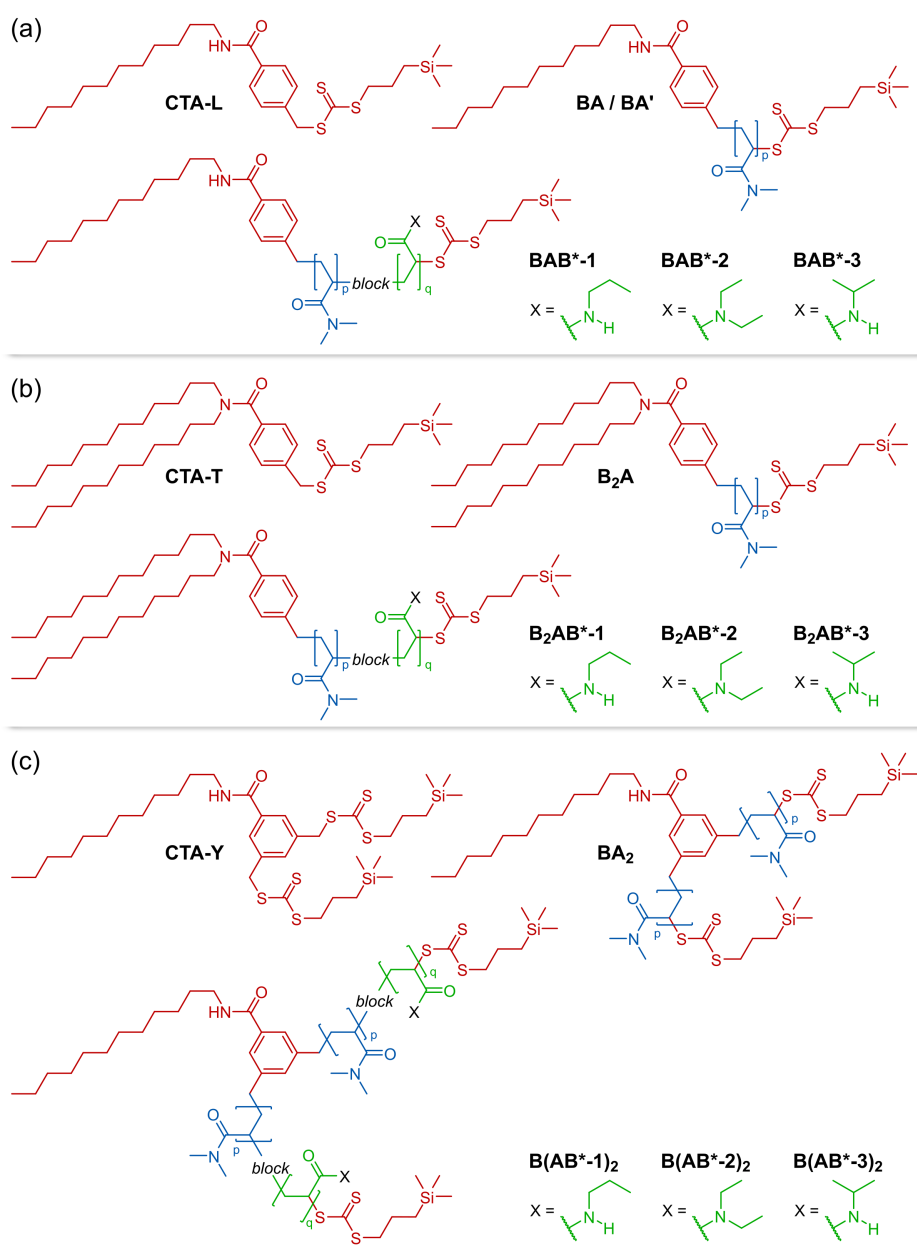
Scheme 4.2: Structure of the HMTR block copolymers of different architectures, and of their intermediates. The different permanently hydrophobic sticker groups "B" (red) are attached via the functional chain transfer agents (**CTA-L**, **CTA-T**, **CTA-Y**) to the permanently hydrophilic first block "A" (blue) made of pDMAm, yielding amphiphilic polymers **BA**, **B₂A**, and **BA₂**. These precursors are chain extended by thermoresponsive blocks "B*" (green) made of pNPAm (**1**), pDEAm (**2**), or pNiPAm (**3**), to yield the corresponding block copolymers of architectures (a) BAB*, (b) B₂AB*, and (c) B(AB*)₂.

4.2 Results and Discussion

4.2.1 Phase Transition Behavior

The macroscopic phase behavior of the various copolymer solutions in the concentration range of 6 to $22\,\mathrm{g\,L^{-1}}$ was first investigated as a function of temperature. The copolymer samples were originally examined by optical observation, which involved tracking the solutions' transparency as a function of temperature, as described in detail in the Sections 2.2.3 and 2.2.4. The copolymer solutions become turbid (gray value increases, "clouding") if, for example, agglomeration takes place. This clouding can happen if the thermoresponsive B* block switches from hydrophilic to hydrophobic. As a consequence, self-assembled polymer domains increase significantly in size above the LCST transition. Figure 4.1 shows the results for samples with a concentration of $\sim22\,\mathrm{g\,L^{-1}}$. The entire data set is displayed in Figure B.1 (Appendix B). First, these experiments demonstrated that the polymers **BA**, **B₂A** and **BA₂**, which do not contain a TR block, do not experience a change in turbidity (Figures 4.1a and B.1a–c). Contrarily, for samples with a TR block, such as those of the BAB*, B₂AB* and B(AB*)₂ architectures, turbidity typically increases when the LCST of the TR block is passed. This clouding temperature is referred to as macroscopic phase separation temperature (CP_{LCST}). Most of the examined polymers show persistent clouding across a somewhat broadened temperature range, rather than sudden clouding (Figure 4.1b).
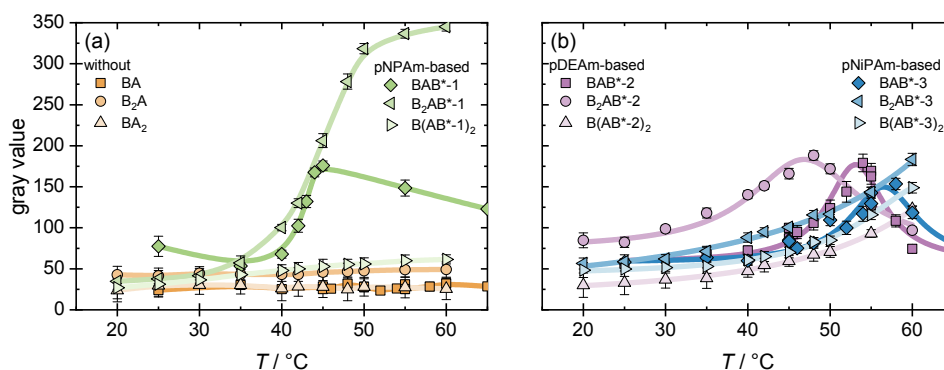
Figure 4.1: Gray values (turbidity) for samples with different architectures of polymers (a) without a TR block and with pNPAm-derived TR block and (b) with pDEAm- and pNiPAm-derived TR block at a concentration of $\sim22\,\mathrm{g\,L^{-1}}$ in D_2O. The solid lines are meant as a guide to the eye. The decay after passing a maximum is due to the onset of macroscopic phase separation and progressing sedimentation of the flocks.

A LCST transition for the pNPAm-containing copolymers (**BAB*-1**, **B₂AB*-1**, and **B(AB*-1)₂**) is only visibly at higher concentrations of the BAB* and B₂AB* types (see Figures 4.1a and B.1d–f). Contrary to what is expected, the clouding transition for the other TR block copolymers containing a pDEAm or pNiPAm block is surprisingly steep. Additionally, the B₂AB* copolymer **B₂AB*-1** has a distinctive trend of rising gray values

as temperature rises, approaching a high and constant value (see Figure B.1e). At the highest concentration of about $22\,\mathrm{g\,L^{-1}}$, it appears that this copolymer aggregates into large structures, yet it does not separate as quickly as the BAB* counterpart. The somewhat more diluted solution ($11\,\mathrm{g\,L^{-1}}$) of the B_2AB^* sample exhibits a similar substantial turbidity increase. But it does not macroscopically phase separate in the observed temperature window. The turbidity evolution with rising temperature in the $B(AB^*)_2$ copolymer solutions, on the other hand, is significantly weaker and lacks a distinct transition. This result was unexpected because it could be anticipated that a copolymer with two TR arms would most likely aggregate above the LCST transition. Nonetheless, the branched architecture does not follow such a behavior.

Similar to this, only the BAB* and B_2AB^* copolymers of the pDEAm-based copolymers, *i. e.*, **BAB*-2** and **B_2AB*-2**, exhibit a LCST-related clouding transition (see Figures 4.1b and B.1g–i). Raising the temperature further causes the macroscopic phase separation to set in at some point, which causes the majority of the solution to clear up. The turbidity of the solution is then decreasing again. For the lowest concentration of the B_2AB^* type, a transition is only observed after the sample has been annealed for at least $1\,\mathrm{h}$ at $60\,^{\circ}\mathrm{C}$. In case of **$B(AB$*-2$)_2$**, the turbidity increased only moderately and no evident clouding transition was noticed. Accordingly, increasing temperatures lead to larger structures but without macroscopic phase separation.

Similar behaviors of the pNiPAm-based copolymers can be seen in Figures 4.1b and B.1j–l, including a modest clouding transition for the B_2AB^* type at lower concentrations. Contrarily, at high temperatures the $B(AB^*)_2$ type demonstrates macroscopic phase separation for all concentrations, even though the phase separation required some annealing, about an hour, for the lowest concentrated sample.
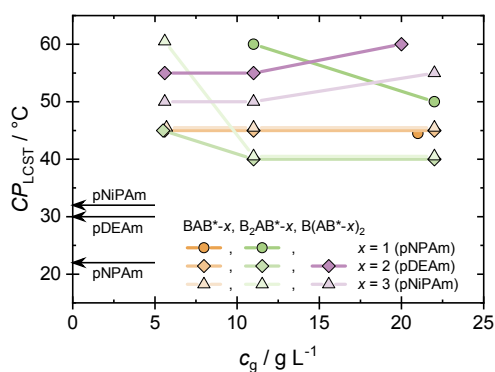
Figure 4.2: Optically observed clouding transitions of the investigated polymers with different architectures and TR blocks as a function of concentration.

Figure 4.2 compiles the derived LCST-related macroscopic phase separation temperature (CP_{LCST}). The pNPAm-, pDEAm-, and pNiPAm-based copolymers exhibit a transition for the BAB* and B_2AB^* copolymer types, with a rather constant transition temperature. It appears that there is a slight tendency for transition temperatures to decrease as con-

centration increases. However, no distinct clouding transition was observed between $20\,^\circ\mathrm{C}$ and $60\,^\circ\mathrm{C}$ for lower concentrations of some pNPAm-systems, *i. e.*, $5.5\,\mathrm{g\,L^{-1}}$ and $11\,\mathrm{g\,L^{-1}}$ for **BAB*-1** and $5.5\,\mathrm{g\,L^{-1}}$ for **B$_2$AB*-1**. Surprisingly, at the highest concentration for the pNPAm-containing BAB* copolymer, the transition takes place at a temperature that is about $20\,\mathrm{K}$ higher than for the corresponding homopolymer. The other pDEAm- and pNiPAm-containing BAB* copolymers exhibit slightly smaller temperature difference of about 15–$20\,\mathrm{K}$ with basically no concentration dependency. In general, the long permanently hydrophilic pDMAm block covalently connected to the relatively short TR block is attributed to cause the observed differences in the transition temperatures.[63,98,101,104–107]

A different behavior is exhibited by the B$_2$AB* copolymers that have a permanently hydrophobic B block that is roughly twice as large as its BAB* and B(AB*)$_2$ equivalents. The clouding transition occurs for the pDEAm- and pNiPAm-containing copolymers, **B$_2$AB*-2** and **B$_2$AB*-3**, at about $40\,^\circ\mathrm{C}$ which is roughly $10\,\mathrm{K}$ above the LCST of the homopolymer. In contrast, for the pNPAm-containing copolymer **B$_2$AB*-1**, it occurs at a temperature that is roughly $40\,\mathrm{K}$ higher than the LCST of the homopolymer. These variations cannot be explained by the size and nature of the TR block. Most likely, they are the result of smaller and slower growing clusters which can be observed by directly looking at the samples.

The pDEAm- and pNiPAm-containing copolymers, **B(AB*-2)$_2$** and **B(AB*-3)$_2$**, for the B(AB*)$_2$ type, reveal a LCST-related clouding transition that marginally rises with concentration from $55\,^\circ\mathrm{C}$ to $60\,^\circ\mathrm{C}$ and from $50\,^\circ\mathrm{C}$ to $55\,^\circ\mathrm{C}$, respectively. The branched pNPAm-containing copolymer **B(AB*-1)$_2$**, on the other hand, does not exhibit a distinct clouding transition. Thus, a generally higher transition temperatures appears to be typical for the two-armed architecture B(AB*)$_2$. This architecture may promote an intra- or even intermolecular shielding of the hydrophobic domains by the hydrophilic blocks against the bulk phase.

4.2.2 Rheological and Structural Characterization

Rheological Behavior

The clouding investigations showed significantly increased aggregation of HMTR polymers with rising temperature which is not expected for simple amphiphilic polymers. Additionally, it was demonstrated that the behavior is specific to both, the architecture type and the TR block chemistry (*cf.* Scheme 4.1). Yet, there is not much structural information provided by the investigation of the macroscopic phase behavior. Therefore, the impact of temperature-induced aggregation behavior on rheological properties was studied (Figures 4.3–4.6, and B.2–B.4). All measurements were conducted at concentrations of about $22\,\mathrm{g\,L^{-1}}$. The concentration is high enough to cause a viscosity considerably above that of water while it is still not in the highly concentrated regime.

Steady Shear Rheology The viscosity of the polymers with a TR block is typically markedly higher than that of the simple HM polymers, *i. e.*, **BA**, **B$_2$A**, and **BA$_2$**. Furthermore, in contrast to their counterparts of the BAB* and B(AB*)$_2$ types bearing only one C$_{12}$ chain, TR copolymers of the B$_2$AB* type bearing two C$_{12}$ chains have an intrinsically higher viscosity. However, the temperature has little impact on this effect, which is most noticeable for pDEAm and pNiPAm B* blocks. This result shows that even below the LCST transition, there is a significant intermolecular interaction between TR blocks or between TR blocks and C$_{12}$ chains. Here, the presence of two hydrophobic C$_{12}$ chains is especially useful, as in the B$_2$AB* architecture. This observation can be explained by a formation of a transient network in which micellar aggregates of the C$_{12}$ chains serve as cross-linking sites. However, the structural relaxation time is insufficient to provide a substantial viscosity with just one hydrophobic C$_{12}$ chain. In contrast, the significantly increased residence time of two geminal C$_{12}$ chains leads to a much higher structural relaxation time and consequently to a higher viscosity.

All samples revealed, at most, modest shear thinning (Figure B.2). However, it is especially noticeable for solutions of the branched copolymers with two TR arms, namely **BAB*-1**, **B(AB*-2)$_2$**, and **B(AB*-3)$_2$**, which all exhibit an increased viscosity at higher temperature.

The viscosity flow data, displayed in Figure B.2, were used to estimate the zero-shear viscosity (η_0) as a function of temperature (Figure 4.3). Here, the zero-shear viscosity of polymers without a TR block lowers with rising temperature (Figure 4.3a). This pattern is reversed by the addition of the TR blocks. After passing the LCST transition, viscosity rises with rising temperature. Although, this effect is seen in all copolymers with a TR block. The branched ones with two TR arms exhibit a viscosity increase in a considerably marked manner. Their viscosity is still lower than that of the copolymers with two C$_{12}$ chains, which, in comparison, barely exhibit a viscosity increase with increasing temperature.
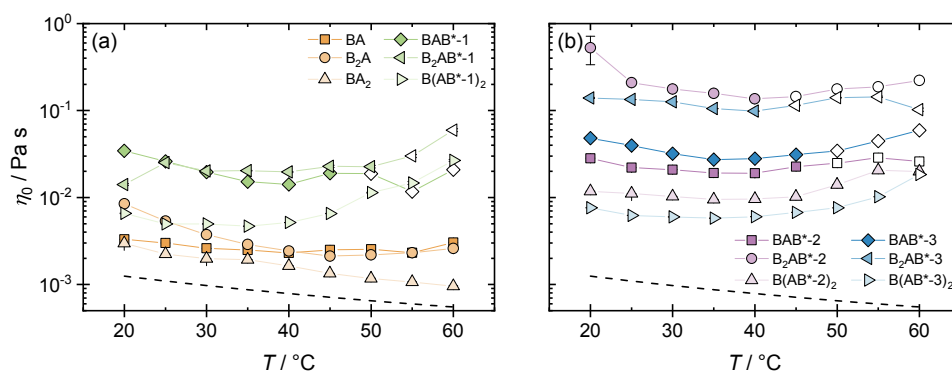
Figure 4.3: Zero-shear viscosity η_0 as a function of temperature for the different copolymers in D$_2$O. The dashed black lines indicate the viscosity of D$_2$O. Data points for which macroscopic phase separation of the sample is observed, are displayed with open symbols.

When the zero-shear viscosity is normalized by the value of the same architecture lacking the TR block, the influence of temperature on the viscosity is much more clearly evident. This information is displayed in Figure 4.4. Correspondingly, it can be seen that for B(AB*)$_2$ systems the increase with temperature is by far the most pronounced, mostly due to the fact that **BA$_2$** exhibits the most pronounced reduction with increasing temperature. The effect always starts to take impact at about 40 °C and causes a steady rise in normalized zero-shear viscosity ($\eta_0/\eta_0^{\text{ref}}$). In comparison to other copolymer architectures, phase separation was not observed in the investigated temperature window. Except for the branched pNiPAm-containing copolymer, where the phase separation occurs slowly at 60 °C. Intriguingly, the pNiPAm- and pNPAm-based copolymers reveal a viscosity enhancement by factors of 8 and 12, respectively, while the pDEAm-based copolymer shows the smallest temperature response (Figure 4.4b) with only a factor of 3–4.
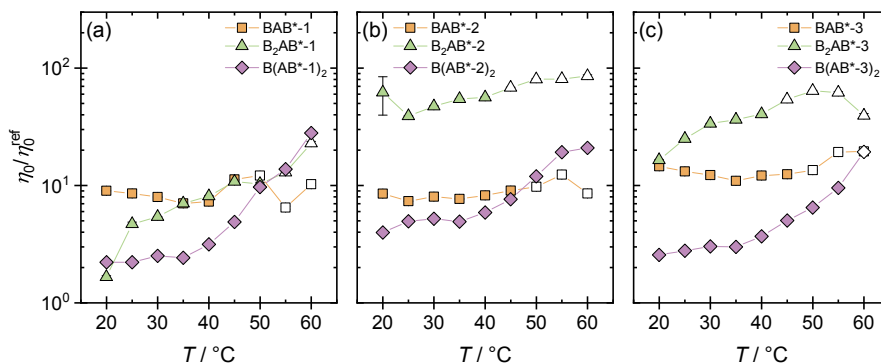
Figure 4.4: Normalized zero-shear viscosity ($\eta_0/\eta_0^{\text{ref}}$) as a function of temperature for (a) pNPAm-containing block copolymers, (b) pDEAm-containing block copolymers, and (c) pNiPAm-containing block copolymers. The zero-shear viscosity of the corresponding pDMAm system without TR block was used as reference η_0^{ref}. Data points for which macroscopic phase separation of the sample is observed, are displayed with open symbols.

In conclusion, two C$_{12}$ chains as the permanently hydrophobic part B (B$_2$AB*) cause a higher viscosity regardless of temperature, while only two-armed polymers of the B(AB*)$_2$ type exhibit a noticeable temperature response. As a result, only the HMTR polymers with two arms effectively cross-link, leading to a longer structural relaxation time as the temperature rises.

Oscillatory Shear Rheology In addition, oscillatory shear experiments were carried out (Figures B.3 and B.4). As expected for a constant viscosity, they exhibit a pretty general increase in the storage (G') and loss modulus (G'') with increasing frequency, essentially following a power law with an exponent of 1. This shows that the samples largely exhibit viscous behavior since the structural relaxation period of the systems is shorter than in the investigated frequency window. The loss factor ($\tan \varphi = G''/G'$, Figure 4.5), which is often much above 1, can be used to quantify this further. This factor changes with temperature,

decreasing for pNPAm-containing copolymers, increasing for pNiPAm-containing copolymers, and behaving relatively erratically for pDEAm-containing copolymers. Accordingly, the copolymers exhibit increasingly elastic properties for systems including pNPAm as TR block, whereas systems with pNiPAm as TR block exhibit increasingly viscous behavior.
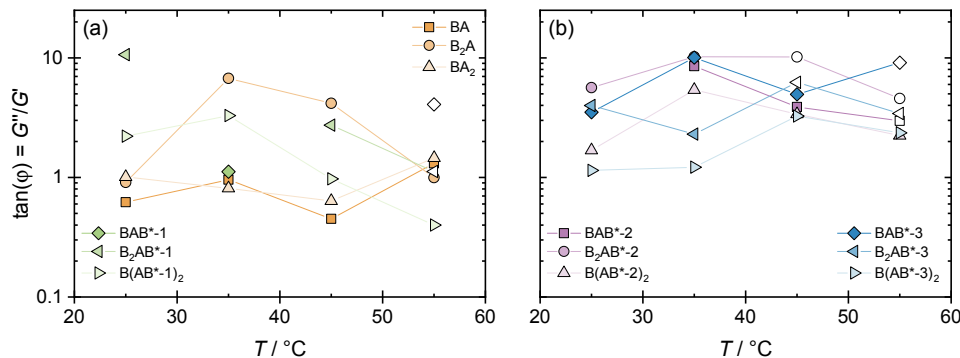
Figure 4.5: Temperature dependent loss factor ($\tan\varphi = G''/G'$) given at a frequency of 1 Hz for polymers (a) without TR block and with pNPAm as TR block, and (b) with pDEAm and pNiPAm as TR block.

Reprinted with permission from Prause *et al.* (2023).[65] Copyright 2023 American Chemical Society.

The oscillatory rheology is only moderately affected by rising temperature, as was previously seen in the constant shear studies. The samples of the copolymers **B(AB*-1)$_2$**, **B$_2$AB*-1**, and to a lesser degree **BA$_2$** are exceptions, where G' and G'' significantly rise at lower frequency when the temperature is raised to 55 °C (Figure B.4a/b). For the two-armed pNPAm-containing copolymer **B(AB*-1)$_2$**, this is especially clear. The cross-over of G' and G'' provides an estimate of its structural relaxation time of ~0.5 s. The pattern of G' and G'' is consistent with the significant rise in zero-shear viscosity for this polymer (Figures 4.3a and 4.4a). However, **BA$_2$** exhibits no such effect (*cf.* Figure B.2a).

Figure 4.3 provides a clearer representation of this phenomenon by plotting G' and G'' as functions of temperature at an intermediate frequency of 1 Hz. Only the copolymers mentioned above exhibit a significant increase in G' and G'' with increasing temperature; all other copolymers exhibit either no or only a modest increase. Interestingly, these samples' zero-shear viscosity is equivalent to that of copolymers containing pDEAm or pNiPAm (Figure 4.3), but they exhibit noticeably stronger viscoelastic characteristics. This suggests that the precise chemistry of the TR block, for which pNPAm seems to play a distinct role, has a significant impact on the viscoelastic temperature response.
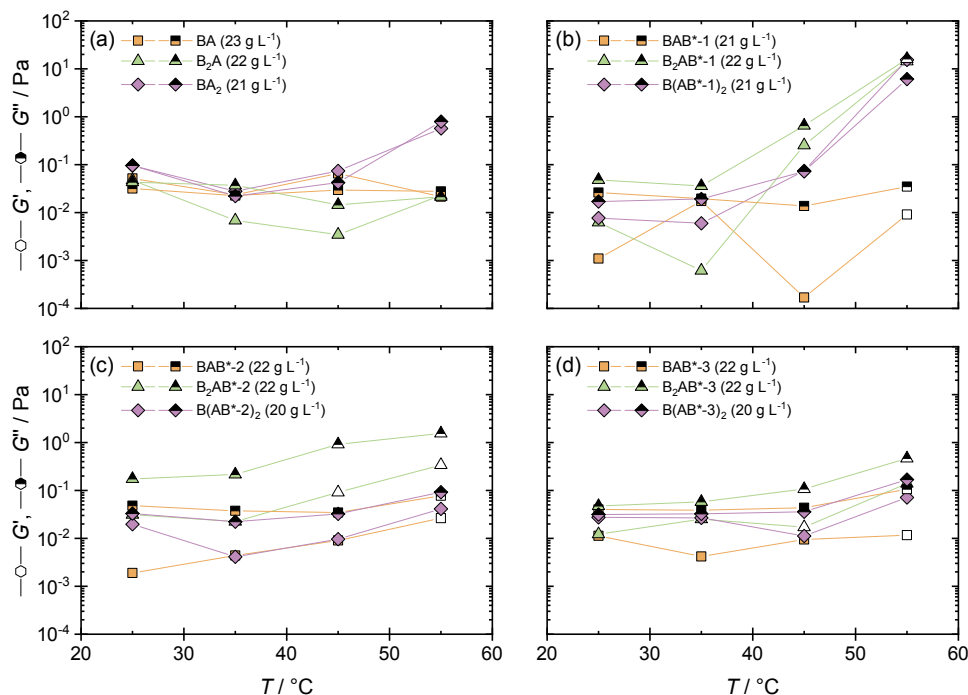
Figure 4.6: Temperature dependent storage (G') and loss (G'') moduli at a frequency of 1 Hz derived from oscillatory rheology measurements for polymers (a) without TR block, and (b) with TR block made of pNPAm, (c) of pDEAm, and (d) of pNiPAm. Data points for which phase separation of the sample is observed are displayed with open symbols.

Light Scattering Studies

Static and dynamic light scattering (SLS and DLS) studies were conducted on the various copolymer solutions to get insight into their mesoscopic organization. To obtain a more comprehensive structural picture, various concentrations of 5.5, 11, and 22 g L^{-1} were studied.

Static Light Scattering Figure B.6a–c shows the SLS data for the copolymers without a TR block. For these copolymers, the scattering intensity is basically unaffected by temperature. The rise in intensity at low q, as can be seen in the data, is generally observed for pure homopolymers or loosely interacting polymers.[113,116] Notably, **B$_2$A** exhibits a significantly higher scattering intensity due to the presence of two C$_{12}$ chains. This could be explained by a significantly more pronounced hydrophobic domain formation which is consistent with the B$_2$AB* type's increased viscosity (*cf.* Figure 4.3). At low temperature (25 °C), the overall increased scattering intensity for copolymers containing two C$_{12}$ chains (B$_2$AB* type) is observed for all corresponding copolymers. At high temperature (55 °C), the scattering intensity of pNPAm-containing copolymer (**B$_2$AB*-1**), is much higher compared to the pDEAm- and pNiPAm-containing copolymers, namely **B$_2$AB*-2** and **B$_2$AB*-3**.

71
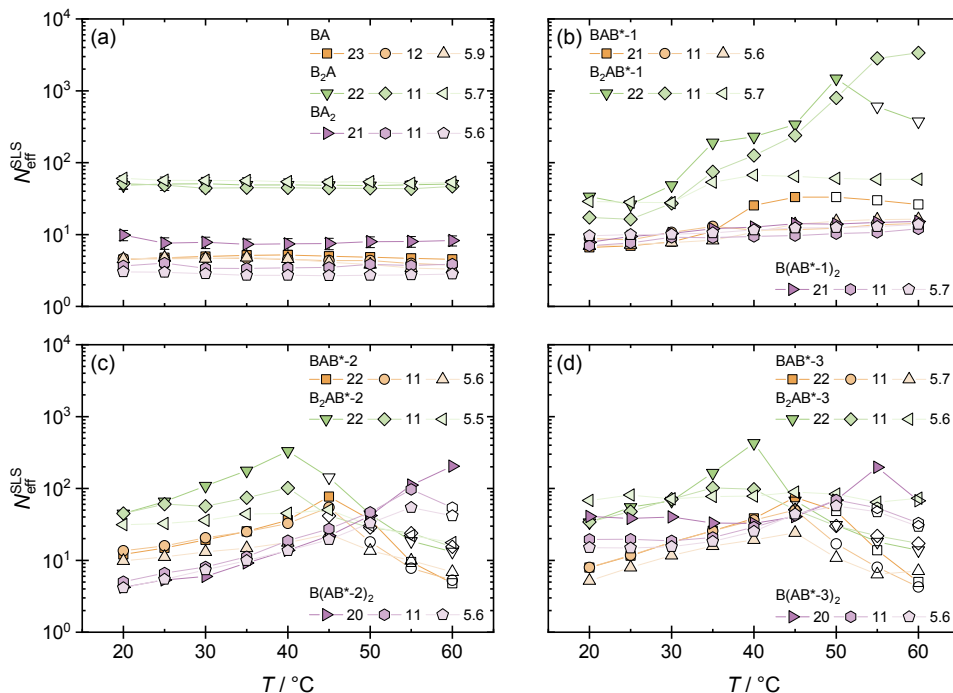
Figure 4.7: Effective aggregation numbers N_{eff}^{SLS} determined from $I(0)$ (extrapolated via a Guinier fit) of the SLS data as a function of temperature for all studied polymers at three mass concentrations (values given in $g\,L^{-1}$). Data points where phase separation of the sample is observed are displayed with open symbols.

Equation 2.3 was used to calculate the effective aggregation number (N_{eff}^{SLS}) of the copolymers using the extrapolated forward scattering intensity at zero scattering angle ($I(0)$, Equation 2.2). In Figure 4.7, N_{eff}^{SLS} values are shown as a function of temperature for the range of 20 to 60 °C. The aggregation numbers for copolymers without a TR block are essentially temperature independent (Figure 4.7a). Only low N_{eff}^{SLS} values of about 5 are found for **BA** at all examined concentrations. This could mean that the formation of larger, spherical micelles is inhibited by the presence of the large hydrophilic block as a head group. Aggregate sizes are similarly small for the HM copolymers with the branched architecture **BA$_2$**, but the behavior of aggregation is noticeably different because aggregation numbers rise with increasing polymer concentration. This could be explained by the copolymer's significantly increased hydrophilicity.

The comparison with SANS data (Figure B.10c) demonstrates that no distinct aggregation is visible in the investigated q range. For the increase in intensity at low q, network formation is most likely to be responsible. The appropriate section below will go over further SANS analyses. Thus, a loose association occurs up to a concentration of about $55\,g\,L^{-1}$, leading to larger clusters with increasing concentration while no micellar aggregates are formed. The polymer **B$_2$A**, which has two C$_{12}$ chains, is the most intriguing example. The reported aggregation numbers of around 60 are almost twice the number of C$_{12}$ chains generally found for micelles generated by low molecular weight surfactants

with a C_{12} chain.[117–120] The micelle must be extended in order to accommodate all the C_{12} chains in the micellar core. The packing parameter concept predicts such micellar elongation because the parameter becomes inherently significantly greater with two C_{12} chains.[1]

The scenario for copolymers with a TR block is quite different where $N_{\text{eff}}^{\text{SLS}}$ values basically rise with temperature. For the pNPAm-based polymers (Figure 4.7b), this effect is only notably present for the B_2AB^* type. It is in line with turbidity measurements (*cf.* Figure 4.1a), and it starts along with the LCST transition. The sample at $22\,\text{g}\,\text{L}^{-1}$, where two aggregation processes can be seen, is the most intriguing. The first step takes place in the 30 to $35\,^\circ\text{C}$ temperature range with $N_{\text{eff}}^{\text{SLS}}$ rising from $\sim$30 up to 200. In the second step, between 45 to $50\,^\circ\text{C}$, macroscopic phase separation is detected with a further increase of $N_{\text{eff}}^{\text{SLS}}$ up to 1000. For the linear BAB^* type, a minor rise of $N_{\text{eff}}^{\text{SLS}}$ is observed in the temperature range of 35–$40\,^\circ\text{C}$. However, while having the most pronounced temperature-induced viscosity enhancement (Figure 4.4a), the values of $N_{\text{eff}}^{\text{SLS}}$ for the branched polymer **B(AB*-1)$_2$** only rise modestly with increasing temperature.

The behavior of the pDEAm- and pNiPAm-containing copolymers (Figure 4.7c/d) is almost identical. The BAB^* architecture's $N_{\text{eff}}^{\text{SLS}}$ values rise from $\sim$10 at $20\,^\circ\text{C}$ to $\sim$80 at $45\,^\circ\text{C}$ before falling below that point due to phase separation. Similar trends are observed for the B_2AB^* type. However, they differ in that respect that there is a stronger concentration dependency, larger $N_{\text{eff}}^{\text{SLS}}$ values up to 400, and a phase separation that begins at a lower temperature of roughly $40\,^\circ\text{C}$. In comparison, the $N_{\text{eff}}^{\text{SLS}}$ value for the two-armed **B(AB*-2)$_2$** starts around 5 and rises with rising temperature up to 200. The effective aggregation numbers for the comparable polymer **B(AB*-3)$_2$** range from 10 to 40 at $20\,^\circ\text{C}$ and climb to values of about 200 at $55\,^\circ\text{C}$.

Dynamic Light Scattering The field auto-correlation functions derived by DLS measurements of various copolymers and at various temperatures exhibit mostly a simple monomodal relaxation (Figure B.7, Appendix B). The Stokes-Einstein equation 2.7 was used to compute the hydrodynamic radii using the average diffusion coefficient obtained by analyzing the initial slope of the correlation data (see Figure 4.8). Furthermore, the ORT analysis was performed on these data to establish the emergence of bigger aggregates or network-like structures and to quantify those (see Figure B.8).

The patterns observed for the effective aggregation numbers and the hydrodynamic radii of the polymers as a function of temperature are strongly correlated (*cf.* Figures 4.7 and 4.8). With rising temperature, R_{h} consistently lowers for all polymers without a TR block. This may result from the hydrophilic pDMAm A block's slightly decreased solvation, which causes the polymer chain to compact.[a] Regardless of concentration, R_{h} values of roughly $10\,\text{nm}$ are observed for the polymer **BA**. The hydrodynamic radii of the related **B$_2$A** and **BA$_2$** polymers rise from 20 to $30\,\text{nm}$ and from 10 to $20\,\text{nm}$, respectively, with increasing concentration. The more pronounced aggregation seen in the SLS studies is confirmed by the significantly higher R_{h} values for polymer **B$_2$A** with two C_{12} chains.

---

[a]This does not refer to the compaction at the LCST of pDMAm.[99]
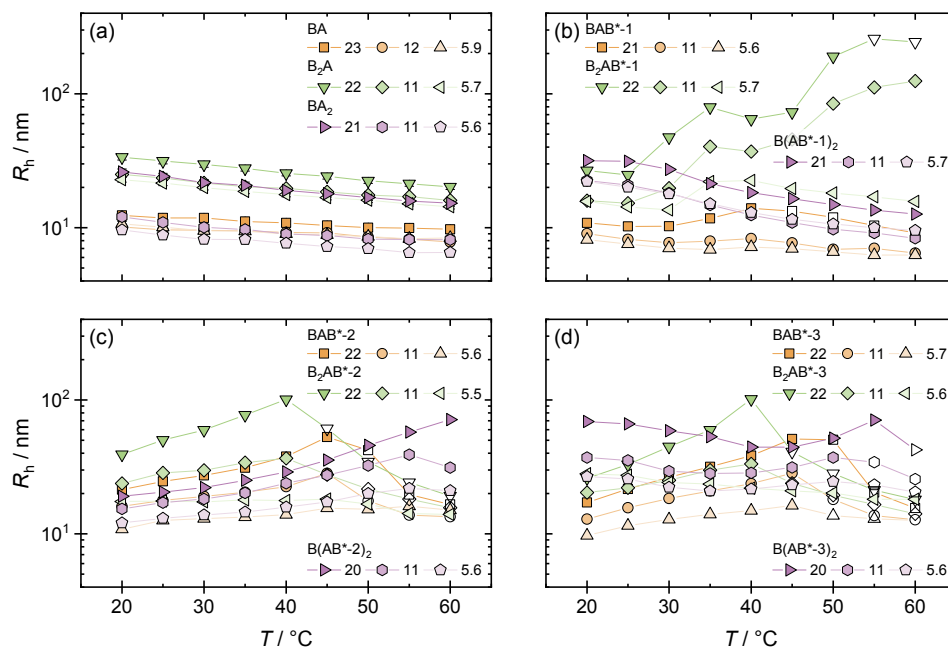
Figure 4.8: Hydrodynamic radius (R_h) as a function of temperature obtained via fitting the initial slopes of the DLS data for all studied polymers at three mass concentrations (values given in $\mathrm{g\,L^{-1}}$). Data points after phase separation of the sample are displayed with open symbols.

Reprinted with permission from Prause *et al.* (2023).[65] Copyright 2023 American Chemical Society.

The pNPAm-system responds differently for the copolymer **B₂AB*-1**, as seen in SLS (*cf.* Figure 4.7b) and turbidity data (*cf.* Figure 4.1a). At a concentration of $22\,\mathrm{g\,L^{-1}}$, the aggregates are growing in size in two steps, from 25 up to 75 nm between 25 and 35 °C and from 75 up to 250 nm between 45 and 50 °C. While the $5.7\,\mathrm{g\,L^{-1}}$ sample only exhibits the initial stage of the transition, the $11\,\mathrm{g\,L^{-1}}$ sample exhibits a comparable but less apparent trend. Only a slight rise in R_h is visible for the copolymers **BAB*-1** and **B(AB*-1)₂** from 8 up to 14 nm and 20 up to 30 nm, respectively, as the concentration increases. The R_h values for the linear **BAB*-1** decrease slightly with temperature whereas the concentration of $21\,\mathrm{g\,L^{-1}}$ exhibits a modest maximum at 40 °C with 14 nm. For the concentration of $21\,\mathrm{g\,L^{-1}}$ of the two-armed analogue **B(AB*-1)₂**, R_h drops by around 20 nm between 20 and 60 °C, going from 30 to 10 nm. Notably, in this temperature range, this sample exhibits a significant rise in the viscoelastic behavior (*cf.* Figures 4.4a and 4.6a). All two-armed copolymers, which exhibit an increase in viscosity with temperature (*cf.* Figure B.7f/i/l), do not, however, show a second relaxation mode. This appears to be related to a formation of a compacted network, that includes more and smaller network units.

The findings for the pDEAm- and pNiPAm-containing copolymers repeat the tendency observed for the $N_\mathrm{eff}^\mathrm{SLS}$ data (*cf.* Figure 4.7c/d). The hydrodynamic radii of the linear BAB* type copolymers, **BAB*-2** and **BAB*-3**, increase with concentration and temperature and range at 20 °C between 10 and 20 nm. R_h reaches a maximum of about 50 nm at

$45\,°\text{C}$ for the $22\,\text{g}\,\text{L}^{-1}$ samples. The B_2AB^* type copolymers **B$_2$AB*-2** and **B$_2$AB*-3**, which have two C_{12} chains each, exhibit a similar pattern. Their R_h values rise from $40\,\text{nm}$ and $30\,\text{nm}$, respectively, to $100\,\text{nm}$ at $40\,°\text{C}$ at the concentration of $22\,\text{g}\,\text{L}^{-1}$. Additionally, even higher temperatures trigger phase separation. At lower temperatures, the two-armed $B(AB^*)_2$ polymers **B(AB*-2)$_2$** and **B(AB*-3)$_2$** act differently. With rising temperatures, the pDEAm-containing copolymer exhibits a rise in R_h from 20 to $70\,\text{nm}$. In comparison, the pNiPAm-containing copolymer exhibits rather stable R_h values between 50 and $70\,\text{nm}$. The situation of the two-armed **B(AB*-3)$_2$** is particularly intriguing. At $20\,°\text{C}$, it already displays a relatively high value for R_h of about $70\,\text{nm}$, which drops marginally as the temperature rises (see Figure 4.8d). But the sample exhibits a noticeable rise in normalized viscosity (*cf.* Figure 4.4d). It appears that there is already a linkage via pNiPAm domains at low temperatures, but when the temperature rises, the lifetime of these physical cross-links rises notably.
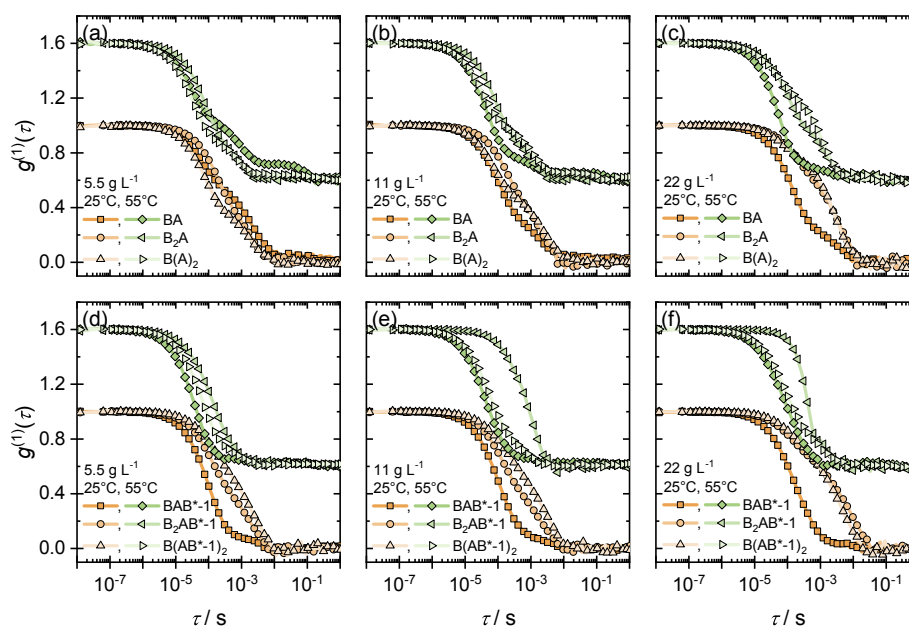
Figure 4.9: Direct comparison of DLS data for the different architectures of polymers (a–c) without a TR block and (d–f) with pNPAm as TR block. The $55\,°\text{C}$ measurements were shifted upwards by 0.6 for better clarity.

The basic copolymer **BA** exhibits a multimodal decay based on ORT studies (Figure B.8a). Although, this multimodal decay is driven by a rather fast initial decay that relates to hydrodynamic radii of around $10\,\text{nm}$. It is very consistent with a formation of spherical micelles. Also, slower relaxation modes were observed which correspond to R_h values between $100–1000\,\text{nm}$. For **B$_2$A** and **BA$_2$**, these relaxation patterns become even more predominant (Figures 4.9b/c and B.8b/c). The behavior is generally pretty similar for the copolymers containing pNPAm as a TR block. However, the ORT analysis shows a larger spread of relaxation modes, with the slow ones generally being less noticeable.

It is worth mentioning that the correlation curves of copolymers with pDEAm and pNi-PAm as TR blocks frequently appear to be more monomodal. In particular, the BAB* type has a dominant contribution of R_h values between 10 and 35 nm. Compared to copolymers with a pNPAm block or those lacking a TR block, this contribution is significantly larger. Since the TR block becomes insoluble at higher temperatures, the drop in R_h with increasing temperature suggests that the polymer shell has been compacted. The R_h value increases significantly with increasing concentration for the B_2AB^* copolymers at low temperatures (see Figure 4.8). This intriguing observation could be attributed to weak interactions between the TR blocks, which cause further aggregation of the initial aggregates with R_h values of 10–15 nm (observed for the lowest concentration). While the TR blocks becoming insoluble and more compact with increasing temperature, the aggregates essentially grow with increasing concentration. Accordingly, the formed aggregates are just somewhat larger than the initially present aggregates.

The scenario is entirely inverted for the branched $B(AB^*)_2$ copolymers. R_h rises with increasing concentration at low temperature. However, with increasing temperature, this effect intensifies notably for the pDEAm-containing copolymers. This suggests that the $B(AB^*)_2$ copolymers greatly favor the development of linked aggregates. The apparent R_h values are in the range of 60 to 500 nm while the aggregates are growing in size with increasing concentrations.

Small-Angle Neutron Scattering Studies

The small-angle neutron scattering (SANS) studies were conducted to obtain more precise insights into the mesoscopic structure of the systems because light scattering is primarily focused on the total scattering mass and not on structural features. The Figure B.9 (Appendix B) contains all the data for the different polymers at concentrations ranging from 5.5 to 60 g L^{-1}.

Firstly, samples containing polymers without a TR block are to be analyzed. At low q, SLS and SANS exhibit basically identical behavior. The effective aggregation numbers by SANS (N_{eff}^{SANS}, Figure 4.10) consistently produce lower values compared to SLS (*cf.* Figure 4.7). The medium q range in SANS, which reflects aggregation in the range of 10–30 nm and disregards larger scale clustering or network formation, was used to evaluate the N_{eff}^{SANS} values. The SANS data reveal that the interactions for all three copolymer architectures become more repulsive as the concentration rises (Figures B.9a–c and B.10a–c, Appendix B). The effective aggregation numbers, which are also declining, demonstrate this (see 4.10a).

For **BA**, the formation of spherical hydrophobic domains becomes visible as concentration rises (Figure 4.11a). A similar and more significant trend is observed for **B$_2$A**, where SANS indicates the formation of well-sized aggregates (Figure 4.11b). Accordingly, a substantially higher scattering intensity is observed for **B$_2$A** compared to **BA**. To further analyze the SANS data, a spherical core-shell model (Equation 2.39) was used for both
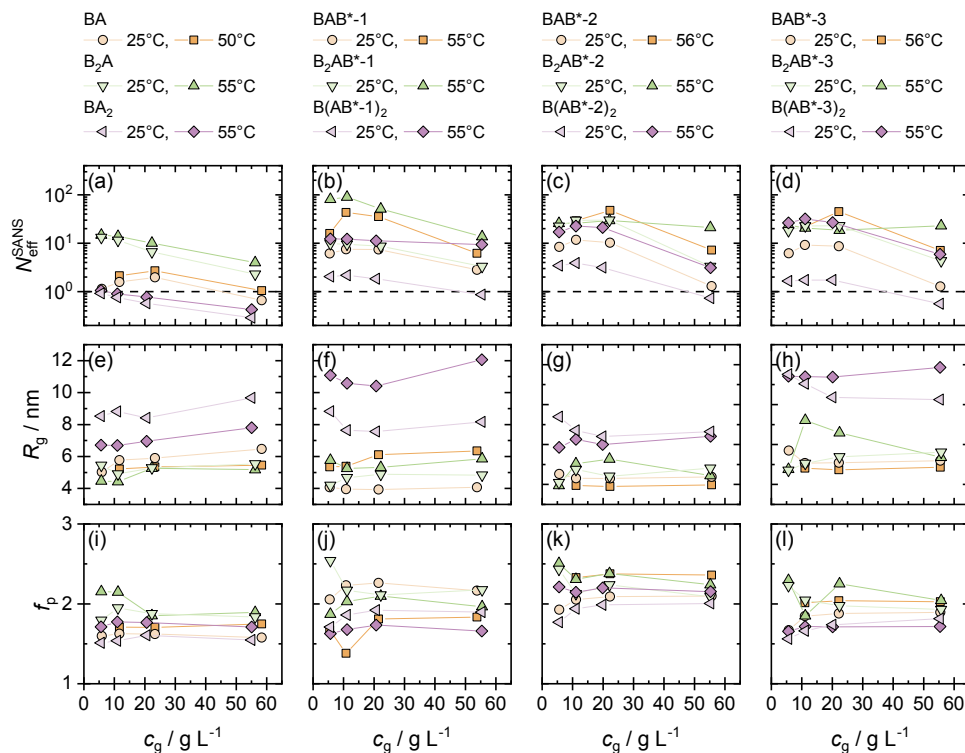
Figure 4.10: (a–d) Effective aggregation numbers determined from Guinier fit of the SANS data, (e–h) Radius of gyration determined from polymer coil fit, and (i–l) mass fractal dimension determined from the polymer coil fit for all studied polymers versus mass concentration.

polymers, **BA** and **B₂A**. The model description is given in the Section 2.2.9 and the fits as well as the best-fit parameters are displayed in Figure 4.11. In case of **BA**, the aggregation number rises from 2 to 5 while the swelling ratio rapidly decreases from 30 to 10 with increasing concentration. For **B₂A** with two C_{12} chains, more well-defined micelles are present. The aggregation number is consistently around 15. When the concentration rises from 5.8 to $56 \, \text{g L}^{-1}$, the swelling ratio marginally reduces from 13 to 9. The rather high aggregate number density, at which the hydrophilic coronas must begin to overlap, can be used to explain this.

The higher hydrophilicity of **BA₂** is caused by the two hydrophilic branches, which is supposedly so high that only scattering of individual polymer coils can be observed experimentally. Accordingly, the SANS data were modeled with a polymer coil model (see Equation 2.14 and Figure 4.12a for the fits), in which the polymer's molecular weight (M_n^{theo}, see Table 2.3) was used to determine the volume of the polymer (V_p). However, as concentration rises, steric repulsion, *i. e.*, repulsive interaction between chains, increases significantly. The diminished scattering intensity in the area highlighted in Figure 4.12b reflects this. The subsequent increase at lower q is ascribed to network formation, confirming the results of SLS.
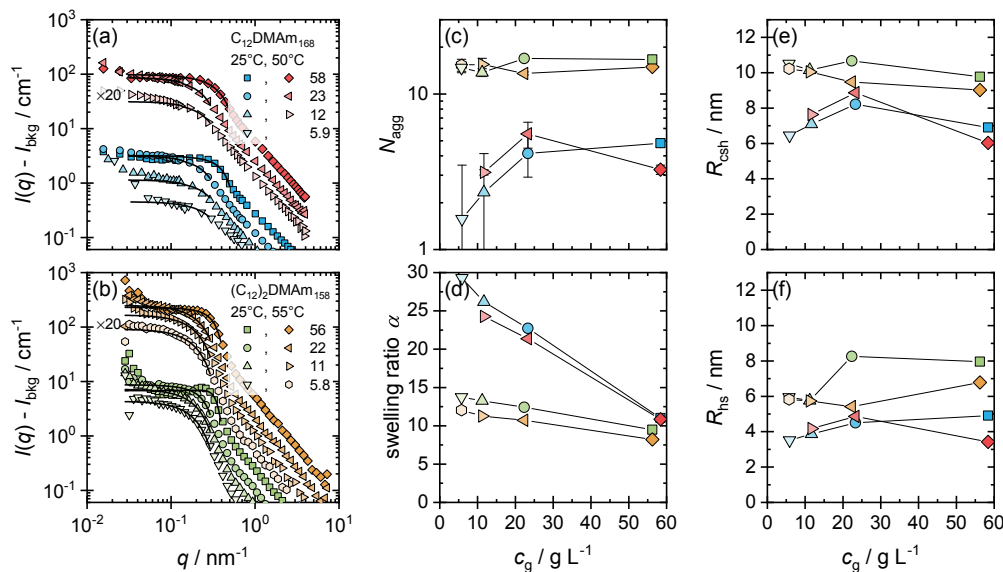
Figure 4.11: Core-shell spheres model fits for the copolymers (a) **BA** and (b) **B₂A**. (c–f) Best-fit parameters of the core-shell spheres model: (c) aggregation number (N_{agg}), (d) swelling ratio (α) of the shell, and (e) core-shell radius (R_{csh}), and (f) hard-sphere radius (R_{hs}) of the micelles (interpenetration of the shell was allowed).

In particular, the medium q range, from which the effective aggregation number determined by SANS ($N_{\text{eff}}^{\text{SANS}}$) was derived using the Guinier law, provides reliable information about the aggregation number of local domains. These domains can be incorporated within networks or clusters, which were detected by the light scattering experiments.

Except for the B(AB*)₂ type, the formation of aggregates is always seen for the pNPAm-containing polymers (Figures B.9d–e and B.10d–e). At low temperatures, **B(AB*-1)₂** shows basically single polymer chains which are slightly larger than for the precursor polymer **BA₂**. For **BAB*-1**, cryo-TEM revealed the presence of globular aggregates (*cf.* Figure B.5a/b, Appendix B). At elevated temperatures, it seems that the effective
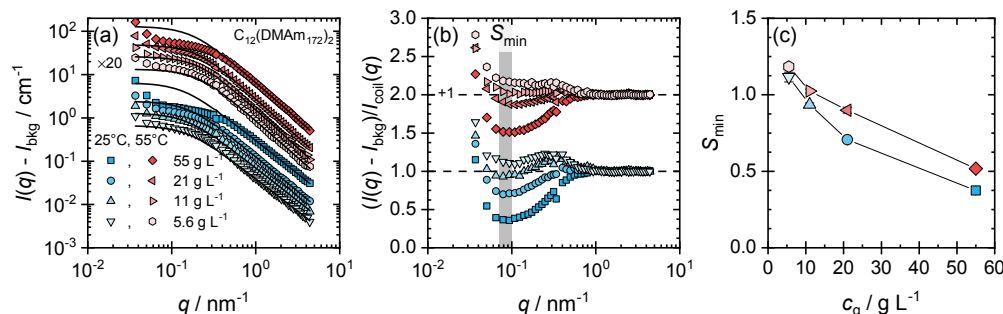
Figure 4.12: (a) Polymer coil model for the copolymer **BA₂**. (b) Effective structure factor (scattering intensity divided by polymer coil intensity). The gray area marks the region of the minimum S_{min} (c) Minimum of the effective structure factor S_{min} as a function of mass concentration.

volume fraction rises to an extent where a correlation peak and, in case of the highest concentration of $55\,\mathrm{g\,L^{-1}}$, a higher order peak, both exist. This is not surprising given that the mass fraction of the solvated polymer chains is only around $5\,\%$, which corresponds to an effective volume fraction of about $20\text{--}25\,\%$.
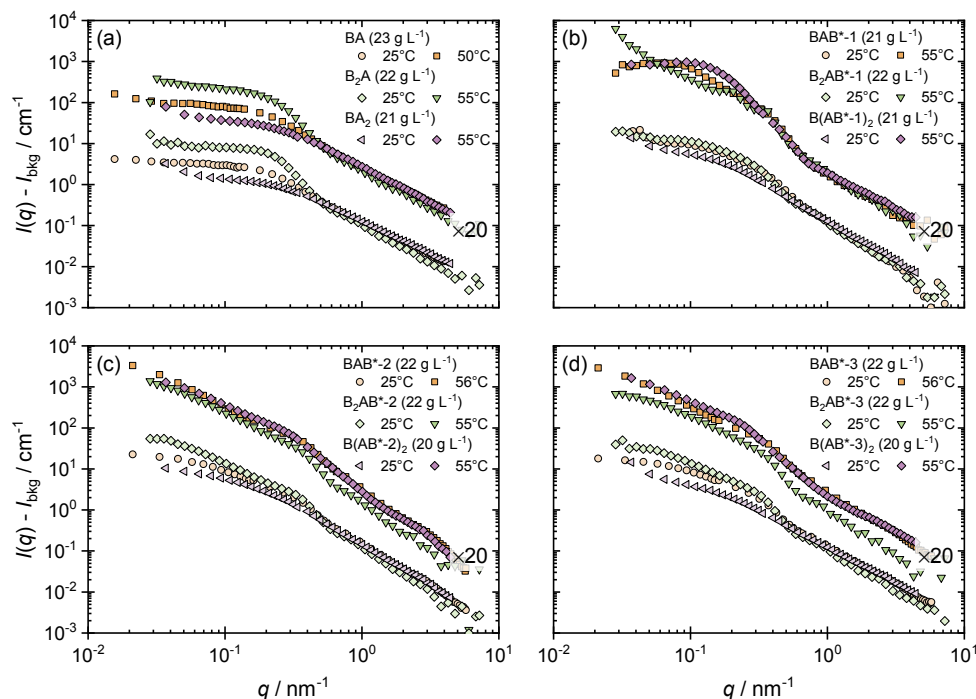
Figure 4.13: SANS intensity as a function of the modulus of the scattering vector q for a concentration of about $22\,\mathrm{g\,L^{-1}}$ for polymers (a) without TR block, and such with (b) pNPAm, (c) pDEAm, or (d) pNiPAm as TR block. The SANS data at $50/55/56\,^\circ\mathrm{C}$ are multiplied by 20 for better visibility.

A comparable aggregation is observed for **B₂AB*-1**. But, due to the presence of a larger number of C_{12} chains, the intensity is approximately two times higher. This result fits the observed aggregates in the cryo-TEM image quite well (Figure B.5c). The primary distinction is visible at high temperatures, when the intensity at low q significantly increases for increasing concentrations. Even two distinct correlation peaks arise for the highest concentration (Figure B.9e). At this point above the LCST transition, the system is highly concentrated so that it cannot phase separate macroscopically. Because of this, tightly packed aggregates can be observed above the CP_{LCST}, which results in a higher viscosity successively.

The temperature response is most pronounced for **B(AB*-1)₂**. While still individual chain scattering is seen at low temperatures, the substantial intensity rise at higher temperatures shows the formation of considerably larger aggregates. These aggregates are basically of globular shape and repel each other, apart from the highest concentration of $55\,\mathrm{g\,L^{-1}}$, where a minor increase at low q suggests bridging and attractive interactions between the aggregates (Figure B.9f). This observation is in excellent agreement with the system's pronounced viscosity enhancement with increasing temperature (*cf.* Figure 4.3a).

The pDEAm- and pNiPAm-based systems exhibit a behavior that is comparable to that seen in the SLS studies (Figure B.9g–l). Globular aggregates are always seen at low temperatures for the BAB* copolymers, **BAB*-2** and **BAB*-3**, and they grow slightly in size at higher temperatures. The interconnection of these aggregates is suggested by the rise in scattering intensity at low q for samples at a concentration of $22\,\mathrm{g\,L^{-1}}$ (Figure 4.13). At an even higher concentration of $55\,\mathrm{g\,L^{-1}}$, this increase at low q is again less pronounced. This observation can be explained by counterbalancing the attractive interaction, driven by the formation of hydrophobic domains of the TR block above the LCST, with a denser packing of aggregates, caused by a high effective volume fraction. The structural behavior for these BAB* copolymers has already been reported in more detail in Chapter 3.[64]

Comparable structural progressions are observed for **B$_2$AB*-2** and **B$_2$AB*-3**. Only the most concentrated samples exhibit a low q upturn that denotes bridging or attractive interactions. This can be explained by the fact that the aggregates produced by the two C_{12} chains are more compact. Additionally, they exhibit higher ordering as indicated by a peak/shoulder at $q = 0.4\,\mathrm{nm^{-1}}$, which denotes a more compact packing with an average spacing of about $15\,\mathrm{nm}$. This finding is nicely supported by cryo-TEM images, which also demonstrate the formation of micellar aggregates (*cf.* Figure B.5d). Additionally, it may be explained by the slightly shorter permanently hydrophilic pDMAm block.

At lower concentrations, the attractive interactions are observed once more for the two-armed copolymers **B(AB*-2)$_2$** and **B(AB*-3)$_2$**. These interactions remain more noticeable than for the linear polymers of the BAB* type, even at the maximum concentration. The branched structure of the B(AB*)$_2$ copolymers causes them to include less C_{12} chains, which results in less material to form hydrophobic domains. These polymers also have a considerably larger TR block proportion, which causes the more distinct attractive interactions.

Fluorescence Probe Studies

The analysis of the polymer systems' mesoscopic organization is made possible by the light and neutron scattering studies. However, they do not really explain how, if at all, the TR blocks B* are involved in the formation of the distinct architectures' structures (see Scheme 4.1). It is unclear, for example, whether the B* blocks combine with the C_{12} chain-based hydrophobic domains, only weakly interact with one another, or create independent domains. Hence, the solvatochromic probe Prodan was introduced to the studied polymer systems and its temperature-dependent emission spectra were monitored to study the association process in more detail. This fluorescent dye's photoluminescence is strongly dependent on the polarity of its immediate surroundings.[68,121–123] Despite having a relatively complicated behavior,[124,125] it allows for studying lipid and surfactant aggregation in water.[68,69,124,126] Figure 4.16 shows the emission spectra for the various copolymers in aqueous solution as a function of temperature. These spectra were examined with regard to the wavelength of their maximum emission and its fluorescence intensity (Figure 4.17).
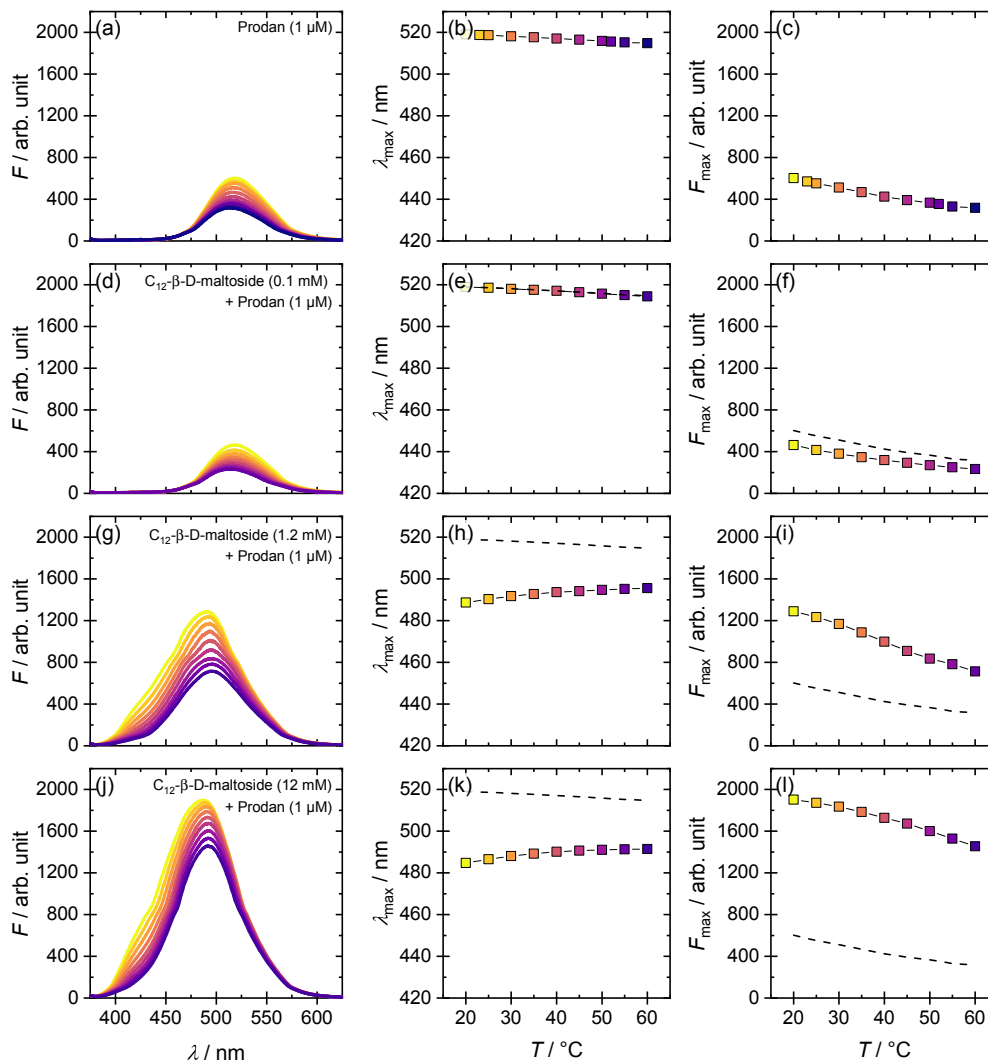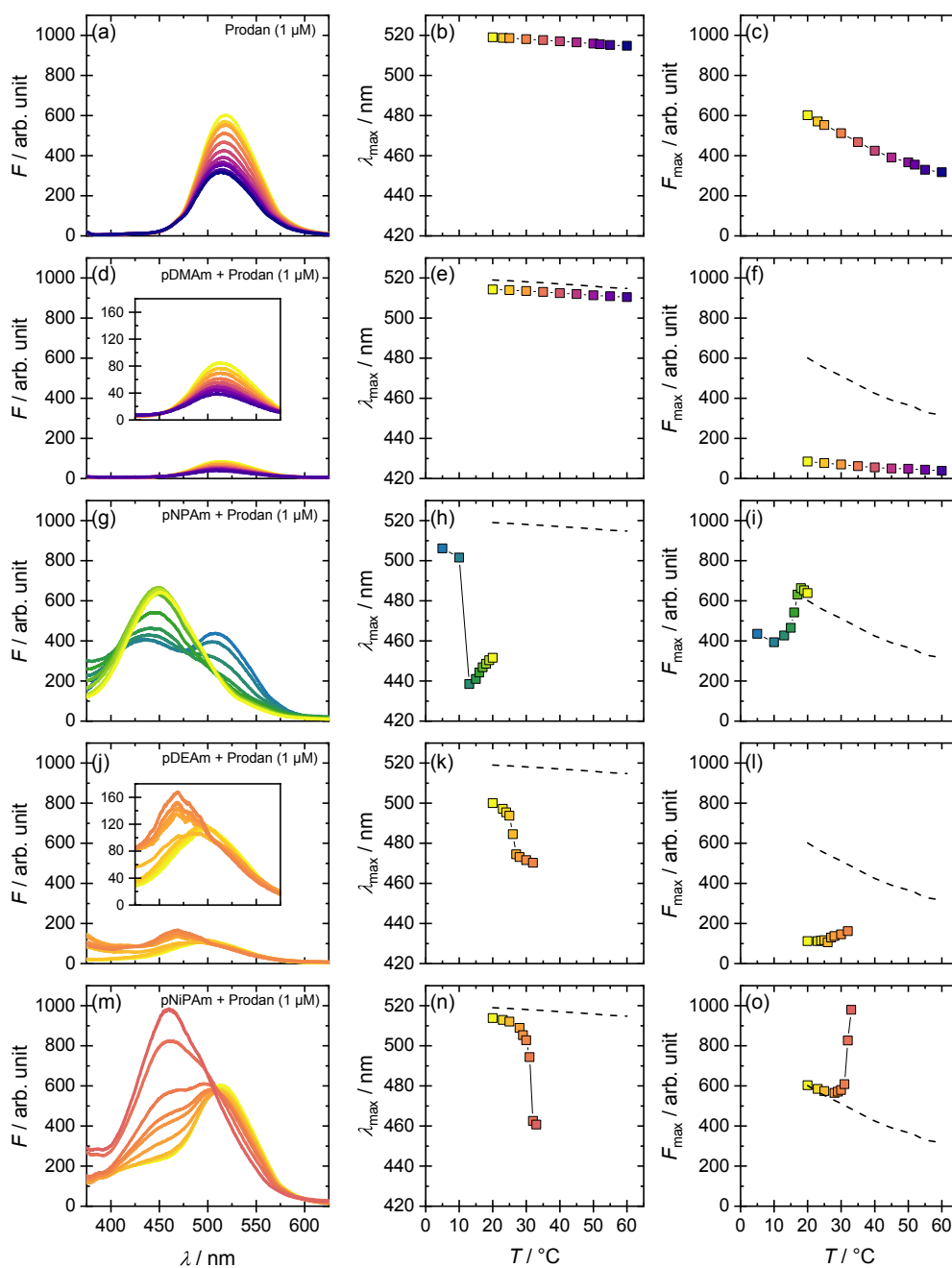
Figure 4.14: Fluorescence spectra of $1\,\mu\mathrm{mol\,L^{-1}}$ Prodan in aqueous solutions (in D_2O) as a function of temperature and added low molecular weight surfactant, with the extracted wavelength of the maximum emission ($\lambda_{\max}$) and its maximum emission ($F_{\max}$): (a–c) in D_2O, (d–f) in a solution of C_{12}-β-D-maltoside ($0.1\,\mathrm{mmol\,L^{-1}}$ in D_2O, $c <$ CMC), (g–i) in a solution of C_{12}-β-D-maltoside ($1.2\,\mathrm{mmol\,L^{-1}}$, $c >$ CMC), and (j–l) in a solution of C_{12}-β-D-maltoside ($12\,\mathrm{mmol\,L^{-1}}$, $c \gg$ CMC). The dashed black lines mark $\lambda_{\max}$ and $F_{\max}$ of $1\,\mu\mathrm{mol\,L^{-1}}$ Prodan in D_2O.

Solvatochromism in Surfactant Reference Solutions A low molecular weight surfactant C_{12}-β-D-maltoside was studied as a reference system, both above and below its critical micelle concentration (CMC, CMC $\approx 0.165\,\mathrm{mmol\,L^{-1}}$,[127] Figure 4.14). Similar to the polymers under investigation, C_{12}-β-D-maltoside is a nonionic amphiphile that shares the B part of the polymers' C_{12} chain as a significant component of the hydrophobic end group. Prodan exhibits a fluorescence emission peak at $520\,\mathrm{nm}$ in pure water (Figure 4.14a–c) or when C_{12}-β-D-maltoside is present below its CMC. As temperature rises, the

peak position only slightly shifts to lower wavelengths (Figure 4.14d–f). Above the CMC of the surfactant, the spectra are hypsochromically shifted by roughly 25–35 nm. This shift compares well to the shift found for the micellization of sodium dodecyl sulfate, which bears a hydrophobic n-dodecyl (C_{12}) chain.[68] A steady, slight thermochromic shift to longer wavelengths is also visible in the spectra, going from ~485 nm at 20 °C to ~495 nm at 60 °C (Figure 4.14h/k). Because the organic dye prefers to reside in the hydrophobic core of the micelles, there is a noticeable hypsochromic shift when the surfactant concentration is above its CMC. Once micelles are formed, they offer the probe a local environment that is significantly less polar than the bulk aqueous phase.[68] Even when the surfactant concentration is increased above the CMC, the observed spectral shift rarely changes (*cf.* Figure 4.14k).

It is uncertain and probably difficult how the modest thermochromic alterations that respond in opposite ways when surfactant micelles are present and absent are explained. One may also invoke temperature-induced changes in the probe's partition coefficient between the aqueous bulk and the micellar microphase, the internal structure of the hydrophobic cores of the micelles, or the average position of the probe within the micellar domains, and, in addition, to temperature-modulated changes in the solvent–dye interactions. In any case, the resulting spectral shift is still markedly lower than the shift experienced as a result of hydrophobic domains being present or absent in the aqueous solutions.

The emission intensity decreases with rising temperature for all reference systems. When C_{12}-β-D-maltoside is below its CMC and in pure water (*cf.* Figure 4.14c/f), this drop is minor. However, it becomes more noticeable when the surfactant is above its CMC (*cf.* Figure 4.14f/i). In the absence of hydrophobic microdomains, the minor decrease in emission intensity with increasing temperature may be caused by the water molecules quenching at higher temperatures. Although, numerous factors may be at play for the significant decrease in fluorescence intensity in micellar solutions with increasing temperature. In any way, there is no straightforward, consistent, and unambiguous relationship between the increase (or decrease) in Prodan's emission intensity and the polarity of its local surroundings, except from qualitatively showing that changes of the probe's environment occur.[68,128]

Thermochromism in Homopolymer Reference Solutions By including the homopolymers that comprise the A and B* blocks of the copolymers, *i.e.*, pDMAm, pNPAm, pDEAm, and pNiPAm (Figure 4.15), a second set of control experiments on the thermal response of Prodan's fluorescence emission was carried out. Prodan's emission spectra are barely impacted by the permanently hydrophilic pDMAm that makes up the A block. However, only a slight hypsochromic shift of roughly 5 nm and markedly diminished fluorescence intensity was observed. Accordingly, it is possible that some trithiocarbonate end-groups, that have been reported to function as an efficient quencher for some fluorophores, can be considered for this partial quenching by the homopolymer.[129,130] Both, the slight decrease in emission intensity and the mild hypsochromic shift, closely resemble

Figure 4.15: Fluorescence spectra of $1\,\mu\mathrm{mol\,L}^{-1}$ Prodan in aqueous solutions (in D_2O) as a function of temperature and various added polyacrylamide homopolymers, with the extracted wavelength of the maximum emission (λ_{max}) and its maximum emission (F_{max}): (a–c) in D_2O, (d–f) in pDMAm solution ($22\,\mathrm{g\,L}^{-1}$, **DMAm$_{187}$**), (g–i) in pNPAm solution ($22\,\mathrm{g\,L}^{-1}$), and (j–l) in pDEAm solution ($22\,\mathrm{g\,L}^{-1}$), and (m–o) in pNiPAm solution ($22\,\mathrm{g\,L}^{-1}$). The dashed black lines mark λ_{max} and F_{max} of $1\,\mu\mathrm{mol\,L}^{-1}$ Prodan in D_2O.

the behavior of the probe by itself in pure water (Figure 4.15e/f). Independently of the reduced fluorescence intensity, there is still enough emission intensity to study solvato- and thermochromism.

The entire temperature window is shifted towards lower temperatures in the case of the pNPAm homopolymer. Two emission bands with comparable intensities are observed at 5 °C and are located at 440–450 nm and 500–510 nm, respectively. The emission intensity is similar to that of the pure Prodan solution. However, as temperature rises, the first band's fluorescence intensity rises while the second band's intensity declines. Subsequently, the second band completely disappears between 15 and 16 °C (*cf.* Figure 4.15g). Additionally, the solution shows clouding in this temperature range, which is roughly 7 K lower than the anticipated LCST of pNPAm of 22 °C.[60] The hydrophobic RAFT-groups from the synthesis are considered to be responsible for this shift.

The measured fluorescence intensity for the pDEAm homopolymer is significantly lower and is comparable to the low fluorescence of the pDMAm sample. The spectra only show one distinct emission band, which shifts in a sigmoidal curve with an inflection point at about 26 °C from 500 nm to about 470 nm (*cf.* Figure 4.15k). At a temperature that is 4 K below the published LCST of pDEAm of 30 °C,[61] the solution starts clouding. Once more, the hydrophobic RAFT-groups from the synthesis are responsible for this difference.

The spectra obtained for the pNiPAm homopolymer exhibit striking similarities in their thermally induced effects on the spectra of Prodan's aqueous solution. The spectral behavior resembles that of the permanently hydrophilic pDMAm block at lower temperatures up to around 25 °C. Above 28 °C, a small shoulder that was observed at about 450–460 nm in the presence of pNiPAm is significantly expanding. At 32 °C, this shoulder becomes the strongest band of the emission spectra, while the persistently decreasing shoulder at the emission band's original position still remains (*cf.* Figure 4.15m). The observed transition temperature of roughly 31 °C is close to the reported LCST of 32 °C.[62]

In particular, these results are contrary to those obtained for the reference C$_{12}$-β-D-maltoside, which are in accordance with the literature. In literature, they showed the presence of only one emission band and its continuous spectrum shift throughout the process of micellization of low molecular weight surfactants.[68,126] Due to the observation of at least two emission bands in both the pNPAm and pNiPAm solutions, it strongly implies the presence of two separate environments with varying polarity, one of which is clearly more hydrophobic and in which the probe molecules are dispersed and exchange slowly (slower than the fluorescence lifetime). Supposedly, the aqueous bulk solution is probably one and the polymer-rich phase separated domains above the LCST transition is the other. Surprisingly, the hypsochromic shift seen for the probe in the pNiPAm-rich phase compared to when it is dissolved in water is very similar to the shift seen when it is dissolved in dimethylformamide.[122,128] Additionally, this shift is also noticeably more marked compared to the presence of micelle forming reference surfactant C$_{12}$-β-D-maltoside. This observation emphasizes how difficult it is to convert the solvatochromic shifts observed in polymer solutions into a precise molecular image.[58,131,132] Spectral shifts

might reflect changes in the probe's partition coefficient between the aqueous bulk and an organic microphase, the microphase's inner structure, its average position and orientation within the microphase or at its interface, as well as its viscosity, to mention a few and potentially influencing variables.

Solvatochromism and Thermochromism in Block Copolymer Solutions Figures 4.16 and 4.17 show the probe Prodan's temperature-dependent fluorescence in solutions of hydrophobically modified thermoresponsive (HMTR) block copolymers. For the various copolymer compositions and architectures, clear variances are seen right away. However, these can be grouped into three categories, which are represented by:

(i) the polymeric amphiphiles **BA**, **B$_2$A** and **BA$_2$** lacking a thermoresponsive B* block,

(ii) HMTR polymers **BAB*-2**, **BAB*-3**, **B(AB*-2)$_2$**, and **B(AB*-3)$_2$**, and

(iii) HMTR polymers **B$_2$AB*-2** and **B$_2$AB*-3** with two C$_{12}$ chains.

The probe's fluorescence in the solutions of the related HMTR polymers **BAB*-1**, **B(AB*-1)$_2$**, and **B$_2$AB*-1**, each of which contains pNPAm as a thermoresponsive block, reveals some of the same features seen in (ii) and (iii), but also some distinctive characteristics.

Prodan's fluorescence is shown in Figures 4.16a–c and 4.17a/e for the basic polymeric amphiphiles **BA**, **B$_2$A** and **BA$_2$** in solution. One main emission band can be seen in all the spectra, with the maximum location varying from ∼510 nm for **BA$_2$** to ∼505 nm for **BA** to ∼490 nm for **B$_2$A**. A second shoulder can be seen at roughly 470 nm upon closer inspection. The spectra rarely alter in the range between 20 and 60 °C, except for a minor hypsochromic shift and a mild continuous decline of emission intensity with rising temperature. This is consistent with the fact that these polymers lack a thermoresponsive block. According to the obtained spectral shifts, the probe is primarily confined in a microenvironment that is less polar than bulk water but gradually becomes more polar in the order **B$_2$A** < **BA** < **BA$_2$**. In contrast, the micelles of the reference C$_{12}$-β-D-maltoside exhibit an even less polar environment. This order is in good agreement with the findings of scattering experiments, where the same relative order and rather low values of aggregation numbers were found (*cf.* Figure 4.10a). It probably reflects the fact that it is getting more difficult to pack the hydrophobic chains into the aggregates as the A blocks' relative size to the hydrophobic C$_{12}$ chains increases.

When HMTR polymers are present, the temperature-dependent Prodan fluorescence significantly differs from that when low molecular weight and simple polymeric surfactants are present (Figures 4.16d–l and 4.17b–d/f–h). With the notable exception of polymer **BAB*-1**, all spectra in the presence of HMTR polymers with one C$_{12}$ chain, *i. e.*, BAB* and B(AB*)$_2$ types, show a significant change as temperature rises. The observed spectral changes indicate the passing through a thermal transition. At lower temperatures, the fluorescence bands match those of their equivalents **BA** and **BA$_2$** without the B* block.
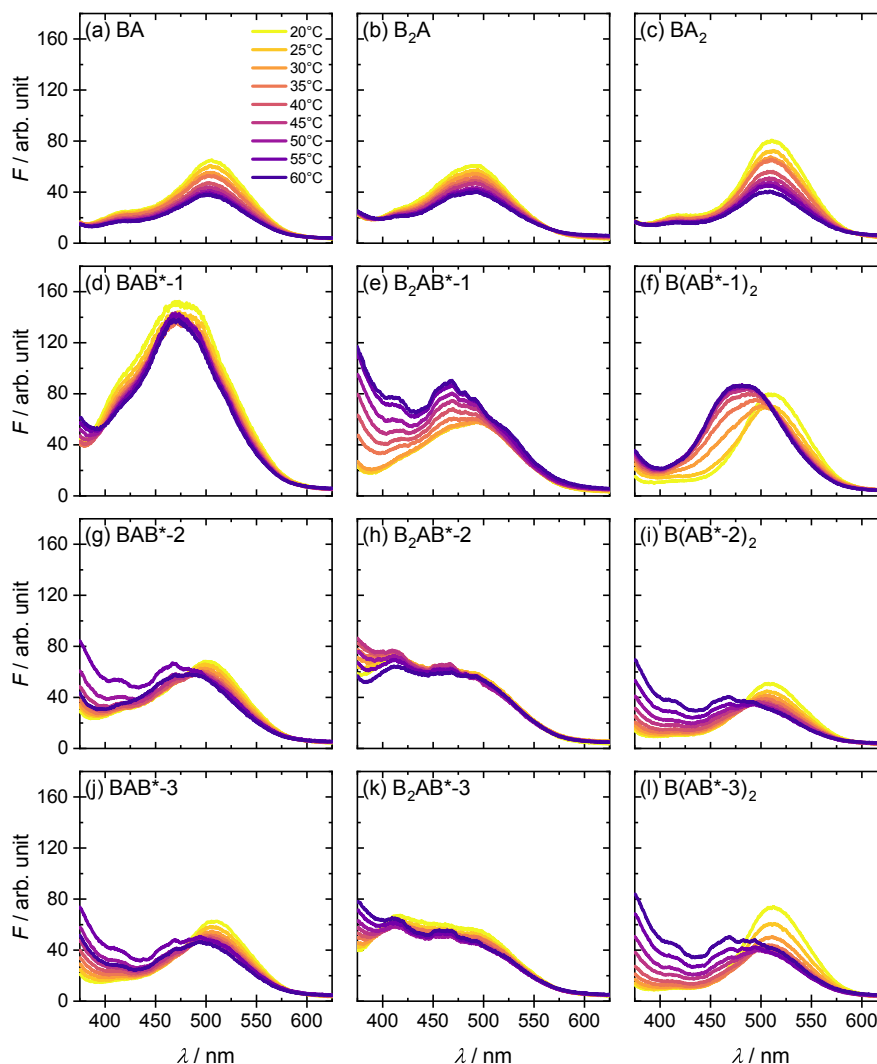
Figure 4.16: Fluorescence spectra of the various hydrophobically modified block copolymer solutions in D_2O ($22\,g\,L^{-1}$) containing $1\,\mu mol\,L^{-1}$ Prodan.

At rising temperatures, at least one extra peak arises at a lower wavelength of around $470\,nm$. A deeper inspection indicates that the BAB* systems exhibit a shoulder which corresponds to the observation for the polymers **BA**, **B₂A**, and at low temperatures also for **BA₂**. Although, the B(AB*)₂ systems do not reveal this shoulder. For systems with pDEAm and pNiPAm as TR blocks, a broad thermal transition takes place at about 40–45 °C (*cf.* Figure 4.17c/d). In contrast, for the solution of **B(AB*-1)₂** with pNPAm as TR block, this transition already occurs at 25–30 °C (*cf.* Figure 4.17b).

This trend is consistent with the latter polymer's lower LCST.[17] Additionally, the new band's emission exhibit a noticeable fluorescence intensity. In contrast, for **BAB*-1**, a fairly intense band is seen throughout the examined temperature range of 20–60 °C, with a maximum at about $470\,nm$. This band barely changes with temperature, even in terms of the emission intensity. According to this result, the thermal transition for **BAB*-1**
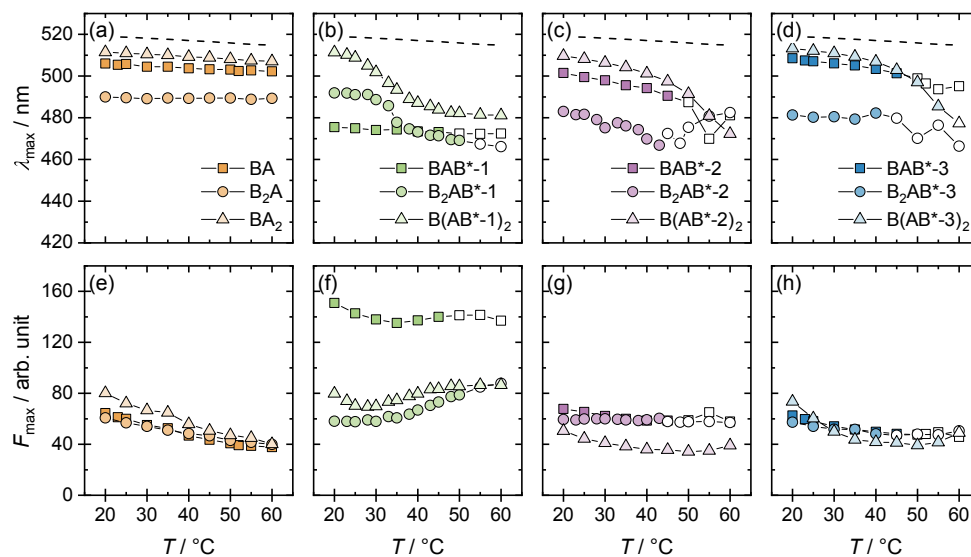
Figure 4.17: (a–d) Wavelength of the maximum emission (λ_{max}) and (e–h) maximum emission (F_{max}) as a function of temperature for the different block copolymers. The solid black lines mark λ_{max} of $1 \, \mu mol \, L^{-1}$ Prodan in D_2O. Symbols in (e–h) have the same meaning as in (a–d). Open symbols mark phase separated samples.

may happen below $20 \, °C$. An identical situation is observed for Prodan's fluorescence spectra in case of the HMTR polymers **B₂AB*-2** and **B₂AB*-3** containing two C_{12} chains. Here, the emission spectra rarely change with rising temperature. This shows that Prodan is predominantly found in the hydrophobic domains formed by the C_{12} chains, which are clearly formed considerably more efficiently than for copolymers of the BAB* and B(AB*)₂ types. The broad complicated emission bands are similar and appear to have three approximately equally intense peaks at ~ 500, 460, and $420 \, nm$. Prodan's fluorescence spectra alter in a specific manner from 20 to $60 \, °C$ when the B* blocks pDEAm or pNiPAm are exchanged by pNPAm (*cf.* Figure 4.16e). In the case of **B₂AB*-1**, the emission band at lower temperature becomes very similar to the spectra obtained for HMTR polymers **BAB*-2** and **BAB*-3** at $60 \, °C$ (which is above their thermal transition; *cf.* Figure 4.16g/j). As temperature rises, a new peak at about $420 \, nm$ is gradually evolving and finally mimics at $60 \, °C$ the shape of the emission bands of **B₂AB*-2** and **B₂AB*-3** copolymers, which have two C_{12} chains. Similar to **B(AB*-1)₂**, the broad thermal transition can be observed at about $30 \, °C$ (*cf.* Figure 4.17b).

4.3 Conclusion

Commonly, the viscosity of aqueous polymer solutions decreases with increasing temperature, but for certain applications a tunable and controlled viscosity increase in a certain temperature window would be beneficial. Nonsymmetrical amphiphilic block copolymers, with a central hydrophilic block "A" of poly(N,N-dimethylacrylamide) (pDMAm) capped by a permanently hydrophobic part "B" containing a n-dodecyl (C_{12}) chain and a thermo-switchable block "B*" with a distinct LCST in aqueous solution were investigated with focus on their temperature-dependent viscosity. Regarding this, a variation of copolymer architectures were employed, such as BAB*, B_2AB*, and $B(AB*)_2$. Compared to the BAB* type, which was already studied in a previous study (see Chapter 3),[64] the B_2AB* type has a larger hydrophobic part featuring two C_{12} chains, while the $B(AB*)_2$ type exhibits two arms of the hydrophilic pDMAm block A with the attached TR block B*. In Scheme 4.3, the aggregation behavior, as well as the emergence of hydrophobic domains above the LCST transition of the B* block, is highlighted.
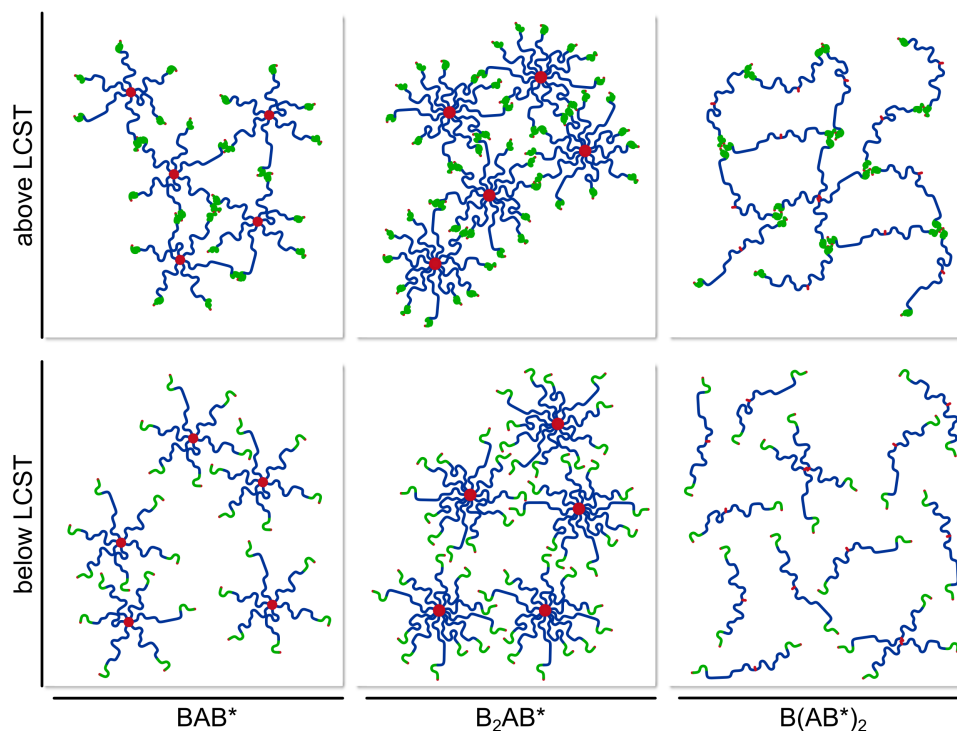
Scheme 4.3: Schematic aggregation behavior of the studied block copolymer architectures, namely BAB*, B_2AB*, and $B(AB*)_2$, below and above the LCST.

Generally, the B_2AB* copolymer solutions exhibit a higher viscosity, which is presumably caused by a superior hydrophobic interaction. However, compared to the other structures, the $B(AB*)_2$ type of the copolymers exhibits the strongest temperature-induced viscosity enhancement. It is interesting to note that the pNPAm-containing system demonstrates the most marked effect. Additionally, this system also exhibits some increase in

elastic properties. For the other TR blocks, *i. e.*, pDEAm- and pNiPAm-containing copolymers, the temperature-induced viscosity enhancement is less pronounced. By contrast, the other architectures, *i. e.*, BAB* and B_2AB*, show just a counterbalancing of the commonly decreasing viscosity with increasing temperature. The static light scattering (SLS) intensities and the effective hydrodynamic radii observed by dynamic light scattering (DLS) both rise as viscosity increases. Small-angle neutron scattering (SANS) studies demonstrated the formation of distinct hydrophobic domains at higher temperatures which improves the mesoscopic picture. Furthermore, insights into the formation of hydrophobic domains of the TR blocks was provided by fluorescence experiments with the solvatochromic probe Prodan. These findings condensate to that the BAB* and B_2AB* types form micellar aggregates which increasingly interact via the TR blocks with rising temperature. Above the LCST, additional TR domains are formed, which lead to a formation of TR domain-bridged clusters. Contrary to this, the $B(AB*)_2$ type shows basically no micellization but interconnects markedly via the TR blocks with rising temperature. Above the LCST, TR blocks form additional domains, which lead to bridging and a formation of a transient network.

In conclusion, the investigated varieties of copolymers' architecture and chemical structure enable systematic control of rheological features that correspond to their mesoscopic organization. The interaction strength between the number of thermoresponsive arms, the number of hydrophobic sticker groups, and the kind and length of the LCST blocks can be adjusted by carefully constructing the copolymer's architecture and composition. If additional enhancement in the overall viscosity of such systems is desired, it is likely that lengthening the permanently hydrophobic component would be the method of choice.

Chapter 5

Modifying the Properties of Microemulsion Droplets by Addition of Thermoresponsive Block Copolymers

Copyright

This chapter is based on the published article

Author Contributions

A. Prause, A. Laschewsky, and M. Gradzielski conceptualized the general experimental design. M. Hechenbichler synthesized and characterized the block copolymers. A. Prause performed the experiments, if not otherwise specified, analyzed the data, and created the figures and schemes. R. F. Schmidt performed the rheology experiments supervised by A. Prause. S. Prévost and L. P. Cavalcanti were the local contacts at the SANS instruments D11/D33, and SANS2D, respectively. The discussion of the results and writing of the manuscript was conducted jointly by A. Prause, A. Laschewsky, and M. Gradzielski. All authors approved on the final version of the manuscript.

Abstract
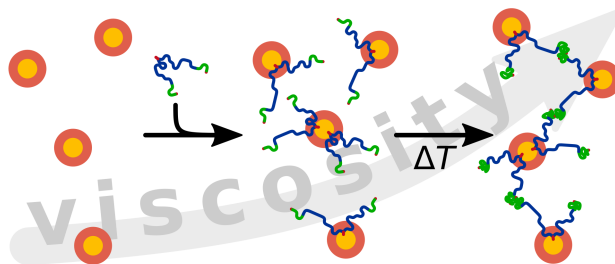
Oil-in-water (O/W) microemulsions (MEs) typically feature a low viscosity and conform to the ordinary viscosity reduction as a function of temperature. However, for certain applications reverting the temperature trend might be required which can be conceived by adding thermoresponsive (TR) block copolymers that induce a network formation as temperature rises. Accordingly, various ME–polymer mixtures were studied for which three different block copolymer architectures of BAB*, B$_2$AB*, and B(AB*)$_2$ type were employed. Here, "B" represents a permanently hydrophobic, "A" a permanently hydrophilic, and "B*" a TR block. For the TR block, three different polyacrylamides, namely poly(N-n-propylacrylamide) (pNPAm), poly(N,N-diethylacrylamide) (pDEAm), and poly(N-iso-propylacrylamide) (pNiPAm), were used which exhibit a lower critical solution temperature (LCST). For a well selected ME concentration, these block copolymers lead to a viscosity enhancement with rising temperature. At a polymer concentration of about 22 g L^{-1}, the most pronounced enhancement was observed for the pNPAm-based systems with factors up to about 3, 5, and 8 for BAB*, B$_2$AB*, and B(AB*)$_2$, respectively. This phenomenon is caused by the formation of a transitory network mediated by TR blocks, as evidenced by the direct correlation between the attraction strength and the viscosity enhancement. For applications requiring a high hydrophobic payload, which is attained via microemulsion droplets, this kind of tailored temperature-dependent viscosity control of surfactant systems should therefore be advantageous.

5.1 Introduction

In this chapter, the focus was set on tuning the rheological properties of low-viscous microemulsions (MEs) by admixing hydrophobically modified thermoresponsive (HMTR) block copolymers. Commonly, the viscosity of a solution reduces with rising temperature. Hence, the idea is that this trend can be overcome by adding thermoresponsive copolymers that increase the viscosity and revert the normally observed viscosity reduction with increasing temperature. For that purpose, symmetrical B*AB* block copolymers with two TR blocks B* could be employed.[134–138] However, in this work, a different approach was chosen as depicted in Scheme 5.1. Here, HMTR block copolymers with a permanently hydrophobic block B and a thermoresponsive block B*, which is hydrophilic below and becomes hydrophobic above the lower critical solution temperature (LCST), were used. Accordingly, the thermoresponsive blocks B* can form new domains above the LCST which will lead to an interconnection of ME droplets.
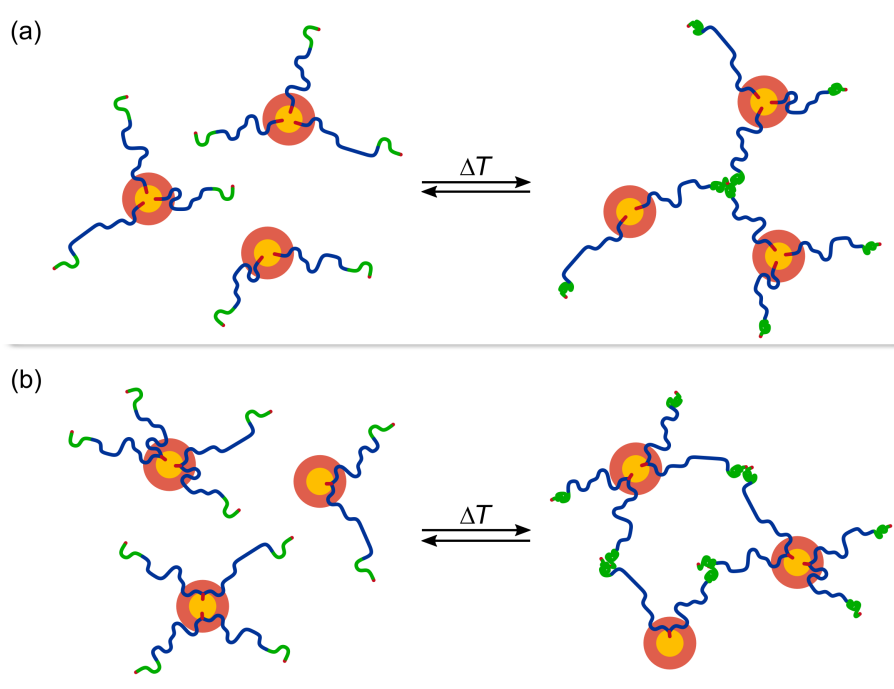
Scheme 5.1: Concept of the temperature dependent network formation of microemulsion (orange and yellow) decorated with (a) BAB*/B$_2$AB* and (b) B(AB*)$_2$ block copolymers (blue: permanently hydrophilic A block, green: hydrophilic/hydrophobic TR B* block).

As in the previous Chapter 4, various block copolymer architectures (Scheme 5.2), *i. e.*, BAB*, B$_2$AB*, and B(AB*)$_2$, were employed with the idea to have a markedly stronger hydrophobic effect, either permanently (B$_2$AB*) or temperature-induced (B(AB*)$_2$). The structural and rheological behavior of the pure block copolymers in aqueous solution can be found in Chapter 4.[65] Here, these previously studied block copolymers were employed in microemulsion–polymer mixtures (Scheme 5.1). As already mentioned, the copolymers

consist of a n-dodecyl (C_{12}) chain, like for typical surfactant molecule, as permanently hydrophobic part B, poly(N,N-dimethylacrylamide) (pDMAm) as permanently hydrophilic block A, and a thermoresponsive (TR) block B* consisting of poly(N-n-propylacrylamide) (pNPAm, LCST $\approx 22\,^{\circ}\mathrm{C}^{[60]}$), poly($N,N$-diethylacrylamide) (pDEAm, LCST $\approx 30\,^{\circ}\mathrm{C}^{[61]}$), or poly($N$-isopropylacrylamide) (pNiPAm, LCST $\approx 32\,^{\circ}\mathrm{C}^{[62]}$).
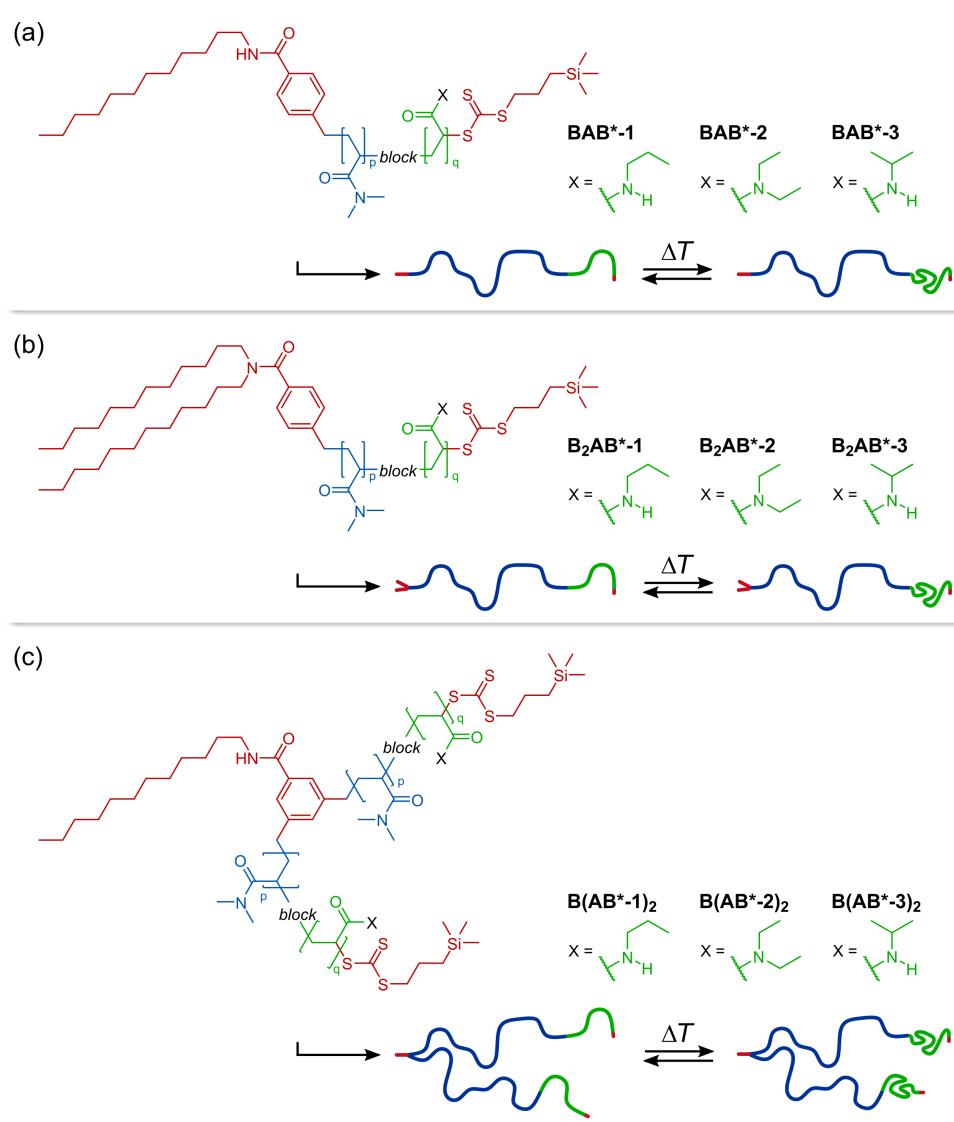
Scheme 5.2: Overview of the investigated hydrophobically modified thermoresponsive (HMTR) architectures (red: permanently hydrophobic block B, blue: permanently hydrophilic block A, green: hydrophilic/hydrophobic TR block B*). (a) The BAB* structures with one n-dodecyl (C_{12}) chain as hydrophobic modification. (b) The B_2AB^* structures with two n-dodecyl chains as hydrophobic modification in geminal position. (c) The $B(AB^*)_2$ structures with two arms.

In the following, the focused was set on studying various ME–polymer mixtures by admixing HMTR block copolymer to different droplet microemulsions (Table 2.6). The droplet microemulsion was previously reported in the bachelor thesis of Schmidt (2020)[67], made of polyethylene glycol (20) sorbitan monolaurate (Tween20) as surfactant, 2-ethyl-hexylglycerin (EHG) as cosurfactant, and isopropyl palmitate (IPP) as oil.[139] For one employed microemulsion, namely **ME-2**, n-decane was used as oil instead of isopropyl palmitate (IPP) to examine if altering the polarity of the oil had an effect on the inter-action with the block copolymers. **ME-2** exhibits a higher molar oil concentration, due to the lower molar volume of n-decane (*cf.* Table 2.1). The three other microemulsions, *i. e.*, **ME-1**, **ME-3**, and **ME-4**, differ only in terms of their molar concentration of micro-emulsion droplets (c_{ME}), which is reflected in the surfactant concentration of Tween20. **ME-1** is about 20% less concentrated, which only reduces slightly the number density of microemulsion droplets.

The amount of solubilized oil was determined to be close to the solubilization capacity at room temperature, requiring the presence of spherical microemulsion droplets. The specific composition of the microemulsions is shown in Table 2.6 The estimated droplet radii were between 3.2 and 3.5 nm (at 25 °C; no hydration assumed). Accordingly, the average distance between the droplets in the solution is approximately 14 and 17 nm at 25 °C and 55 °C, respectively, for the surfactant concentration of 40–50 mmol L^{-1}. For the majority of the experiments, the polymer concentration was set that each droplet of the microemulsion is decorated by 1–4 polymer molecules on average (Table 2.7). As a consequence, every microemulsion droplet comprises at least two TR blocks which effec-tively allows for cross-linking. Here, it is notable that the B(AB*)$_2$ architecture has two arms which means that already a single polymer molecule can cross-link microemulsion droplets. To further examine how these compositional variables affect the behavior of the ME–polymer mixtures, the concentration of the polymer or microemulsion droplets were varied on a few chosen examples (Table 2.8).

The macroscopic phase behavior, their rheological characteristics, and the mesoscopic structure were investigated using static and dynamic light scattering (SLS and DLS) and small-angle neutron scattering (SANS). To better understand how different systems re-spond to temperature, all of these studies were conducted in the temperature range of 20–60 °C. It should be emphasized that all the samples fell within the monophasic phase range. None of the investigated samples showed any macroscopic phase separation under the experimental conditions within the observed time span and temperature window.

5.2 Results and Discussion

5.2.1 Rheological Behavior

Architecture and Thermoresponsive Block Variations

Upon evaluating the temperature-dependent viscosity of a pure microemulsion, the dynamic viscosity (η) is somewhat higher than for the solvent and rises slightly as the temperature rises (Figure C.1). This suggests an anisometric deformation of the droplets with increasing temperature. As expected for EO-containing nonionic surfactants, the hydration decreases with increasing temperature,[140] and consequently the effective volume fraction of the dispersed micelles is reduced. The shear viscosity for various ME–copolymer mixtures was determined between 20–60 °C. As shown in Figure C.2, the measurements revealed a viscosity in the range of 7 to 50 mPa s with no dependency on the shear-rate. When examining the zero-shear viscosity (η_0) as a function of temperature, at low temperatures it always decreases as temperature rises, but this pattern reverses towards higher temperatures, causing a noticeable increase in η_0 (Figures 5.1a–c and C.3).
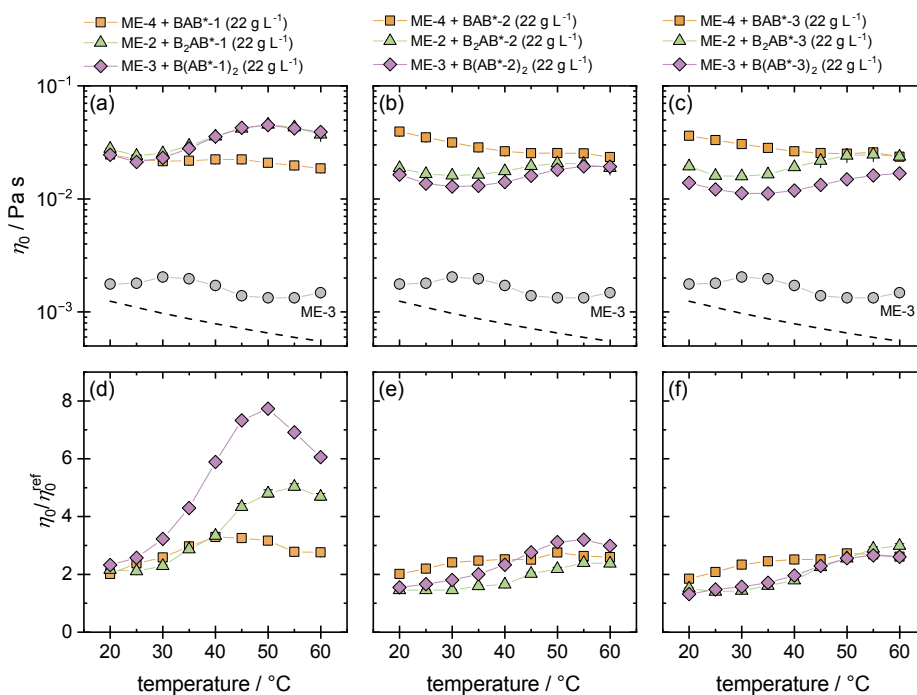
Figure 5.1: (a–c) Temperature dependent zero-shear viscosity (η_0) for ME–polymer mixtures with (a) pNPAm-, (b) pDEAm-, and (b) pNiPAm-containing block copolymers. The dashed black line indicates the viscosity of the solvent D_2O. (e–f) Normalized zero-shear viscosity ($\eta_0\big/\eta_0^{\mathrm{ref}}$) of ME–polymer mixtures with (d) pNPAm-, (e) pDEAm-, and (f) pNiPAm-containing block copolymers. The zero-shear viscosity data are normalized to the reference zero-shear viscosity (η_0^{ref}) of the corresponding pDMAm system without TR block, namely **ME-4 + BA**, **ME-2 + B$_2$A**, and **ME-3 + BA$_2$**.

The zero-shear viscosity of ME–polymer mixtures containing polymers with a TR block was divided by η_0 of the reference ME–polymer mixtures, *i. e.*, ME–**BA** (η_0^{ref}), ME–**B$_2$A**, and ME–**BA$_2$**. With this, the viscosity effect of the TR block B* can be emphasized. In Figure 5.1e–f, the normalized zero-shear viscosity ($\eta_0 / \eta_0^{\text{ref}}$) is displayed as a function of temperature. The $\eta_0 / \eta_0^{\text{ref}}$ values are basically larger than 1 which means that the TR block adds some additional friction. Although, only the pNPAm-containing copolymers induced a viscosity enhancement that was notably more pronounced. Here, the $\eta_0 / \eta_0^{\text{ref}}$ value increases up to 3, 5, and 8 for the samples containing **BAB*-1**, **B$_2$AB*-1**, and **B(AB*-1)$_2$**, respectively, in the temperature range of 20–50 °C. Their pDEAm and pNiPAm equivalents, however, behave very similarly with a significantly subdued enhancement.

In summary, the pNPAm-based ME–polymer mixture with the copolymer of the B(AB*)$_2$ type exhibits the most pronounced viscosity increase. The B$_2$AB* type reveals only a reduced impact and the BAB* type essentially no impact on the viscosity, respectively. Accordingly, the longer pNPAm block, with 49 units, for the B(AB*)$_2$ architecture may also be a contributing factor to the higher value, as opposed to the shorter TR blocks of the pDEAm and pNiPAm copolymers with 29 and 32 units (*cf.* Table 2.3), respectively.

Polymer and Microemulsion Concentration Variations

On certain samples, the effects of polymer and microemulsion concentration were examined (for more details see Table 2.8). For the pDEAm- and pNiPAm-containing samples, three polymer concentrations were employed (Figure 5.2). The microemulsion concentration, defined as the concentration of the surfactant, was $41\,\text{mmol}\,\text{L}^{-1}$ and $50\,\text{mmol}\,\text{L}^{-1}$ for samples containing **ME-1** and **ME-4**, respectively. As anticipated, the sample without a TR block exhibits a decreasing η_0 with increasing temperature while the zero-shear viscosity increases with increasing concentration (Figure 5.2a).
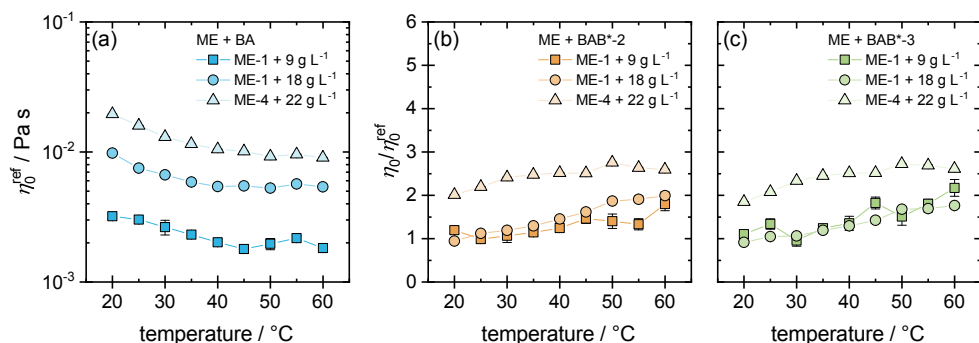
Figure 5.2: Polymer concentration effects on (a) the zero-shear viscosity (η_0) of the reference ME–polymer mixture with the polymer **BA**, and the normalized zero-shear viscosity ($\eta_0 / \eta_0^{\text{ref}}$) for ME–BAB* mixtures containing polymers with (b) pDEAm, and (c) pNiPAm as TR block.

The normalized zero-shear viscosity for the copolymers with TR block for a polymer concentration of 9 and 18 g L^{-1} (with **ME-1**) rises by about 1 up to a $\eta_0 / \eta_0^{\text{ref}}$ value of 2. A fairly similar trend is seen for the pDEAm- and pNiPAm-containing samples. For the 22 g L^{-1} samples (with **ME-4**), the normalized zero-shear viscosity ($\eta_0 / \eta_0^{\text{ref}}$) starts at around 2 and rises just over 2.5 in the observed temperature range. At lower temperatures, the TR block merely decorates the droplets without attractively associating. Although, it appears that some kind of attraction is already present at a polymer concentration of 22 g L^{-1}. This difference might be governed by the slightly increased ME concentration. Nonetheless, attractive interaction is observed for all copolymers at higher temperatures above the LCST.
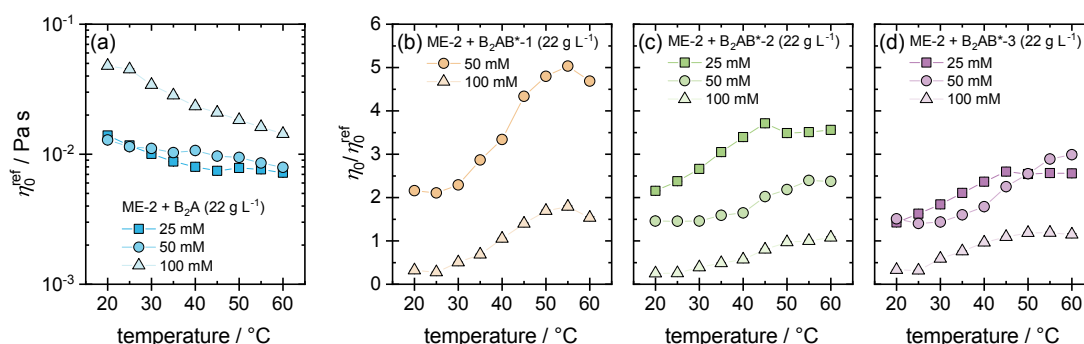
Figure 5.3: Microemulsion concentration effects on (a) the zero-shear viscosity (η_0) of the reference ME–polymer mixture with the polymer **B$_2$A**, and the normalized zero-shear viscosity ($\eta_0 / \eta_0^{\text{ref}}$) for ME–B$_2$AB* mixtures containing polymers with (b) pNPAm, (c) pDEAm, and (d) pNiPAm as TR-block (microemulsion concentrations are given as concentration of the contained surfactant).

Because of the B$_2$AB*'s type's generally higher viscosity, the effect of the microemulsion concentration was examined using this architecture. At a constant polymer concentration of 22 g L^{-1}, the microemulsion concentrations of 25, 50, and 100 mmol L^{-1} were investigated (Figure 5.3). With increasing microemulsion concentration, particularly between 50 to 100 mmol L^{-1}, the reference sample without a TR block exhibit a viscosity increase (Figure 5.3a). This can be explained by the growing volume fraction of dispersed material. For samples with TR block-containing polymers, the lowest microemulsion concentration has the highest normalized zero-shear viscosity ($\eta_0 / \eta_0^{\text{ref}}$). With increasing microemulsion concentration, the values for $\eta_0 / \eta_0^{\text{ref}}$ decrease. The temperature trend remains similar, where values rise with increasing temperature. This temperature dependent increase is particularly noticeable for the pNPAm system which was previously observed when directly comparing the different TR blocks (*cf.* Figure 5.1). It is interesting to note that given a ME concentration of 100 mmol L^{-1} of surfactant, the $\eta_0 / \eta_0^{\text{ref}}$ value decreases below 1 at low temperatures and rises roughly towards 1 at high temperatures. Generally speaking, the decreased temperature dependency can be attributed to the presence of fewer polymer chains per microemulsion droplet, limiting the capacity to form a commensurate network.

Additionally, the spacing between the microemulsion droplets should be in a particular distance determined by the end-to-end distance of the block copolymer.[52] Thus, a microemulsion concentrations of about or below $50\,\mathrm{mmol\,L^{-1}}$ of surfactant is acceptable for the used copolymers in order to create an effective bridging via the TR blocks.

5.2.2 Light Scattering Studies

Static Light Scattering As the first method to obtain structural insights, static light scattering (SLS) was used to extrapolate the forward scattering intensity $I(0)$ via the Guinier law (Equation 2.2, Figures C.4 and C.6). These results already exhibit a significant rise in $I(0)$ for temperatures above $40\,^{\circ}\mathrm{C}$ for pure microemulsions (Figure C.5). This rise must be related to the head group's affinity to dehydrate with rising temperature which is well-known for nonionic surfactants.[141] Consequently, the packing parameter changes, which can cause a sphere-to-rod transition and lead to larger elongated aggregates. As a result of this, the aggregates may also interact more attractively. Thus, both effects would enhance the viscosity and scattering intensity.
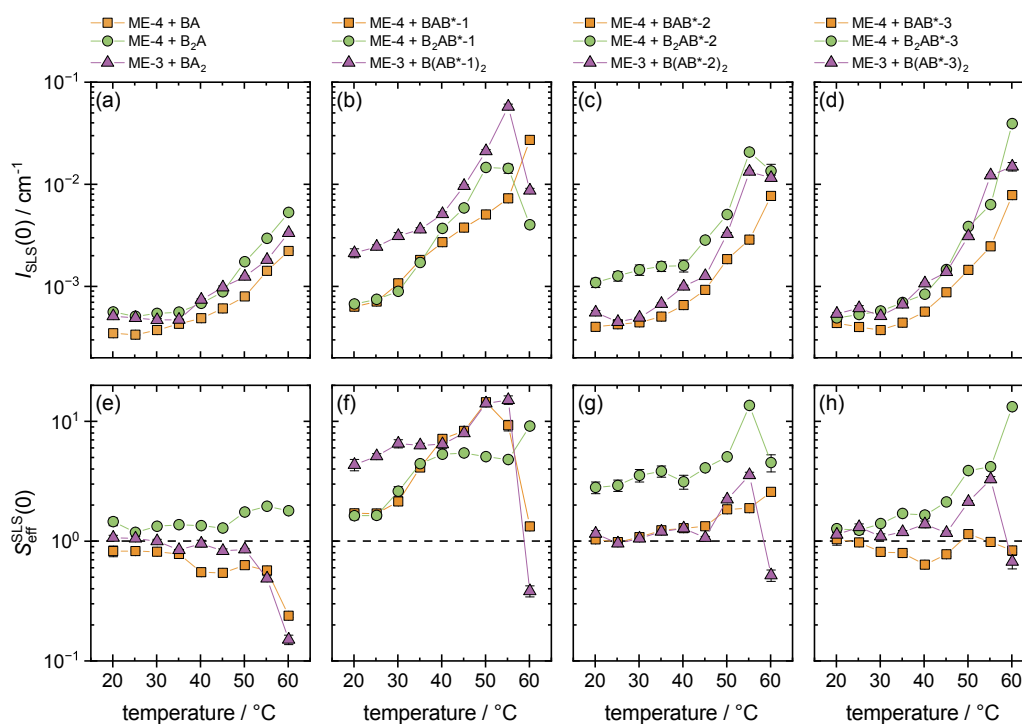
Figure 5.4: (a–d) Forward scattering intensity and (e–f) effective structure ($S_{\mathrm{eff}}^{\mathrm{SLS}}(0) = I_{\mathrm{SLS}}^{\mathrm{ME-polymer}}(0)/S_{\mathrm{SLS}}^{\mathrm{ME}}(0)$) factor as a function of temperature of ME–polymer mixtures plotted for polymers (a/e) without TR block, (b/f) with pNPAm as TR block, (c/g) with pDEAm as TR block, and (d/h) with pNiPAm as TR block.

For the samples containing polymers without a TR block, a slightly similar pattern is observed (Figure 5.4). Although, generally speaking, the scattering intensity is already a slightly higher and above $40\,^{\circ}\mathrm{C}$ the intensity increase is less pronounced. Contrarily, the

increase with rising temperature for the samples with TR block copolymers is generally much more pronounced, but also begins to set in primarily above 40 °C, which is significantly higher than the LCST of the pure TR polymers. The LCSTs of the copolymers were moderately higher compared to the homopolymers as reported in Section 4.2.1.[65] The scattering intensity for the samples containing copolymers with a TR block is around 10 times higher at the highest temperatures than for the corresponding samples with polymers without a TR block. This demonstrates that larger scattering domains are present, which corresponds to 5–10 ME droplets within such scattering domain.

Dynamic Light Scattering   The dynamic light scattering (DLS) data (Figures C.7 and C.9) nicely corroborate the observation seen by SLS. The microemulsion droplet size increases with increasing temperature. For ME–polymer mixtures with copolymers without a TR block, a subdued growth is observed. However, a slower relaxation mode can also be seen, which is attributed to the presence of the well-dissolved protruding pDMAm chains (Figure 5.5a).
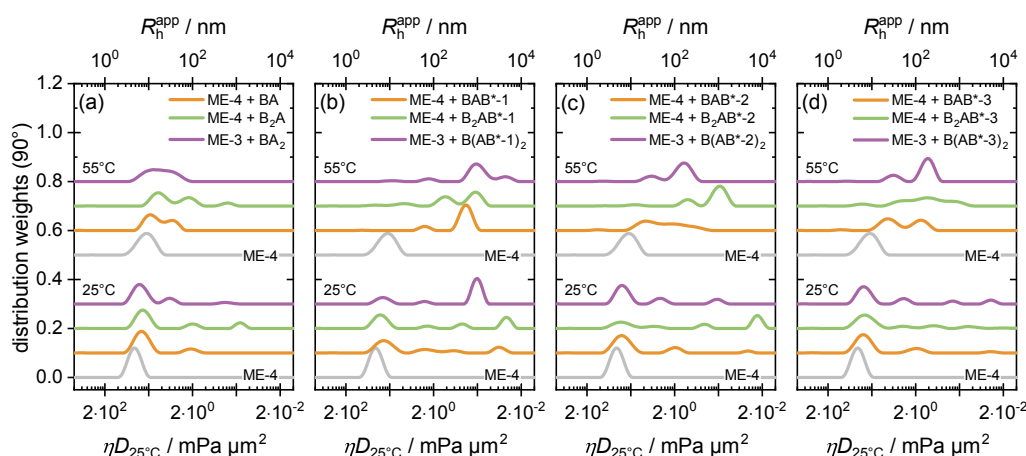
Figure 5.5: Size distributions at 90° for temperatures of 25 °C and 55 °C of ME–polymer mixtures for polymers (a) without TR block, (b) with pNPAm as TR block, (c) with pDEAm as TR block, and (d) with pNiPAm as TR block. The size distributions of **ME-4** (gray curves) were added as a reference.

The DLS results for samples with the TR block-containing copolymers are shown in Figure 5.5b–d (see Figure C.10 for all temperatures). The results closely match the viscosity trend for samples containing these copolymers. Nevertheless, at higher temperatures some fast relaxation modes were observed for the samples containing copolymers of the BAB* type. These modes can be attributed to freely moving microemulsion droplets which coincides well with minor viscosity enhancement observed for those samples. Additionally, slower relaxation modes become more prevalent at higher temperatures. For the samples containing B$_2$AB* and B(AB*)$_2$ type copolymers, these slower modes are only partially visible at low temperatures and become more prominent at higher temperatures.

It demonstrates conclusively that network association occurs which is considered to be the reason for the observed viscosity increase. Additionally, regarding the B(AB*)$_2$ type copolymers, it is clear that the pNPAm-containing sample exhibits the most marked shift towards slower relaxations, which is consistent with the system's most significant viscosity enhancement.

5.2.3 Small-Angle Neutron Scattering Studies

In order to acquire a more in-depth structural understanding, SANS measurements were carried out at 25 and 55 °C which corresponds to temperatures below and above the expected LCST for the TR blocks. A significant alteration in scattering intensity at low q is observed even for the pure microemulsion (Figure C.11). It correlates well with the data obtained by light scattering (Figure C.5). Thus, the anisometric expansion of the microemulsion droplets is partially responsible for the change at low q. At high q only minor changes are observed, inferring that the local droplet structure renders basically unchanged.

Architecture and Thermoresponsive Block Variations

Focussing on how the architecture of the copolymer and the used TR block might affect the microemulsion's properties was the first part to investigate. For this reason, the copolymer concentration was set to $22\,\mathrm{g\,L^{-1}}$ while maintaining the microemulsion's surfactant concentration fairly constant at 40–$50\,\mathrm{mmol\,L^{-1}}$. Under this condition, roughly 1–4 copolymer molecules decorate the ME droplets which mainly depends on the choice of copolymer and temperature which modifies the size of the droplets (Table 2.7). As previously observed in light scattering, the addition of a polymer without a TR block only slightly alters the SANS patterns. However, the scattering intensity increases slightly toward low q (Figure 5.6a), which is likely caused by the long pDMAm chains correspondingly raising the molecular weight of the aggregates while decorating the microemulsion droplet (*cf.* Scheme 5.1).

The behavior for the samples with copolymers containing a TR block is clearly different. At high temperatures, a consistently pronounced increase toward low q is observed for the pDEAm- and pNiPAm-containing copolymers (Figure 5.6c/d). In case of pNPAm, this rise is noticeably more pronounced as already seen in SLS (*cf.* Figure 5.4), which also revealed a significantly enhanced viscosity (Figure 5.1). Thus, this low q intensity increase may be attributed to considerably increased attraction and the ensuing formation of a larger network (Figure 5.6b). At this point, it would mark the origin of the increased viscosity of the samples.

Before further analyzing the SANS data, it should be emphasized that the scattering of the microemulsion droplets and their spatial arrangement, which is altered by the presence of the polymers, dominate the displayed scattering patterns. Expectably, the copolymers' B part will be integrated into the core of the microemulsion droplets, while the A part
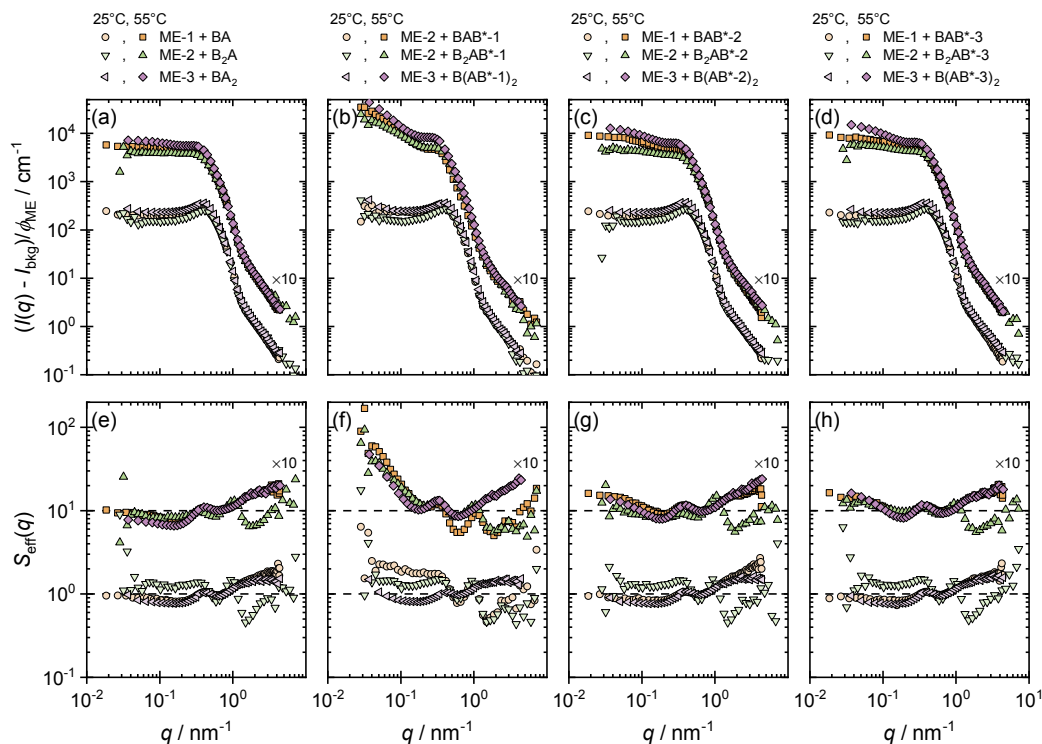
Figure 5.6: ME–polymer mixtures at $25\,^{\circ}\mathrm{C}$ and $55\,^{\circ}\mathrm{C}$ with a polymer concentration of about $22\,\mathrm{g\,L^{-1}}$. (a–d) SANS data for polymers (a) without TR block, and (b) with pNPAm, (c) pDEAm, and (d) pNiPAm as TR block. The scattering intensity is normalized to the volume fraction of the microemulsion. (e–h) Effective structure factor for polymers (e) without TR block, and (f) with pNPAm, (g) pDEAm, and (h) pNiPAm as TR block. The data at $55\,^{\circ}\mathrm{C}$ are multiplied by 10 for clarity.

protrudes into the aqueous environment which leads essentially to a steric repulsion of the droplets. Below the LCST of the B* block, it will behave similar to the A block. But above the LCST, it will tend to form additional domains which could result in an additional attractive or repulsive interaction of the ME droplets. The type of interaction mainly depends on the average distance between droplets and the copolymer's end-to-end distance.

In the following, the SANS intensities were analyzed with an attractive ellipsoidal core-shell model (Equation 2.46, described in detail in Section 2.2.9). The above-mentioned attractive or repulsive interactions were modelled with a sticky hard-sphere structure factor. The ellipsoidal core-shell model is made up of a core and a shell. Thus, the core is constructed of the oil, the surfactant's tail, cosurfactant, and the B group, mainly consisting of a C_{12} chain, of the copolymers. The number of B groups in the core was calculated based on the ratio of polymer chains per microemulsion droplet ($N_{\mathrm{p}}/N_{\mathrm{ME}}$, listed in Table 2.7). Accordingly, the shell consists of the surfactant's head group which is assumed to be swollen by the solvent D_2O.

The model was parameterized with the number of surfactant molecules per microemulsion droplet (N_{surf}), the swelling ratio (α) of the shell (ratio of solvent volume per surfactant head group volume in the shell, *e. g.*, $\alpha = 0$: dry, $\alpha = 1$: equal volume of head groups and water in the shell), and the aspect ratio (ε, < 1: oblate, 1: sphere, > 1: prolate). The equatorial core-shell radius (R_{csh}) is computed based on N_{surf}, α, and ε via $R_{\text{csh}} = \sqrt[3]{\frac{3V_{\text{csh}}}{4\pi\varepsilon}}$, where V_{csh} is the core-shell volume of the ellipsoid.

The polymer coil scattering contribution (I_{p}, Equation 2.14) takes into account the AB* blocks which protrude from the ME droplets. An ellipsoidal form factor was used to describe the microemulsion droplets which does not necessarily indicate the presence of ellipsoidal aggregates; rather, it effectively considers the polydispersity, shape fluctuations as well as the anisometric shape of the aggregates. In this regard, it should be emphasized that fully swollen microemulsion droplets will have a spherical shape with certain polydispersity while the shape fluctuations are caused by the bending modulus of the amphiphilic monolayer.[142,143] With deviation in the droplet composition from the equilibrated and fully swollen droplet, the anisometric shape of the aggregates is expected to increase which is seen here at higher temperatures.

According to Baxter (1968)[94], the sticky hard-sphere structure factor was introduced to alter the strength of the attractive interaction between ME droplets decorated with polymer chains. The attraction is defined by the attraction strength (λ_{shs}), where 0 corresponds to a fully repulsive interaction and increasing values correspond to an increasingly attractive interaction of the hard-spheres. Further details of the scattering model can be found in Section 2.2.9. Figure C.12 shows the fits of the ME–polymer samples of various architectures.

Figure 5.7 displays the obtained parameters for the ellipsoidal core-shell form factor. In contrast, for the MEs and ME–polymer samples, the number of surfactant molecules per microemulsion droplet (N_{surf}), the swelling ratio (α), and the aspect ratio (ε) essentially remain unchanged at 25 °C. The aspect ratio for the ME–polymer samples reduces from $\sim$0.9 to $\sim$0.6 for the *n*-decane-based **ME-2**, revealing that the phase boundary for an oil-saturated microemulsion may be further away. Additionally, the surfactant's temperature-sensitive ethylene oxide (EO) groups caused the increase of N_{surf}, decrease of α, and decrease of ε for the pure MEs at 55 °C. The ME–polymer mixtures exhibit the same general tendencies. Only samples containing **ME-2** show a minor increase in the swelling ratio, while a significant increase can be seen for the sample with **BAB*-1**. Although, it is true that ε is always less than 1, it is frequently noticed that oblate ellipsoids generally appear to fit the experimental scattering data of polydisperse spherical particles more accurately.

For microemulsions, the surfactant aggregation numbers (N_{surf}) between 70 and 170 are considered to be comparatively small. However, it can be related to the rather bulky head group of Tween20, the equimolar amount of surface-active EHG molecules, and the moderate solubilization capacity of about 0.5 IPP or 0.7 *n*-decane molecules per Tween20 molecule. The number of water molecules per surfactant molecule or EO unit can be
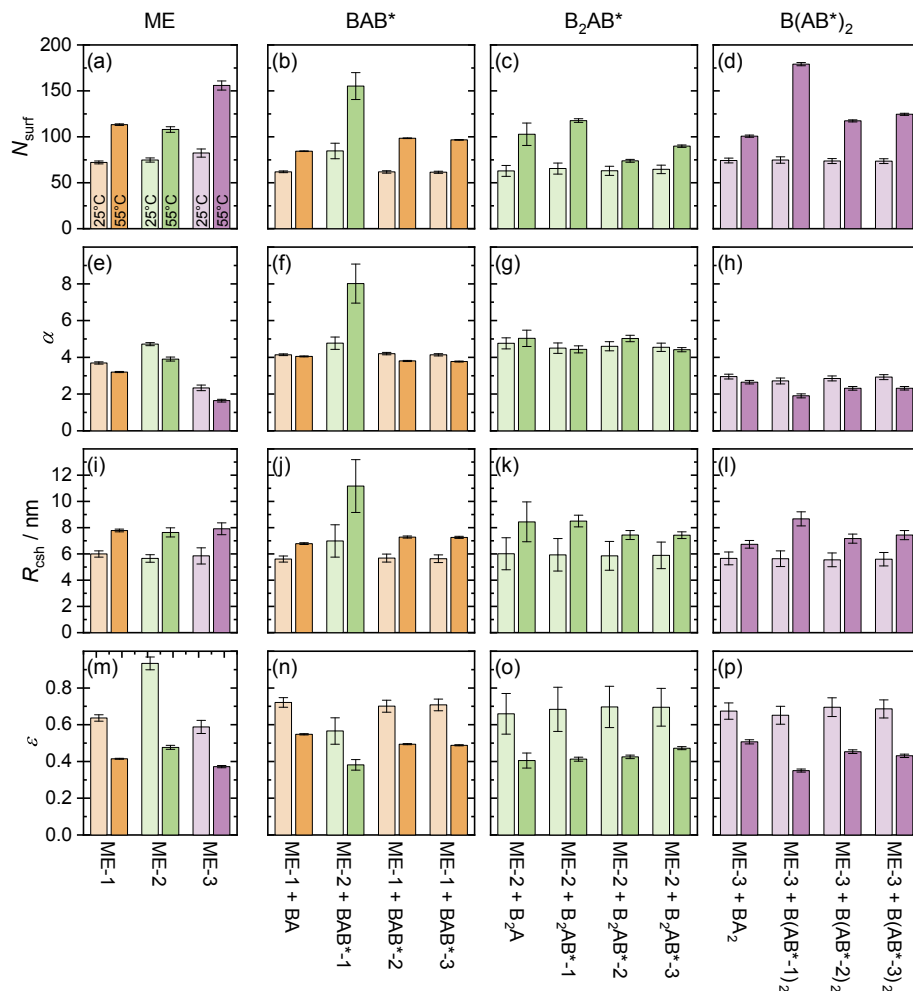
Figure 5.7: Best-fit parameters of the ellipsoidal core-shell form factor at 25 °C and 55 °C. (a–d) The number of surfactant molecules per microemulsion droplet (N_{surf}), (e–h) swelling ratio (α) of the ME droplet shell, *i. e.*, swelling of the Tween20 head group, (i–l) equatorial core-shell radius (R_{csh}) of the ME droplets, and (m–p) aspect ratio (ε, < 1: oblate, 1: sphere, > 1: prolate) of the ME droplets for **ME-1**, **ME-2**, and **ME-3** before and after adding the three types of copolymer architectures.

calculated from the swelling ratio of the shell. This value ranges from about 80 to 240 for pure MEs (approximately 4–12 per EO unit). Compared to EO-surfactants, the lower boundary of this range is in good agreement with the estimate of 4 to 5 water molecules per EO unit.[144,145] The comparably high values for the upper boundary can be related to the simple geometrical model that includes also water molecules which are not directly bound to EO groups.

The two variables for the sticky hard-sphere structure factor are hard-sphere radius (R_{hs}) and attraction strength (λ_{shs}). For R_{hs}, the volume equivalent radius ($R_v = R_{csh} \sqrt[3]{\varepsilon}$), which is derived from the volume of the ellipsoids, is used as a fixed value for the pure MEs and as the lower boundary for the ME–polymer samples to consider the protruding polymer chains. Figure 5.8 shows the best-fit values. All ME–polymer samples exhibit hard-sphere
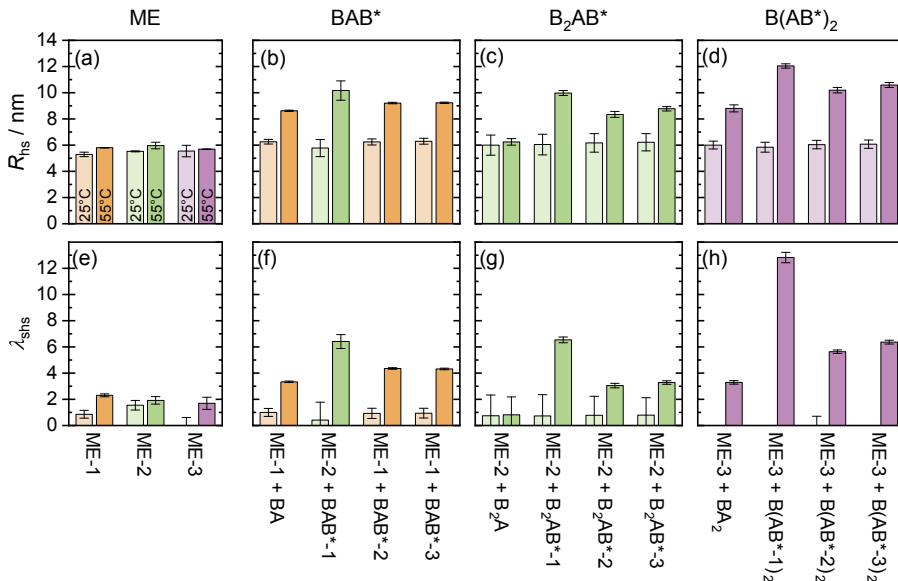
Figure 5.8: Best-fit parameters of the sticky hard-sphere structure factor, *i. e.*, (a–d) hard-sphere radius (R_{hs}), and (e–h) attraction strength (λ_{shs}, 0: purely repulsive, > 0: increasing attraction) of the hard-spheres for **ME-1**, **ME-2**, and **ME-3** before and after adding the three types of copolymer architectures.

radii of nearly 6 nm at 25 °C, which is roughly 1 nm bigger than for the pure ME droplets. As above mentioned, the additional polymer chains are attributed to cause the higher values of R_{hs}. In comparison to measurements at 25 °C, the observed hard-sphere radii are substantially larger at 55 °C. Only for the sample containing **B$_2$A**, R_{hs} essentially stayed unaltered. R_{hs} is about 1–2 nm larger for samples with pNPAm-containing polymers compared to the very similar behaving pDEAm- and pNiPAm-containing polymers. In terms of architecture, the samples with B(AB*)$_2$ type polymers exhibit the largest R_{hs}, which are again roughly 1–2 nm larger than for the samples with polymers of BAB* and B$_2$AB* architectures.

The attraction strength (λ_{shs}) and the measured trends for the hard-sphere radius at 55 °C must be considered together because they both have an impact on the scattering patterns. The samples with polymers without a TR block show the lowest attraction, followed by the samples containing polymers with pDEAm and pNiPAm as TR blocks that have slightly higher values for λ_{shs}. The samples containing polymers with pNPAm as a TR block exhibit the most pronounced attractive interaction. In particular, the sample with **B(AB*-1)$_2$** reveals a λ_{shs} value of ∼13. A λ_{shs} value nearly half as large is found for samples with the polymers **BAB*-1** and **B$_2$AB*-1**. Additionally, the still clearly discernible correlation peak is evidence for increased degree of ordering while exhibiting also the largest R_{hs} values. At 25 °C, when basically no attractive interactions are expected, λ_{shs} values of about 1 or less with significant error bars can be seen. This may be due to interactions between TR blocks or to polymer chain entanglement.
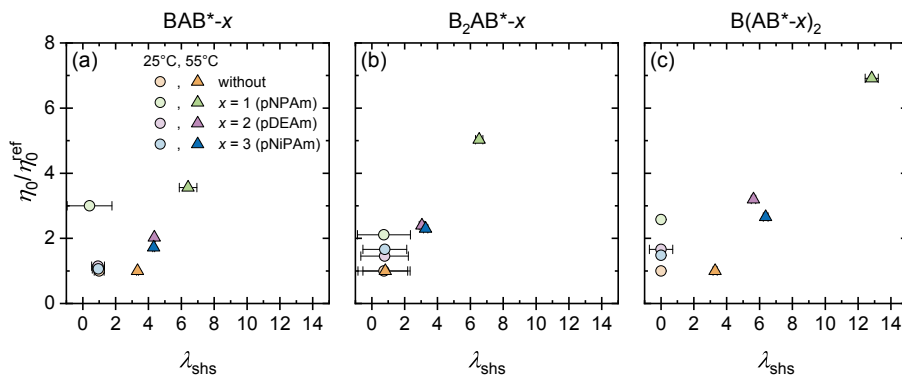
Figure 5.9: Normalized zero-shear viscosity ($\eta_0 \big/ \eta_0^{\text{ref}}$) as a function of the attraction strength (λ_{shs}) at 25 and 55 °C for the investigated block copolymer types (a) BAB*, (b) B$_2$AB*, and (c) B(AB*)$_2$.

The attractive potential between the microemulsion droplets can be correlated with the observed viscosity enhancement. The viscosity is directly proportional to the lifetime of the network nodes of the formed transient network, which constitutes the structural relaxation time of the system. The correlation between normalized zero-shear viscosity ($\eta_0 \big/ \eta_0^{\text{ref}}$) and λ_{shs} is displayed in Figure 5.9. This linear correlation is expected since λ_{shs} describes the strength of the interaction and should, therefore, be proportional to the lifetime of the formed transient network. The lifetime of the transient network with its structural relaxation time must be shorter than 20 ms. This upper limit for the structural relaxation time is evidenced by the constant viscosity with shear-rates up to $50\,\text{s}^{-1}$ (*cf.* Figure C.2).

Polymer and Microemulsion Concentration Variations

After investigating how the polymer architecture impacts the structure of ME–polymer mixtures, the concentration effect of each component is examined. Accordingly, the copolymer concentration and the microemulsion concentration were altered.

The increasing polymer concentration leads to an increase of the low q upturn at 55 °C (Figure C.13). This observation is already apparent without a TR block, therefore it is partially brought on by rising attraction of the microemulsion droplets. However, in the presence of TR blocks, this impact gets noticeably more pronounced. As a result of the presence of TR blocks, the attractive interaction above the LCST increases. By using the above-mentioned ellipsoidal core-shell model to fit the SANS data, this observation has been quantified. Figure C.14 provides a summary of the best-fit parameters. Most frequently, an increase in both parameters, R_{hs} and λ_{shs} can be seen. At 55 °C, R_{hs} increases from 6 to 8 nm, and the hard-sphere radius difference rises equally between 25 and 55 °C. The existence of more polymer chains protruding from the microemulsion droplets is the explanation for the rise in R_{hs}. However, the rise in λ_{shs} from 2 to as high

as 4 with increasing polymer concentration at 55 °C may be attributable to the TR blocks' increased attraction above the LCST. All findings are in line with the expectation that the attractive interaction would improve as the number of polymer chains per microemulsion droplet increases.[48]
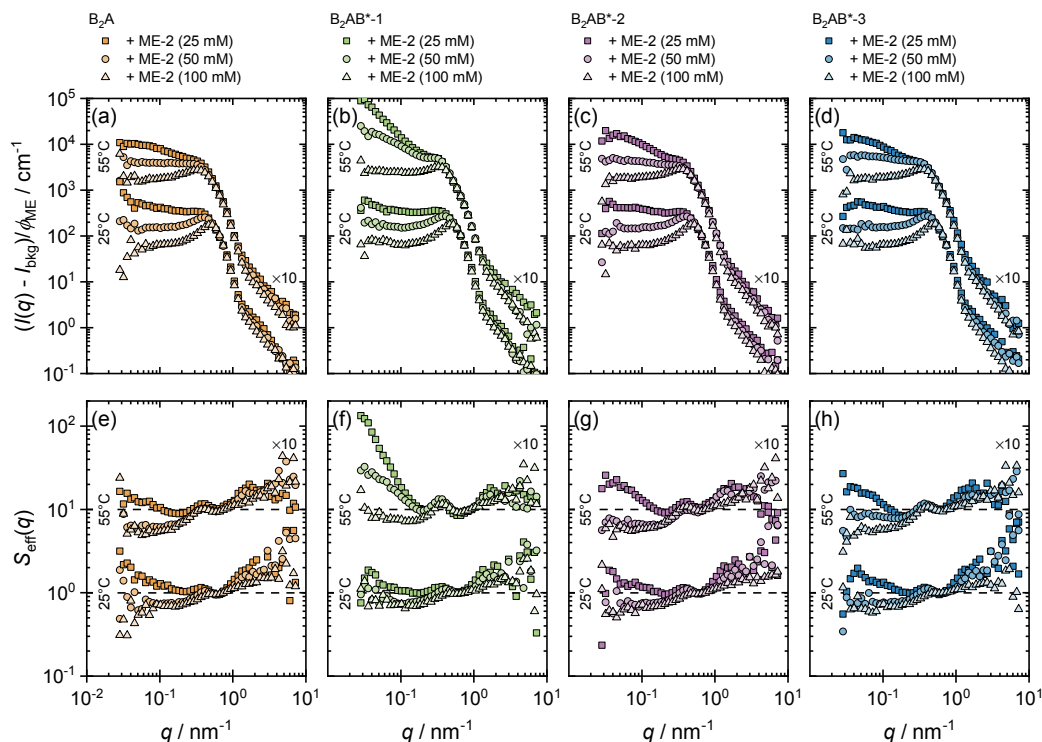
Figure 5.10: ME–polymer mixtures at 25 °C and 55 °C for different ME concentrations (25, 50, and 100 mmol L^{-1}; given as surfactant concentration) at a polymer concentration of about 22 g L^{-1}. (a–d) SANS data for polymers (a) without TR block, and (b) with pNPAm, (c) pDEAm, and (d) pNiPAm as TR block. The scattering intensity is normalized to the volume fraction of the microemulsion. (e–h) Effective structure factor for polymers (e) without TR block, and (f) with pNPAm, (g) pDEAm, and (h) pNiPAm as TR block. The data at 55 °C are multiplied by 10 for clarity.

The variation of microemulsion concentration was examined with the B$_2$AB* copolymers at a constant concentration of 22 g L^{-1} (for more details see Table 2.8). For the different microemulsion concentrations, expressed as concentration of Tween20, the ratio of polymer chains per microemulsion droplet (N_p/N_{ME}) increases up to 4.1 at 25 °C and 6.0 at 55 °C for 25 mmol L^{-1}. For a Tween20 concentration of 100 mmol L^{-1}, the N_p/N_{ME} value decreases down to 0.9 at 25 °C and 1.2 at 55 °C. Additionally, for the Tween20 concentrations of 25, 50, and 100 mmol L^{-1}, the average droplet distance in solution reduces to approximately 17, 14, and 11 nm at 25 °C, and 19, 16, and 12 nm at 55 °C, respectively. Figures 5.10 and C.15 displays the SANS data that depict a particularly pronounced low q upturn for samples with a surfactant concentration of 25 mmol L^{-1}. This upturn becomes less pronounced for samples with higher microemulsion concentrations. Furthermore, with

increasing Tween20 concentration the correlation peak, caused by repulsive interactions, becomes increasingly marked which can be attributed to the progressively tighter packing of the microemulsion droplets. For the lowest ME concentration, the largest attraction is observed at $55\,°C$ while already weak attraction is noticeable at $25\,°C$. For samples with pNPAm-containing copolymers, this impact is again significantly more marked (Figures 5.10b/f and C.15g). At $100\,\mathrm{mmol\,L^{-1}}$, however, only repulsive interactions are seen between the droplets.
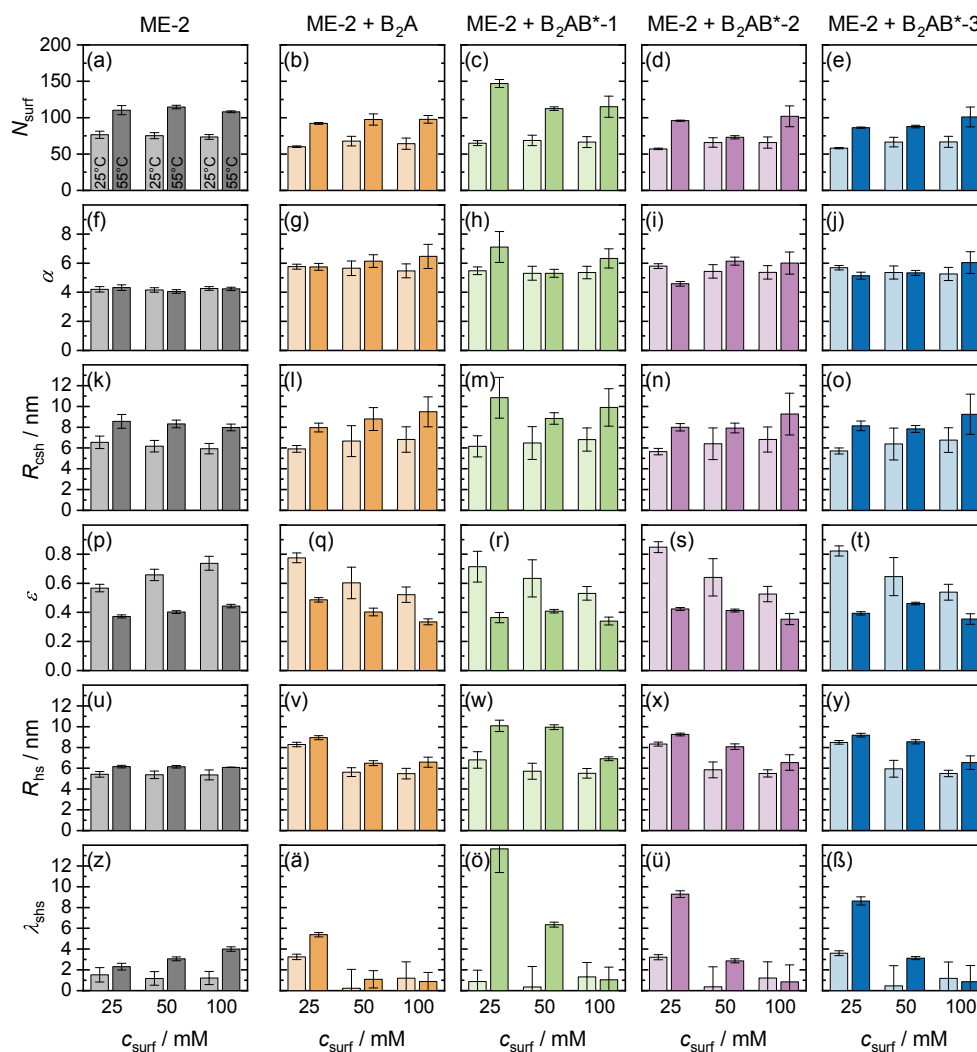
Figure 5.11: Best-fit parameters of the ellipsoidal core-shell form factor for **ME-2**–B_2AB^* mixtures with different microemulsion concentrations (25, 50, and $100\,\mathrm{mmol\,L^{-1}}$; given as surfactant concentration) at a polymer concentration of $22\,\mathrm{g\,L^{-1}}$ at $25\,°C$ and $55\,°C$. (a–d) The number of surfactant molecules per microemulsion droplet (N_{surf}), (e–h) swelling ratio (α) of the ME droplet shell, *i. e.*, swelling of the Tween20 head group, (i–l) equatorial core-shell radius of the ME droplets, (m–p) aspect ratio (ε, < 1: oblate, 1: sphere, > 1: prolate) of the ME droplets, (q–t) hard-sphere radius (R_{hs}), and (u–x) attraction strength (λ_{shs}, 0: purely repulsive, > 0: increasing attraction) of the hard-spheres.

The trend for the hard-sphere radius (R_{hs}) is less pronounced in the case of altering the microemulsion concentration (for best-fit parameters see Figure 5.11). Hence, R_{hs} is at its lowest value for the highest ME concentration and gradually increases toward the lowest ME concentration. The attraction strength (λ_{shs}) has a more distinct pattern at 55 °C, where it significantly decreases with increasing ME concentration and eventually reaches a value of about 1, which is equivalent to the value at 25 °C. This pattern can be expected given the decreasing average distance between ME droplets and the declining number of copolymer molecules per droplet. It can also be explained by counteracting the attractive interaction of TR blocks by the rising repulsive interaction of ME droplets. The distance between the permanently hydrophobic part B, which is located inside the microemulsion droplets, and the TR block B* is already much smaller than the size of the copolymer. As a result, the formation of hydrophobic B* domains or contacts between the B* blocks that belong to distinct microemulsion droplets cannot impose an attractive interaction.

5.3 Conclusion

In this chapter, the rheological behavior of various microemulsion–copolymer mixtures were examined as a function of temperature. The copolymers were varied in terms of their architecture and thermosensitive block B*. As microemulsion, a biocompatible oil-in-water (O/W) droplet microemulsion was used which is based on polyethylene glycol (20) sorbitan monolaurate as surfactant, 2-ethylhexylglycerin (EHG) as cosurfactant, and isopropyl palmitate (IPP) as oil.[139] For comparison, several tests were conducted using *n*-decane as oil, which had minimal impact on the microemulsion's structure or their interaction with the copolymers. The copolymer architectures BAB*, B$_2$AB*, and B(AB*)$_2$ were employed where either the permanently hydrophobic sticker B or the thermosensitive block B* is doubled. The copolymers consist of a permanently hydrophobic sticker B comprised of a *n*-dodecyl (C$_{12}$) group, a permanently hydrophilic block A based on poly(*N,N*-dimethylacrylamide) (pDMAm), and a hydrophilic/hydrophobic thermoresponsive (TR) block composed of poly(*N-n*-propylacrylamide) (pNPAm), poly(*N,N*-diethylacrylamide) (pDEAm), or poly(*N*-isopropylacrylamide) (pNiPAm). While the anomalous rheological properties of the pure block copolymers in solution were examined in the previous Chapter 4, comparable results are found for ME–polymer mixtures. Contrary to common shear thinning with rising temperature, a shear thickening was observed with rising temperature. These observations were caused by the formation of additional B* domains for which fluorescence probe measurements provided evidence (for more details see Section 4.2.2 in Chapter 4).[65] The most marked temperature-induced shear thickening was observed for the B(AB*)$_2$ architecture. Surprisingly, the sample with the pNPAm-containing copolymer exhibited the most marked viscosity increase.

The ME–polymer mixtures with pDEAm- and pNiPAm-containing copolymers experienced a slight viscosity increase independent of the copolymer's architecture. However, a noticeable viscosity increase of up to a factor of 5 and 8 compared to the samples with copolymer without TR block is seen for samples with pNPAm-containing copolymers of

the B_2AB^* and $B(AB^*)_2$ type. These findings were correlated with structural changes observed by the scattering methods (SLS, DLS, and SANS). SLS shows that aggregate sizes increase as temperature rises, which is related to the emergence of a network. At low temperatures, the diffusion of the microemulsion droplets can be seen via DLS. At higher temperatures, the contribution of the individual microemulsion droplets disappears, and all copolymers with a TR block exhibit only slower relaxation modes, which can be attributed to a formation of clusters and network fluctuations.
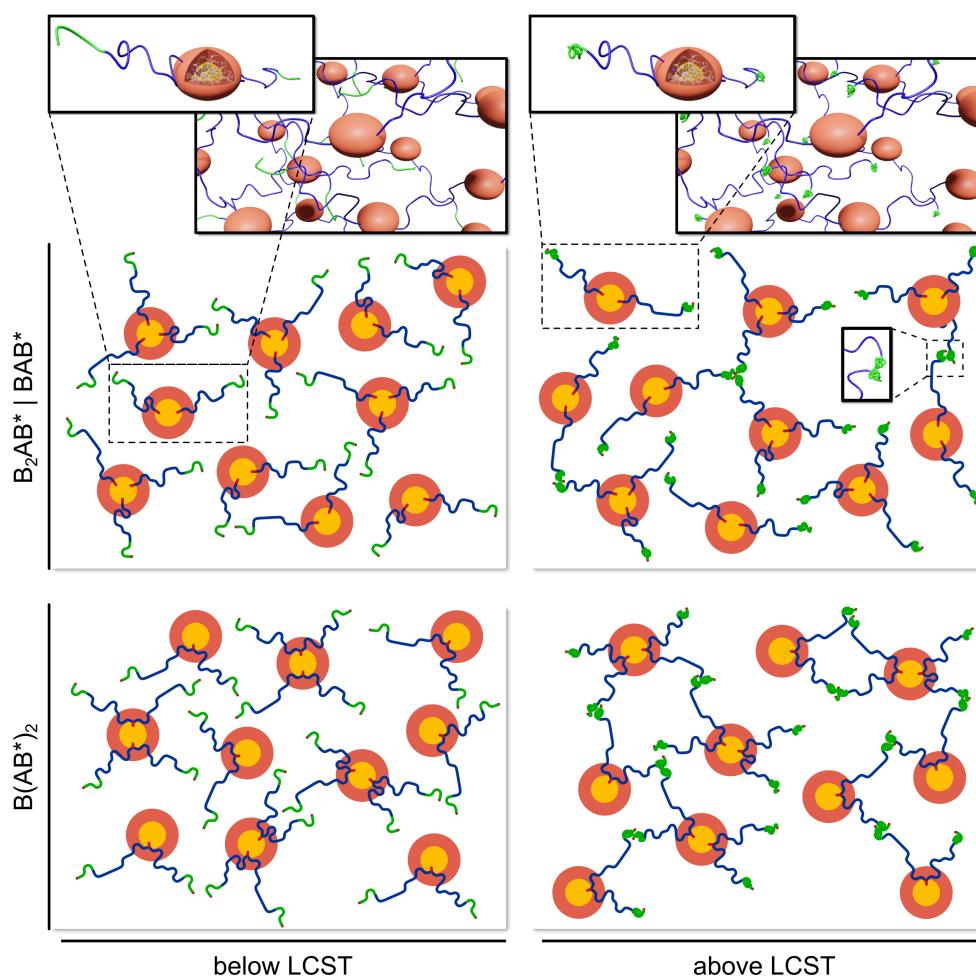
Scheme 5.3: Structural representation of the formed ME–polymer mixtures below and above the LCST of the block copolymers for the investigated architectures. The temperature-triggered cluster/network formation leads to the observed viscosity increase.

Reprinted with permission from Prause *et al.* (2023).[133] Copyright 2023 American Chemical Society.

Similar patterns evolved when examining the SANS data. The interactions between polymer-decorated droplets are primarily repulsively at low temperatures ($25\,^\circ$C), whereas at higher temperatures ($55\,^\circ$C), attractive interactions between ME droplets appear that result from the formation of new domains made up of TR blocks (Scheme 5.3). According to the attractive interaction, the formation of a transient network correlates well with the observed viscosity enhancement.

By changing the concentration of the polymer or microemulsion, which affects the number of polymer chains per ME droplet and the average distance between ME droplets, the observed viscosity rise can also be adjusted. Here, it was found that viscosity increases with increasing polymer content while the temperature trend largely stays unchanged. For varying ME concentrations, the normalized zero-shear viscosity reduces with rising ME concentration, which can be attributed to fewer polymer chains decorating each ME droplet as well as the reduced average distance between droplets. These findings are consistent with earlier research, which showed that a higher ratio of polymer chains to ME droplets leads to an increased viscosity.[55] The polymer size should also be compatible with the typical spacing between ME droplets in solution.[51] According to experiments done with analogously produced microemulsions that included n-decane instead of IPP, the type of oil had no major impact on the structure of microemulsions and their interaction with polymers.

In conclusion, it was feasible to reverse the typical trend of decreasing viscosity with increasing temperature and enhance the viscosity of a microemulsion solution using the examined block copolymers. The B(AB*)$_2$ architecture exhibited the strongest temperature-response, which is not surprising given that there is the largest relative quantity of TR block in these systems. Particularly, for all three architecture, $i.\,e.$, BAB*, B$_2$AB*, and B(AB*)$_2$, the samples with pNPAm-containing copolymers show a very noticeable rise in viscosity with increasing temperature by a factor of about 3, 5, and 8, respectively. This indicates that the temperature dependency of the examined TR block containing copolymers can be adjusted while causing a viscosity enhancement over a predetermined temperature range by appropriately choosing the TR block type and architecture of the copolymers. A high solubilization capacity of a payload, guaranteed by microemulsion droplets, is often paired with a certain viscosity behavior as a function of temperature in a number of applications, therefore viscosity control of this sort is undoubtedly intriguing.

Chapter 6

General Conclusion

Various nonsymmetrical hydrophobically modified thermoresponsive BAB* copolymers were studied in terms of their self-assembly properties, their rheological properties, and their ability to modify the rheological properties of microemulsions as a function of temperature. The experiments were conducted for various concentrations between 5 and $60\,\mathrm{g\,L^{-1}}$ in a well accessible temperature window of 20–60 °C. All thermoresponsive block copolymers consist of a permanently hydrophilic poly(N,N-dimethylacrylamide) (pDMAm) block ("A"), a permanently hydrophobic n-dodecyl (C_{12}) chain ("B"), and a thermoresponsive (TR) block ("B*") which features a lower critical solution temperature (LCST) transition characteristic. This LCST behavior was varied by employing different polyacrylamides as TR block with varying LCST values and types (Type I and Type II), such as poly(N-n-propylacrylamide) (pNPAm), poly(N,N-diethylacrylamide) (pDEAm), poly(N-isopropyl-acrylamide) (pNiPAm), and poly(N-acryloylpyrrolidine) (pNAP).

Aggregation Behavior and Rheological Properties of Block Copolymers The studied BAB* copolymers typically formed small globular aggregates, as demonstrated by light and neutron scattering (SLS, DLS, and SANS), which is a direct consequence of the permanent hydrophobicity of the B end-group. Further quantitative information were obtained by analyzing the SANS data with the clustered polymer-micelle model. This model describes both the attracting and repulsive interactions that govern the self-assembling process as well as the aggregation itself. For the majority of the investigated copolymers, the temperature response is minor. Only getting truly significant for more than 20 monomer units in the TR block. For the pNAP-containing copolymer, the transition temperature is merely shifted outside the selected temperature observation window. In contrast, for the polymers with pNiPAm and pDEAm B* blocks, an attractive interaction is observed above the effective transition temperature of the polymers. This temperature decreases with increasing length of the TR block. In particular, pNiPAm and pDEAm blocks of about 50 monomer units exhibit a significantly distinct aggregation behavior, as observed by light scattering and SANS, once the LCST is exceeded. These polymers experience a very noticeable structural change at about 35–40 °C, resulting in the formation of compacted, highly organized hydrophobic domains with an average spacing of about 35–40 nm. Thus, increasing the temperature causes a noticeable ordering. Surprisingly, this ordering is consistently seen across the entire experimental concentration range of 5–60 $\mathrm{g\,L^{-1}}$ which indicates that the thermoresponsive blocks predominately control the aggregation behavior.

Regarding the different architectures, B_2AB^* copolymer solutions exhibited the highest viscosity, which is presumably caused by a superior hydrophobic interaction. Additionally, this architecture as well as the BAB^* architecture featured just a counterbalancing of the commonly decreasing viscosity with increasing temperature. However, the copolymers of the $B(AB^*)_2$ type exhibited the strongest temperature-induced viscosity enhancement. Notably, the pNPAm-based system revealed the most marked viscosity enhancement and exhibited also some increase in elastic properties. For the other TR blocks, *i.e.*, pDEAm- and pNiPAm-based copolymers, the temperature-induced viscosity rise was less pronounced. The SLS intensities and the effective hydrodynamic radii observed in DLS both rise as viscosity increases. The SANS studies demonstrated the formation of distinct hydrophobic domains at higher temperatures which improves the mesoscopic picture. Furthermore, insights into the formation of hydrophobic domains of the TR blocks were provided by the fluorescence experiments with the solvatochromic probe Prodan. These observations depict that the BAB^* and B_2AB^* types form micellar aggregates which increasingly interact via the TR blocks with rising temperature. Above the LCST, additional TR domains are formed which results in cluster/network formation of micellar aggregates. In contrast, the $B(AB^*)_2$ type basically shows no micellization but marked interconnections via the formation of TR domains with rising temperature, which leads to bridging and network formation above the LCST.

In summary, the aggregation behavior can be altered as a function of temperature by altering the length as well as type of temperature-responsive B^* block used for the BAB^* copolymers. Depending on the B^* block selected, a rise in temperature may have little to no impact, but it may result in an increase in attractive interaction or the development of compacted, highly structured aggregates. The investigated variants of copolymers' architecture and chemical structure allow for systematic control of rheological features that correspond to their mesoscopic organization. The interaction strength between the number of thermoresponsive arms, the number of hydrophobic sticker groups, and the kind and length of the LCST blocks can be adjusted by carefully constructing the copolymer's architecture and composition. As a result, these systems enable customization of the self-assembling response, which may be useful in a range of applications, such as the field of cosmetics or delivery systems. If additional enhancement in the overall viscosity of such systems is desired, it is likely that lengthening the permanently hydrophobic component would be the method of choice.

Modification of Rheological Properties of Microemulsions Tuning the temperature-dependent viscoelastic properties of microemulsions by adding thermoresponsive block copolymers was examined by using a biocompatible oil-in-water (O/W) droplet microemulsion based on polyethylene glycol (20) sorbitan monolaurate as surfactant, 2-ethylhexyl-glycerin (EHG) as cosurfactant, and isopropyl palmitate (IPP) as oil. For comparison, several tests were conducted using *n*-decane as oil, which had minor impact on the microemulsion's structure or their interaction with the copolymers. The ME–polymer mixtures

with pDEAm- and pNiPAm-containing copolymers featured a slight viscosity increase independent of the copolymer's architecture. In contrast, samples with pNPAm-containing copolymers of the B_2AB^* and $B(AB^*)_2$ types exhibited a notable viscosity increase by factors up to 5 and 8 compared to the samples with copolymers without a TR block, respectively. These results were correlated with structural changes revealed by the scattering methods (SLS, DLS, and SANS). SLS shows that aggregate sizes increase as temperature rises, which is related to the emergence of a network. At low temperatures, the diffusion of the microemulsion droplets is observed via DLS. At higher temperatures, the contribution of the individual microemulsion droplets disappears, and all copolymers with a TR block only exhibit slower relaxation modes, which can be attributed to a formation of clusters and network fluctuations.

Similar patterns evolved when examining the SANS data. The interactions between polymer-decorated droplets were primarily repulsively at low temperatures ($25\,^{\circ}\text{C}$), whereas at higher temperatures ($55\,^{\circ}\text{C}$), attractive interactions between ME droplets appeared that resulted from a formation of additional domains made up of TR blocks. According to the attractive interaction, the formation of a transient network correlates well with the observed viscosity enhancement. To quantify this further, the attraction strength (λ_{shs}) of the sticky hard-sphere model was used which corresponds to the attractive potential between the microemulsion droplets. Additionally, the viscosity is directly proportional to the lifetime of network nodes of the formed transient network, which constitutes the structural relaxation time of the system. Consistently, a direct correlation was observed between normalized zero-shear viscosity ($\eta_0 \big/ \eta_0^{\text{ref}}$) and λ_{shs}. This correlation was expected since λ_{shs} describes the strength of the interaction and should, therefore, be proportional to the lifetime of the formed transient network. By changing the concentration of the polymer or microemulsion, which affects the number of polymer chains per ME droplet and the average distance between ME droplets, the viscosity enhancement can also be adjusted. Here, it was observed that viscosity increases with increasing polymer content while the temperature trend largely stays unchanged. For varying ME concentrations, the normalized zero-shear viscosity reduces with rising ME concentration, which can be attributed to fewer polymer chains decorating each ME droplet as well as the reduced average distance between droplets.

Using the examined block copolymers to alter viscoelastic properties of a microemulsion solution, it was feasible to reverse the typical trend of decreasing viscosity with rising temperature and enhance the viscosity. The $B(AB^*)_2$ architecture exhibited the strongest temperature-response, which is not surprising given that there is the largest relative quantity of TR block in these systems. Especially, for all three architectures, *i. e.*, BAB^*, B_2AB^*, and $B(AB^*)_2$, the samples with pNPAm-containing copolymers show a very pronounced viscosity enhancement by factors of about 3, 5, and 8, respectively, with increasing temperature. This indicates that the temperature dependency of the TR block containing copolymers can be adjusted while causing a viscosity enhancement over a predetermined temperature range by appropriately choosing the TR block type and

architecture of the copolymers. A high solubilization capacity of a payload, which is guaranteed by microemulsion droplets, is often paired with a certain viscosity behavior as a function of temperature in a number of applications, therefore viscosity control of this sort is undoubtedly intriguing.

Outlook A library of various block copolymers with a set of different architectures and TR blocks was studied in solution as well as in combination with microemulsions. Further research would be interesting to cover additional parameters, *e. g.*, type of hydrophobic modification, other (advanced) architectures, combination of different LCST values in a single block copolymer, and mixture of block copolymers with different LCST values. For example, by using longer alkyl chains as hydrophobic modification, it can be tested if the temperature-dependent viscosity enhancement factor depends on the initial viscosity of the system. This question to answer would be important for applications that need a high initial viscosity.

Appendix A

Aggregation Behavior of Nonsymmetrically End-Capped Thermoresponsive Block Copolymers in Aqueous Solution

A.1 Light Scattering Studies
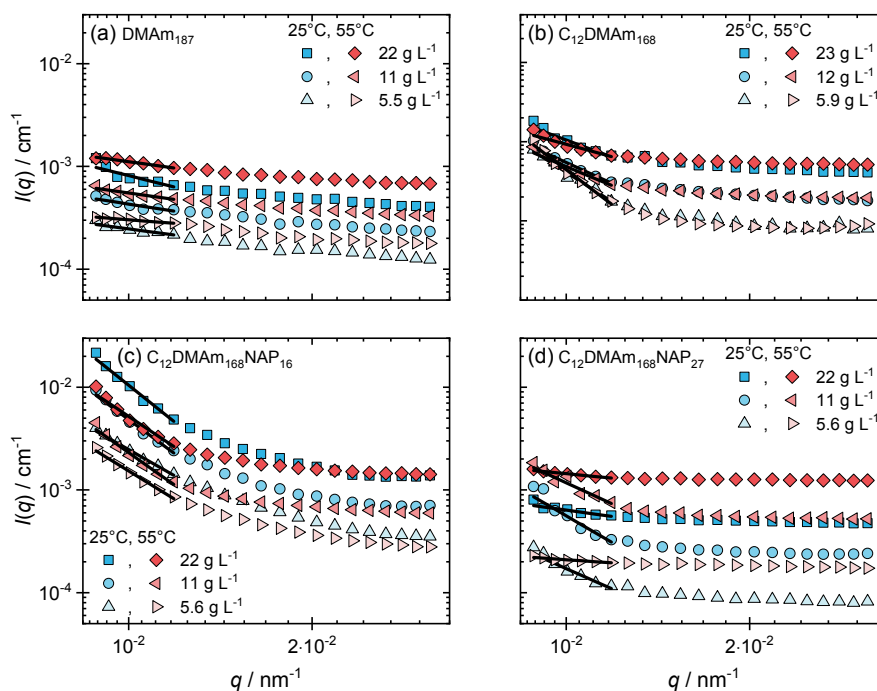
Figure A.1: SLS scattering intensities, Rayleigh ratio, plotted as $I(q)$ versus q with a log-scaled $I(q)$-axis and a q-axis with quadratic scaling. The solid lines correspond to the Guinier fits of (a) **DMAm$_{187}$**, (b) **C$_{12}$DMAm$_{168}$**, (c) **C$_{12}$DMAm$_{168}$NAP$_{16}$** and (d) **C$_{12}$DMAm$_{168}$NAP$_{27}$**. For better clarity, data are shown only for 25 °C and 55 °C.
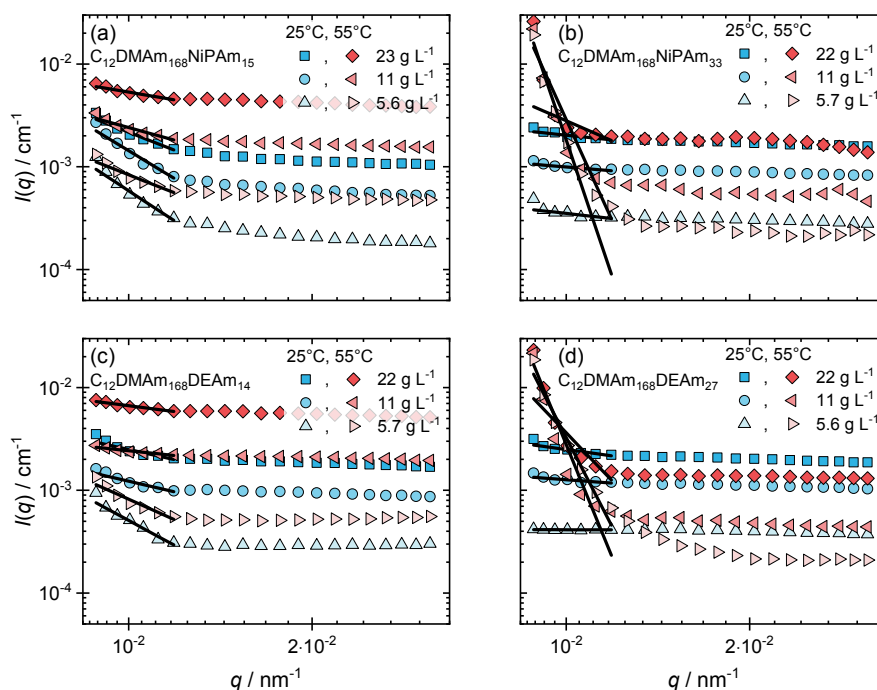
Figure A.2: SLS scattering intensities, Rayleigh ratio, plotted as $I(q)$ versus q with a log-scaled $I(q)$-axis and a q-axis with quadratic scaling. The solid lines correspond to the Guinier fits of (a) **$C_{12}DMAm_{168}NiPAm_{15}$**, (b) **$C_{12}DMAm_{168}NiPAm_{33}$**, (c) **$C_{12}DMAm_{168}DEAm_{14}$** and (d) **$C_{12}DMAm_{168}DEAm_{27}$**. For better clarity, data are shown only for 25 °C and 55 °C.
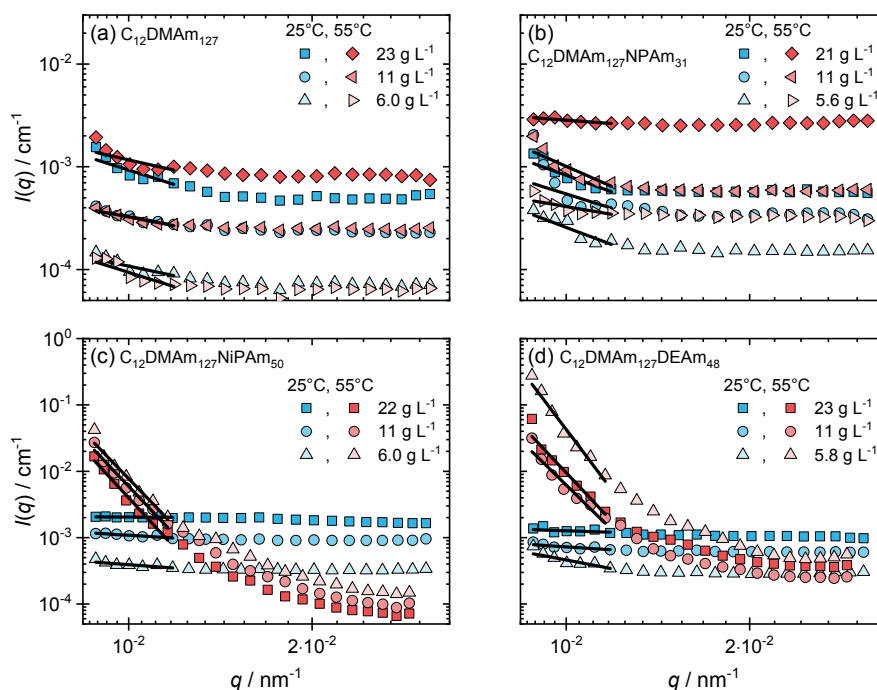
Figure A.3: SLS scattering intensities, Rayleigh ratio, plotted as $I(q)$ versus q with a log-scaled $I(q)$-axis and a q-axis with quadratic scaling. The solid lines correspond to the Guinier fits of (a) **$C_{12}DMAm_{127}$**, (b) **$C_{12}DMAm_{127}NPAm_{31}$**, (c) **$C_{12}DMAm_{127}$-NiPAm$_{50}$** and (d) **$C_{12}DMAm_{127}DEAm_{48}$**. For better clarity, data are shown only for 25 °C and 55 °C.
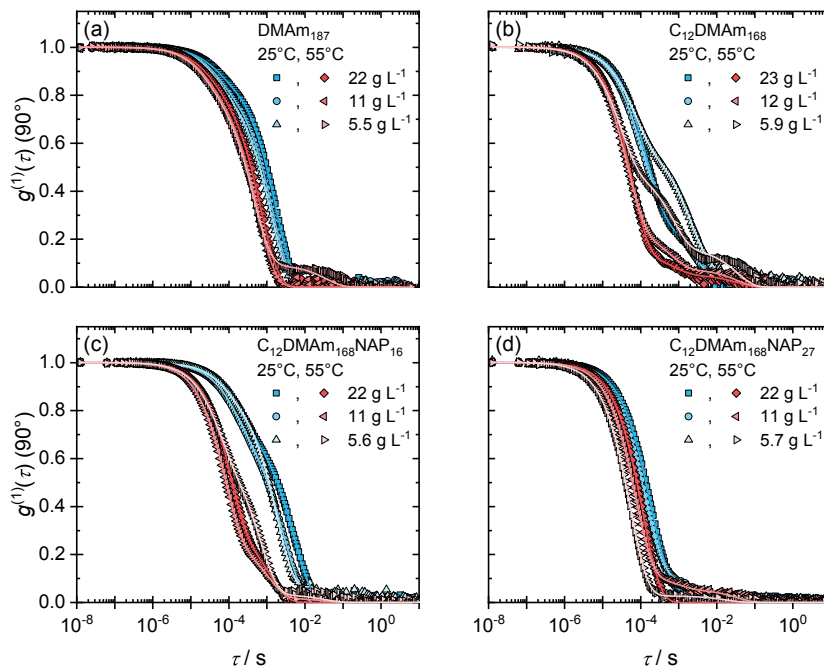
Figure A.4: Field autocorrelation function ($g^{(1)}$) data at 90° with corresponding ORT fits (solid lines) of (a) **DMAm$_{187}$**, (b) **C$_{12}$DMAm$_{168}$**, (c) **C$_{12}$DMAm$_{168}$NAP$_{16}$** and (d) **C$_{12}$DMAm$_{168}$NAP$_{27}$**. For better clarity, data are shown only for 25 °C and 55 °C.
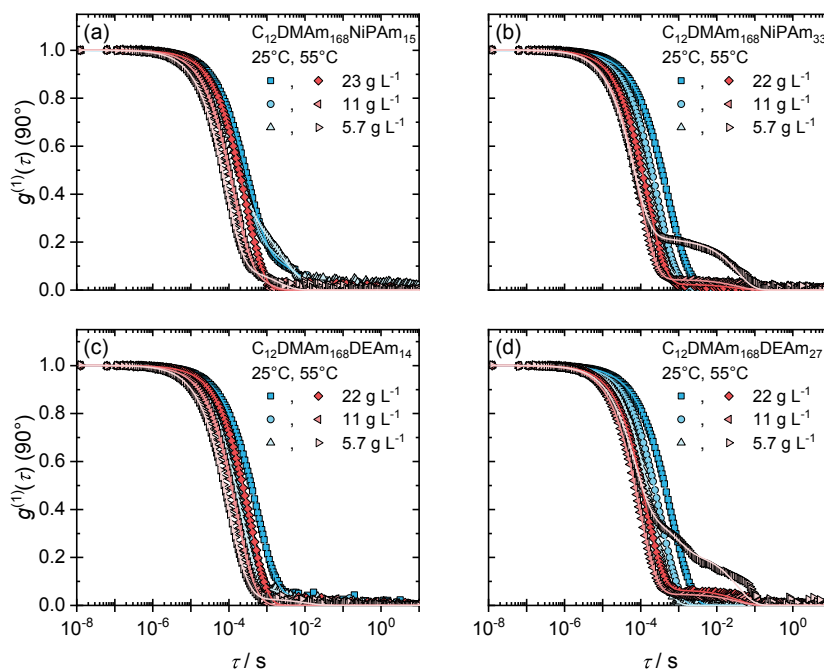
Figure A.5: Field autocorrelation function ($g^{(1)}$) data at 90° with corresponding ORT fits (solid lines) of (a) **C$_{12}$DMAm$_{168}$NiPAm$_{15}$**, (b) **C$_{12}$DMAm$_{168}$NiPAm$_{33}$**, (c) **C$_{12}$-DMAm$_{168}$DEAm$_{14}$** and (d) **C$_{12}$DMAm$_{168}$DEAm$_{27}$**. For better clarity, data are shown only for 25 °C and 55 °C.
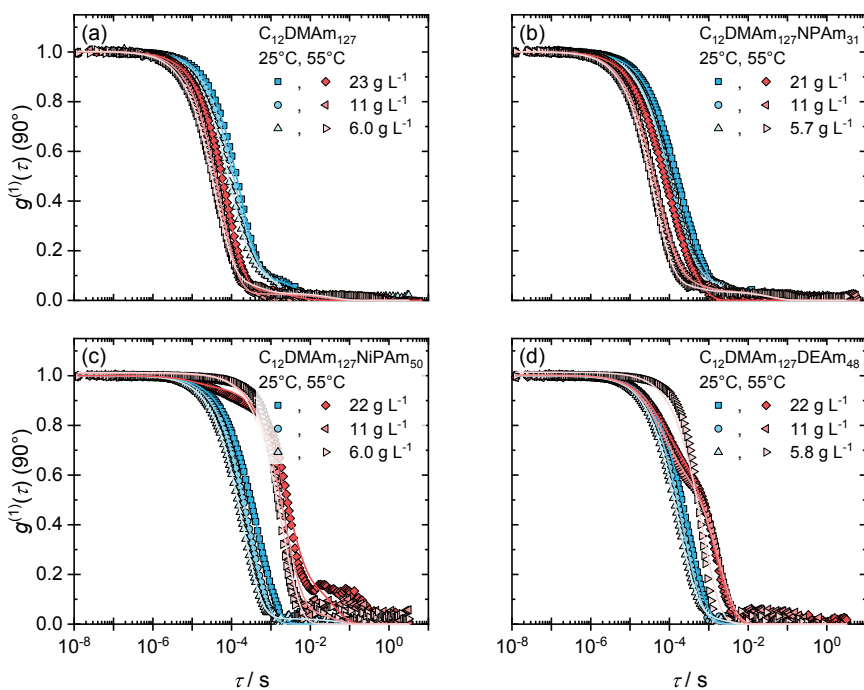
**Figure A.6:** Field autocorrelation function ($g^{(1)}$) data at 90° with corresponding ORT fits (solid lines) of (a) **$C_{12}DMAm_{127}$**, (b) **$C_{12}DMAm_{127}NPAm_{31}$**, (c) **$C_{12}DMAm_{127}$-NiPAm$_{50}$** and (d) **$C_{12}DMAm_{127}DEAm_{48}$**. For better clarity, data are shown only for 25 °C and 55 °C.
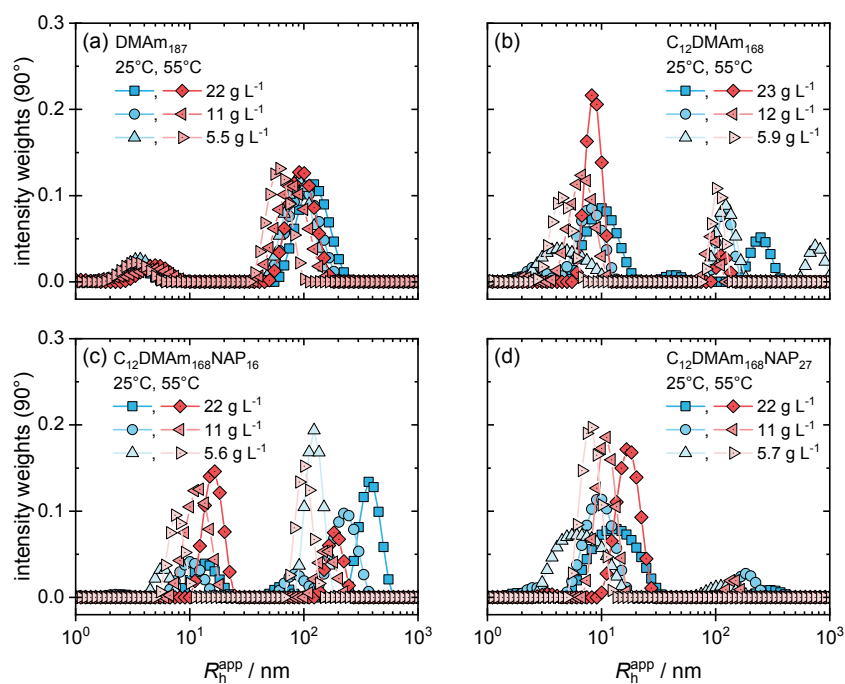
Figure A.7: Intensity weights of the size distributions of (a) **DMAm$_{187}$**, (b) **C$_{12}$-DMAm$_{168}$**, (c) **C$_{12}$DMAm$_{168}$NAP$_{16}$** and (d) **C$_{12}$DMAm$_{168}$NAP$_{27}$** at 25 °C and 55 °C represented as weights of the underlying ORT analysis. The weights were used for better presentability.
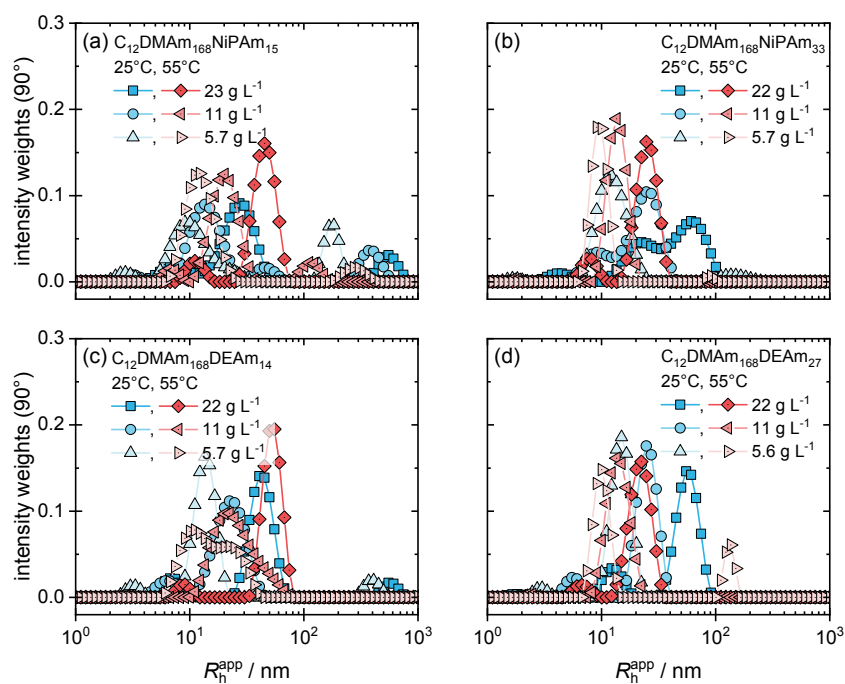
Figure A.8: Intensity weights of the size distributions of (a) $\mathbf{C_{12}DMAm_{168}NiPAm_{15}}$, (b) $\mathbf{C_{12}DMAm_{168}NiPAm_{33}}$, (c) $\mathbf{C_{12}DMAm_{168}DEAm_{14}}$ and (d) $\mathbf{C_{12}DMAm_{168}}$-$\mathbf{DEAm_{27}}$ at $25\,°C$ and $55\,°C$ represented as weights of the underlying ORT analysis. The weights were used for better presentability.
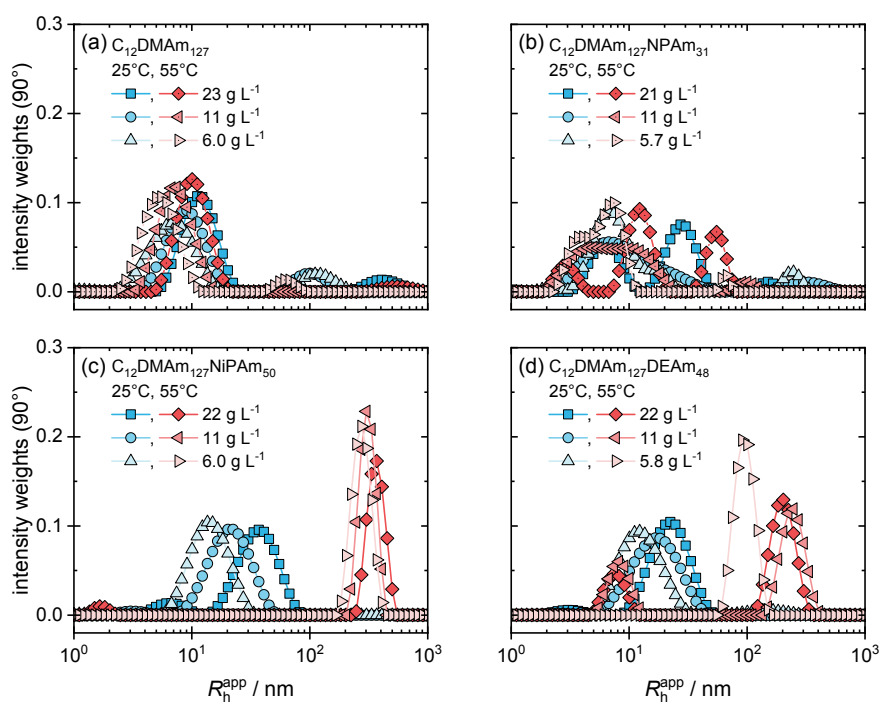
Figure A.9: Intensity weights of the size distributions of (a) **C$_{12}$DMAm$_{127}$**, (b) **C$_{12}$-DMAm$_{127}$NPAm$_{31}$**, (c) **C$_{12}$DMAm$_{127}$NiPAm$_{50}$** and (d) **C$_{12}$DMAm$_{127}$DEAm$_{48}$** at 25 °C and 55 °C represented as weights of the underlying ORT analysis. The weights were used for better presentability.

A.2 Small-Angle Neutron Scattering Studies
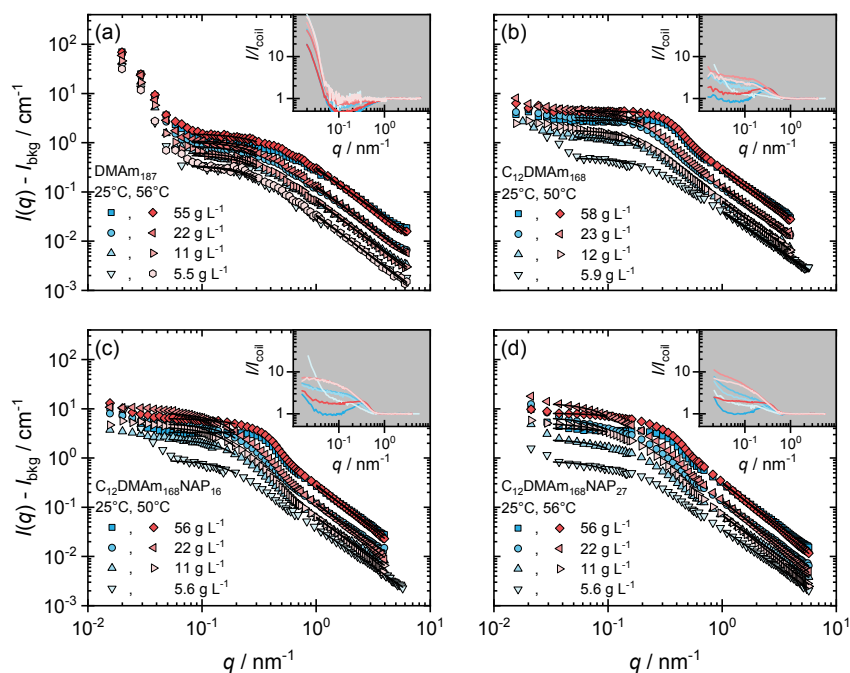
Figure A.10: SANS data of (a) **DMAm$_{187}$**, (b) **C$_{12}$DMAm$_{168}$**, (c) **C$_{12}$DMAm$_{168}$-NAP$_{16}$** and (d) **C$_{12}$DMAm$_{168}$NAP$_{27}$**. The black solid lines represent the Guinier fit (low q) and the fit of the polymer coil model with excluded volume effects (high q). The insets show the scattering intensity normalized to the polymer coil intensity (I/I_{coil}). For better clarity, only half of the data points are shown.
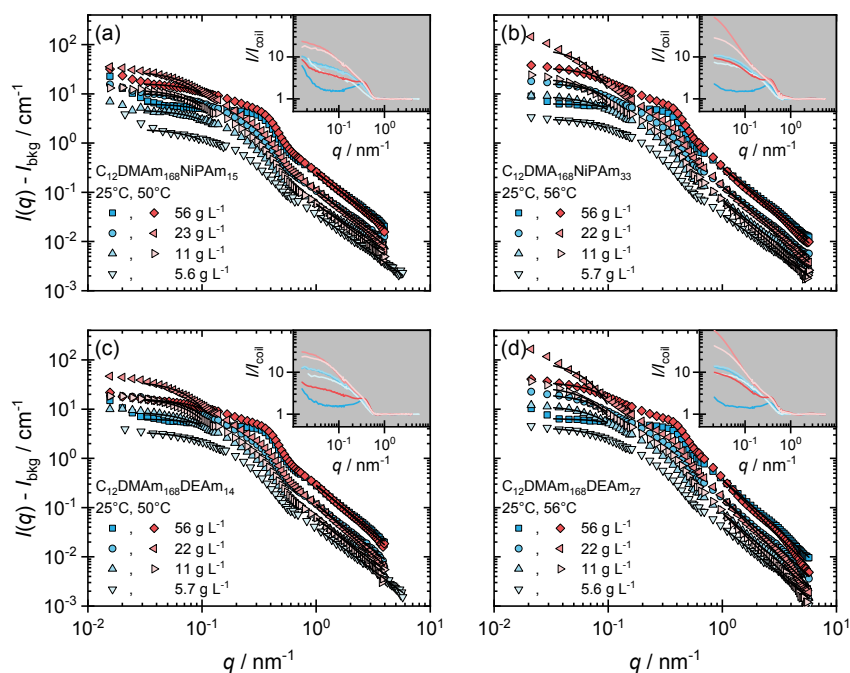
Figure A.11: SANS data of (a) **C$_{12}$DMAm$_{168}$NiPAm$_{15}$**, (b) **C$_{12}$DMAm$_{168}$-NiPAm$_{33}$**, (c) **C$_{12}$DMAm$_{168}$DEAm$_{14}$** and (d) **C$_{12}$DMAm$_{168}$DEAm$_{27}$**. The black solid lines represent the Guinier fit (low q) and the fit of the polymer coil model with excluded volume effects (high q). The insets show the scattering intensity normalized to the polymer coil intensity (I/I_{coil}). For better clarity, only half of the data points are shown.
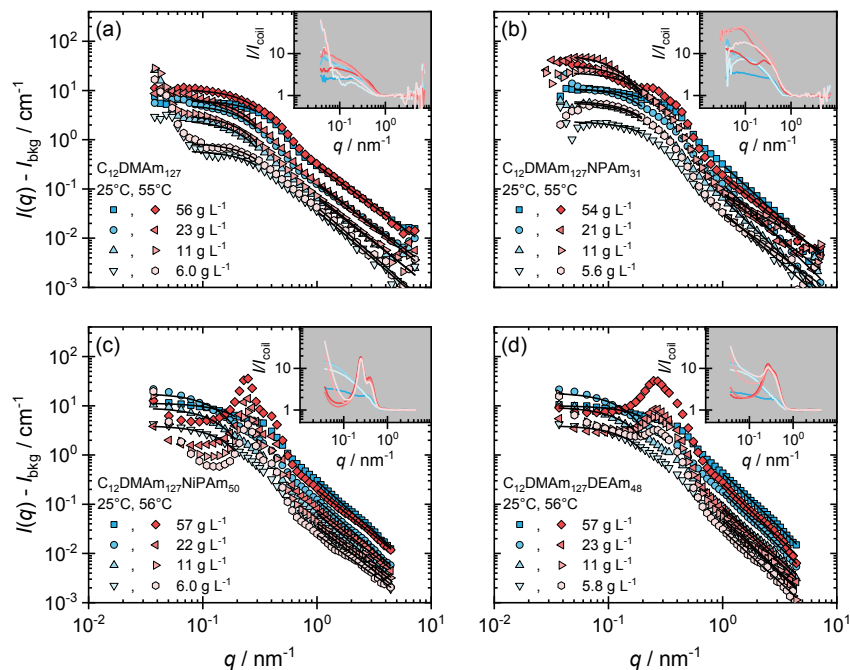
Figure A.12: SANS data of (a) $\mathbf{C_{12}DMAm_{127}}$, (b) $\mathbf{C_{12}DMAm_{127}NPAm_{31}}$, (c) $\mathbf{C_{12}}$-$\mathbf{DMAm_{127}NiPAm_{50}}$ and (d) $\mathbf{C_{12}DMAm_{127}DEAm_{48}}$. The black solid lines represent the Guinier fit (low q) and the fit of the polymer coil model with excluded volume effects (high q). The insets show the scattering intensity normalized to the polymer coil intensity (I/I_{coil}). For better clarity, only half of the data points are shown.
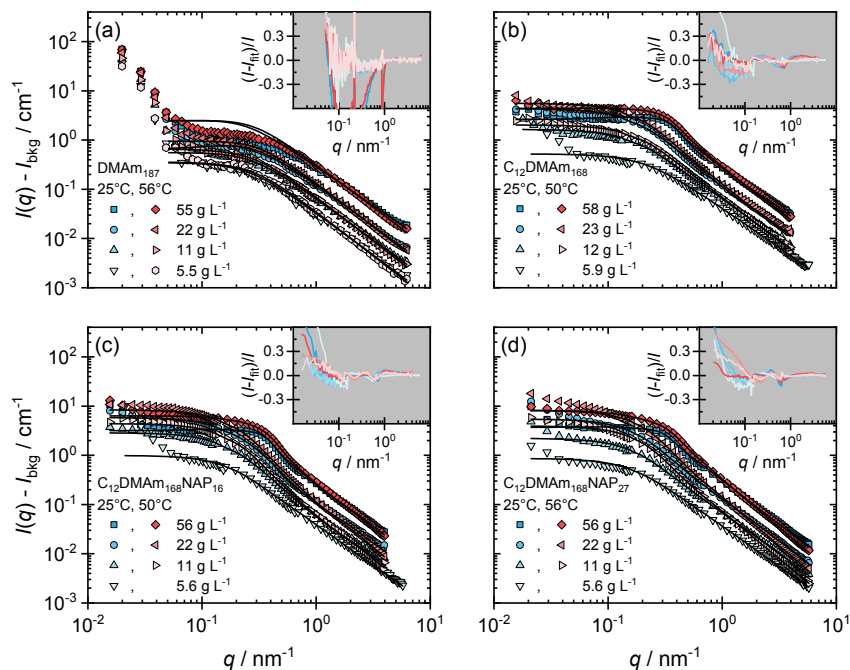
Figure A.13: SANS model fits of (a) $\mathbf{DMAm_{187}}$, (b) $\mathbf{C_{12}DMAm_{168}}$, (c) $\mathbf{C_{12}}$-$\mathbf{DMAm_{168}NAP_{16}}$ and (d) $\mathbf{C_{12}DMAm_{168}NAP_{27}}$. The solid black lines represent the best fits. The insets show the normalized fit residuals, $(I - I_{\mathrm{fit}})/I$.
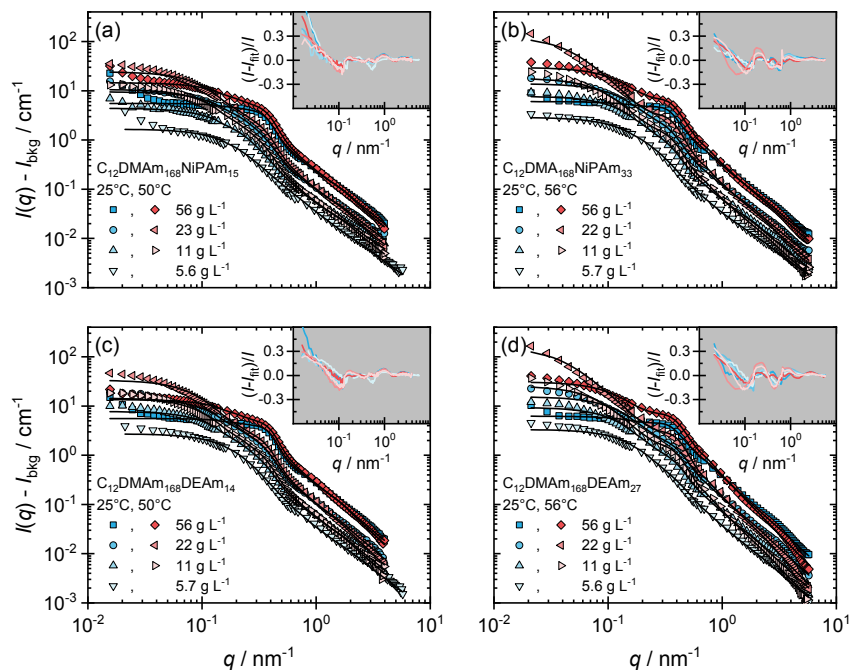
Figure A.14: SANS model fits of (a) **C$_{12}$DMAm$_{168}$NiPAm$_{15}$**, (b) **C$_{12}$DMAm$_{168}$-NiPAm$_{33}$**, (c) **C$_{12}$DMAm$_{168}$DEAm$_{14}$** and (d) **C$_{12}$DMAm$_{168}$DEAm$_{27}$**. The solid black lines represent the best fits. The insets show the normalized fit residuals, $(I - I_{\text{fit}})/I$.
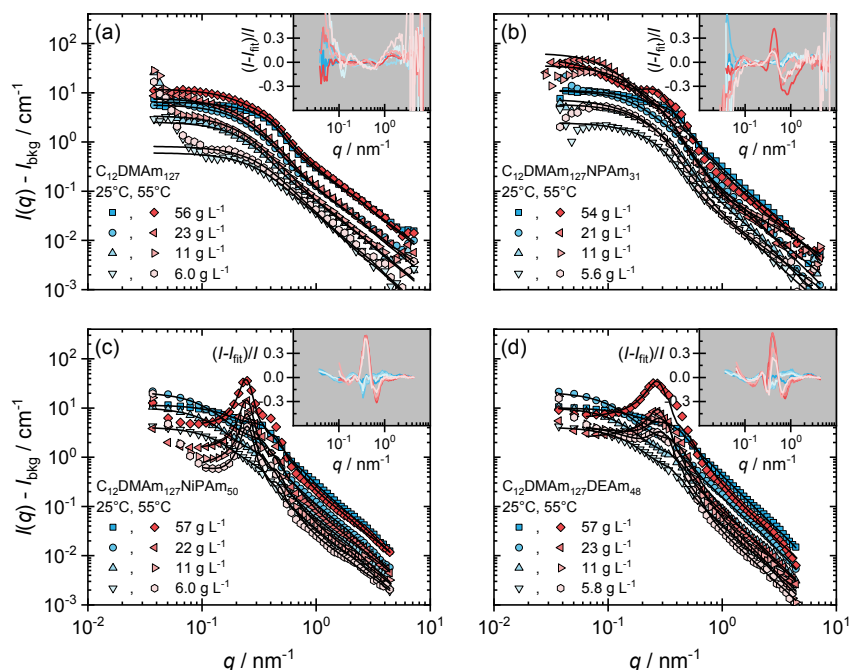
Figure A.15: SANS model fits of (a) **C$_{12}$DMAm$_{127}$**, (b) **C$_{12}$DMAm$_{127}$NPAm$_{31}$**, (c) **C$_{12}$DMAm$_{127}$NiPAm$_{50}$** and (d) **C$_{12}$DMAm$_{127}$DEAm$_{48}$**. The solid black lines represent the best fits. The insets show the normalized fit residuals, $(I - I_{\text{fit}})/I$.

Appendix B

Rheological Control of Aqueous Dispersions by Thermoresponsive Block Copolymers of Different Architectures

B.1 Phase Behavior
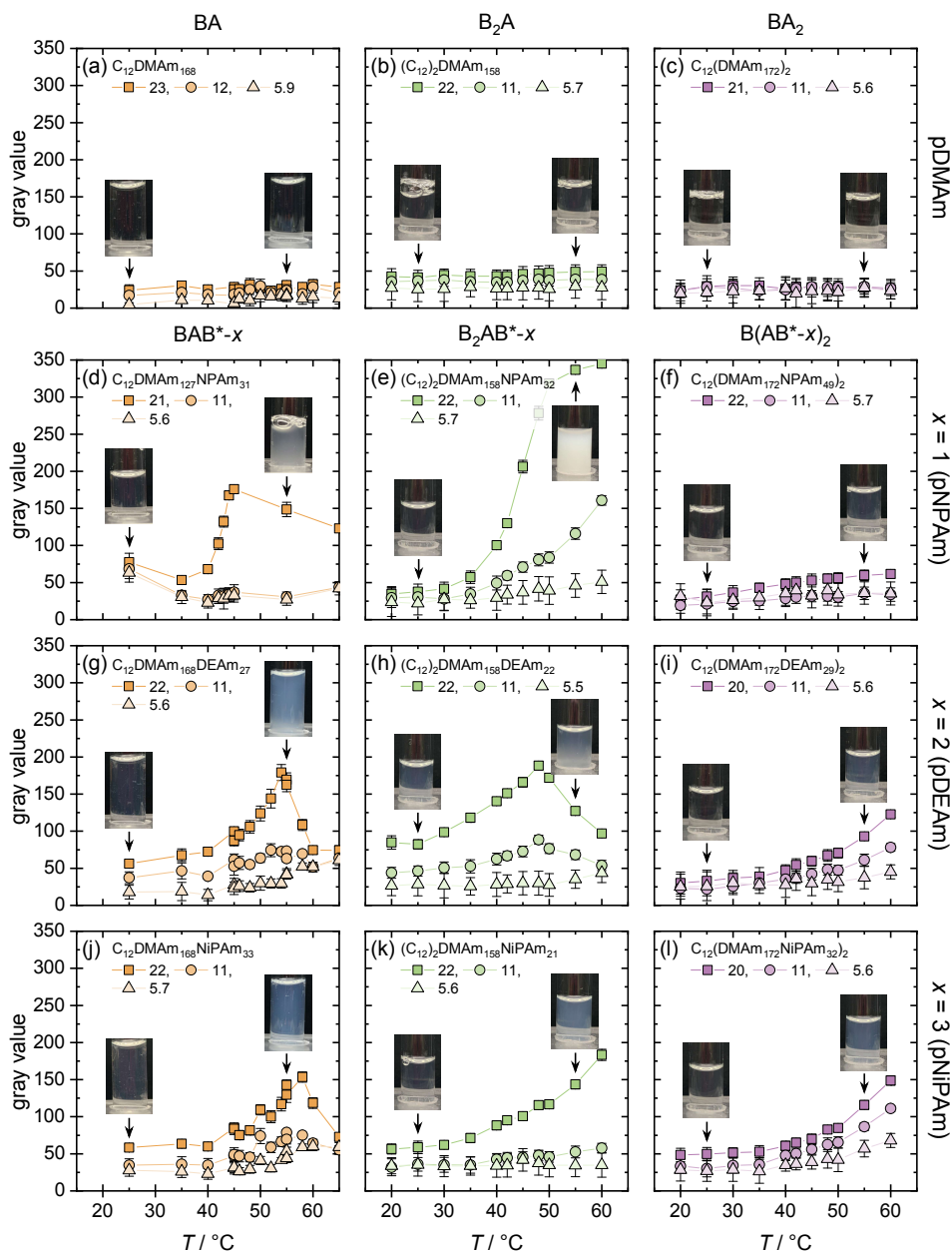
Figure B.1: Gray values based on the visual analysis of photographs of (a) **BA**, (b) **B₂A**, (c) **BA₂**, (d) **BAB*-1**, (e) **B₂AB*-1**, (f) **B(AB*-1)₂**, (g) **BAB*-2**, (h) **B₂AB*-2**, (i) **B(AB*-2)₂**, (j) **BAB*-3**, (k) **B₂AB*-3**, and (l) **B(AB*-3)₂**. The given values next to the symbols are the mass concentration in $g\,L^{-1}$.

B.2 Rheological Behavior
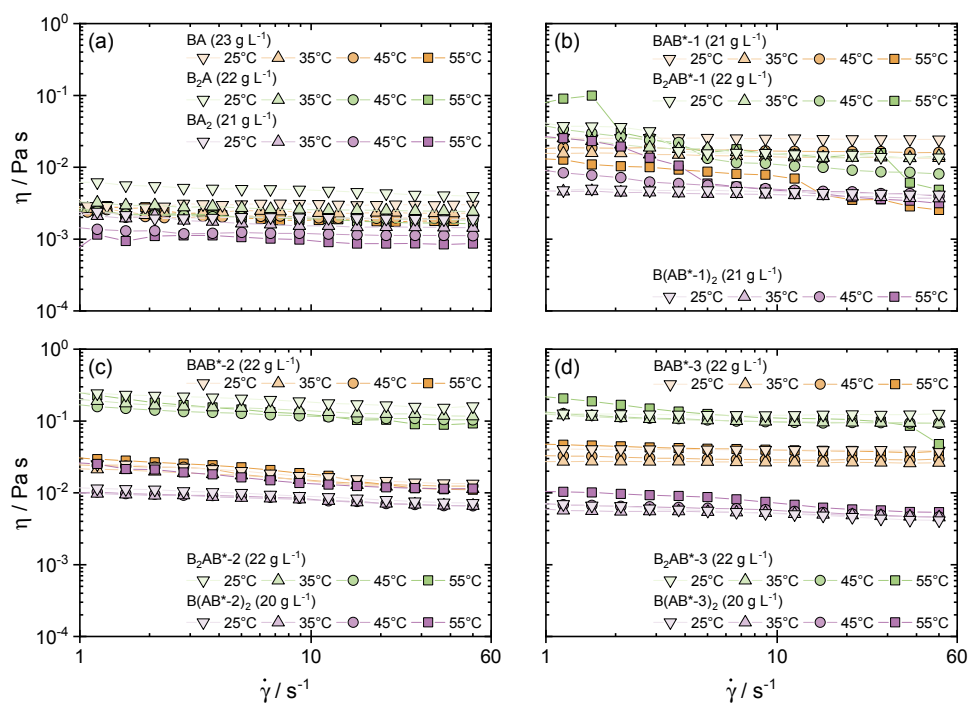
Figure B.2: Dynamic viscosity (η) as a function of the shear-rate ($\dot{\gamma}$) for the studied HMTR polymers with (a) no TR block, (b) pNPAm as TR block, (c) pDEAm as TR block, and (d) pNiPAm as TR block.
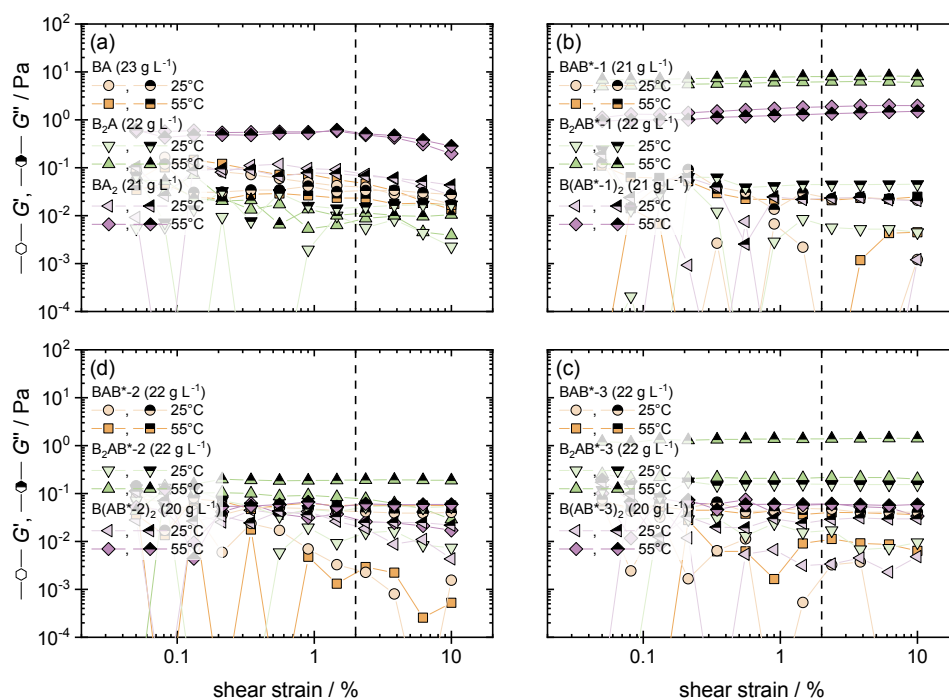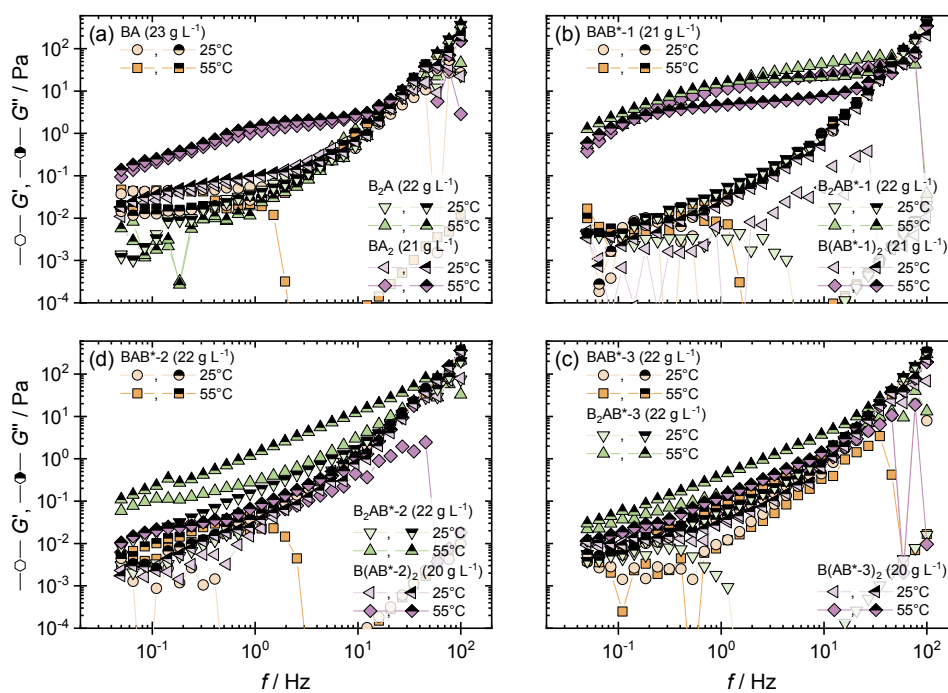
Figure B.3: Oscillatory rheology measurements of the studied HMTR polymers. Storage (G') and loss (G'') moduli displayed versus shear strain at a frequency of $1\,\mathrm{Hz}$ for polymers (a) without TR block, (b) with pNPAm as TRblock, (c) with pDEAm as TR block, and (d) with pNiPAm as TR block. The dashed black lines mark the used shear strain of $2\,\%$ for all frequency sweeps.

Reprinted with permission from Prause *et al.* (2023).[65] Copyright 2023 American Chemical Society.

Figure B.4: Oscillatory rheology measurements of the studied HMTR polymers. Storage (G') and loss (G'') moduli displayed versus frequency at a shear strain of $2\,\%$ for polymers (a) without TR block, (b) with pNPAm as TRblock, (c) with pDEAm as TR block, and (d) with pNiPAm as TR block.

Reprinted with permission from Prause *et al.* (2023).[65] Copyright 2023 American Chemical Society.
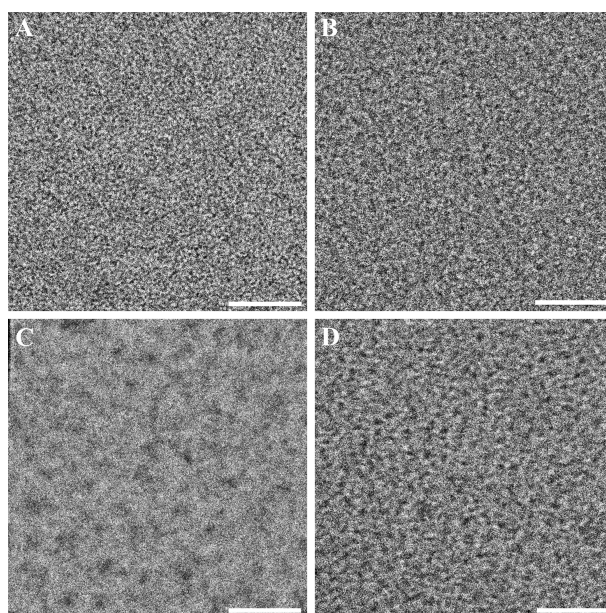
B.3 Cryogenic Transmission Electron Microscopy

Figure B.5: cryo-TEM images of **BAB*-1** at (A) 25 °C and (B) 55 °C, (C) **B$_2$AB*-1**, and (D) **B$_2$AB*-3**. Many small micellar aggregates are visible, but no size estimate was done due to the poor contrast conditions. Scale bars equal 50 nm. Picture (A), (C), and (D) were imaged using the Tecnai T12 G2 and (B) was imaged on the Talos F200C using a Volta phase plate.

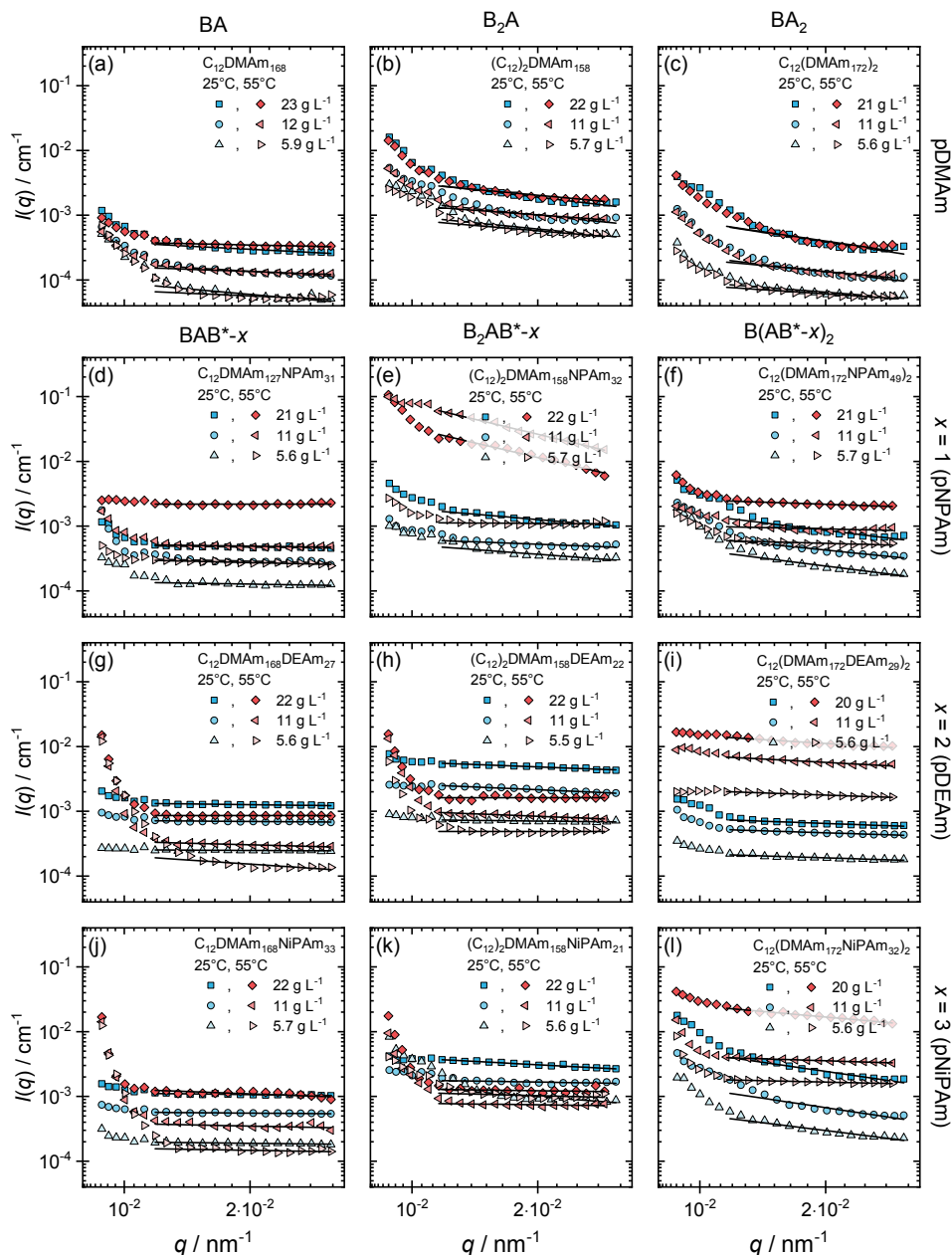# B.4 Light Scattering Studies

Figure B.6: Normalized static light scattering intensities, Rayleigh ratios, versus the magnitude of the scattering vector q shown for: (a) **BA**, (b) **B₂A**, (c) **BA₂**, (d) **BAB*-1**, (e) **B₂AB*-1**, (f) **B(AB*-1)₂**, (g) **BAB*-2**, (h) **B₂AB*-2**, (i) **B(AB*-2)₂**, (j) **BAB*-3**, (k) **B₂AB*-3**, and (l) **B(AB*-3)₂**. Here concentrations of ~5.5, 11, and 22 g L^{-1} were displayed at 25 °C and 55 °C. The solid black lines indicate the Guinier fits.
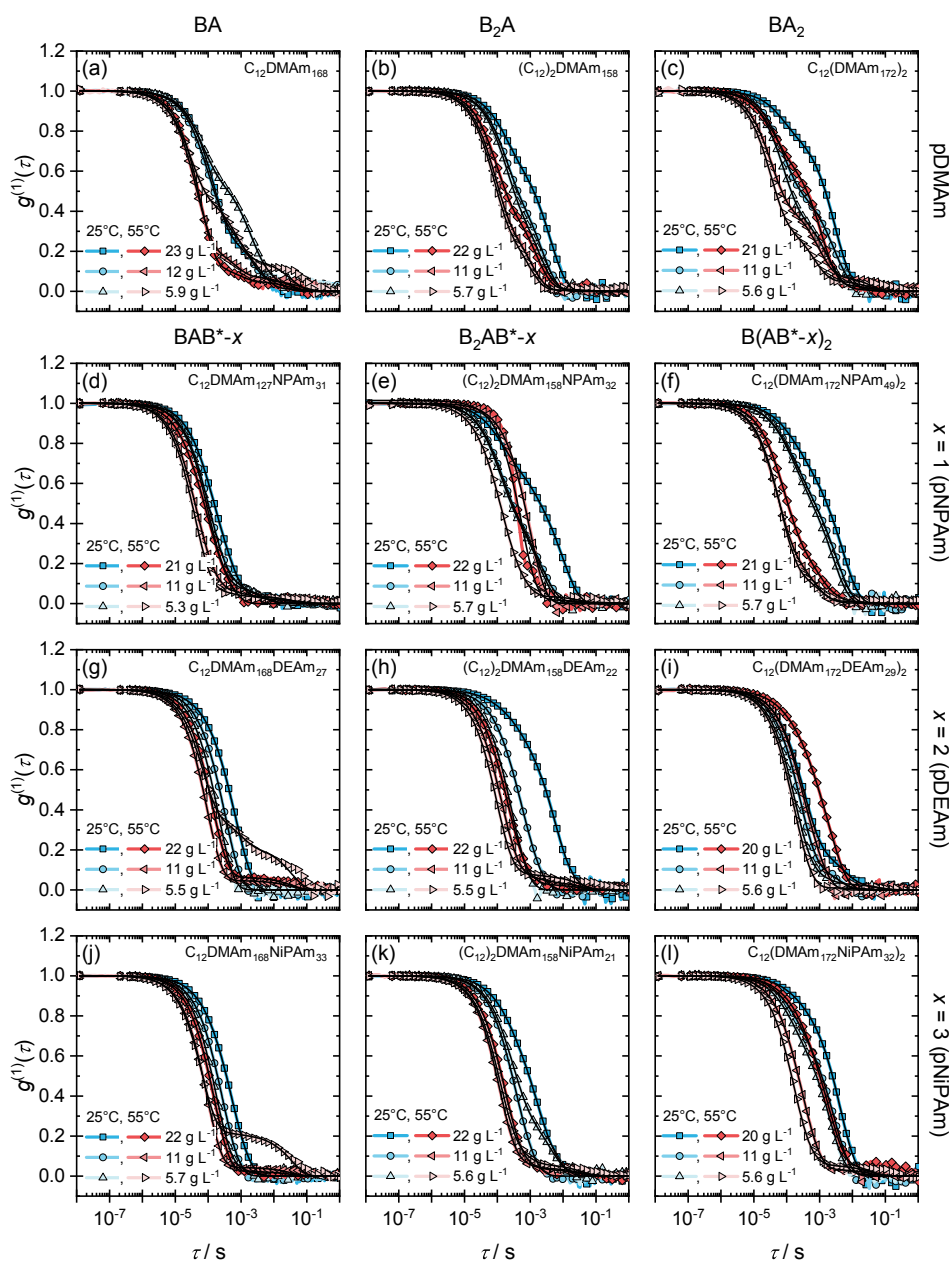
Figure B.7: Dynamic light scattering data measured at an angle of 90° shown for: (a) **BA**, (b) **B$_2$A**, (c) **BA$_2$**, (d) **BAB*-1**, (e) **B$_2$AB*-1**, (f) **B(AB*-1)$_2$**, (g) **BAB*-2**, (h) **B$_2$AB*-2**, (i) **B(AB*-2)$_2$**, (j) **BAB*-3**, (k) **B$_2$AB*-3**, and (l) **B(AB*-3)$_2$**. Here concentrations of ~5.5, 11, and 22 g L^{-1} were displayed at 25 °C and 55 °C. The solid black lines indicate the ORT fits.
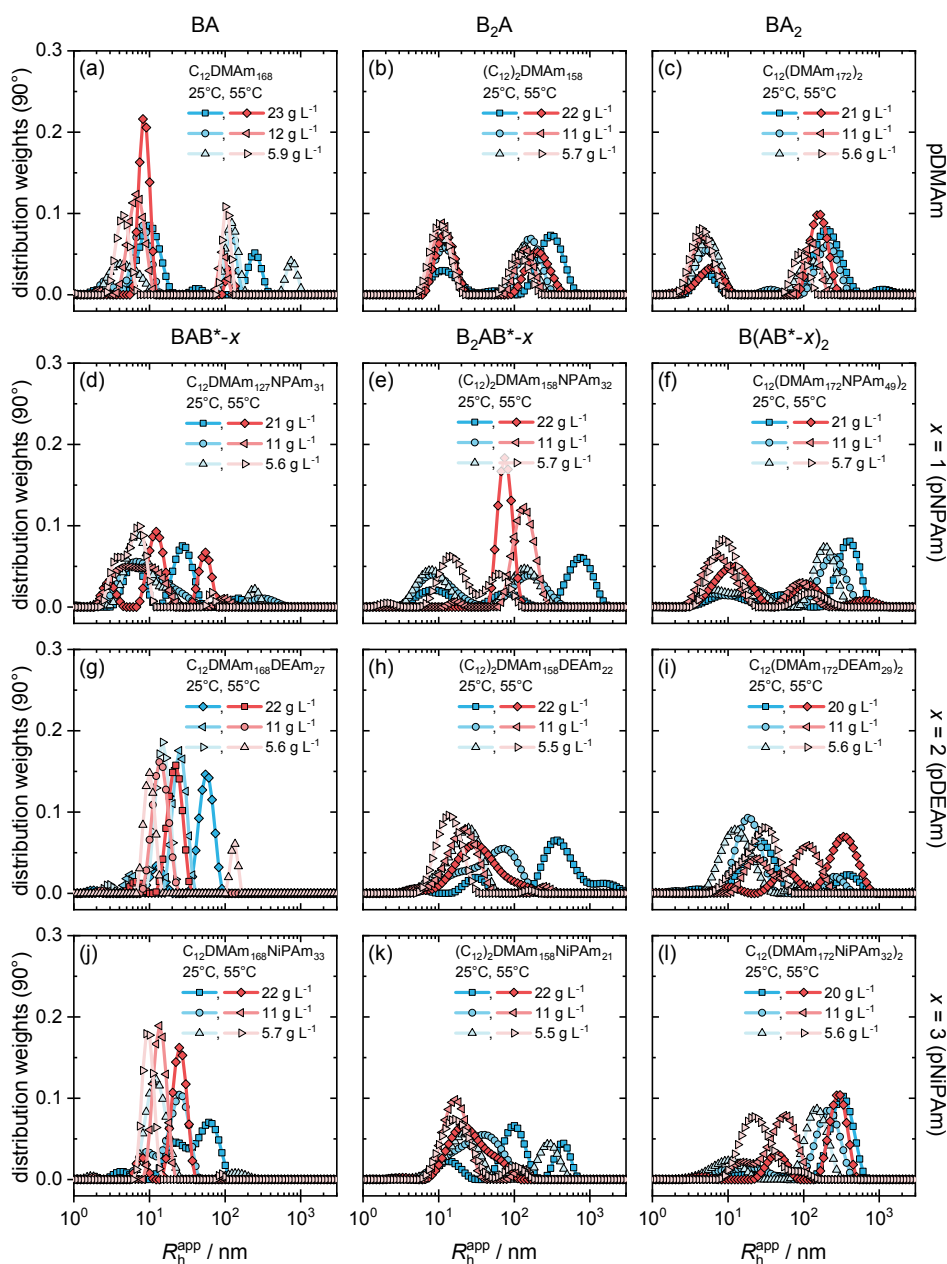
Figure B.8: ORT analysis with the obtained distribution weights at a scattering angle of 90°, shown for: (a) **BA**, (b) **B$_2$A**, (c) **BA$_2$**, (d) **BAB*-1**, (e) **B$_2$AB*-1** (sample at $22\,\mathrm{g\,L^{-1}}$ was precipitated at the highest temperature), (f) **B(AB*-1)$_2$**, (g) **BAB*-2**, (h) **B$_2$AB*-2**, (i) **B(AB*-2)$_2$**, (j) **BAB*-3**, (k) **B$_2$AB*-3**, and (l) **B(AB*-3)$_2$**. Here mass concentrations of $\sim$5.5, 11, and $22\,\mathrm{g\,L^{-1}}$ were displayed at $25\,^\circ\mathrm{C}$ and $55\,^\circ\mathrm{C}$.

B.5 Small-Angle Neutron Scattering Studies

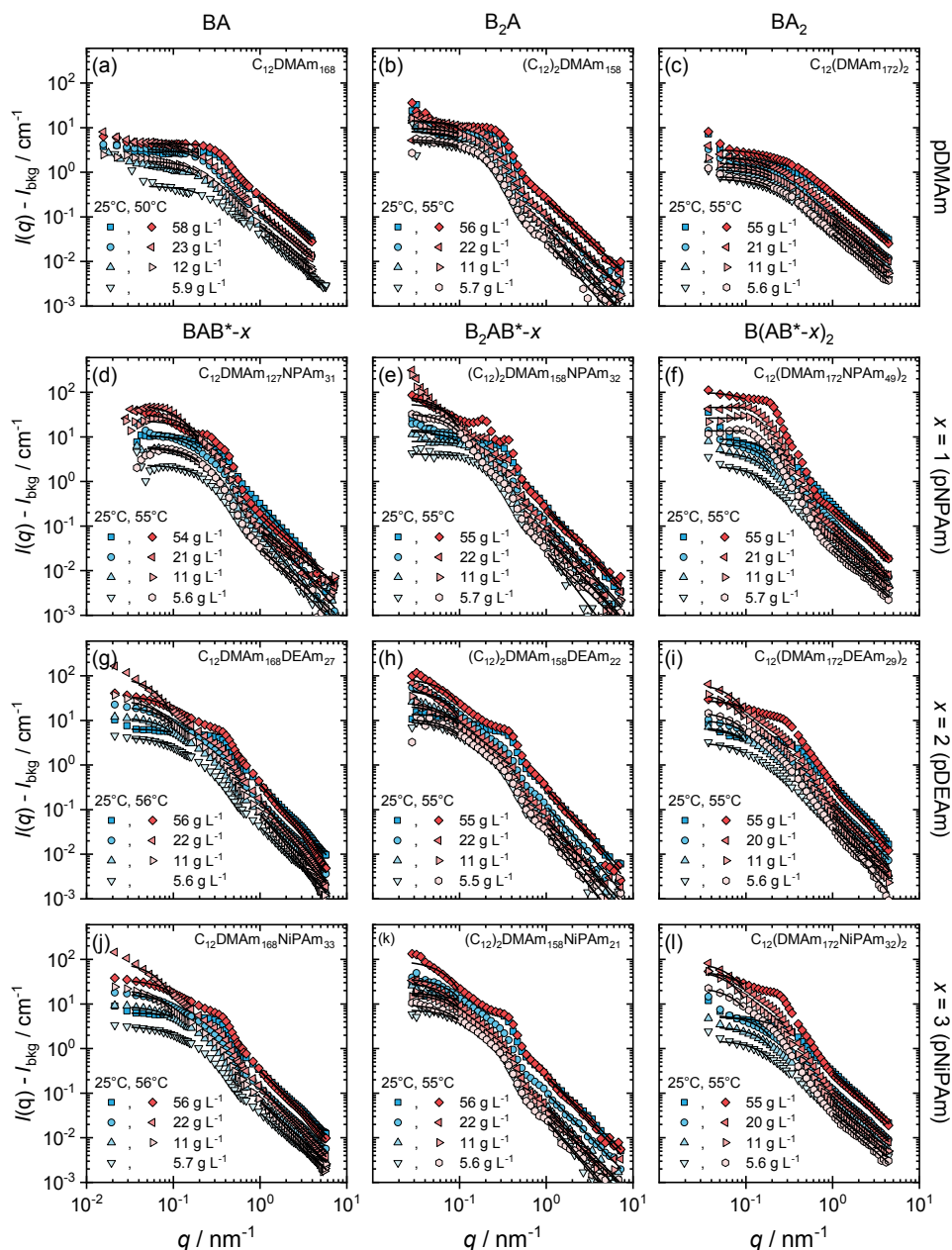**Figure B.9:** SANS data with Guinier fit (black solid line at low q) and polymer coil fit (black solid line at high q) for: (a) **BA**, (b) **B$_2$A**, (c) **BA$_2$**, (d) **BAB*-1**, (e) **B$_2$AB*-1**, (f) **B(AB*-1)$_2$**, (g) **BAB*-2**, (h) **B$_2$AB*-2**, (i) **B(AB*-2)$_2$**, (j) **BAB*-3**, (k) **B$_2$AB*-3**, and (l) **B(AB*-3)$_2$**. Here mass concentrations of ∼5.5, 11, and 22 g L^{-1} were studied at 25 °C and 55 °C.

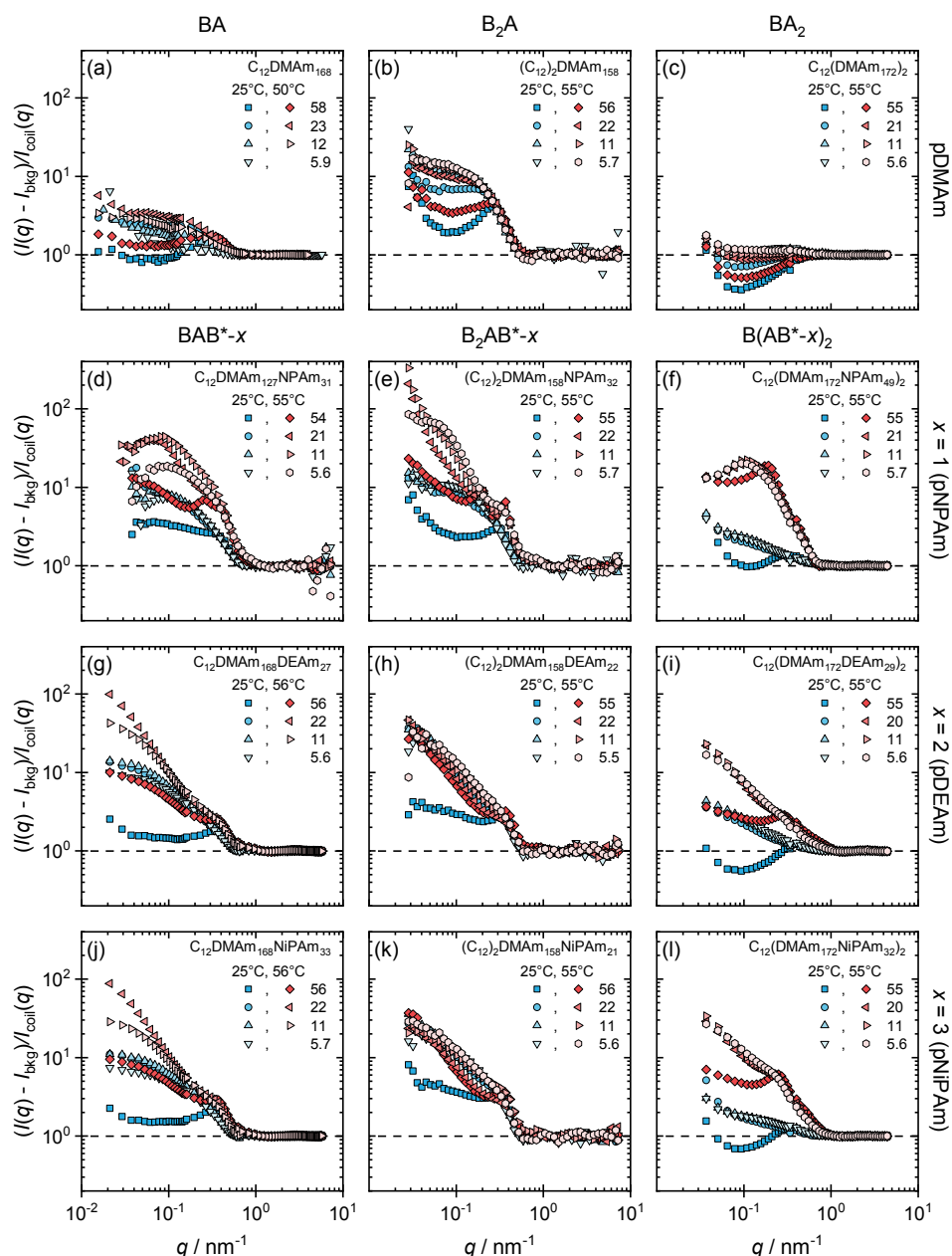**Figure B.10:** SANS intensities normalized to the corresponding scattering intensity of polymer coils $I_{coil}(q)$ (see Equation 2.14) for: (a) **BA**, (b) **B₂A**, (c) **BA₂**, (d) **BAB*-1**, (e) **B₂AB*-1**, (f) **B(AB*-1)₂**, (g) **BAB*-2**, (h) **B₂AB*-2**, (i) **B(AB*-2)₂**, (j) **BAB*-3**, (k) **B₂AB*-3**, and (l) **B(AB*-3)₂**. Here mass concentrations (given in $g\,L^{-1}$) were displayed at $25\,°C$ and $55\,°C$.

Appendix C

Modifying the Properties of Microemulsion Droplets by Addition of Thermoresponsive Block Copolymers

C.1 Rheological Behavior
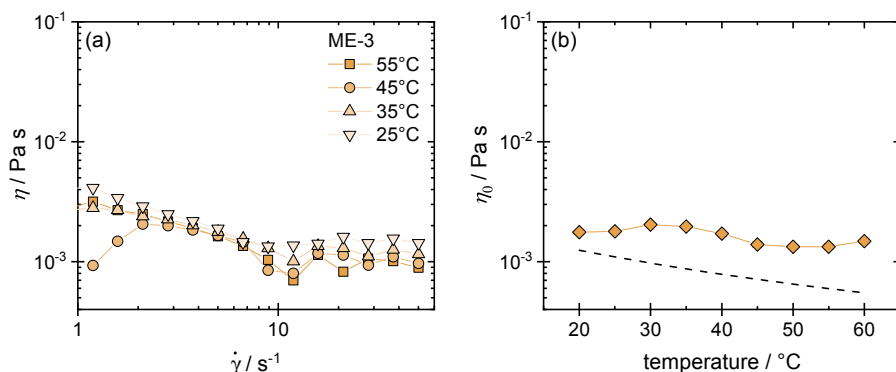
Figure C.1: (a) Exemplary shear rheology measurements of **ME-3**. (b) Zero-shear viscosity (η_0) as a function of temperature. The dashed black line indicates the viscosity of the solvent D_2O.
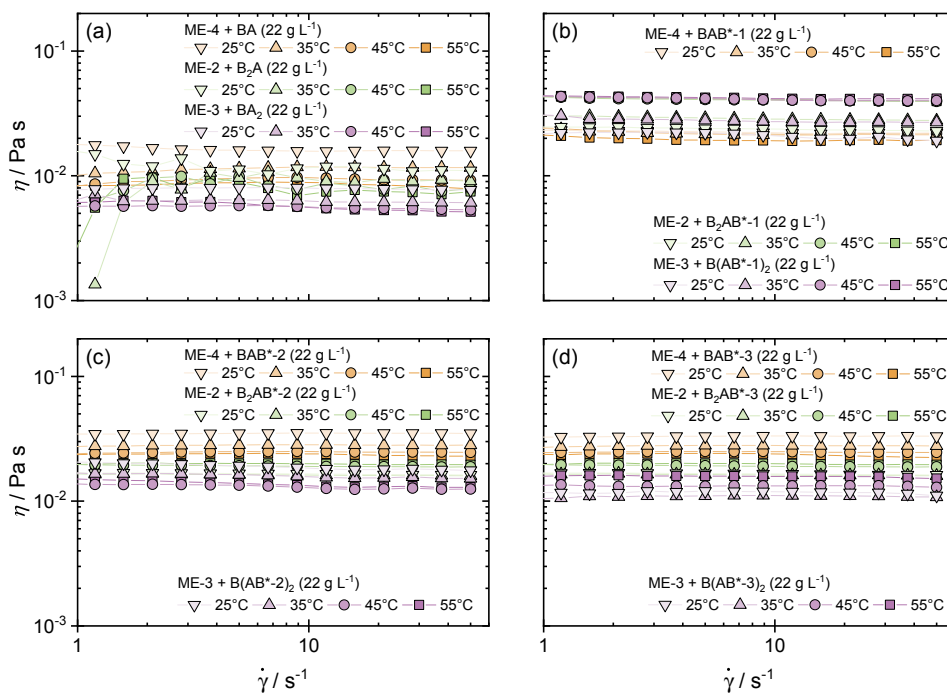
Figure C.2: Shear rheology measurements (up- and downwards measurements were averaged) of the studied ME–polymer mixtures containing polymers (a) without TR block, (b) with pNPAm, (c) with pDEAm, and (d) with pNiPAm TR block.
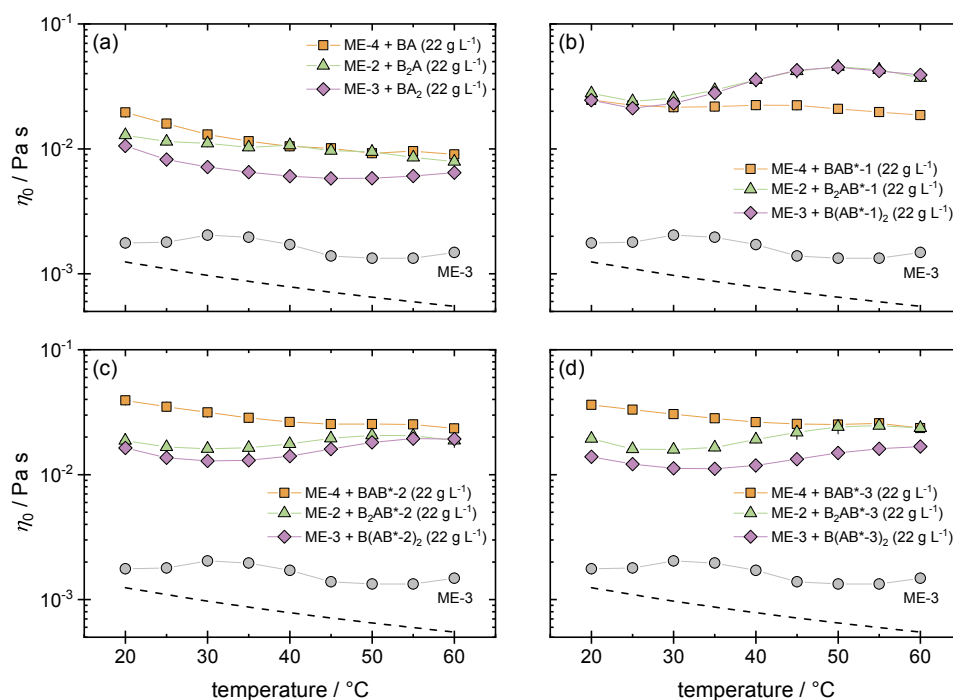
Figure C.3: Zero-shear viscosity (η_0) as a function of temperature shown of the studied ME–polymer mixtures containing polymers (a) without TR block, (b) with pNPAm, (c) with pDEAm, and (d) with pNiPAm TR block. The dashed black lines indicate the viscosity of the solvent D_2O.

C.2 Light Scattering Studies
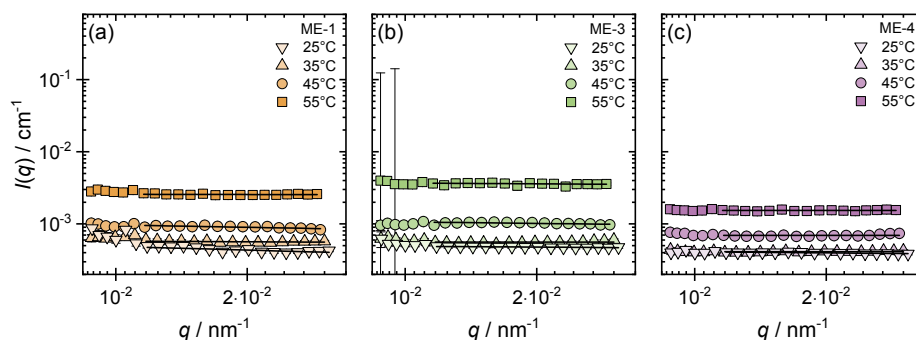
Figure C.4: Guinier plot (logarithmically scaled $I(q)$ axis *vs.* quadratically scaled q axis) of static light scattering (SLS) intensities of the microemulsion solutions (a) **ME-1**, (b) **ME-3**, and (c) **ME-4**. Data of 25, 35, 45, and 55 °C were shown. The solid black lines represent the Guinier fit.
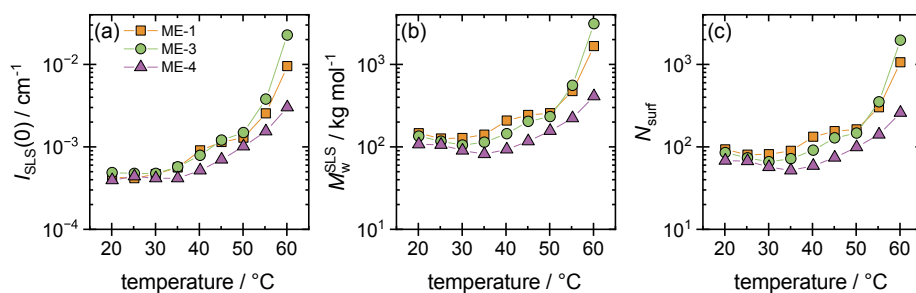
Figure C.5: (a) Forward scattering intensity, (b) mass averaged molecular weight, and (c) number of surfactants molecules per droplet as a function of temperature for the used microemulsions. The values for **ME-1** and **ME-3** are higher compared to the SANS data, which can be attributed to dust in the samples. The values for **ME-4** coincide with the SANS data of the similar **ME-3**.
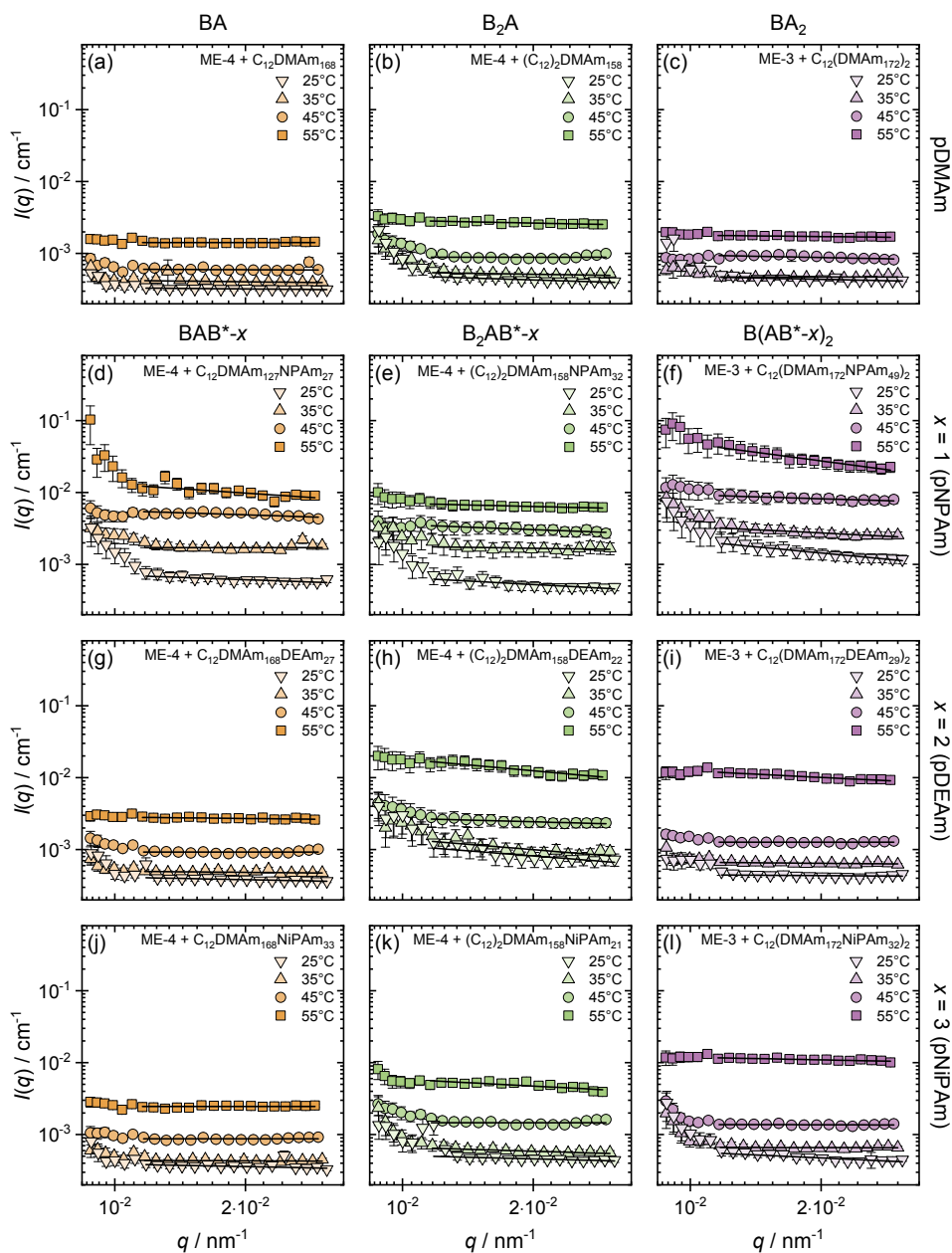
Figure C.6: Guinier plot (logarithmically scaled $I(q)$ axis *vs.* quadratically scaled q axis) of static light scattering (SLS) intensities of ME–polymer mixtures for polymers: (a) **BA**, (b) **B$_2$A**, (c) **BA$_2$**, (d) **BAB*-1**, (e) **B$_2$AB*-1**, (f) **B(AB*-1)$_2$**, (g) **BAB*-2**, (h) **B$_2$AB*-2**, (i) **B(AB*-2)$_2$**, (j) **BAB*-3**, (k) **B$_2$AB*-3**, and (l) **B(AB*-3)$_2$**. Data were shown for temperatures of 25, 35, 45, and 55 °C. The solid black lines represent the Guinier fit.
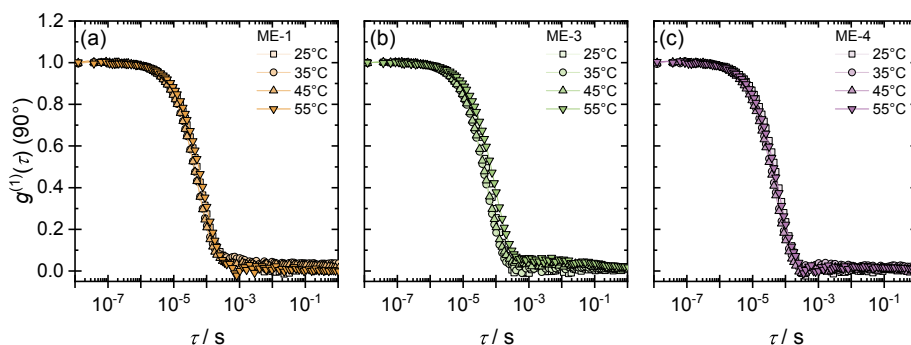
Figure C.7: Field autocorrelation curves of microemulsions at 90° for selected temperatures of 25, 35, 45, and 55 °C for microemulsions (a) **ME-1**, (b) **ME-3**, and (c) **ME-4**.
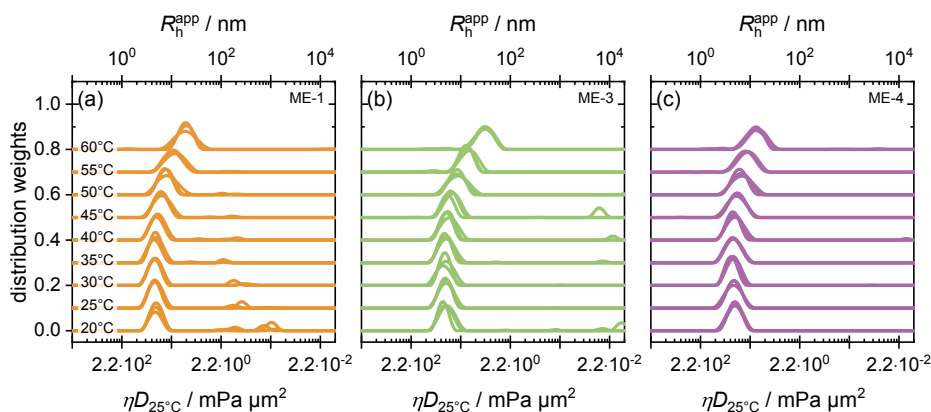
Figure C.8: Size distribution of microemulsions (a) **ME-1**, (b) **ME-3**, and (c) **ME-4** for temperatures between 20 and 60 °C. The size distribution of three angles (60, 90, and 120°) are superimposed to illustrate the angle-dependency. For a diffusive angle-dependency, the distributions should nicely overlap.

Figure C.9: Field autocorrelation curves of ME–polymer mixtures at 90° for polymers: (a) **BA**, (b) **B₂A**, (c) **BA₂**, (d) **BAB*-1**, (e) **B₂AB*-1**, (f) **B(AB*-1)₂**, (g) **BAB*-2**, (h) **B₂AB*-2**, (i) **B(AB*-2)₂**, (j) **BAB*-3**, (k) **B₂AB*-3**, and (l) **B(AB*-3)₂**. Data were shown for temperatures of 25, 35, 45, and 55 °C.
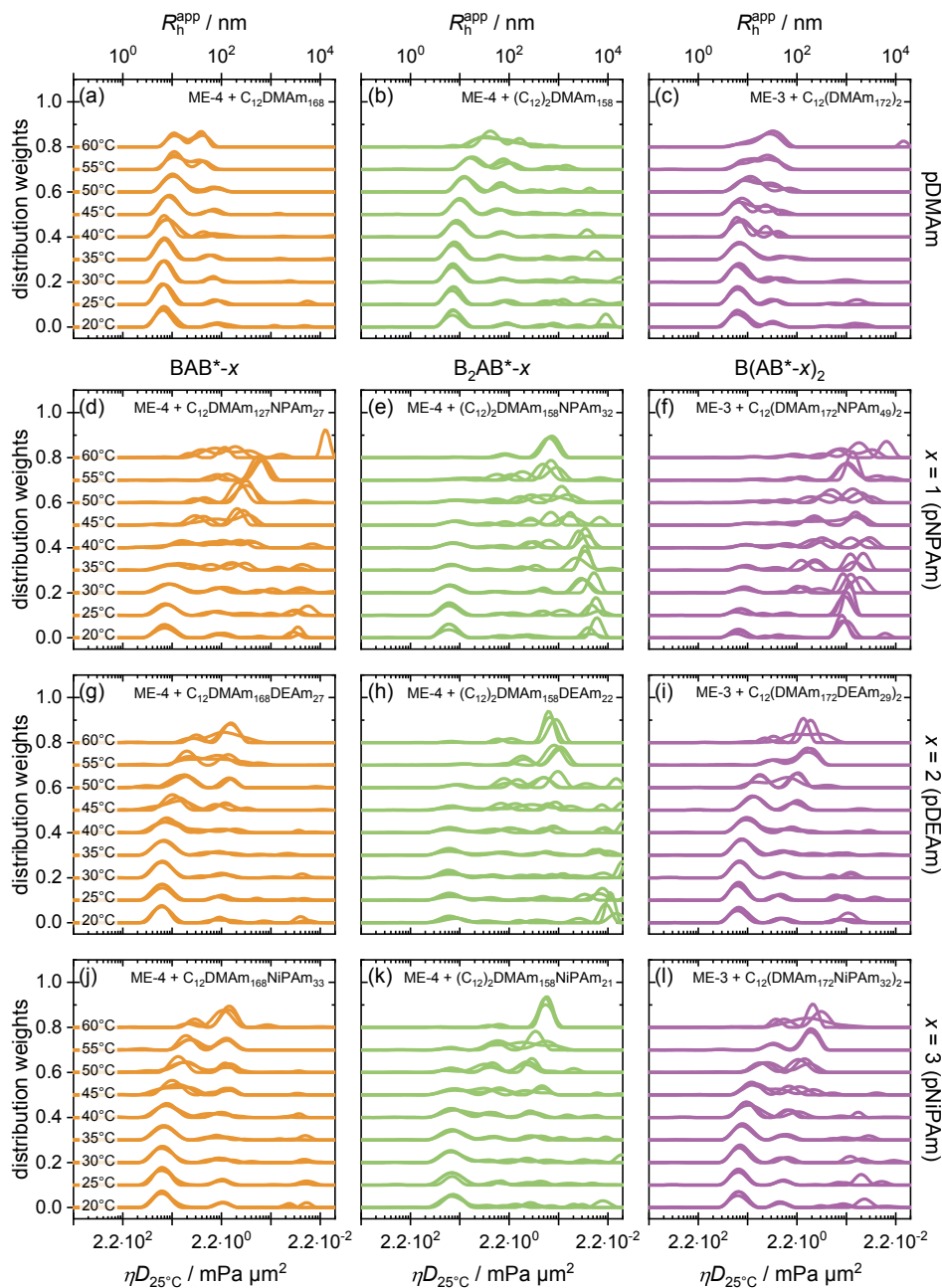
Figure C.10: Size distribution for temperatures between 20 and 60 °C of ME–polymer mixtures for polymers (a) **BA**, (b) **B₂A**, (c) **BA₂**, (d) **BAB*-1**, (e) **B₂AB*-1**, (f) **B(AB*-1)₂**, (g) **BAB*-2**, (h) **B₂AB*-2**, (i) **B(AB*-2)₂**, (j) **BAB*-3**, (k) **B₂AB*-3**, and (l) **B(AB*-3)₂**. The size distribution of three angles (60, 90, and 120°) are superimposed to illustrate the angle-dependency. For a diffusive angle-dependency, the distributions should nicely overlap.

Reprinted with permission from Prause *et al.* (2023).[133] Copyright 2023 American Chemical Society.

C.3 Small-Angle Neutron Scattering Studies
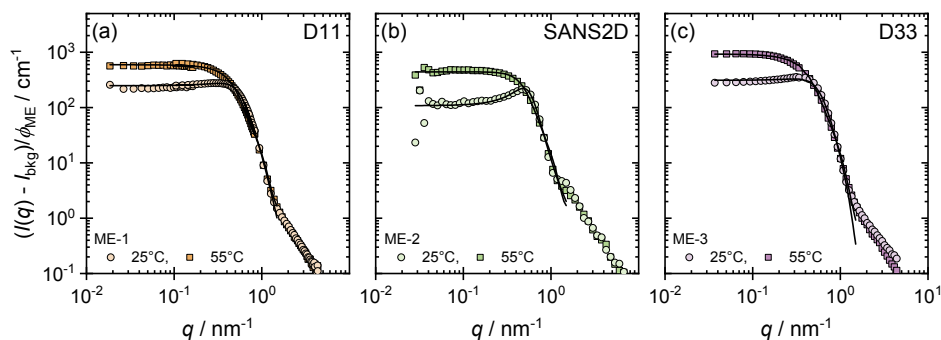
Figure C.11: SANS data of pure microemulsions normalized to the volume fraction of microemulsion for (a) **ME-1**, (b) **ME-2**, and (c) **ME-3** displayed for 25 °C and 55 °C. The solid black lines represent the fits (q range for fits up to $1.5\,\mathrm{nm}^{-1}$) of the ellipsoidal core-shell model.
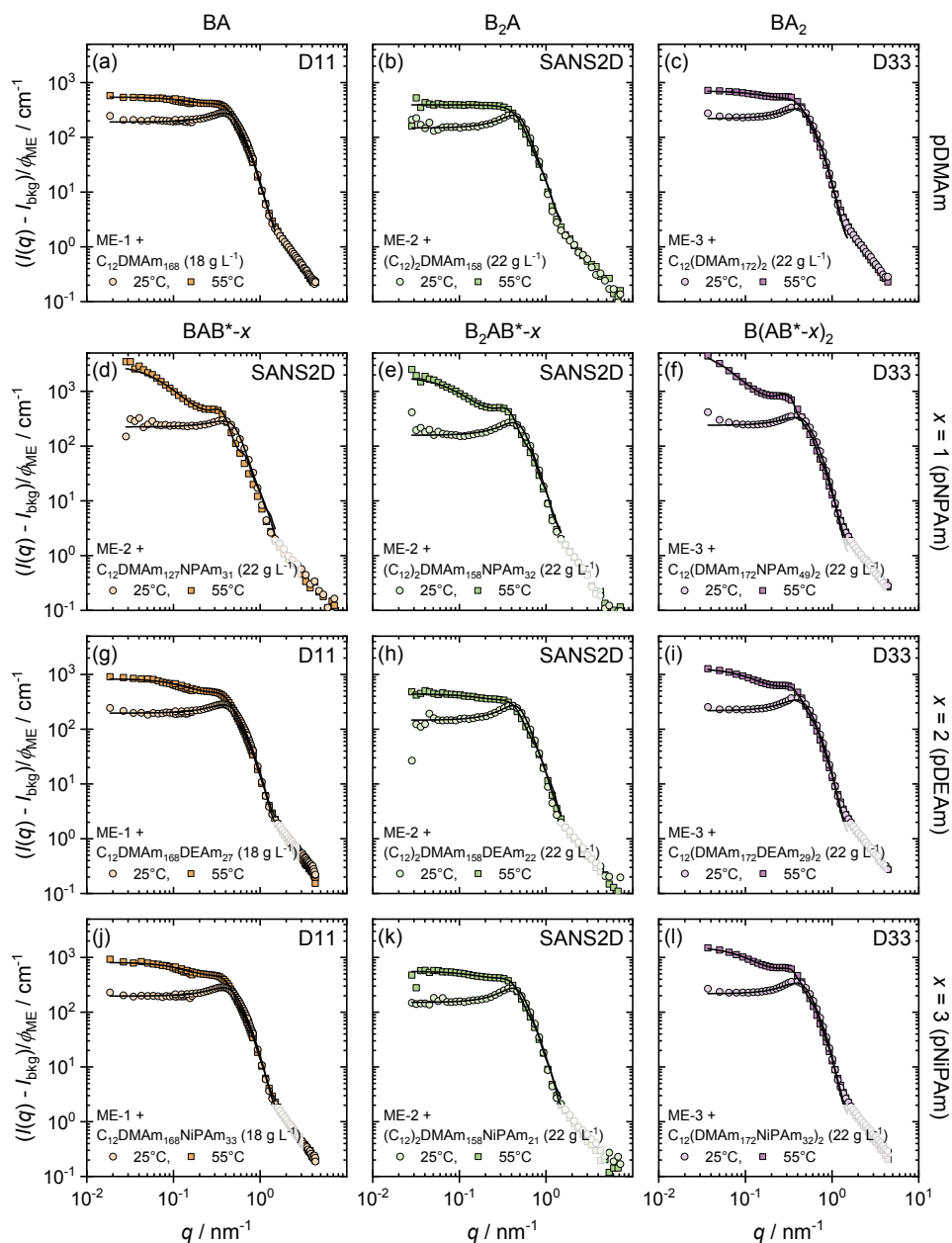
Figure C.12: SANS data with fits of ME–polymer mixtures at $25\,^{\circ}\mathrm{C}$ and $55\,^{\circ}\mathrm{C}$ containing polymers: (a) **BA**, (b) **B$_2$A**, (c) **BA$_2$**, (d) **BAB*-1**, (e) **B$_2$AB*-1**, (f) **B(AB*-1)$_2$**, (g) **BAB*-2**, (h) **B$_2$AB*-2**, (i) **B(AB*-2)$_2$**, (j) **BAB*-3**, (k) **B$_2$AB*-3**, and (l) **B(AB*-3)$_2$**. The scattering intensity is normalized to the volume fraction of the microemulsion. The solid black lines represent the fits (q range for fits up to $1.5\,\mathrm{nm}^{-1}$) of the ellipsoidal core-shell model.
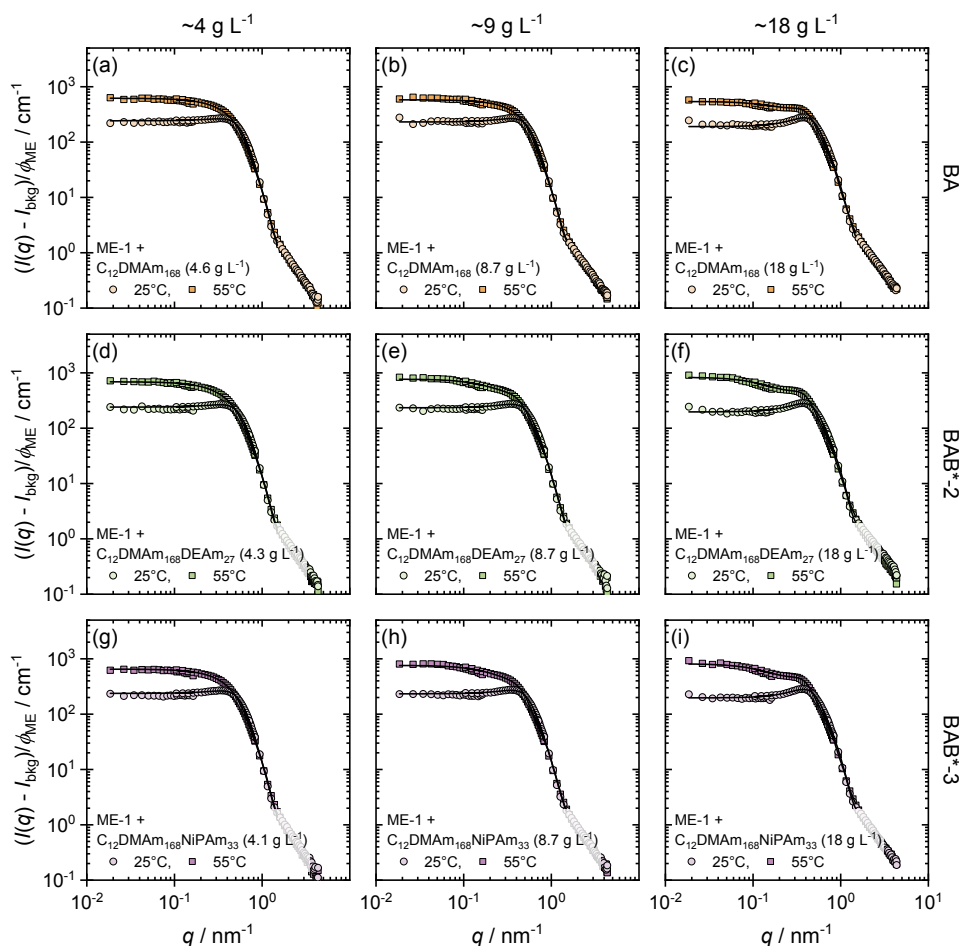
Figure C.13: SANS data with fits for **ME-1**–BAB* mixtures containing different polymer concentrations at a microemulsion concentration of $41\,\mathrm{mmol\,L^{-1}}$ (given as surfactant concentration) at $25\,^\circ$C and $55\,^\circ$C. (a–c) **ME-1 + BA**, (d–f) **ME-1 + BAB*-2**, and (g–i) **ME-1 + BAB*-3**. The scattering intensity is normalized to the volume fraction of the microemulsion. The solid black lines represent the fits (q range for fits up to $1.5\,\mathrm{nm^{-1}}$) of the ellipsoidal core-shell model. Data measured at D11.
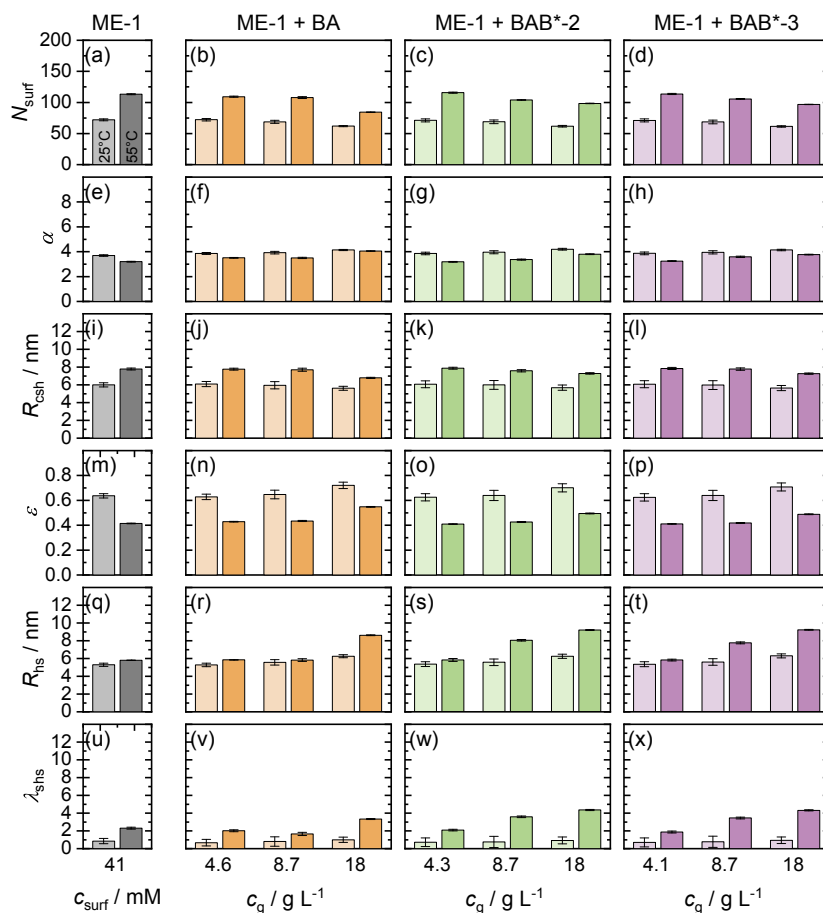
Figure C.14: Best-fit parameters of the ellipsoidal core-shell form factor for **ME-1**–BAB* mixtures with different polymer concentrations at a microemulsion concentration of $41\,\mathrm{mmol\,L^{-1}}$ (given as surfactant concentration) at $25\,^\circ\mathrm{C}$ and $55\,^\circ\mathrm{C}$. (a–d) The number of surfactant molecules per microemulsion droplet (N_{surf}), (e–h) swelling ratio (α) of the ME droplet shell, *i. e.*, swelling of the Tween20 head group, (i–l) equatorial core-shell radius of the ME droplets, (m–p) aspect ratio (ε, < 1: oblate, 1: sphere, > 1: prolate) of the ME droplets, (q–t) hard-sphere radius (R_{hs}), and (u–x) attraction strength (λ_{shs}, 0: purely repulsive, > 0: increasing attraction) of the hard-spheres.

Figure C.15: SANS data with fits for **ME-2**–B_2AB^* mixtures with different microemulsion concentrations (25, 50, and $100 \, \text{mmol} \, \text{L}^{-1}$; given as surfactant concentration) at a polymer concentration of $22 \, \text{g} \, \text{L}^{-1}$ at $25 \, ^\circ\text{C}$ and $55 \, ^\circ\text{C}$. (a–c) **ME-2**, (d–f) **ME-2 + B_2A**, (g–i) **ME-2 + B_2AB^*-1**, (j–l) **ME-2 + B_2AB^*-2**, and (m–p) **ME-2 + B_2AB^*-3**. The scattering intensity is normalized to the volume fraction of the microemulsion. The solid black lines represent the fits (q range for fits up to $1.5 \, \text{nm}^{-1}$) of the ellipsoidal core-shell model. Data measured at SANS2D.

References

[1] J. N. Israelachvili, D. J. Mitchell, B. W. Ninham, "Theory of self-assembly of hydrocarbon amphiphiles into micelles and bilayers", *J. Chem. Soc. Faraday Trans. 2 Mol. Chem. Phys.* **1976**, *72*, 1525–1568, DOI: 10.1039/F29767201525.

[2] M. Karayianni, S. Pispas, "Block copolymer solution self-assembly: Recent advances, emerging trends, and applications", *J. Polym. Sci.* **2021**, *59*, 1874–1898, DOI: 10.1002/pol.20210430.

[3] J. F. Gohy, "Block copolymer micelles", *Adv. Polym. Sci.* **2005**, *190*, 65–136, DOI: 10.1007/12_048.

[4] P. Raffa, D. A. Z. Wever, F. Picchioni, A. A. Broekhuis, "Polymeric surfactants: Synthesis, properties, and links to applications", *Chem. Rev.* **2015**, *115*, 8504–8563, DOI: 10.1021/cr500129h.

[5] H. Cabral, K. Miyata, K. Osada, K. Kataoka, "Block Copolymer Micelles in Nanomedicine Applications", *Chem. Rev.* **2018**, *118*, 6844–6892, DOI: 10.1021/acs.chemrev.8b00199.

[6] C. Chassenieux, T. Nicolai, L. Benyahia, "Rheology of associative polymer solutions", *Curr. Opin. Colloid Interface Sci.* **2011**, *16*, 18–26, DOI: 10.1016/j.cocis.2010.07.007.

[7] P. Malo de Molina, C. Herfurth, A. Laschewsky, M. Gradzielski, "Multi-Bridging Polymers. Synthesis and Behaviour in Aqueous Solution", *Prog. Colloid Interface Sci.* **2011**, *138*, 67–72, DOI: 10.1007/978-3-642-19038-4.

[8] C. Booth, D. Attwood, "Effects of block architecture and composition on the association properties of poly(oxyalkylene) copolymers in aqueous solution", *Macromol. Rapid Commun.* **2000**, *21*, 501–527, DOI: 10.1002/1521-3927(20000601)21:9<501::AID-MARC501>3.0.CO;2-R.

[9] U. Kortemeier, J. Venzmer, A. Howe, B. Grüning, S. . Herrwerth, "Thickening Agents for Surfactant Systems", *SÖFW J.* **2010**, *136*, 30–40.

[10] B. Quienne, J. Pinaud, J. J. Robin, S. Caillol, "From Architectures to Cutting-Edge Properties, the Blooming World of Hydrophobically Modified Ethoxylated Urethanes (HEURs)", *Macromolecules* **2020**, *53*, 6754–6766, DOI: 10.1021/acs.macromol.0c01353.

[11] S. Wu, Q. Chen, "Advances and New Opportunities in the Rheology of Physically and Chemically Reversible Polymers", *Macromolecules* **2022**, *55*, 697–714, DOI: 10.1021/acs.macromol.1c01605.

[12] A. J. Reuvers, "Control of rheology of water-borne paints using associative thickeners", *Prog. Org. Coatings* **1999**, *35*, 171–181, DOI: 10.1016/S0300-9440(99)00014-4.

[13] I. Mussard in *Addit. Water-Borne Coatings*, Royal Society of Chemistry, Cambridge, **2007**, pp. 46–52, DOI: 10.1039/9781847550057-00046.

[14] K. Solc, K. Dusek, R. Koningsveld, H. Berghmans, ""Zero" and "off-zero" critical concentrations in solutions of polydisperse polymers with very high molar masses", *Collect. Czechoslov. Chem. Commun.* **1995**, *60*, 1661–1688, DOI: 10.1135/cccc19951661.

[15] D. G. Lessard, M. Ousalem, X. X. Zhu, A. Eisenberg, P. J. Carreau, "Study of the Phase Transition of Poly(N,N-diethylacrylamide) in Water by Rheology and Dynamic Light Scattering", *J. Polym. Sci. Part B Polym. Phys.* **2003**, *41*, 1627–1637, DOI: 10.1002/polb.10517.

[16] F. Meeussen, E. Nies, H. Berghmans, S. Verbrugghe, E. Goethals, F. Du Prez, "Phase behaviour of poly(N-vinyl caprolactam) in water", *Polymer* **2000**, *41*, 8597–8602, DOI: 10.1016/S0032-3861(00)00255-X.

[17] V. Aseyev, H. Tenhu, F. M. Winnik, "Non-ionic thermoresponsive polymers in water", *Adv. Polym. Sci.* **2011**, *242*, 29–89, DOI: 10.1007/12_2010_57.

[18] B. Jeong, Y. H. Bae, S. W. Kim, "Drug release from biodegradable injectable thermosensitive hydrogel of PEG-PLGA-PEG triblock copolymers", *J. Control. Release* **2000**, *63*, 155–163, DOI: 10.1016/S0168-3659(99)00194-7.

[19] Y. J. Kim, S. Choi, J. J. Koh, M. Lee, K. S. Ko, S. W. Kim, "Controlled release of insulin from injectable biodegradable triblock copolymer", *Pharm. Res.* **2001**, *18*, 548–550, DOI: 10.1023/A:1011074915438.

[20] S. Chen, J. Singh, "In Vitro Release of Levonorgestrel from Phase Sensitive and Thermosensitive Smart Polymer Delivery Systems", *Pharm. Dev. Technol.* **2005**, *10*, 319–325, DOI: 10.1081/pdt-54479.

[21] S. E. Kirkland, R. M. Hensarling, S. D. McConaughy, Y. Guo, W. L. Jarrett, C. L. McCormick, "Thermoreversible hydrogels from RAFT-synthesized BAB triblock copolymers: Steps toward biomimetic matrices for tissue regeneration", *Biomacromolecules* **2008**, *9*, 481–486, DOI: 10.1021/bm700968t.

[22] A. Basu, K. R. Kunduru, S. Doppalapudi, A. J. Domb, W. Khan, "Poly(lactic acid) based hydrogels", *Adv. Drug Deliv. Rev.* **2016**, *107*, 192–205, DOI: 10.1016/j.addr.2016.07.004.

[23] S. K. Filippov, A. Bogomolova, L. Kaberov, N. Velychkivska, L. Starovoytova, Z. Cernochova, S. E. Rogers, W. M. Lau, V. V. Khutoryanskiy, M. T. Cook, "Internal Nanoparticle Structure of Temperature-Responsive Self-Assembled PNIPAM-b-PEG-b-PNIPAM Triblock Copolymers in Aqueous Solutions: NMR,

SANS, and Light Scattering Studies", *Langmuir* **2016**, *32*, 5314–5323, DOI: 10.1021/acs.langmuir.6b00284.

[24] S. Cui, L. Yu, J. Ding, "Thermogelling of Amphiphilic Block Copolymers in Water: ABA Type versus AB or BAB Type", *Macromolecules* **2019**, *52*, 3697–3715, DOI: 10.1021/acs.macromol.9b00534.

[25] M. T. Cook, P. Haddow, S. B. Kirton, W. J. McAuley, "Polymers Exhibiting Lower Critical Solution Temperatures as a Route to Thermoreversible Gelators for Healthcare", *Adv. Funct. Mater.* **2021**, *31*, DOI: 10.1002/adfm.202008123.

[26] A. Sosnik, D. Cohn, "Ethoxysilane-capped PEO-PPO-PEO triblocks: A new family of reverse thermo-responsive polymers", *Biomaterials* **2004**, *25*, 2851–2858, DOI: 10.1016/j.biomaterials.2003.09.057.

[27] S. P. Quah, A. J. Smith, A. N. Preston, S. T. Laughlin, S. R. Bhatia, "Large-area alginate/PEO-PPO-PEO hydrogels with thermoreversible rheology at physiological temperatures", *Polymer* **2018**, *135*, 171–177, DOI: 10.1016/j.polymer.2017.12.003.

[28] B. M. Kahlweit, R. Strey, "Phase Behavior of Ternary Systems of the Type H2O-Oil-Nonionic Amphiphile (Microemulsions)", *Angew. Chem. Int. Ed.* **1985**, *24*, 654–668, DOI: 10.1002/anie.198506541.

[29] E. Ruckenstein, "The origin of thermodynamic stability of microemulsions", *Chem. Phys. Lett.* **1978**, *57*, 517–521, DOI: 10.1016/0009-2614(78)85311-1.

[30] V. Fischer, J. Marcus, D. Touraud, O. Diat, W. Kunz, "Toward surfactant-free and water-free microemulsions", *J. Colloid Interface Sci.* **2015**, *453*, 186–193, DOI: 10.1016/j.jcis.2015.04.069.

[31] D. Langevin, "Microemulsions and liquid crystals", *Mol. Cryst. Liq. Cryst.* **1986**, *138*, 259–305, DOI: 10.1080/00268948608071764.

[32] M. Gradzielski, H. Hoffmann, D. Langevin, "Solubilization of decane into the ternary system TDMAO/1-hexanol/water", *J. Phys. Chem.* **1995**, *99*, 12612–12623, DOI: 10.1021/j100033a039.

[33] H. Hoffmann, G. Ebert, "Tenside, Micellen und faszinierende Phänomene", *Angew. Chemie* **1988**, *100*, 933–944, DOI: 10.1002/ange.19881000707.

[34] M. Gradzielski, M. Duvail, P. M. De Molina, M. Simon, Y. Talmon, T. Zemb, "Using Microemulsions: Formulation Based on Knowledge of Their Mesostructure", *Chem. Rev.* **2021**, *121*, 5671–5740, DOI: 10.1021/acs.chemrev.0c00812.

[35] M. Simon, P. Krause, L. Chiappisi, L. Noirez, M. Gradzielski, "Structural control of polyelectrolyte/microemulsion droplet complexes (PEMECs) with different polyacrylates", *Chem. Sci.* **2019**, *10*, 385–397, DOI: 10.1039/c8sc04013c.

[36] A. Prause, A. Hörmann, V. Cristiglio, G. J. Smales, A. F. Thünemann, M. Gradzielski, G. H. Findenegg, "Incorporation and structural arrangement of microemulsion droplets in cylindrical pores of mesoporous silica", *Mol. Phys.* **2021**, *119*, e1913255, DOI: 10.1080/00268976.2021.1913255.

[37] T. F. Tadros, "Future developments in cosmetic formulations", *Int. J. Cosmet. Sci.* **1992**, *14*, 93–111, DOI: 10.1111/j.1467-2494.1992.tb00045.x.

[38] M.-J. Schwuger, K. Stickdorn, R. Schomäcker, "Microemulsions in Technical Processes", *Chem. Rev.* **1995**, *95*, 849–864, DOI: 10.1021/cr00036a003.

[39] *Industrial Applications of Microemulsions*, (Eds.: C. Solans, H. Kunieda), Marcel Dekker, Inc., New York, **1997**.

[40] F. H. Haegel, F. Dierkes, S. Kowalski, K. Mönig, M. J. Schwuger, G. Subklew, P. Thiele, "Soil remediation with microemulsions: Basic properties", *ACS Symp. Ser.* **1999**, *740*, 35–56, DOI: 10.1021/bk-2000-0740.ch004.

[41] A. Zarur, J. Ying, "Reverse microemulsion synthesis of nanostructured complex oxides for catalytic combustion", *Nature* **2000**, *403*, 65–67, DOI: 10.1038/47450.

[42] X. Zhao, R. P. Bagwe, W. Tan, "Development of organic-dye-doped silica nanoparticles in a reverse microemulsion", *Adv. Mater.* **2004**, *16*, 173–176, DOI: 10.1002/adma.200305622.

[43] R. Y. Parapat, V. Parwoto, M. Schwarze, B. Zhang, D. S. Su, R. Schomäcker, "A new method to synthesize very active and stable supported metal Pt catalysts: thermo-destabilization of microemulsions", *J. Mater. Chem.* **2012**, *22*, 11605, DOI: 10.1039/c2jm15468d.

[44] M. J. Lawrence, G. D. Rees, "Microemulsion-based media as novel drug delivery systems", *Adv. Drug Deliv. Rev.* **2012**, *64*, 175–193, DOI: 10.1016/j.addr.2012.09.018.

[45] M. Gradzielski, H. Hoffmann in *Handb. Sci. Technol.* (Eds.: P. Kumar, K. L. Mittal), CRC Press, New York, **1999**, Chapter 11, DOI: 10.1201/9780203752739.

[46] M. Magno, R. Tessendorf, B. Medronho, M. G. Miguel, C. Stubenrauch, "Gelled polymerizable microemulsions. Part 3 Rheology", *Soft Matter* **2009**, *5*, 4763–4772, DOI: 10.1039/b914281a.

[47] F. E. Antunes, K. Thuresson, B. Lindman, M. G. Miguel, "A rheological investigation of the association between a non-ionic microemulsion and hydrophobically modified PEG. Influence of polymer architecture", *Colloids Surfaces A Physicochem. Eng. Asp.* **2003**, *215*, 87–100, DOI: 10.1016/S0927-7757(02)00418-1.

[48] P. Malo De Molina, M. S. Appavou, M. Gradzielski, "Oil-in-water microemulsion droplets of TDMAO/decane interconnected by the telechelic C18-EO150-C18: Clustering and network formation", *Soft Matter* **2014**, *10*, 5072–5084, DOI: 10.1039/c4sm00501e.

[49] W. Meier, A. Falk, M. Odenwald, F. Stieber, "Microemulsion elastomers", *Colloid Polym. Sci.* **1996**, *274*, 218–226, DOI: 10.1007/BF00665638.

[50] C. Quellet, H. F. Eicke, W. Sager, "Formation of microemulsion-based gelatin gels", *J. Phys. Chem.* **1991**, *95*, 5642–5655, DOI: 10.1021/j100167a050.

[51] M. Filali, R. Aznar, M. Svenson, G. Porte, J. Appell, "Swollen micelles plus hydrophobically modified hydrosoluble polymers in aqueous solutions: Decoration versus bridging. A small angle neutron scattering study", *J. Phys. Chem. B* **1999**, *103*, 7293–7301, DOI: 10.1021/jp990980d.

[52] V. Testard, J. Oberdisse, C. Ligoure, "Monte Carlo simulations of colloidal pair potential induced by telechelic polymers: Statistics of loops and bridges", *Macromolecules* **2008**, *41*, 7219–7226, DOI: 10.1021/ma8005813.

[53] J. M. Sarraguça, A. A. Pais, P. Linse, "Structure of microemulsion - ABA triblock copolymer networks", *Langmuir* **2008**, *24*, 11153–11163, DOI: 10.1021/la801658k.

[54] S. Maccarrone, H. Frielinghaus, J. Allgaier, D. Richter, P. Lindner, "SANS study of polymer-linked droplets", *Langmuir* **2007**, *23*, 9559–9562, DOI: 10.1021/la7020353.

[55] P. Malo de Molina, F. S. Ihlefeldt, S. Prévost, C. Herfurth, M. S. Appavou, A. Laschewsky, M. Gradzielski, "Phase behavior of nonionic microemulsions with multi-end-capped polymers and its relation to the mesoscopic structure", *Langmuir* **2015**, *31*, 5198–5209, DOI: 10.1021/acs.langmuir.5b00817.

[56] D. E. Bergbreiter, R. Hughes, J. Besinaiz, C. Li, P. L. Osburn, "Phase-Selective Solubility of Poly(N-alkylacrylamide)s", *J. Am. Chem. Soc.* **2003**, *125*, 8244–8249, DOI: 10.1021/ja0349498.

[57] R. Pelton, "Poly(N-isopropylacrylamide) (PNIPAM) is never hydrophobic", *J. Colloid Interface Sci.* **2010**, *348*, 673–674, DOI: 10.1016/j.jcis.2010.05.034.

[58] M. Hechenbichler, A. Prause, M. Gradzielski, A. Laschewsky, "Thermoresponsive Self-Assembly of Twofold Fluorescently Labeled Block Copolymers in Aqueous Solution and Microemulsions", *Langmuir* **2022**, *38*, 5166–5182, DOI: 10.1021/acs.langmuir.1c02318.

[59] C. Valenta, K. Schultz, "Influence of carrageenan on the rheology and skin permeation of microemulsion formulations", *J. Control. Release* **2004**, *95*, 257–265, DOI: 10.1016/j.jconrel.2003.11.020.

[60] S. Ito, "Phase Transition of Aqueous Solution of Poly(N-alkylacrylamide) Derivatives - Effects of Side Chain Structures", *Kobunshi Ronbunshu* **1989**, *46*, 437–443, DOI: 10.1295/koron.46.437.

[61] K. Ulbrich, J. Kopeček, "Cross-linked copolymers of N,N-diethylacrylamide with improved mechanical properties", *J. Polym. Sci.* **1979**, *66*, 209–219, DOI: 10.1002/polc.5070660122.

[62] M. Heskins, J. E. Guillet, "Solution Properties of Poly(N-isopropylacrylamide)", *J. Macromol. Sci. Part A - Chem.* **1968**, *2*, 1441–1455, DOI: 10.1080/10601326808051910.

[63] K. Skrabania, J. Kristen, A. Laschewsky, Ö. Akdemir, A. Hoth, J. F. Lutz, "Design, synthesis, and aqueous aggregation behavior of nonionic single and multiple thermoresponsive polymers", *Langmuir* **2007**, *23*, 84–93, DOI: 10.1021/la061509w.

[64] A. Prause, M. Hechenbichler, B. von Lospichl, A. Feoktystov, R. Schweins, N. Mahmoudi, A. Laschewsky, M. Gradzielski, "Aggregation Behavior of Nonsymmetrically End-Capped Thermoresponsive Block Copolymers in Aqueous Solutions: Between Polymer Coils and Micellar States", *Macromolecules* **2022**, *55*, 5849–5863, DOI: 10.1021/acs.macromol.2c00878.

[65] A. Prause, M. Hechenbichler, R. F. Schmidt, M. Simon, S. Prévost, L. P. Cavalcanti, Y. Talmon, A. Laschewsky, M. Gradzielski, "Rheological Control of Aqueous Dispersions by Thermoresponsive BAB* Copolymers of Different Architectures", *Macromolecules* **2023**, *56*, 104–121, DOI: 10.1021/acs.macromol.2c01965.

[66] C. Wohlfarth, *Polymers*, (Eds.: M. D. Lechner, K. F. Arndt), Springer-Verlag Berlin Heidelberg, **2010**, pp. 14–148, DOI: 10.1007/978-3-642-02890-8_724.

[67] R. F. Schmidt, Bachelor Thesis, Technische Universität Berlin, **2020**.

[68] J. E. Wong, T. M. Duchscherer, G. Pietraru, D. T. Cramb, "Novel fluorescence spectral deconvolution method for determination of critical micelle concentrations using the fluorescence probe PRODAN", *Langmuir* **1999**, *15*, 6181–6186, DOI: 10.1021/la981716z.

[69] T. Parasassi, E. K. Krasnowska, L. Bagatolli, E. Gratton, "Laurdan and Prodan as Polarity-Sensitive Fluorescent Membrane Probes", *J. Fluoresc.* **1998**, *8*, 365–373, DOI: 10.1023/A:1020528716621.

[70] J. R. Bellare, H. T. Davis, L. E. Scriven, Y. Talmon, "Controlled environment vitrification system: An improved sample preparation technique", *J. Electron Microsc. Tech.* **1988**, *10*, 87–111, DOI: 10.1002/jemt.1060100111.

[71] Y. Talmon, "The study of nanostructured liquids by cryogenic-temperature electron microscopy - A status report", *J. Mol. Liq.* **2015**, *210*, 2–8, DOI: 10.1016/j.molliq.2015.03.054.

[72] A. Prause, SimplightQt, https://git.tu-berlin.de/MolMat/SimplightQt (last access on 2022-04-28).

[73] H. Wu, "Correlations between the Rayleigh ratio and the wavelength for toluene and benzene", *Chem. Phys.* **2010**, *367*, 44–47, DOI: 10.1016/j.chemphys.2009.10.019.

[74] O. Glatter, J. Sieberer, H. Schnablegger, "A Comparative Study on Different Scattering Techniques and data evaluation methods for sizing of colloidal systems using light scattering", *Part. Part. Syst. Charact.* **1991**, *8*, 274–281, DOI: 10.1002/ppsc.19910080150.

[75] S. W. Provencher, "A constrained regularization method for inverting data represented by linear algebraic or integral equations", *Comput. Phys. Commun.* **1982**, *27*, 213–227, DOI: 10.1016/0010-4655(82)90173-4.

[76] H. Frielinghaus, A. Feoktystov, I. Berts, G. Mangiapia, "KWS-1: Small-angle scattering diffractometer", *J. large-scale Res. Facil. JLSRF* **2015**, *1*, 26–29, DOI: 10.17815/jlsrf-1-26.

[77] A. V. Feoktystov, H. Frielinghaus, Z. Di, S. Jaksch, V. Pipich, M. S. Appavou, E. Babcock, R. Hanslik, R. Engels, G. Kemmerling, H. Kleines, A. Ioffe, D. Richter, T. Brückel, "KWS-1 high-resolution small-angle neutron scattering instrument at JCNS: Current state", *J. Appl. Crystallogr.* **2015**, *48*, 61–70, DOI: 10.1107/S1600576714025977.

[78] V. Pipich, QtiSAS: user-friendly program for reduction, visualization, analysis and fit of SA(N)S data, http://www.qtisas.com (last access on 2022-04-28).

[79] P. Lindner, R. Schweins, "The D11 small-angle scattering instrument: A new benchmark for SANS", *Neutron News* **2010**, *21*, 15–18, DOI: 10.1080/10448631003697985.

[80] C. D. Dewhurst, GRASP, https://www.ill.eu/users/support-labs-infrastructure/software-scientific-tools/grasp/ (last access on 2022-05-05).

[81] C. D. Dewhurst, "D33 - A third small-angle neutron scattering instrument at the Institut Laue Langevin", *Meas. Sci. Technol.* **2008**, *19*, DOI: 10.1088/0957-0233/19/3/034007.

[82] D. Richard, M. Ferrand, G. J. Kearley, "Analysis and visualisation of neutron-scattering data", *J. Neutron Res.* **1996**, *4*, 33–39, DOI: 10.1080/10238169608200065.

[83] STFC Rutherford Appleton Laboratory, ISIS Pulsed Neutron Source, https://www.isis.stfc.ac.uk (last access on 2022-04-28).

[84] O. Arnold, J. C. Bilheux, J. M. Borreguero, A. Buts, S. I. Campbell, L. Chapon, M. Doucet, N. Draper, R. Ferraz Leal, M. A. Gigg, V. E. Lynch, A. Markvardsen, D. J. Mikkelson, R. L. Mikkelson, R. Miller, K. Palmen, P. Parker, G. Passos, T. G. Perring, P. F. Peterson, S. Ren, M. A. Reuter, A. T. Savici, J. W. Taylor, R. J. Taylor, R. Tolchenov, W. Zhou, J. Zikovsky, "Mantid - Data analysis and visualization package for neutron scattering and μ SR experiments", *Nucl. Instruments Methods Phys. Res. Sect. A Accel. Spectrometers Detect. Assoc. Equip.* **2014**, *764*, 156–166, DOI: 10.1016/j.nima.2014.07.029.

[85] R. K. Heenan, S. E. Rogers, D. Turner, A. E. Terry, J. Treadgold, S. M. King, "Small angle neutron scattering using sans2d", *Neutron News* **2011**, *22*, 19–21, DOI: 10.1080/10448632.2011.569531.

[86] SASview, Instrumental Smearing, https://www.sasview.org/docs/user/qtgui/Perspectives/Fitting/resolution.html (last access on 2022-05-09).

[87] T. Zinn, L. Willner, K. D. Knudsen, R. Lund, "Self-Assembly of Mixtures of Telechelic and Monofunctional Amphiphilic Polymers in Water: From Clusters to Flowerlike Micelles", *Macromolecules* **2017**, *50*, 7321–7332, DOI: 10.1021/acs.macromol.7b01501.

[88] R. Schweins, K. Huber, "Particle scattering factor of pearl necklace chains", *Macromol. Symp.* **2004**, *211*, 25–42, DOI: 10.1002/masy.200450702.

[89] J. S. Pedersen, M. C. Gerstenberg, "Scattering Form Factor of Block Copolymer Micelles", *Macromolecules* **1996**, *29*, 1363–1365, DOI: 10.1021/ma9512115.

[90] B. Hammouda, M. H. Kim, "The empirical core-chain model", *J. Mol. Liq.* **2017**, *247*, 434–440, DOI: 10.1016/j.molliq.2017.09.114.

[91] Y. Wei, M. J. Hore, "Characterizing polymer structure with small-angle neutron scattering: A Tutorial", *J. Appl. Phys.* **2021**, *129*, DOI: 10.1063/5.0045841.

[92] D. J. Kinning, E. L. Thomas, "Hard-Sphere Interactions Between Spherical Domains in Diblock Copolymers", *Macromolecules* **1984**, *17*, 1712–1718, DOI: 10.1021/ma00139a013.

[93] S. E. Paulin, B. J. Ackerson, "Observation of a phase transition in the sedimentation velocity of hard spheres", *Phys. Rev. Lett.* **1990**, *64*, 2663–2666, DOI: 10.1103/PhysRevLett.64.2663.

[94] R. J. Baxter, "Percus-Yevick equation for hard spheres with surface adhesion", *J. Chem. Phys.* **1968**, *49*, 2770–2774, DOI: 10.1063/1.1670482.

[95] M. Gradzielski, A. Rauscher, H. Hoffmann, "Hydrophobically cross-linked micellar solutions: microstructure and properties of the solutions", *J. Phys. IV* **1993**, *3 (C1)*, 65–79, DOI: 10.1051/jp4:1993107.

[96] F. Molino, J. Appell, M. Filali, E. Michel, G. Porte, S. Mora, E. Sunyer, "A transient network of telechelic polymers and microspheres: Structure and rheology", *J. Phys. Condens. Matter* **2000**, *12*, A491–A498, DOI: 10.1088/0953-8984/12/8A/368.

[97] C. Herfurth, D. Voll, J. Buller, J. Weiss, C. Barner-Kowollik, A. Laschewsky, "Radical addition fragmentation chain transfer (RAFT) polymerization of ferrocenyl (Meth)-acrylates", *J. Polym. Sci. Part A Polym. Chem.* **2012**, *50*, 108–118, DOI: 10.1002/pola.24994.

[98] C. Herfurth, A. Laschewsky, L. Noirez, B. von Lospichl, M. Gradzielski, "Thermoresponsive (star) block copolymers from one-pot sequential RAFT polymerizations and their self-assembly in aqueous solution", *Polymer* **2016**, *107*, 422–433, DOI: 10.1016/j.polymer.2016.09.089.

[99] F. Fischer, D. Zufferey, R. Tahoces, "Lower critical solution temperature in superheated water: The highest in the poly(N,N-dialkylacrylamide) series", *Polym. Int.* **2011**, *60*, 1259–1262, DOI: 10.1002/pi.3071.

[100] N. A. Platé, T. L. Lebedeva, L. I. Valuev, "Lower Critical Solution Temperature in Aqueous Solutions of N-Alkyl-Substituted Polyacrylamides", *Polym. J.* **1999**, *31*, 21–27, DOI: 10.1295/polymj.31.21.

[101] M. Hechenbichler, A. Laschewsky, M. Gradzielski, "Poly(N,N-bis(2-methoxyethyl)acryl-amide), a thermoresponsive non-ionic polymer combining the amide and the ethyleneglycolether motifs", *Colloid Polym. Sci.* **2021**, *299*, 205–219, DOI: 10.1007/s00396-020-04701-9.

[102] H. Mao, C. Li, Y. Zhang, S. Furyk, P. S. Cremer, D. E. Bergbreiter, "High-throughput studies of the effects of polymer structure and solution components on the phase separation of thermoresponsive polymers", *Macromolecules* **2004**, *37*, 1031–1036, DOI: 10.1021/ma035590a.

[103] H. Shirota, N. Kuwabara, K. Ohkawa, K. Horie, "Deuterium isotope effect on volume phase transition of polymer gel: Temperature dependence", *J. Phys. Chem. B* **1999**, *103*, 10400–10408, DOI: 10.1021/jp992401a.

[104] H. Y. Liu, X. X. Zhu, "Lower critical solution temperatures of N-substituted acrylamide copolymers in aqueous solutions", *Polymer* **1999**, *40*, 6985–6990, DOI: 10.1016/S0032-3861(98)00858-1.

[105] A. Miasnikova, A. Laschewsky, G. De Paoli, C. M. Papadakis, P. Müller-Buschbaum, S. S. Funari, "Thermoresponsive hydrogels from symmetrical triblock copolymers poly-(styrene-block-(methoxy diethylene glycol acrylate)-block-styrene)", *Langmuir* **2012**, *28*, 4479–4490, DOI: 10.1021/la204665q.

[106] A. J. Convertine, B. S. Lokitz, Y. Vasileva, L. J. Myrick, C. W. Scales, A. B. Lowe, C. L. McCormick, "Direct synthesis of thermally responsive DMA/NIPAM diblock and DMA/NIPAM/DMA triblock copolymers via aqueous, room temperature RAFT polymerization", *Macromolecules* **2006**, *39*, 1724–1730, DOI: 10.1021/ma0523419.

[107] K. Skrabania, W. Li, A. Laschewsky, "Synthesis of double-hydrophilic BAB triblock copolymers via RAFT polymerisation and their thermoresponsive self-assembly in water", *Macromol. Chem. Phys.* **2008**, *209*, 1389–1403, DOI: 10.1002/macp.200800108.

[108] A. Halperin, M. Kröger, F. M. Winnik, "Poly(N-isopropylacrylamide) Phase Diagrams: Fifty Years of Research", *Angew. Chemie - Int. Ed.* **2015**, *54*, 15342–15367, DOI: 10.1002/anie.201506663.

[109] A. M. Bivigou-Koumba, J. Kristen, A. Laschewsky, P. Müller-Buschbaum, C. M. Papadakis, "Synthesis of symmetrical triblock copolymers of styrene and N-isopropyl-acrylamide using bifunctional bis(trithiocarbonate)s as RAFT agents", *Macromol. Chem. Phys.* **2009**, *210*, 565–578, DOI: 10.1002/macp.200800575.

[110] P. Kujawa, F. Segui, S. Shaban, C. Diab, Y. Okada, F. Tanaka, F. M. Winnik, "Impact of end-group association and main-chain hydration on the thermosensitive properties of hydrophobically modified telechelic poly(N-isopropylacrylamides) in water", *Macromolecules* **2006**, *39*, 341–348, DOI: 10.1021/ma051876z.

[111] J. Weiss, C. Böttcher, A. Laschewsky, "Self-assembly of double thermoresponsive block copolymers end-capped with complementary trimethylsilyl groups", *Soft Matter* **2011**, *7*, 483–492, DOI: 10.1039/c0sm00531b.

[112] H. Cheng, L. Shen, C. Wu, "LLS and FTIR studies on the hysteresis in association and dissociation of poly(N-isopropylacrylamide) chains in water", *Macromolecules* **2006**, *39*, 2325–2329, DOI: 10.1021/ma052561m.

[113] B. Hammouda, "Analysis of the Beaucage model", *J. Appl. Crystallogr.* **2010**, *43*, 1474–1478, DOI: 10.1107/S0021889810033856.

[114] E. Hecht, K. Mortensen, H. Hoffmann, "L3 Phase in a Binary Block Copolymer/Water System", *Macromolecules* **1995**, *28*, 5465–5476, DOI: 10.1021/ma00120a010.

[115] K. Mortensen, Y. Talmon, "Cryo-TEM and SANS Microstructural Study of Pluronic Polymer Solutions", *Macromolecules* **1995**, *28*, 8829–8834, DOI: 10.1021/ma00130a016.

[116] W. F. Polik, W. Burchard, "Static Light Scattering from Aqueous Poly(ethylene oxide) Solutions in the Temperature Range 20-90 Â°C", *Macromolecules* **1983**, *16*, 978–982, DOI: 10.1021/ma00240a030.

[117]   Y. Croonen, E. Geladé, M. Van Der Zegel, M. Van Der Auweraer, H. Vandendriessche, F. C. De Schryver, M. Almgren, "Influence of salt, detergent concentration, and temperature on the fluorescence quenching of 1-methylpyrene in sodium dodecyl sulfate with m-dicyanobenzene", *J. Phys. Chem.* **1983**, *87*, 1426–1431, DOI: 10.1021/j100231a029.

[118]   A. Malliaris, J. Lang, R. Zana, "Micellar aggregation numbers at high surfactant concentration", *J. Colloid Interface Sci.* **1986**, *110*, 237–242, DOI: 10.1016/0021-9797(86)90372-3.

[119]   L. Wattebled, A. Laschewsky, A. Moussa, J. L. Habib-Jiwan, "Aggregation numbers of cationic oligomeric surfactants: A time-resolved fluorescence quenching study", *Langmuir* **2006**, *22*, 2551–2557, DOI: 10.1021/la052414h.

[120]   R. Zana, J. H. Mathias, M. J. Rosen, L. Davenport, "Fluorescence Study of Premicellar Aggregation in Cationic Gemini Surfactants", *Langmuir* **2002**, *18*, 7759–7761, DOI: 10.1021/la0200360.

[121]   O. A. Kucherak, P. Didier, Y. Mèly, A. S. Klymchenko, "Fluorene analogues of prodan with superior fluorescence brightness and solvatochromism", *J. Phys. Chem. Lett.* **2010**, *1*, 616–620, DOI: 10.1021/jz9003685.

[122]   F. Moyano, M. A. Biasutti, J. J. Silber, N. M. Correa, "New insights on the behavior of PRODAN in homogeneous media and in large unilamellar vesicles", *J. Phys. Chem. B* **2006**, *110*, 11838–11846, DOI: 10.1021/jp057208x.

[123]   S. Sun, M. P. Heitz, S. A. Perez, L. A. Colón, S. Bruckenstein, F. V. Bright, "6-Propionyl-2-(N,N-dimethylamino)naphthalene (PRODAN) revisited", *Appl. Spectrosc.* **1997**, *51*, 1316–1322, DOI: 10.1366/0003702971941980.

[124]   B. A. Rowe, C. A. Roach, J. Lin, V. Asiago, O. Dmitrenko, S. L. Neal, "Spectral heterogeneity of PRODAN fluorescence in isotropic solvents revealed by multivariate photokinetic analysis", *J. Phys. Chem. A* **2008**, *112*, 13402–13412, DOI: 10.1021/jp802260y.

[125]   C. C. Vequi-Suplicy, Y. Orozco-Gonzalez, M. T. Lamy, S. Canuto, K. Coutinho, "A new interpretation of the absorption and the dual fluorescence of Prodan in solution", *J. Chem. Phys.* **2020**, *153*, DOI: 10.1063/5.0025013.

[126]   M. S. Orellano, D. A. Chiappetta, J. J. Silber, R. D. Falcone, N. M. Correa, "Monitoring the microenvironment inside polymeric micelles using the fluorescence probe 6-propionyl-2-dimethylaminonaphthalene (PRODAN)", *J. Mol. Liq.* **2021**, *343*, 117552, DOI: 10.1016/j.molliq.2021.117552.

[127]   T. VanAken, S. Foxall-VanAken, S. Castleman, S. Ferguson-Miller, "Methods Thin-Layer Chromatographic Systems for Analyzing the Reaction Alkyl Glycoside Formation from Acetobromo Sugar and Alcohol", *Methods Enzymol.* **1986**, *125*, 27–35, DOI: 10.1016/S0076-6879(86)25005-3.

[128] G. Weber, F. J. Farris, "Synthesis and Spectral Properties of a Hydrophobic Fluorescent Probe: 6-Propionyl-2-(dimethylamino)naphthalene", *Biochemistry* **1979**, *18*, 3075–3078, DOI: 10.1021/bi00581a025.

[129] M. Chen, K. P. Ghiggino, A. W. Mau, E. Rizzardo, S. H. Thang, G. J. Wilson, "Synthesis of light harvesting polymers by RAFT methods", *Chem. Commun.* **2002**, *19*, 2276–2277, DOI: 10.1039/b206166j.

[130] N. Zhou, Z. Zhang, W. Zhang, J. Zhu, X. Zhu, "RAFT polymerization of styrene mediated by naphthalene-containing RAFT agents and optical properties of the polymers", *Polymer* **2009**, *50*, 4352–4362, DOI: 10.1016/j.polymer.2009.06.029.

[131] A. Enzenberg, A. Laschewsky, C. Boeffel, E. Wischerhoff, "Influence of the near molecular vicinity on the temperature regulated fluorescence response of poly(N-vinylcapro-lactam)", *Polymers* **2016**, *8*, DOI: 10.3390/polym8040109.

[132] S. Inal, J. D. Kölsch, L. Chiappisi, D. Janietz, M. Gradzielski, A. Laschewsky, D. Neher, "Structure-related differences in the temperature-regulated fluorescence response of LCST type polymers", *J. Mater. Chem. C* **2013**, *1*, 6603–6612, DOI: 10.1039/c3tc31304b.

[133] A. Prause, M. Hechenbichler, R. F. Schmidt, S. Prévost, L. Cavalcanti, A. Laschewsky, M. Gradzielski, "Modifying the Properties of Microemulsion Droplets by Addition of Thermoresponsive BAB* Copolymers", *Langmuir* **2023**, DOI: 10.1021/acs.langmuir.2c03103.

[134] U. Batra, W. B. Russel, M. Pitsikalis, S. Sioula, J. W. Mays, J. S. Huang, "Phase behavior and viscoelasticity of AOT microemulsions containing triblock copolymers", *Macromolecules* **1997**, *30*, 6120–6126, DOI: 10.1021/ma970465i.

[135] O. A. Chat, N. Nazir, P. A. Bhat, P. A. Hassan, V. K. Aswal, A. A. Dar, "Aggregation and Rheological Behavior of the Lavender Oil-Pluronic P123 Microemulsions in Water-Ethanol Mixed Solvents", *Langmuir* **2018**, *34*, 1010–1019, DOI: 10.1021/acs.langmuir.7b02845.

[136] I. Lynch, L. Piculell, "Size, concentration, and solvency effects on the viscosifying behavior of PEO-PS-PEO triblock copolymers in AOT oil-continuous microemulsions", *J. Phys. Chem. B* **2004**, *108*, 7515–7522, DOI: 10.1021/jp049147t.

[137] M. Odenwald, H. F. Eicke, W. Meier, "Transient Networks by ABA Triblock Copolymers and Microemulsions: A Rheological Study", *Macromolecules* **1995**, *28*, 5069–5074, DOI: 10.1021/ma00118a040.

[138] X. Y. Zhao, J. Xu, L. Q. Zheng, X. W. Li, "Preparation of temperature-sensitive microemulsion-based gels formed from a triblock copolymer", *Colloids Surfaces A Physicochem. Eng. Asp.* **2007**, *307*, 100–107, DOI: 10.1016/j.colsurfa.2007.05.006.

[139] R. F. Schmidt, A. Prause, S. Prévost, M. Gradzielski, "Formulation of a Biocompatible Microemulsion Based on Tween 20, 2-Ethylhexylglycerin and Isopropyl Palmitate", **2022**, in preparation.

[140] M. Corti, C. Minero, V. Degiorgio, "Cloud point transition in nonionic micellar solutions", *J. Phys. Chem.* **1984**, *88*, 309–317, DOI: 10.1021/j150646a029.

[141] R. Zana, C. Weill, "Effect of temperature on the aggregation behaviour of nonionic surfactants in aqueous solutions", *J. Phys. Lettres* **1985**, *46*, 953–960, DOI: 10.1051/jphyslet:019850046020095300.

[142] B. Farago, M. Gradzielski, "The effect of the charge density of microemulsion droplets on the bending elasticity of their amphiphilic film", *J. Chem. Phys.* **2001**, *114*, 10105–10122, DOI: 10.1063/1.1362690.

[143] M. Gradzielski, D. Langevin, B. Farago, "Experimental investigation ofthe structure of nonionic microemulsions and their relation to the bending elasticity of the amphiphilic film", *Phys. Rev. E* **1996**, *53*, 3900–3919, DOI: 10.1103/PhysRevE.53.3900.

[144] P. G. Nilsson, H. Wennerström, B. Lindman, "Structure of micellar solutions of nonionic surfactants. Nuclear magnetic resonance self-diffusion and proton relaxation studies of poly(ethylene oxide) alkyl ethers", *J. Phys. Chem.* **1983**, *87*, 1377–1385, DOI: 10.1021/j100231a021.

[145] T. Shikata, M. Okuzono, N. Sugimoto, "Temperature-Dependent Hydration/Dehydration Behavior of Poly(ethylene oxide)s in Aqueous Solution", *Macromolecules* **2013**, *46*, 1956–1961, DOI: 10.1021/ma3026282.

Abbreviations

Acronyms

CMC . . . . . . critical micelle concentration

cryo-TEM . . . cryogenic transmission electron microscopy

DLS . . . . . . dynamic light scattering

FRET . . . . . Förster resonance energy transfer

HM . . . . . . hydrophobically modified

LCST . . . . lower critical solution temperature

LVE . . . . . . linear viscoelastic regime

ME . . . . microemulsion

NMR . . . . . nuclear magnetic resonance

O/W . . . . . . oil-in-water

ORT . . . . . . optimized regularization technique

RAFT . . . . reversible-addition-fragmentation chain-transfer

ROI . . . . . . region of interest

SANS . . . . . small-angle neutron scattering

SEC . . . . . . size exclusion chromatography

SLS . . . . . . static light scattering

TOF . . . . . . time-of-flight

TR . . . . thermoresponsive

UV . . . . ultraviolet light

Vis . . . . visible light

W/O . . . . . . water-in-oil

Physical Properties

φ . . . . angle of orientation (—)

2θ . . . . scattering angle (°)

$g^{(1)}$ . . . . field autocorrelation function (—)

$g^{(2)}$ . . . . intensity autocorrelation function (—)

D . . . . diffusion coefficient ($\mu m^2 s^{-1}$)

c_g . . . . mass concentration ($g\,L^{-1}$)

c . . . . molar concentration ($mmol\,L^{-1}$)

c_{ME} . . . . . . molar concentration of microemulsion droplets ($mmol\,L^{-1}$)

c_{surf} . . . . . . molar concentration of surfactant ($mmol\,L^{-1}$)

N_{Av} . . . . . . Avogadro's number (mol^{-1})

k_B . . . . Boltzmann constant ($J\,K^{-1}$)

DP_n . . . . . . degree of polymerisation (—)

DP_n^{NMR} . . . . degree of polymerisation determined by NMR (—)

DP_n^{theo} . . . . . degree of polymerisation determined by yield (—)

ρ . . . . mass density ($g\,cm^{-3}$)

ρ_{ME} . . . . . . mass density of microemulsion ($g\,cm^{-3}$)

ρ_p . . . . mass density of polymer ($g\,cm^{-3}$)

^1N . . . . number density (nm^{-3})

SLD . . . . . . scattering length density ($10^{-4}\,nm^{-2}$)

SLD_p . . . . . . scattering length density of polymer ($10^{-4}\,nm^{-2}$)

$Đ$ . . . . dispersity (—)

R_{ee} . . . . end-to-end distance (nm)

F_{max} . . . . . . maximum emission (—)

β . . . . coherence factor (—)

K . . . . contrast factor ($mol\,cm^2\,g^{-2}$)

P . . . . laser intensity (mW)

I . . . . scattering intensity (cm^{-1})

l_C . . . . collimation (m)

L_p . . . . contour length of polymer (nm)

l_SD . . . . sample–detector distance (m)

a . . . . statistical segment length (nm)

G' . . . . storage modulus (Pa)

G'' . . . . loss modulus (Pa)

M_w . . . . mass averaged molecular weight ($\mathrm{kg\,mol^{-1}}$)

M_n . . . . number averaged molecular weight ($\mathrm{kg\,mol^{-1}}$)

$M_\mathrm{n}^\mathrm{NMR}$ . . . . . number averaged molecular weight determined by NMR ($\mathrm{kg\,mol^{-1}}$)

$M_\mathrm{n}^\mathrm{SEC}$ . . . . . number averaged molecular weight determined by SEC ($\mathrm{kg\,mol^{-1}}$)

$M_\mathrm{n}^\mathrm{UV/Vis}$ . . . . number averaged molecular weight determined by UV/Vis ($\mathrm{kg\,mol^{-1}}$)

$M_\mathrm{n}^\mathrm{theo}$ . . . . number averaged molecular weight determined by yield ($\mathrm{kg\,mol^{-1}}$)

N_agg . . . . . . aggregation number (—)

N_eff . . . . . . effective aggregation number (—)

$N_\mathrm{eff}^\mathrm{SANS}$ . . . . effective aggregation number determined by SANS (—)

$N_\mathrm{eff}^\mathrm{SLS}$ . . . . . effective aggregation number determined by SLS (—)

N_clu . . . . . . number of micelles per cluster (nm)

N_surf . . . . . number of surfactant molecules per microemulsion droplet (—)

λ_shs . . . . . . attraction strength (—)

ν . . . . excluded volume parameter (—)

x_sh . . . . polymer chain fraction in the shell (%)

f_p . . . . polymer mass fractal dimension (—)

n_hs . . . . scaling parameter for R_hs (—)

R_c . . . . core radius (nm)

R_csh . . . . . core-shell radius (nm)

R_g . . . . radius of gyration (nm)

R_hs . . . . hard-sphere radius (nm)

R_h . . . . hydrodynamic radius (nm)

R_s . . . . spherical radius (nm)

R_v . . . . volume equivalent radius (nm)

CR . . . . count-rate (kHz)

Γ . . . . decay-rate (s^{-1})

$\dot{\gamma}$ . . . . shear-rate (s^{-1})

ε . . . . aspect ratio (—)

$c_\mathrm{co}/c_\mathrm{surf}$ . . . . cosurfactant-to-surfactant ratio (—)

$c_\mathrm{oil}/c_\mathrm{surf}$ . . . . oil-to-surfactant ratio (—)

$N_\mathrm{p}/N_\mathrm{ME}$ . . . polymer chains per microemulsion droplet (—)

α . . . . swelling ratio (—)

$\mathrm{d}n/\mathrm{d}c_\mathrm{g}$ . . . . refractive index increment (cm^3 g^{-1})

q . . . . modulus of the scattering vector (nm^{-1})

S_eff . . . . effective structure factor (—)

T . . . . absolute temperature (K)

CP_LCST . . . . macroscopic phase separation temperature (°C)

T_sh . . . . shell thickness (nm)

τ . . . . correlation time (s)

η . . . . dynamic viscosity (Pa s)

η_0 . . . . zero-shear viscosity (Pa s)

η_0^ref . . . . . . reference zero-shear viscosity (Pa s)

$\eta_0\big/\eta_0^\mathrm{ref}$ . . . . normalized zero-shear viscosity (—)

V . . . . volume (nm^3)

ϕ_hs . . . . hard-sphere volume fraction (—)

ϕ_ME . . . . . . volume fraction of the microemulsion (—)

V_n . . . . molecular volume (nm^3)

V_sp . . . . . . partial specific volume (cm^3 g^{-1})

λ . . . . wavelength (nm)

λ_max . . . . . . wavelength of the maximum emission (nm)